Atomistic and Continuum Modeling of Laser-Induced Phase Transformations, Generation of Crystal Defects, and Modification of Surface Morphology in Silicon and Metal Targets

---

A Dissertation

Presented to

the faculty of the School of Engineering and Applied Science

University of Virginia

---

in partial fulfillment of the requirements for the degree of

Doctor of Philosophy

by

Miao He

July

2019

Approval Sheet

The dissertation

is submitted in partial fulfilment of the requirements

for the degree of

Doctor of Philosophy

Miao He
Author

The dissertation has been read and approved by the examining committee:

Leonid V. Zhigilei
Advisor

Jerrold A. Floro

Mool C. Gupta

James M. Fitz-Gerald

Petra Reinke

Accepted for the School of Engineering and Applied Science:

Graig H. Benson, Dean, School of Engineering and Applied Science

July 2019

Acknowledgement

I would like to first express my deepest appreciation and gratitude to my advisor, Prof. Leonid V. Zhigilei, for his excellent mentorship throughout my PhD study. Since I joined the Computational Materials Group in 2013, Prof. Zhigilei has been helping me in developing my professional skills and knowledge. His great passion and deep insights in materials science have always been a great inspiration to me. I sincerely appreciate his professional guidance and constructive feedback for my projects. Prof. Zhigilei is not only a great advisor, but also a model for my future career, from whom I learned a rigorous attitude and persistent commitment to scientific research. Although the PhD study is quite challenging and sometimes my progress is slow, Leo has always been patient and supportive. Without his encouragement and help, I could not solve the problems and grow fast in my academic life. I am also extremely grateful to Leo for involving me in a variety of interesting projects in collaboration with other research groups, and providing opportunities to present my results in international conferences, from which I benefit a lot.

I would also like to thank Prof. Jerrold A. Floro, Prof. Mool C. Gupta, Prof. James M. Fitz-Gerald, and Prof. Petra Reinke, for their kind acceptance to serve as members in my dissertation committee. Their advices have been greatly valuable to my research.

I would like to express my gratitude to all the faculty members who have taught me in class and inspired my curiosity in materials science: Prof. Elizabeth J. Opila, Prof. Jerrold A. Floro, Prof. William C. Johnson, Prof. Leonid V. Zhigilei, Prof. Petra Reinke, Prof. William Soffa, Prof. James M. Howe, and Prof. James M. Fitz-Gerald. I would also like to give my special thanks to Prof. Sean R. Agnew. The experience of working with you as a teaching assistance for two semesters is really enjoyable. I would like to thank the administrative staff in the Department of Materials Science and Engineering, Jeannie Reese, Peggy Gibson, Sherri Sullivan, Ig Jakovac, and the former staff, Kim Fitzhugh-Higgins and Eric Newsome, for all of their help and support.

I would like to especially thank my collaborators, Dr. Zeming Sun and Dr. Aida Naghilou. I truly appreciate your friendship, and enjoy working with you and learning from your experimental works. I would like to thank Benjamin Hernandez Arreguin at the Oak Ridge National Laboratory, who helped me develop a great tool to view the snapshots from my super-large simluations. Furthermore, I would like to give thanks to all my former and current colleagues in the Computational Materials Group, Dr. Chengping Wu, Dr. Richard Salaway, Dr, Cheng-Yu Shih, Dr. Eaman Karim, Dr. Bernard Wittmaack, Dr. Maxim Shugaev, Dr. Han Wu, Dr. Kaushik Joshi, Hao huang, Chaobo Chen, Shaoning Geng, Lingyu Guo, Mikhail Arefev. I had very close collaboration and many discussions with Dr. Chengping Wu, Dr. Maxim Shugaev, Dr. Cheng-Yu Shih, and Dr. Eaman Karim. Thank you very much for sharing your knowledge and fruitful discussions.

My graduate studies and life have been made full of happiness by my partner, Wen Zhang. I am so grateful for her enduring support.

Finally, I want to give my greatest gratitude to my family. Being away from home for almost six years, I deeply miss my parents. Their unconditional support and love throughout my entire life have always encouraged me to achieve my dreams. Words are insufficient to express my appreciation to them.

Contents

Abstract

Short pulse laser irradiation can create conditions of strong electronic, thermal, phase, and mechanical non-equilibrium in the irradiated targets and trigger a cascade of processes leading to the modification of surface morphologies and formation of unique microstructures of interest to various practical applications. Materials processing techniques based on the laser-induced phase and structural transformations have been widely used and continuously developed for tailoring materials structures to meet desired properties, with the advantages of low manufacturing cost and high accuracy of laser-modified microstructures. Further advancement of the laser processing applications, however, is limited by incomplete fundamental understanding of the highly non-equilibrium processes driven by rapid laser energy deposition, which include fast melting and solidification, generation of crystal defects, collective materials ejection (ablation), and expansion of multi-phase ablation plume. In this dissertation, a combination of atomistic and continuum-level computational methods is used to reveal the mechanisms of the laser-induced modification of surface morphology and microstructure in Si and metal targets under a wide range of irradiation conditions.

The processes of laser-induced melting, resolidification, and generation of crystal defects in a Si wafer are investigated with a continuum-level model parametrized based on the results of atomistic simulations. The propagation of the solidification front under conditions of strong undercooling is found to produce high densities of vacancies and interstitials. The effects of laser parameters on the concentration of point defects in the transiently melted region, and the mitigation of point defects by means of following low power laser annealing, are examined and related to experimental observations. At a sufficiently high level of undercooling, the solidification velocity drops to zero, leading to the transition of the remaining molten region into amorphous phase. The irradiation regimes corresponding to different surface microstructure, with amorphous region formed either at the center or at the periphery of the laser spot, are established for a broad range of laser fluence, pulse duration, and spot size.

The laser-induced generation of crystal defects is also investigated for Ni and Ni-based binary single phase solid-solution alloys through atomistic simulations. The decrease in the thermal conductivity and strengthening of the electron-phonon coupling due to the intrinsic chemical disorder in the Ni-based alloys are found to have important implications on localization of the energy deposition and generation of thermoelastic stresses. The interaction of the laser-induced stress waves with the melting front is demonstrated to play a key role in the formation of dislocations during crystal growth. While the generation of high vacancy concentrations is observed in all irradiated targets, it is found to be partially suppressed in the alloy targets due to a combined effect of reduced solidification velocity and increased vacancy mobility. A detailed analysis of the mechanisms of vacancy generation at a rapidly advancing solidification front is carried out for Ni, Cr, and Ni-based alloys using molecular dynamics modeling of solidification at fixed levels of undercooling. The dependence of the vacancy concentration on material properties, crystallographic orientation of the solidification front, temperature and pressure are discussed based on the simulation results.

The formation of microbumps and nanojets on films composed of single and double Cu/Ag layers deposited on a glass substrate and irradiated by 60 fs laser pulses are investigated in atomistic simulations. Intra-layer cavitation and photomechanical spallation driven by the relaxation of the laser-induced stresses, as well as an explosive release of vapor at the interface with the substrate, are found to be responsible for the formation of frozen microbumps and nanojets observed in experiments.

Finally, the femtosecond laser ablation of a bulk Ag target in the regime of phase explosion is investigated. The processes leading to the explosive material decomposition are revealed and related to the characteristics of the ablation plume, including the spatial segregation of clusters and nanoparticles of different size in the plume. The dynamics of the nucleation, growth, and coalescence of subsurface voids, leading to the formation of a transient interconnected liquid structure, is used for explaining the origins of complex surface morphology featuring multiple frozen nanospikes of various shapes, commonly observed on laser-processed surfaces.

List of Publications

Published:

1. A. Naghilou, M. He*, J. S. Schubert, L. V. Zhigilei, and W. Kautek, Femtosecond laser generation of microbumps and nanojets on single and bilayer Cu/Ag thin films, *Phys. Chem. Chem. Phys.* **21**, 11846-11860 (2019).

2. M. He, C. Wu, M. V. Shugaev, G. D. Samolyuk, and L. V. Zhigilei, Computational study of short-pulse laser-induced generation of crystal defects in Ni-based single-phase binary solid-solution alloys, *J. Phys. Chem. C* **123**, 2202-2215 (2019).

3. M. V. Shugaev, M. He, S. A. Lizunov, Y. Levy, T. J. -Y. Derrien, V. P. Zhukov, N. M. Bulgakova, and L. V. Zhigilei, Insights into laser-materials interaction through modeling on atomic and macroscopic scales, in *Advances in the Application of Lasers in Materials Science*, Springer Series in Materials Science, Vol. **274**, edited by P. M. Ossi (Springer International Publishing Switzerland, 2018), pp. 107-148.

4. N. I. Polushkin, V. Oliveira, R. Vilar, M. He, M. V. Shugaev, and L. V. Zhigilei, Phase-change magnetic memory: rewritable ferromagnetism by laser quenching of chemical disorder in $Fe_{60}Al_{40}$ alloy, *Phys. Rev. Applied* **10**, 024023 (2018).

5. J. Ehrler, M. He, M. V. Shugaev, N. I. Polushkin, S. Wintz, V. Liersch, S. Cornelius, R. Hübner, K. Potzger, J. Lindner, J. Fassbender, A. A. Ünal, S. Valencia, F. Kronast, L. V. Zhigilei, and R. Bali, Laser-rewriteable ferromagnetism at thin-film surfaces, *ACS Appl. Mater. Interfaces* **10**, 15232-15239 (2018).

Ready for submission:

1. M. V. Shugaev, M. He, Y. Levy, A. Mazzi, A. Miotello, N. M. Bulgakova, and L. V. Zhigilei, Laser-induced thermal process: heat transfer, generation of stresses, melting and solidification, vaporization and phase explosion, in *Handbook of Laser Micro- and Nano-Engineering*, edited by K. Sugioka, Springer, 2020.

2. M. He,** E. T. Karim, M. V. Shugaev, and L. V. Zhigilei, Atomistic simulation of the generation of vacancies in rapid solidification of metals.
3. M. He, M. V. Shugaev, and L. V. Zhigilei, Molecular dynamics study of suppressed generation and configuration evolution of vacancies in Ni-based single-phase binary solid solution alloys.
4. M. He and L. V. Zhigilei, Computational study of phase transformations induced by short pulse laser irradiation on single crystalline silicon.
5. Z. Sun, M. He***, L. V. Zhigilei, and M. C. Gupta, Laser-induced point defects in silicon: Combined experimental and simulation investigations.

* M. He and A. Naghilou contributed equally to this paper.

** M. He and E. T. Karim contributed equally to this paper.

*** M. He and Z. Sun contributed equally to this paper.

List of Presentations

Oral Presentation:

1. M. He, Z. Sun. M. C. Gupta, and L. V. Zhigilei, Simulations and experiments on microstructure evolution in nanosecond laser melting and resolidification of silicon, *2016 International High Power Laser Ablation Symposium*, Santa Fe, New Mexico, April 2016.
2. M. He, C. Wu, M. V. Shugaev, and L. V. Zhigilei, Computational study of short pulse laser induced generation of crystal defects in Ni and Ni-based single phase binary alloys, *2018 International High Power Laser Ablation Symposium*, Santa Fe, New Mexico, April 2018.
3. M. He, C. Wu, and L. V. Zhigilei, Large scale atomistic simulation of the generation of surface morphology and plume evolution in femtosecond laser ablation of Ag, *15th International Conference on Laser Ablation (COLA-2019)*, Maui-Hawaii, USA, September 8-13, 2019.

Poster Presentation:

1. M. He, Z. Sun, M. C. Gupta, A. Naghilou, O. Armbruster, W. Kautek, and L. V. Zhigilei, Simulations and experiments on laser-induced phase transformation and generation of crystal defects in silicon, *2018 International High Power Laser Ablation Symposium*, Santa Fe, New Mexico, April 2018. (***Second Place Award***)
2. M. He, C. Wu, M. V. Shugaev, and L. V. Zhigilei, Generation of point defects in solidification of Ni and Ni-based binary alloys under conditions of deep undercooling, *Center for Energy Dissipation and Defect Evolution (EDDE) All-Hands Meeting*, Oak Ridge National Laboratory, Oak Ridge, Tennessee, January 2017.
3. M. He, Z. Sun, M. C. Gupta, and L. V. Zhigilei, Simulations on microstructure evolution in nanosecond laser melting and resolidification of silicon, *5th Venice International School on Lasers in Materials Science*, Isola di San Servolo, Venice, Italy, July 2016.
4. M. He, C. Wu, and L. V. Zhigilei, Molecular dynamics simulations of phase explosion in overheated metal systems and analysis of cluster distribution, *5th Venice International School on Lasers in Materials Science*, Isola di San Servolo, Venice, Italy, July 2016.
5. M. He, C. Wu, M. V. Shugaev, and L. V. Zhigilei, Atomistic modeling of short-pulse laser-induced generation of crystal defects in Ni-based single-phase binary solid-solution alloys, *15th International Conference on Laser Ablation (COLA-2019)*, Maui-Hawaii, USA, September 8-13, 2019.

6. M. He, Z. Sun, M. C. Gupta, A. Naghilou, O. Armbruster, W. Kautek, and L. V. Zhigilei, Simulations and experiments on laser-induced phase transformation and generation of crystal defects in silicon, *15th International Conference on Laser Ablation (COLA-2019)*, Maui-Hawaii, USA, September 8-13, 2019.

List of Figures

List of Tables

1. Introduction

Over the past several decades, the special characteristics of the laser interaction with materials have been widely acknowledged and utilized in the development of numerous laser processing techniques that enable a wide range of applications in fields such as mechanics, chemistry, and life science.[1-5] The ability of short pulse lasers to rapidly deposit energy in a small surface region of an irradiated target provides unique opportunities for high-precision processing and for investigation of materials behavior under extreme conditions, far from electronic, thermal, phase, and mechanical equilibrium. In particular, the confinement of laser energy in a shallow depth of the surface region (heat affected zone) leads to the establishment of strong temperature gradient, rapid heating and melting,[6,7] as well as buildup of thermoelastic stress,[8-12] triggering a series of complex processes that are responsible for the generation of a variety of unusual phases and microstructures in the irradiated target surface.[13-26]

In the regime of laser melting and resolidification, the strong localization of laser energy deposition can result in melting of a shallow surface region of the target which, due to the high temperature gradient and thermal conductivity, is followed by rapid cooling with a rate of around 10^{12} K/s and resolidification that proceeds under conditions of strong undercooling below the equilibrium melting temperature.[19,20,23-31] The question on the kinetics of solidification under conditions of deep undercooling, beyond the regime of linear dependence of the solidification front velocity on temperature, has been targeted in a number of short pulse laser pump-probe experiments.[31-34] The results of these studies suggest that the solidification front velocity can approach or even exceed 100 m/s at laser fluences close to the surface melting threshold, when the whole melting and resolidification process is completed on sub-nanosecond timescale. At an undercooling level of more than ~30%, homogeneous nucleation of new crystallites, rather than the epitaxial crystal growth, provides the main mechanism of the rapid solidification and leads to the formation of nanocrystalline structure in the surface region of the irradiated target.[23-25] Kinetics of the crystallization processes may be inhibited with increasing undercooling, and the solidification results in the transformation of the deeply undercooled liquid into a stable amorphous phase.[29,35-37]

When the laser pulse duration is shorter or comparable to the characteristic time of mechanical equilibration of the absorbing volume, *i.e.*, under conditions of so-called stress confinement,[10-12,27] the laser excitation can produce strong compressive stresses in the absorbing volume. The interaction of the laser-induced compressive thermoealstic stresses with the free surface of the irradiated sample can result in the generation of an unloading tensile wave sufficiently intense to cause the formation of subsurface voids. At a sufficiently high laser fluence, the growth and percolation of the voids may lead to the separation and ejection of a thin layer and/or multiple droplets from the irradiated target, which is commonly referred to as photomechanical spallation. Further increase of the laser fluence may bring the irradiated target to the regime of phase explosion, where the target surface is melted and overheated above the limit of thermodynamic stability of the liquid phase, leading to a rapid decomposition of the overheated melted material into a mixture of vapor and liquid droplets.[38-43] In longer pulse laser ablation, where the photomechanical ablation is inactive due to the absence of stress confinement, the onset of the phase explosion leads to the direct transition from surface evaporation to the collective material ejection.[41,43] The material ejection, hydrodynamic motion, and redistribution under the laser-induced strongly non-equilibrium temperature and pressure conditions result in the formation of a variety of complex surface morphologies on the irradiated targets, which are the research focus of many experimental and theoretical studies due to the scientific interests and practical implications.[26,44-51]

The ultrahigh rates of laser-induced heating and cooling, the resulting resolidification proceeding under conditions of strong undercooling, combined with the generation and relaxation of strong compressive stresses, create conditions for the formation of unique microstructures. In particular, highly non-equilibrium concentrations and configurations of crystal defects can be created at the rapidly advancing solidification front[19,21,26,52-54] and through emission of dislocations driven by the dynamic relaxation of laser-induced thermoelastic stresses.[14-18,52,53] The laser-induced generation of crystal defects, namely, dislocations, stacking faults, twin boundaries, and vacancies, has important implications for the modification of mechanical, optical, and chemical properties of the irradiated targets. The accumulation of subsurface defects has also been discussed as one of the possible mechanisms responsible for the incubation effect observed in multipulse irradiation regime, when the laser fluence threshold for ablation/damage of the targets decreases with increasing number of laser pulses applied to the same area[21,55-61]. In particular, the generation of high density of vacancies may be related to the formation of nanovoids and degradation of mechanical properties. On the other hand, strong vacancy supersaturation in the surface region of laser-processed target can enhance atomic diffusion, thus playing an important role in redistribution of impurities or mixing/alloying in multi-component systems, and even facilitating order-disorder transitions.[62,63]

The continuous advancement of laser-enabled techniques in practical applications requires a thorough understanding of the laser-induced processes that are responsible for the modification of materials microstructure. Due to the relatively shallow depth of the laser-modified region and the ultrashort time scales of the processes involved in laser-materials interactions, experimental probing of the laser-induced melting and resolidification, generation and evolution of the crystal defects, modification of surface morphology, as well as formation and expansion of ablation plume remain extremely challenging. Even with the development of most advanced pump-probe techniques with diagnostic capability of resolving the laser-induced processes on femto-/picosecond time-scales and on sub-micrometer length-scales,[31,34, 64 - 69], the highly non-equilibrium and intertwined complex processes triggered by short pulse laser irradiation are difficult to completely uncover based on the experimental data alone.

Given the challenges of direct time-resolved experimental probing of the rapid laser-induced phase and structural transformations, the computer modeling is playing an important role in providing physical insights into the material response to laser irradiation and assisting in interpretations of the results of *ex-situ* characterization of the microstructural changes in the irradiated target. A large variety of computational models have been developed for addressing the diverse range of processes involved in the laser-materials interactions. In particular, molecular dynamics (MD) simulations, typically combined with a continuum two-temperature model (TTM) representing the laser excitation of electrons, electron heat transfer, and the energy exchange between electrons and phonons, have been shown to be suitable for the exploration of laser-induced processes with atomic resolution, especially when materials are driven far out of electronic, thermal, and mechanical equilibrium.[52,53,70-72] For investigation of laser-induced processes at experimental time- and length-scales, computationally efficient continuum-level modeling is usually adopted.[72] The combination of different computational methods by integrating the predictive power of each approach into an advanced multiscale model, as will be demonstrated in this dissertation, opens the possibility to fully address the processes occurring on the scale of the whole laser spot, but still retain the atomic-level information on the laser-induced structural changes in the irradiated material.

This dissertation is primarily aimed at utilizing multiscale modeling approach to reveal the kinetics and mechanisms of the laser-induced processes that are responsible for the modification of materials surface microstructure and/or morphology, thus facilitating the optimization of experimental conditions for manufacturing and processing of high-performance materials. Two main computational approaches used in this dissertation are a hybrid TTM-MD model and an advanced continuum-level thermal model designed and parameterized based on the information from atomistic simulations. Together, these models are capable of addressing various aspects of laser-materials interactions in a wide range of irradiation regimes. A brief technical description of the two models is provided in Section 2.

The results of the application of the computational models to several systems of scientific and practical importance are presented in the remaining part of the dissertation. In particular, laser-induced phase transformations as well as the generation and evolution of crystal defects in silicon targets are discussed in Section 3, where the formation of amorphous structure and generation of interstitials and vacancies during rapid solidification under strong undercooling conditions are investigated in atomistic simulations, and the effect of laser parameters (fluence, pulse duration, wavelength, number of pulses, etc.) on the modification of surface microstructure and evolution of point defects are analyzed by continuum-level modeling.

In Section 4, the generation of crystal defects in the course of laser-induced melting and resolidification is investigated for Ni and Ni-based binary single phase solid-solution alloys. The effect of the chemical disorder in the Ni-based alloys on the redistribution of laser energy and generation of crystal defects are evaluated, and the mechanisms responsible for the suppression of vacancy generation, as well as the evolution of vacancy configurations to preferable atomic surroundings, is revealed. The interpretation of the generation of high density of vacancies during the laser-induced resolidification is assisted by extensive simulations of crystal growth under well-controlled temperature and pressure conditions performed for bcc Cr, fcc Ni and Ni-based alloys. The effects of the crystal structure, crystallographic orientation, and pressure on the temperature dependence of vacancy concentration are uncovered.

The results of computational investigation of the key processes and mechanisms responsible for the formation of micro-/nano-bumps on Ag-Cu bilayer films irradiated by ultrashort laser pulses, observed in experiments by our collaborators, are reported in Section 5. The record-setting large-scale TTM-MD simulation of laser interaction with a Ag bulk target in the regime of phase explosion is described in Section 6. The large scale of the simulation makes it possible to obtain statistically reliable information on the composition of the ejected ablation plume and the shapes of the frozen features generated on the surface of the irradiated target. Moreover, the comparison of the results of the large-scale simulation with predictions of smaller-scale simulations enable analysis of the effects of the size of the computational domain on the results. The main conclusions and suggestions for future work are summarized in Section 7.

2. Computational methods for simulations of laser interaction with materials

2.1 Atomistic modeling of laser interaction with materials

Atomistic modeling of laser-materials interactions is playing an increasingly important role in the advancement of modern laser technologies due to its ability of describing the highly non-equilibrium processes induced by short pulse laser irradiation with atomic resolution. In particular, MD simulations provide unprecedented opportunities of tracking the movement of particles in a system without prior assumptions on the processes and mechanisms under study, and have been applied to obtain atomic-level insights into complex laser-induced phase and structural evolutions and reveal new physical phenomena.

In laser interaction with materials, the deposition of laser energy in the irradiated targets proceeds through the excitation of valance band electrons to the conduction band in semiconductors or direct absorption of photon energy by conduction band electrons in metals. This process is followed by electron-electron collisions leading to thermal equilibration in the electronic sub-system within tens of femtoseconds[73,74] and electron-phonon collisions leading to the equilibration of hot electrons with phonons on the picosecond time scale. In order to describe the non-equilibrium processes in the target material under short pulse laser irradiation, a Two-Temperature Model (TTM) accounting for the laser excitation of electrons, electron heat conduction, and electron-phonon coupling is incorporated into the MD simulations.

The basic concepts of the classic MD technique are briefly introduced in Section 2.1.1. The continuum-level TTM accounting for the laser excitation and subsequent relaxation of the conduction band electrons is described in Section 2.1.2. A hybrid computational model combining the TTM with the MD method is discussed in Section 2.1.3.

2.1.1 Molecular dynamics technique for investigating systems of interacting particles

MD simulations have been widely applied in the fields of materials science, chemistry, and biology.[75,76] This technique simulates the time evolution of a system of interacting particles by solving the classical Newtonian equations of motion for all particles in the system, $m_i \frac{d^2\vec{r}_i}{dt^2} = \vec{F}_i$, thus providing the atomic-level insights into the complex dynamic processes in systems consisting of many particles. In the classical equations of motion, m_i and $\vec{r}_i$ are the mass and position of a particle i, $\vec{F}_i$ is the force acting on particle i due to its interaction with other particles in the system. The force acting on each particle can be determined as $\overrightarrow{F_i} = -\frac{\partial U(\overrightarrow{r_1},\overrightarrow{r_2},\ldots,\overrightarrow{r_N})}{\partial \overrightarrow{r_i}}$, where $U(\overrightarrow{r_1},\overrightarrow{r_2},\ldots,\overrightarrow{r_N})$ is the interatomic interaction potential energy, which is a function of the position of all particles in the system, and N is the total number of particles. After defining the interatomic potential and initial conditions, such as initial positions and velocities of all particles, the Newtonian equations of motion can be numerically solved, providing a set of trajectories of individual atoms or particles that defines the evolution of the system and its thermodynamic parameters.

In MD, the only input is the description of interatomic interaction potential, and no further assumptions are needed, which makes MD simulations an ideal approach in exploring various laser-induced processes, such as rapid non-equilibrium melting, solidification under strong undercooling, generation of high density of crystal defects, photomechanical spallation, and phase explosion. The biggest challenge in MD is the implementation of realistic interaction potentials, which are typically designed via *ab-initio* calculations and fitted to reproduce basic equilibrium properties of materials. Other thermodynamic and mechanical properties, such as melting point, elastic modulus, lattice heat capacity, and activation energies of phase and structural transformations, are fully defined by the interatomic potential. In this dissertation, two sets of potentials are selected for the atomistic simulations of different materials. A three-body bond-order potential[77] is used to describe the interactions between silicon atoms, and the Embedded Atom Method (EAM)[78, 79] potential with several parameterizations developed for different systems is used for pure metals and alloy systems, as discussed in Sections 4-6.

2.1.2 Two-temperature model for material response to laser irradiation

The original two-temperature model (TTM)[80,81] describes the time evolution of electron temperature, T_e, and phonon temperature that is commonly referred to as lattice temperature, T_l, by solving two coupled nonlinear differential equations. The equations account for the laser absorption by conduction band electrons, the energy exchange between the excited electrons and atomic vibrations, and the electron heat conduction:

$$C_e(T_e)\frac{\partial T_e}{\partial t} = \nabla[K_e(T_e,T_l)\nabla T_e] - g(T_e)(T_e - T_l) + S(\vec{r},t), \qquad (2.1)$$

$$C_l(T_l)\frac{\partial T_l}{\partial t} = \nabla[K_l(T_l)\nabla T_l] + G(T_e)(T_e - T_l), \qquad (2.2)$$

where C_e and C_l are the electron and lattice heat capacities; K_e and K_l are the electron and lattice thermal conductivities; G is the electron-phonon coupling parameter; S is a source term representing the laser energy density deposited in the target at position $\vec{r}$ and time t.

Since the laser spot size is typically much larger than the laser absorption depth in metals, the analysis of thermodynamic conditions created in the surface region of an irradiate target is often based on quasi one-dimensional (1D) modeling of the laser energy deposition and heat transfer.[12,27,31,82,83] The processes occurring at the scale of the entire laser spot can then be evaluated through a "mosaic" approach based on combining the results of a series of 1D simulations performed for a range of local fluences chosen from the laser beam profile.[72,84]

The laser pulse is commonly assumed to have a Gaussian temporal profile and, with the 1D representation of laser irradiation, an exponential attenuation of laser intensity with depth z under the target surface following the Beer-Lambert law, leading to the following form of the source term in Eq. (2.1):

$$S(z,t) = (1-R)I_0 \frac{\exp(-z/L_P)}{L_P} \exp\left[-\frac{(t-t_0)^2}{2{\sigma_t}^2}\right]. \tag{2.3}$$

Here, I_0 is the peak intensity of the laser profile, R is the reflectivity of target surface, L_P is the absorption depth, and σ_t is the standard deviation of the Gaussian profile which is related to the laser pulse duration τ_L defined as full width at half maximum, $\tau_L = \sqrt{8\ln(2)}\sigma_t$. In order to correctly describe the irradiation by whole laser pulse, the center of the Gaussian temporal profile t_0 corresponding to peak intensity is set as 1.5-2.5 τ_L, so that the laser energy deposition before the simulation, $t < 0$, is negligible. To account for the energy transport occurring before the thermalization of the excited electrons, the penetration depth L_P is computed as a sum of the optical absorption depth L_{opt} and an effective depth of the "ballistic" energy transport, L_b[74,85]. Due to the complexity in the dependence of R on the temperature and microstructure of the target surface, the absorbed intensity $I_{\text{abs}} = (1-R)I_0$ is typically used. The absorbed laser fluence F_{abs} used in the discussion of the simulation results is related to the absorbed intensity as $F_{\text{abs}} = \sqrt{2\pi}\sigma_t I_{\text{abs}} = \sqrt{\pi/4\ln(2)}\tau_L I_{\text{abs}} \approx 1.0645\tau_L I_{\text{abs}}$. In cases when quantitative comparison with experimental irradiation conditions is required, the absorbed fluence is estimated for a given incident fluence accounting for the dependence of reflectivity on the evolving electron temperature of target surface, as discussed in Section 5.3.1.

The temperature dependences of the thermophysical properties included in Eq. (2.1) are highly sensitive to details of the electronic structure of materials and can deviate up to an order of magnitude from the commonly used approximations of a linear dependence for $C_e(T_e)$ and a constant value for G.[74,86-88] More accurate description of these properties as a function of electron temperature, which explicitly considers the electron density of states for a particular material and accounts for the thermal excitation from the electron states below the Fermi level,[87,89,90] is used in this dissertation. The electron thermal conductivity is described by the Drude model relationship,

$$K_e(T_e,T_l) = v^2 C_e(T_e)\tau_e(T_e,T_l)/3. \tag{2.4}$$

In Eq. (2.4), v^2 is the mean square velocity of the electrons contributing to the electron heat conductivity, approximated in this work as the Fermi velocity squared, ${v_F}^2$; $\tau_e(T_e, T_l)$ is the total electron scattering time and its inverse is the electronic collision frequency defined as a sum of the electron-electron and electron-phono scattering rates,

$$\nu_e = 1/\tau_e = 1/\tau_{e-e} + 1/\tau_{e-ph} = A{T_e}^2 + BT_l. \qquad (2.5)$$

The value of the coefficient A can be estimated based on the free electron model,[91] and the coefficient B can be set as a constant value or a function of lattice temperature and material phase state, so that the experimental temperature dependences of thermal conductivity of solid and liquid material under conditions of electron-phonon equilibrium, $T_e = T_l$, are reproduced by Eq. (2.4).

2.1.3 Hybrid TTM-MD model

To obtain insights into the fast non-equilibrium processes responsible for the modification of surface morphologies induced by laser irradiation, the classic MD technique capable of providing atomistic representation of the structural and phase transformations is incorporated in the general framework of the continuum-level TTM describing the laser excitation of conduction band electron and following electron-phonon equilibration, leading to the combined TTM-MD model schematically illustrated in Figure 1.

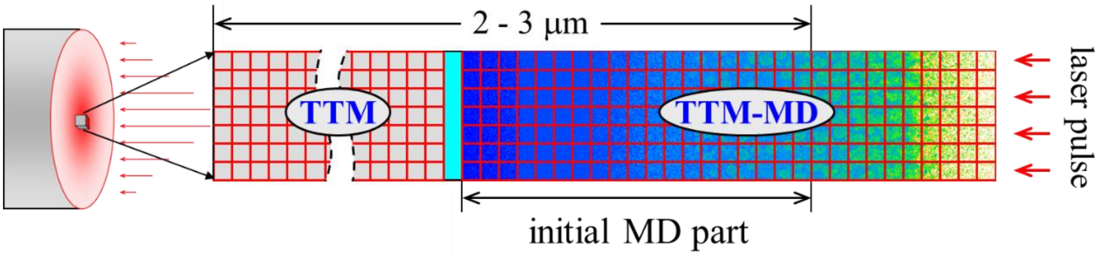

Figure 1. Schematic representation of the hybrid TTM-MD model developed for simulations of laser interaction with materials. The corresponding computational domains are marked, and the nonreflecting boundary condition is illustrated by the light blue rectangle at the interface between the TTM-MD and TTM domains.

In the hybrid TTM-MD model, the TTM equation for the lattice temperature is substituted by the MD equations of atomic motion in the surface region of the computational system, where the laser-induced structural and phase transformations take place, overcoming the limitations of the continuum level approach in the description of these ultrafast non-equilibrium processes. The diffusion equation for the electron temperature is solved by a finite difference method simultaneously with the MD integration of the equations of atomic motion. The cells in the finite difference discretization are mapped to the corresponding volumes of the MD system, and the local lattice temperature, T_l^{cell}, is defined for each cell from the average kinetic energy of thermal motion of atoms:

$$T_l^{cell} = \frac{\sum_{i=1}^{N_{cell}} m_i\left(\vec{v}_i^{\,th}\right)^2}{3k_B(N_{cell}-1)}. \tag{2.6}$$

In Eq. (2.6), N_{cell} is the number of atoms in the cell; and $\vec{v}_i^{\,th}$ is the thermal velocity of atom i defined as $\vec{v}_i^{\,th} = \vec{v}_i - \vec{v}^{\,c}$, where $\vec{v}_i$ the actual velocity and $\vec{v}^{\,c}$ is the velocity of the center of mass of the cell to which the atom *i* belongs. The size of the cells is typically selected as 1-2 nm in z direction and 4-6 nm in lateral directions. The atoms crossing cell boundaries carry the corresponding electron thermal energy along, thus ensuring the total energy conservation.[92] The electron temperature enters a coupling term added to the MD equations of motion, $\xi m_i \vec{v}_i^{\,th}$, to account for the energy exchange between the excited electrons and phonons:

$$m_i \frac{d^2\vec{r}_i}{dt^2} = \vec{F}_i + \xi m_i \vec{v}_i^{\,th}. \tag{2.7}$$

Here, ξ is a coefficient that depends on the instantaneous difference between the local lattice and electron temperatures following the expression

$$\xi = \frac{1}{n} \frac{\sum_{k=1}^{n} G V_{cell}\left(T_e^k - T_l^{cell}\right)}{\sum_{i=1}^{N_{cell}} m_i\left(\vec{v}_i^{\,th}\right)^2}. \tag{2.8}$$

In this expression, V_{cell} is the volume of the cell, n is the number of TTM steps corresponding to each MD step, and T_e^k is the electron temperature calculated at each step of TTM integration. Because the time step of TTM integration, Δt_{TTM}, need to satisfy the von Neumann stability criterion,

$$\Delta t_{TTM} \leq 0.125[\min(\Delta x_{TTM}, \Delta y_{TTM}, \Delta z_{TTM})]^2 C_e/K_e, \tag{2.9}$$

where Δx_{TTM}, Δy_{TTM}, and Δz_{TTM} are the discretization size of TTM cells along x, y, and z directions. Considering the high thermal conductivity of metals, the maximum time step that can be used in the finite difference integrations in TTM is typically much smaller than the time step used in the integration of MD equations of atomic motion, Δt_{MD}, leading to n TTM steps for each MD step.

The expansion, density variations, and, at high fluences, disintegration of the irradiated target predicted in the MD subsystem are accounted for when solving the TTM equations for electron temperature through the corresponding changes in the thermophysical parameters. Three-dimensional (3D) grid of the finite difference discretization is implemented to ensure an adequate representation of the electronic heat transfer especially in large-scale simulations in the irradiation regime of laser ablation, where large density variations at the initial stage of the spallation or ablation process may create conditions of complex 3D heat flow in the surface region of the irradiated targets. Solution for the electron temperature is temporarily deactivated for cells in which the number of atoms drops below a certain critical number, taken in this work to be 10% of the average number of atoms in the corresponding cell volume in a crystalline system equilibrated at 300 K and zero pressure, due to material expansion or disintegration.

In the simulations of laser-interaction with bulk material, due to the high cost of MD simulations that limits the maximum depth of the computational system, the evolution of electron and lattice temperatures beyond the surface region represented by the MD model are solved by the conventional TTM equations. The continuum TTM part is extended down to the depth of 2-3 μm, so that no significant change in the temperature is observed at the bottom of the computational domain during the simulations. At the interface between the TTM-MD and TTM domains, a dynamic heat-conducting pressure-transmitting boundary condition[93,94] is applied to the bottom two atomic layers in the MD subsystem to ensure nonreflecting propagation of the laser-induced pressure wave from the MD region to the bulk of the target.

2.2 Continuum modeling of laser-induced phase transformation and generation of crystal defects in silicon

The high computational cost of atomistic simulations limits the spatial and temporal scales accessible in the modeling, resulting in typical system sizes and durations of simulations on the scale of hundreds of nanometers and nanoseconds, respectively. In order to map the computational predictions to observations in experimental systems, which typically have dimensions of micrometers or more, methods capable of addressing the processes occurring on the scale of the whole laser spot and experimental timescales are needed. To address this model, a multiscale computational approach is developed where atomistic simulations inform the large-scale continuum models on the kinetics and mechanisms of laser-induced structural and phase transformations, and help to design advanced continuum-level models fully accounting for the complexity of short pulse laser-material interactions. In this dissertation, we focus on applying this advanced continuum-level model specifically to silicon and describing the phase transformations and generation of crystal defects in the regime of laser-induced melting and resolidification. Indeed, the advanced continuum-level modeling of thermal and structural processes occurring on the scale of the laser spot can be applied to any material once the thermodynamic properties are known and atomistic simulations are correctly established to provide desired kinetic and mechanistic information.

2.2.1 Continuum-level description of laser energy absorption, thermal transport, and phase transformations

The continuum model describing the thermal processes in the laser-material interactions is based on numerical solution of the heat diffusion equation complemented by source terms describing the laser energy deposition and the latent heat of phase transformations:

$$\rho C_P \frac{\partial T}{\partial t} = \nabla(K_{th}\nabla T) + S_{laser} - S_m - S_e, \tag{2.10}$$

where ρ, C_P, and K_{th} are the density, heat capacity, and thermal conductivity of the target material, respectively. In simulations of laser interaction with silicon target discussed in this dissertation, the laser pulse duration ranges from tens of picosecond to hundreds of nanosecond, much longer than the thermal equilibration between electrons and phonons. Therefore, the electron-phonon energy exchange and two-temperature heat diffusion for electron and lattice subsystems, as described in Section 2.1, are not considered in Eq. (2.10). The three source terms on the right side of Eq. (2.10) represent the thermal energy sources/sinks due to the laser energy deposition S_{laser}, the release/absorption of heat at melting/resolidification front S_m, and the energy loss through vaporization from the surface of the irradiated target S_e.

In 1D simulations, the source term of laser energy deposition follows the form in Eq. (2.3). In order to provide realistic description of laser-induced processes occurring on the scale of whole laser spot, however, 2D simulations based on the cylindrical coordinate system (r, z) are performed, as illustrated in Figure 2, assuming a circular laser beam with Gaussian energy distribution in both temporal and lateral profile. In this case, S_{laser} is expressed as

$$S_{laser}(r,z,t) = (1-R)I_0 \frac{\exp(-z/L_P)}{L_P} \exp\left[-\frac{(t-t_0)^2}{2\sigma_t^2}\right] exp\left[-\frac{r^2}{2\sigma_r^2}\right], \tag{2.11}$$

where σ_r is the standard deviation of the Gaussian profile in lateral dimension, which is related to the laser spot diameter D_L (defined as full width at $1/e^2$ height) as $\sigma_r = D_L/4$.

In the description of melting and resolidification, a simple phase-change model based on conventional assumptions of local equilibrium at the solid-liquid interface (heat-flow limited interface kinetics formulated within the framework of the Stefan problem[95,96]) is not suitable for the conditions of short pulse laser irradiation, when strong temperature gradients are created and fast thermal energy flow to/from the solid-liquid interface can lead to significant superheating/undercooling at the melting/solidification front.[19,23-25, 97] Therefore, a non-equilibrium kinetic description,[19,98-100] in which the instantaneous velocity of the solid-liquid interface is defined by local temperature of the interface predicted by Eq. (2.10), is needed for a realistic representation of the movement of the solid-liquid interface. The temperature dependence of the velocity of the melting/solidification front can be described by a kinetic equation formulated as follows:

$$V_{sl}(T_{sl}) = V_0(T_{sl})\left[1 - \exp\left(-\frac{\Delta G(T_{sl})}{k_B T_{sl}}\right)\right], \tag{2.12}$$

where T_{sl} is the temperature at the solid-liquid interface, V_0 is a pre-factor proportional to the self-diffusivity of liquid atoms depending on temperature, and ΔG is the difference in the Gibbs free energy between the liquid and solid phases. At moderate deviations from the equilibrium melting temperature T_m, the free energy difference can be approximated as $\Delta G(T_{sl}) \approx \Delta H_m(T_{sl})(1 - T_{sl}/T_m)$, where $\Delta H_m(T_{sl})$ is the latent heat of solid-liquid phase transformation. The pre-factor V_0 can be fitted to the results of a series of solid-liquid coexistence atomistic simulations providing the temperature dependence of the interface velocity, as shown in Figure 2 and described in Section 3.2.

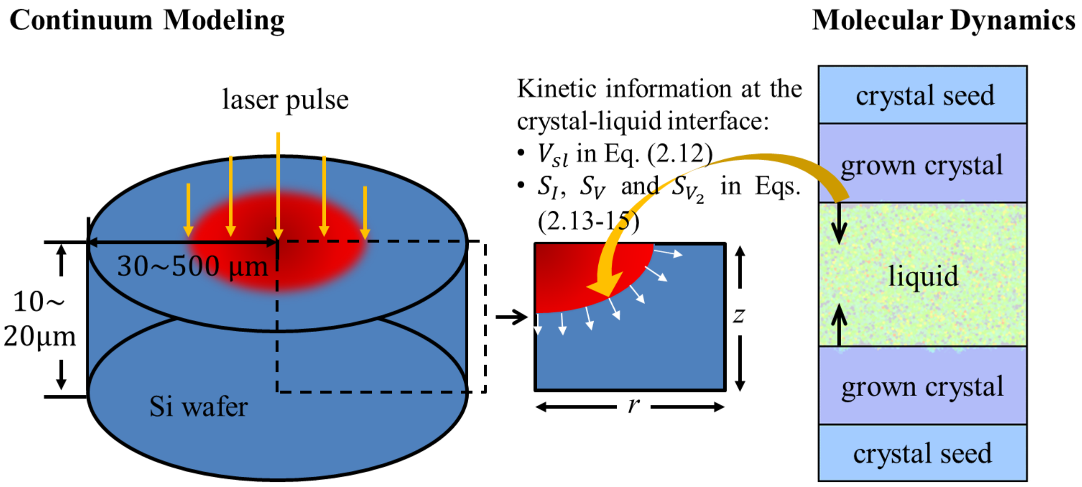

Figure 2. Schematic representation of the multiscale model developed for simulations of laser interaction with silicon. The left figure shows the continuum model of the Si wafer and the 2D computational system with cylindrical coordinate system (*r*, *z*). The right figure illustrates the MD simulation of a solid-liquid coexistence system under fixed temperature. The velocity of crystal-liquid interface and concentration of point defects generated in the resolidified region are computed as a function of temperature from the MD simulations, and are used to parameterize the continuum-level formulation of propagation of crystal-liquid interface (V_{sl}) and generation of interstitials (S_I), vacancies (S_V), and di-vacancies (S_{V2}) at the solidification front, as denoted by the yellow curved arrow directing from MD to the continuum system.

The propagation of melting/solidification front is then described by movement of a series of discrete points along the crystal-liquid interface in the direction normal to the melting/solidification front with the velocities determined in Eq. (2.12). Note that the decrease of the solidification velocity with increasing undercooling, predicted by Eq. (2.12) may permit the transformation of the undercooling liquid into a stable amorphous phase, which would stop the advancement of the crystallization front and result in the formation of amorphous regions in the resolidified target. In detail, for 2D simulations, a set of discrete points are initially set at the free surface at $z = 0$, with distance between each point around 1 nm. When laser heating brings the target surface beyond the melting temperature, the points belong to the overheated cells in the finite difference discretization move into the bulk of the target, representing the onset of surface melting. Following the formulation in Eq. (2.12), the velocity of each point can be calculated based on the local temperature, which is defined by linear extrapolation from the temperature of the two closest neighboring cells along z direction that high temperature gradient is generated. Therefore, although all points have initially the same position along z axis, their motion with different velocities, due to non-uniform temperature distribution along r axis, provides a realistic representation of the crystal-liquid interface. The points move in the direction determined by the shape of the interface, specifically, the distance each point moves along z and r directions during each time step is expressed as $\Delta z = -V(T)\cos(\alpha)\Delta t$ and $\Delta r = -V(T)\sin(\alpha)\Delta t$, respectively. Here, $V(T)$ is the velocity of this point determined by local temperature following Eq. (2.12) as discussed above, Δt is the time step, and α is the angle between the segment connecting its two neighboring points along the interface and r axis. The z and r coordinates increase deep into the bulk of the target and from the center of laser spot to its periphery, respectively. Therefore, the negative value of $V(T)$ predicted in Eq. (2.12) ensures the advancing of the crystal-liquid interface towards the solid bulk of the target through melting and the positive value is associated with the propagation of the solidification front towards the molten surface. The motion of the points is stopped once the condition of amorphization is achieved, and the remaining highly undercooled liquid freezes into amorphous phase.

The possibility of phase transformations occurring through the homogeneous nucleation of a new phase is also included to account for the formation of liquid regions inside a crystal superheated up to the limit of its stability against melting or homogeneous nucleation of new crystallites in a strongly undercooled liquid region. The temperature dependence of the nucleation rate and critical nuclei radius are related to the free energy difference between solid and liquid phases using the classic nucleation theory,[101] and the change of phase fraction due to nucleation and growth of liquid or crystalline regions is computed based on the Kolmogorov-Johnson-Mehl-Avrami (KJMA) equation.[102,103]

2.2.2 Generation and evolution of laser-induced point defects

The rapid solidification proceeding under conditions of strong undercooling may produce high density of crystal defects, such as vacancies, interstitials, dislocations, twins, and grain boundaries. In order to investigate the generation and evolution of point defects in the course of laser-induced melting and resolidification, the continuum-level description of the thermal model, Eqs. (2.10) and (2.12), is complemented with the following equations accounting for the generation, diffusion, and recombination of vacancies and interstitials in the irradiated target:[104-107]

$$\frac{\partial C_I}{\partial t} = \nabla(D_I \nabla C_I) - R_{I,V} - R_{I,V_2} + S_I, \tag{2.13}$$

$$\frac{\partial C_V}{\partial t} = \nabla(D_V \nabla C_V) - R_{I,V} - 2R_{V,V} + R_{I,V_2} + S_V, \tag{2.14}$$

$$\frac{\partial C_{V_2}}{\partial t} = \nabla\left(D_{V_2} \nabla C_{V_2}\right) + R_{V,V} - R_{I,V_2} + S_{V_2}, \tag{2.15}$$

where C_I, C_V, and C_{V_2} denote the instantaneous concentrations of single interstitials, single vacancies, and di-vacancies, respectively, and D_I, D_V, and D_{V_2} are their diffusion coefficients depending on temperature.[108,109] $R_{I,V}$, R_{I,V_2}, and $R_{V,V}$ are the terms associated with reactions between different types of point defects, describing the annihilation of an interstitial and a vacancy, the combination of a single interstitial and a di-vacancy creating a single vacancy, and the formation of a di-vacancy from two individual vacancies, respectively, that can be expressed as:

$$R_{I,V} = K_{I,V}\left(C_I C_V - C_I^{eq} C_V^{eq}\right), \tag{2.16}$$

$$R_{I,V_2} = K_{I,V_2}\left(C_I C_{V_2} - C_I^{eq} C_{V_2}^{eq} C_V / C_V^{eq}\right), \tag{2.17}$$

$$R_{V,V} = K_{V,V}\left[C_V C_V - C_{V_2} \rho \exp\left(-E_{V_2}^{bind}\right)\right]. \tag{2.18}$$

Here, $K_{I,V}$, K_{I,V_2}, and $K_{V,V}$ are the interstitial-vacancy, interstitial-di-vacancy, and vacancy-vacancy combination rates, respectively, which depend on the diffusivity of associated point defects and energy changes in the corresponding events;[104] C_I^{eq}, C_V^{eq}, and $C_{V_2}^{eq}$ are the equilibrium concentrations of single interstitials, single vacancies, and di-vacancies; $E_{V_2}^{bind}$ is the binding energy of a di-vacancy. The source terms describing the generation of non-equilibrium interstitials and vacancies at the propagating solidification front, S_I, S_V, and S_{V_2} in Eqs. (2.13-2.15), can be parameterized based on the results of atomistic simulations as shown in Figure 2 and discussed in Section 3.2. Di-interstitials and larger clusters of point defects are neglected in the current model, due to their significantly lower concentration and mobility compared with the individual point defects and di-vacancies.

3. Computational study of laser-induced formation of amorphous structure and generation of crystal defects in silicon

3.1 Introduction

Laser processing of silicon has been widely adopted in the past decades due to the ability of lasers to provide localized non-contact energy deposition, thus enabling low cost and high throughput manufacturing. Applications of the laser-based fabrication processes on silicon devices, such as solar cells, include laser doping,[110-113] surface microtexturing,[114-116] and laser direct writing.[117-119] These fabrication approaches typically involve melting and resolidification of the silicon target surface, which proceed under conditions of strong temperature gradients generated by the rapid localized laser heating. As a result, the solidification takes place far from the equilibrium conditions, under strong undercooling, leading to the generation of high concentrations of crystal defects[113,120-122] which, acting as recombination sites for photo generated charge carriers, results in degradation of electrical properties and the efficiency of photovoltaic devices.[123,124]

Laser-induced modification of the surface microstructure may also feature amorphous regions formed by femtosecond,[37, 125-130] picosecond,[36, 131] and even nanosecond[132] laser pulse irradiation. The formation of the amorphous region is commonly attributed to the conditions of strong undercooling of the transiently melted surface region, all the way down to the glass transition temperature, during the resolidification process.[133] However, previous investigations conducted with different laser pulses produced complex and even controversial results on the shape and scale of the amorphous regions. For example, the thickness of the amorphous layer is found to be uniform and not sensitive to the number of applied laser pulses or fluence, but dependent on the optical absorption depth that is determined by laser wavelength.[127,128] The amorphous regions are reported to exhibit a parabolic thickness profile,[126] or even a ring-shaped[36,125,130] morphology. Due to the challenges of *in-situ* imaging of the kinetics of amorphization, theoretical studies of the key processes responsible for the formation of amorphous regions and the effect of irradiation conditions on their morphology are needed.

Investigations of the laser generation of crystal defects such as dislocations[124,134] and microtwins[135,136] have been reported, and efforts have been made to optimize the irradiation conditions to avoid the undesirable structure, *e.g.*, by adjusting the laser wavelength, fluence, pulse duration, and even the shape of the laser beam.[120,135] However, few studies have been carried out on the generation of point defects, which plays an important role in determining the electrical and chemical properties in semiconductors.[137-139] The scarcity of data on the point defects can be, at least partly, attributed to the difficulty of experimental identification of point defects. Further expansion of the range of applications of laser processing and improvement of the device performance require a fundamental understanding of the laser-induced phase and structural transformations that are responsible for the generation of crystal defects, as well as the dependence of their concentrations on laser parameters.

Elimination of the crystal defects can be also achieved by post treatment of the devices through annealing. Previous studies have reported the reduction of defects in a Si wafer and the corresponding improvement of the device performance using conventional annealing[140] or rapid thermal processing (RTP).[141,142] These techniques, however, usually cause heating of the entire wafer and may lead to the diffusion of defects or impurities into the bulk of the sample. Recently, laser annealing of defects has attracted great attention due to its ability of providing selective, localized, and potentially cost-effective heating of the surface region in silicon. This approach has been demonstrated to be effective in removing defects generated by ion implantation[143,144] or laser processing of silicon targets.[113,121,122]

Despite of the earlier explorations of laser-induced generation and evolution of crystal defects, a solid understanding of the effect of laser parameters, such as laser fluence, pulse duration, wavelength, and spot size, on the concentrations of defects is still lacking. The continuum-level modeling provides a computationally-efficient description of a broad range of laser-induced processes at experimental time- and length-scales, and can be used to provide general guidance for proper selection of the experimental irradiation conditions to control the levels of laser-induced defects. The predictive power of the continuum methods, however, is limited by the need of a priori knowledge of all processes that take place under given irradiation conditions and the availability of reliable mathematical description of these processes. The complexity and highly non-equilibrium nature of the laser-induced processes, particularly in the short-pulse laser irradiation regime, can challenge some of the key assumptions of the continuum models and calls for complementary approaches that may help to design and verify the continuum models.

In this work, an advanced continuum-level model is developed to fully account for the complexity of short pulse laser interactions with silicon on the scale of the entire laser spot. The laser-induced phase and structural transformations, proceeding through the movement of solid-liquid interface and transition from undercooled liquid to amorphous structure, as well as the generation of point defects at the propagating solidification front, are informed and parameterized by the atomistic modeling based on the MD technique, which is capable of providing atomic-level physical insights into the laser-induced rapid non-equilibrium processes. The mechanisms of formation of amorphous structure and generation of crystal defects during solidification are revealed in MD simulations. Based on the non-equilibrium formulation of the temperature dependence of solidification velocity and density of different types of point defects predicted in the MD modeling, a comprehensive study of the formation of amorphous regions, as well as the generation and mitigation of point defects, by laser irradiation is carried out through a series of continuum simulations performed with a broad range of laser parameters. The results of the simulations are used for suggesting approaches for optimizing the experimental conditions for manufacturing and processing of high-performance devices.

3.2 Molecular dynamics study of amorphization and generation of crystal defects at solidification front under conditions of strong undercooling

As discussed in Section 2.2, the continuum-level description of the material modification by short laser pulses heavily relies on the availability of kinetic models for the laser-induced melting and resolidification, as well as the generation of crystal defects at the rapidly advancing solidification front. The atomistic MD modeling has an important advantage of not requiring any assumptions on the processes or mechanisms to be investigated. Thus, the MD simulations can play an important role in uncovering the processes contributing to material modification by short pulse lasers and providing the information needed for design and parameterization of the continuum model. In this section, MD simulations are performed to reveal the temperature dependence of the melting/solidification front propagation velocity, conditions for the formation of stable amorphous phase, and the generation of point defects. The computational methods for computing the thermodynamic properties of silicon and modeling the melting/solidification processes under well-controlled temperature and pressure conditions are described in Section 3.2.1. The transition from undercooled liquid phase to amorphous structure predicted in MD simulations is discussed in Section 3.2.2. The temperature dependence of the velocity of the crystal-liquid interface and the generation of the crystal defects at the propagating solidification front are evaluated in MD simulations of melting/solidification, and the results are reported in Section 3.2.3. The main conclusions obtained from the analysis of the results of MD simulations are summarized in Section 3.2.4.

3.2.1 Computational Setup

The thermodynamic properties and structures of crystal and liquid silicon are studied by a series of MD simulations of 4096 atoms in a cubic system with size of 4 nm. The systems are controlled at constant zero pressure and constant temperature, with periodic boundary conditions applied on all three dimensions. The internal energy, density, and structure of each system are investigated as a function of temperature, in order to reveal the possible structural or phase transformations induced by short pulse laser irradiation. The undercooled systems are formed by cooling the liquid at 1 K/ps from the melting temperature.

In order to evaluate the propagation velocity of the crystal-liquid interface during the melting and resolidification processes, as well as to determine the concentrations and types of point defects formed at the solidification front, a set of MD simulations are performed for Si crystal-liquid coexistence systems under well-controlled temperature and pressure conditions. The system is generated by combining a 40-nm-thick liquid part located at the center of the system with two 5-nm-thick crystalline parts from each side along z axis, creating two crystal-liquid interfaces perpendicular to the [001] orientation of the Si diamond structural crystal. While in simulations of melting, the thickness of the liquid part is chosen as 10 nm, and the thickness of each crystalline part is 20 nm. Both liquid and crystal parts have lateral dimension of 22×22 nm^2 and are pre-equilibrated at a constant temperature and zero pressure before combined into the single coexistence system consisting of one million atoms. Periodic boundary conditions are applied in all three directions. The system is controlled at desired temperatures above or below the equilibrium melting temperature under constant zero pressure, leading to the steady-state propagation of the crystal-liquid interfaces. To avoid the local increase/decrease of temperature at the rapidly advancing interfaces due to the release/absorption of latent heat during solidification/melting, the systems are divided into 12 layers with a thickness of 4 nm and the local temperature is controlled for each layer. In order to obtain statistically reliable data, the quantitative results are averaged over four independent simulations performed at each temperature.

The interatomic interaction potential in the MD simulations is described by a bond-order potential[77] modified from the formula and parameterization developed by Tersoff .[145] This potential is fitted to both the elastic constants and the melting point of diamond silicon, and also well reproduces the cohesive energies as well as equilibrium bond length. Moreover, the modified Tersoff potential reproduces the experimental melting temperature of Si as accurately as the commonly used Stillinger-Weber potential[146] and further provides more realistic description of liquid structure.[147] The point defects generated in the process of rapid solidification are identified from local atomic configurations, and four independent simulations have been performed for each temperature to obtain statistically reliable results on defect concentrations.

3.2.2 Formation of amorphous structure under conditions of strong undercooling

The internal energies of crystal and undercooled liquid silicon calculated from the small-scale MD simulations as well as the corresponding latent heat of crystal-liquid transformation are plotted in Figure 3a. The undercooled liquid undergoes a drop of internal energy from 0.83 T_m (1400 K) to 0.71 T_m (1200 K) and, as indicated by the density profile in Figure 3b, transits to a low-density state. The Abraham factor g_{min}/g_{max} is calculated from the pair correlation function for liquid at different temperature, where g_{min} and g_{max} correspond to the magnitudes of the pair correlation function at the first minimum and first maximum, respectively. The temperature dependence of the Abraham factor reveals an obvious structural transition from 0.83 T_m to 0.71 T_m. This transition has been observed in other computational studies and recognized as the liquid-amorphous phase transformation,[148,149] which proceeds as the undercooled high-density high-coordinated liquid transits into low-density tetrahedrally coordinated liquid followed by freezing into amorphous state.[150] In conclusion, a temperature of 0.71 T_m is identified as the amorphous transition temperature T_g, below which the undercooled liquid transits to amorphous state.

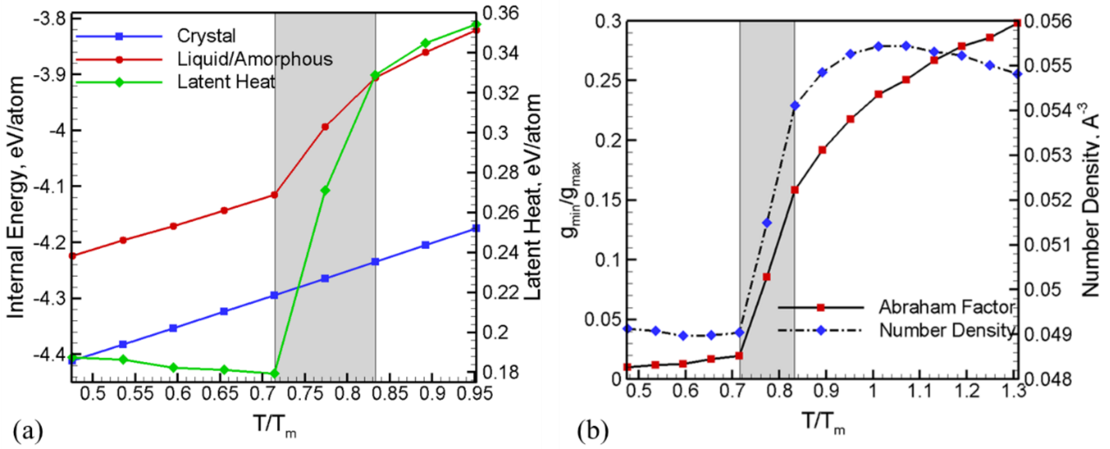

Figure 3. The temperature dependence of the internal energy of undercooled liquid/amorphous and crystal phase, as well as the latent heat of phase transformations (a), and the Abraham factor calculated from the pair correlation function g_{min}/g_{max} and number density for liquid/amorphous (b). g_{min} and g_{max} correspond to the magnitudes of the pair correlation function at the first minimum and first maximum, respectively. The gray region highlighted in both plots indicates the transition region from liquid to amorphous structure, from 0.83 T_m (1400 K) to 0.71 T_m (1200 K).

3.2.3 Generation of crystal defects at the solidification front propagating at fixed undercooling level

The melting and solidification processes are simulated by a series of crystal-liquid coexistence MD simulations under controlled pressure and temperature. Figure 4 shows the temperature dependence of the velocity of the (001) crystal-liquid interface during heterogeneous melting/solidification under different overheating/undercooling conditions. The velocity of the melting front as a function of degree of overheating is calculated from MD simulations performed at 1.07 T_m, 1.13 T_m, and 1.19 T_m, as shown in the inset of Figure 4, and the results are used to define the parameters of the analytical dependence given by Eq. (2.12). The simulations of solidification are performed at temperatures ranging from 0.75 T_m to 0.95 T_m, with the increment of 0.05 T_m. At these temperatures, the crystal-liquid interface propagates through epitaxial crystal growth, and no homogeneous nucleation is observed by the end of solidification. Depending on the interface velocity, the simulation time varies between 1 ns and 3 ns at different undercooling level before complete solidification. As illustrated in Figure 4, the solidification velocity reaches the maximum value at 0.85

T_m. In the temperature range from 0.85 T_m to melting temperature, the velocity decreases with the degree of undercooling, which can be explained by decreasing driving force for solidification. At the temperature below 0.85 T_m, the velocity decreases with increasing undercooling level because the atomic mobility decreases at reduced temperature thus decelerating the movement of the solidification front. The solidification velocities calculated from MD simulations are not used in fitting to Eq. (2.12), but have a good agreement with the kinetic equation. For temperatures lower than 0.71 T_m, the liquid freezes to amorphous structure and the solidification velocity approximates zero, leading to a stable crystal-amorphous interface.

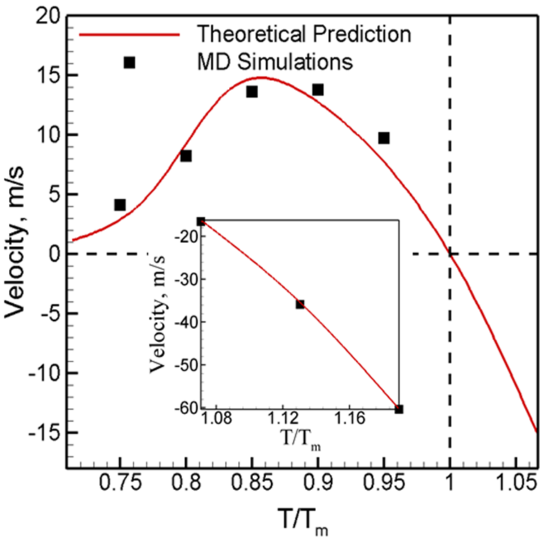

Figure 4. Velocity of crystal growth of (001) silicon system at different temperature predicted in MD simulations (black squares) and described by Eq. (2.12) (red line). The error bars represent the sample standard deviation of the values obtained in four independent simulations performed for each temperature and are smaller than the size of each point. The inset shows the data points for melting front propagation at 1.07T_m, 1.13T_m, and 1.19T_m used for fitting the pre-factor V_0 in Eq. (2.12).

The analysis of the resolidified parts of the system reveals that a substantial number of individual point defects and their clusters are generated. Figure 5 shows the temporal evolution of the atomic configurations during the solidification process in a system controlled at 0.85 T_m, illustrating the generation of various point defects as well as several dislocation loops at the rapidly propagating solidification front. The local structural of each point defect is analyzed and the configurations after the completion of solidification are compared between systems fixed at different levels of undercooling as shown in Figure 6. The type of point defect surrounded by each cluster of atoms is identified and marked as single interstitials (I) or vacancies (V), or small clusters with 2 or more number of individual point defects. To provide a clear view of the crystal defects, the atoms in Figures 5 and 6 are colored according to their potential energies, and all atoms which belong to diamond crystal structure of silicon associated with low potential energy (<-4.35 eV) are blanked.

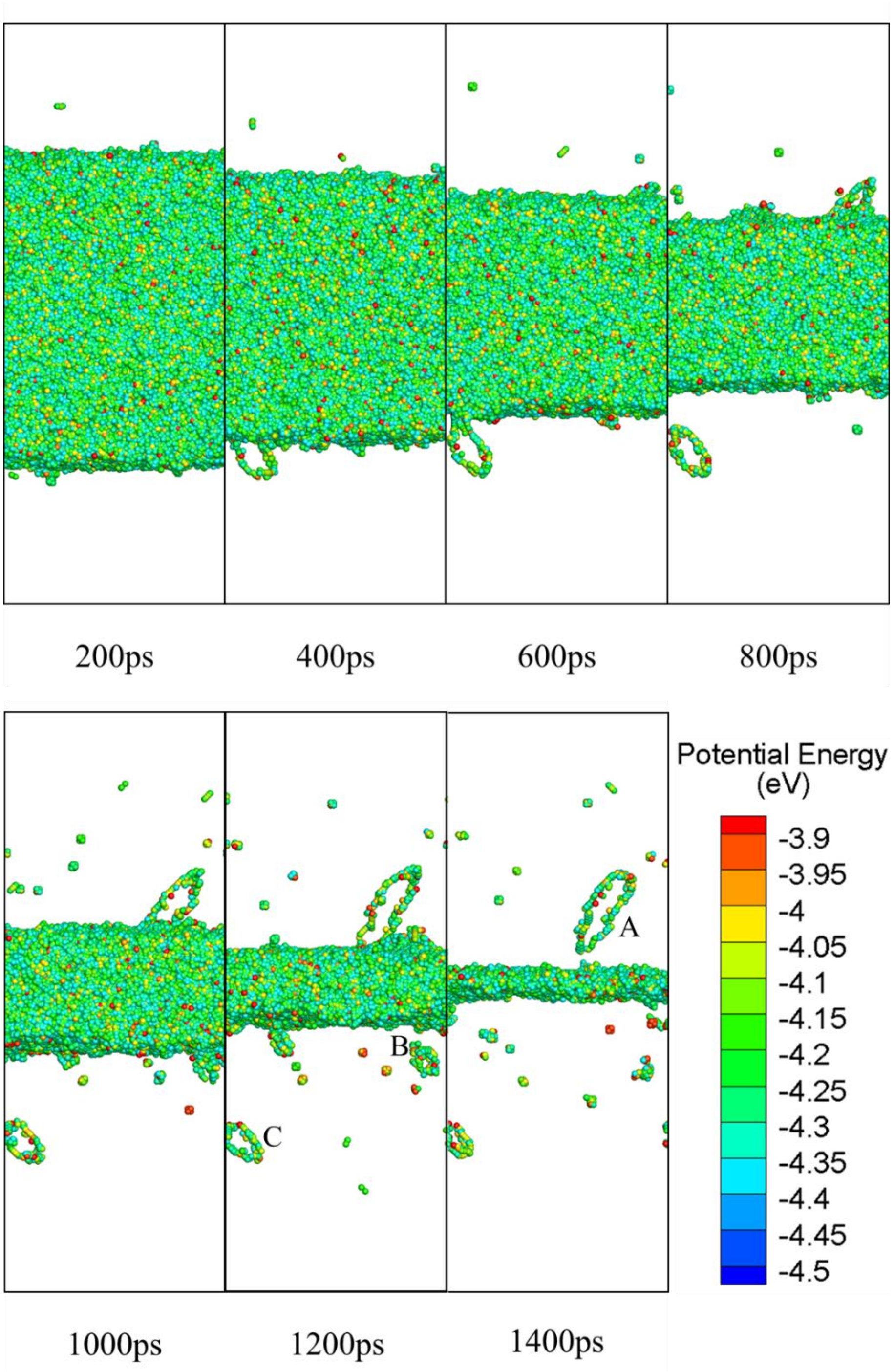

Figure 5. Snapshots showing the time evolution of a Si crystal-liquid coexistent system experiencing solidification controlled at 0.85 T_m and zero pressure. Two crystal-liquid interfaces propagate toward each other along [001] direction. Atoms are colored by potential energy, and atoms that belong to local diamond structure with corresponding low potential energy (<-4.35 eV) are blanked. The dislocation loops marked by letters are analyzed and discussed below.

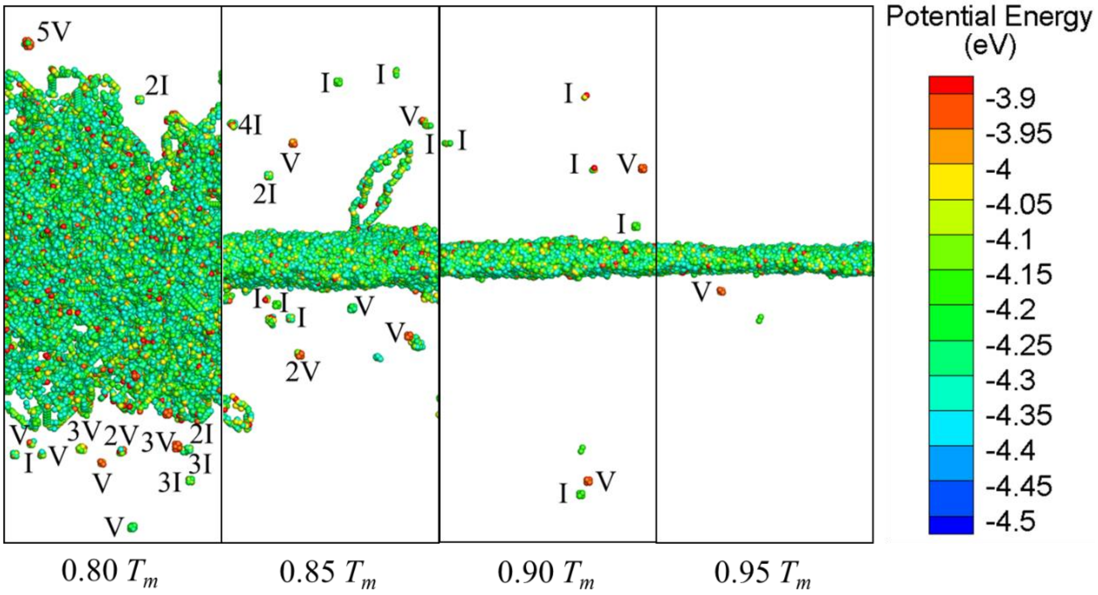

Figure 6. Crystal defects generated in the MD simulations of solidification in the Si crystal-liquid coexistent systems controlled at 0.8 T_m, 0.85 T_m, 0.9 T_m, and 0.95 T_m, respectively. Atoms are colored by potential energy, and atoms that belong to local diamond structure with corresponding low potential energy (<-4.35 eV) are blanked. Each type of point defect is labeled with V or I denoted as vacancy or interstitial, respectively, and the marked value represents the number of point defects forming each cluster, such as 3V for a tri-vacancy cluster.

The concentrations of individual point defects, di-vacancies and di-interstitials are calculated as dependent on the degree of undercooling as shown in Figure 7. The concentrations are expressed in the unit of atomic percentage calculated by dividing the number density of point defects by that of lattice sites (~5×10^{22} cm^{-3}). The results are averaged over four independent simulations performed at the same undercooling conditions, and the statistic error bars are evaluated. The defective regions at the center of the system, where the solid-liquid interfaces meet and large amount of dislocations are generated, are excluded from the calculation. Figure 7 indicates that substantially high density of point defects are generated in the course of solidification, as compared to the equilibrium values plotted by the dashed lines predicted from Ref. 108. As will be discussed in Section 4, the point defects can be regarded as “errors” during the process of building the crystal structure at the crystal-liquid interface, which can diffuse to the sink of point defects, *i.e.*, the liquid, or be trapped by the rapidly advancing solidification front. At small undercooling, where temperature is higher than 0.9 T_m, only a few individual interstitials and vacancies are observed, and the interstitials have higher density than vacancies, which can be explained by that excess of atoms tend to be left behind the solidification front, since the liquid density is larger than that of solid for silicon. At 0.85 T_m, the concentration of both interstitials and vacancies are considerably increased, together with the observation of small clusters. The increase of point defects concentration can be attributed to a combined effect of the increase of solidification velocity, as shown in Figure 4, and decrease of atomic diffusivity, both enhancing the possibility of trapping of these "errors" by solidification front due to insufficient atomic rearrangements to correct them. At deeper undercooling, more point defects including clusters are generated, and even complex structures of dislocations are observed.

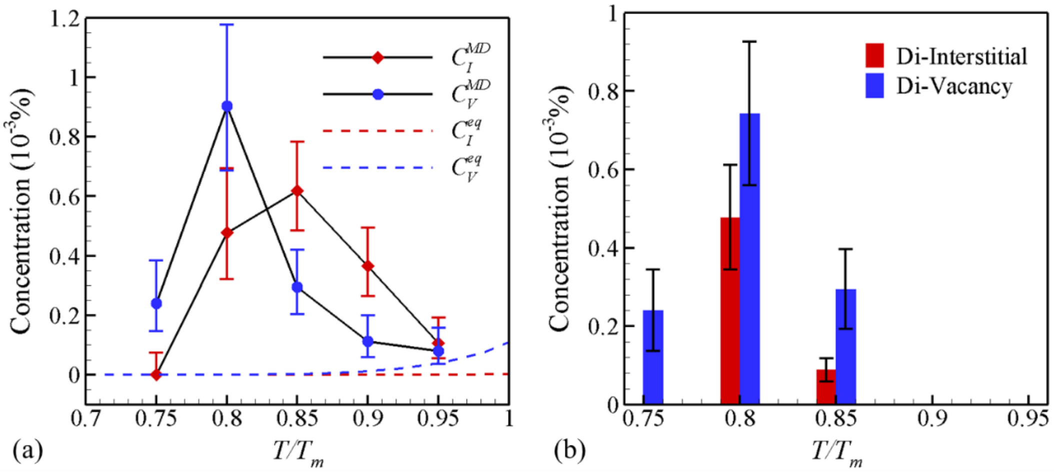

Figure 7. MD predictions of temperature dependence of atomic concentrations of individual interstitials (red squares) and individual vacancies (blue circles) (a), as well as di-interstitials (red bars) and di-vacancies (blue bars) (b), averaged over four simulations performed under the same conditions. In (a), error bars are calculated as the range with 68% confidence assuming a Poisson distribution of point defects; in (b), error bars are calculated as standard deviation of the mean. Predictions of equilibrium concentrations of interstitials and vacancies from Ref. 108 are shown in (a) as red and blue dashed lines, respectively.

Detailed analysis of the structure of the dislocation loop marked by "A" in Figure 5 at the time of 1400 ps reveals the presence of a twinning domain consisting of six consecutive $(11\bar{1})$ atomic planes, as illustrated in Figure 8, where the <110> projections of several atomic layers in the vicinity of the loop is shown. As shown in Figure 5, the crystal-liquid interface is rough and several facets with {111} planes appear, leading to the crystal growth proceeding through nucleation of atomic layer on the {111} facetted planes. Similar as the case of FCC structure, the nucleation of a new layer on {111} planes in diamond crystal can be arranged in a regular CcAaBb sequence, or in a sequence of CcAaCc leading to the formation of a coherent twin boundary consisting of CcAaCcBbAa sequence of planes, as schematically illustrated in Figure 9. Once formed on the {111} facetted planes, as indicated in Figure 5, the twin domains grow in lateral directions with the propagation of solidification front, which is followed by the separation ("A"), shrinkage ("B"), even the disappearance ("C") of the twinned domains, by motion of the incoherent twin boundaries surrounding them. As illustrated in Figure 9, incoherent twin boundaries surrounding the twin domain "A" can be represented by arrays of Shockley partial dislocations each located at one $(11\bar{1})$ glideset planes,[151] with Burgers vectors determined to be $\frac{a}{6}[2\bar{1}1]$, $\frac{a}{6}[\bar{1}\bar{1}\bar{2}]$, and $\frac{a}{6}[\bar{1}21]$, where $a = 5.48$ Å is the lattice parameter. The formation of twin boundary in the process of solidification in silicon has been demonstrated in numerous previous studies of experimental investigations,[152-154] theoretically analyses[155,156] or atomistic simulations.[19, 157 - 159] No twin structure is observed in the solidification process occurring under conditions of weak undercooling at $T > 0.85\, T_m$.

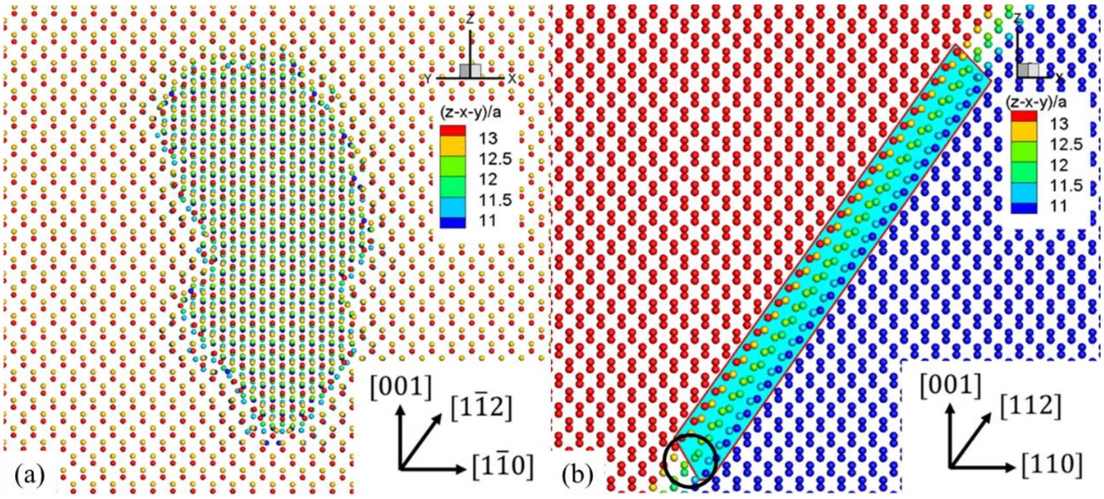

Figure 8. Atomic snapshots of the [110] projection of six $(11\bar{1})$ layers (a), and $[\bar{1}10]$ projection of two $(\bar{1}10)$ layers (b), across the twinning domain. Atoms are colored by the index of the corresponding $(11\bar{1})$ plane where they are located. The lattice parameter a is 5.48 Å. The local structure of the incoherent twin boundary outlined by black circle is analyzed in Figure 9.

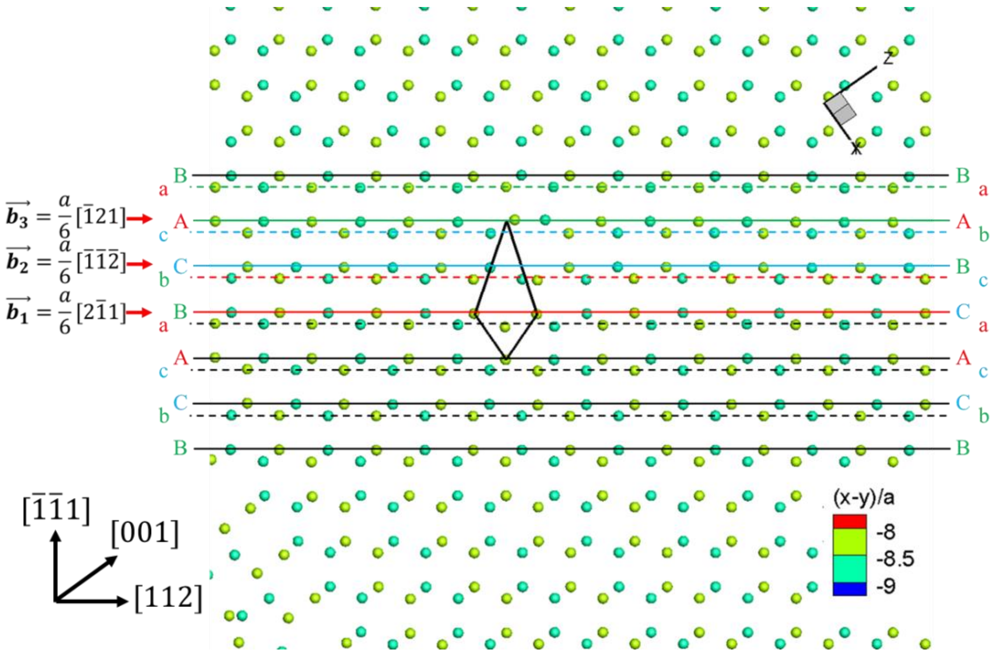

Figure 9. Structure of the incoherent twin boundary at the position marked by a circle in Figure 8b. Burgers vectors of partial dislocations building the twin boundary are shown. The diamond structure of silicon can be regarded as two set of FCC lattice represented by letters of upper and lower case, respectively. The atoms are colored by the index of $(1\bar{1}0)$ planes where they are located.

3.2.4 Summary

The MD simulations provide detailed insights into the kinetics and mechanisms of the structural and phase transformations possibly induced by short pulse laser irradiation. The transition from liquid to amorphous structure at strong undercooling, steady-state propagation of the melting/solidification front under conditions of superheating/undercooling, and the generation of crystal defects at the advancing solidification front are investigated.

The computational predictions of the amorphous transition temperature, $T_g =$ 1200 K, the temperature dependence of the crystal-liquid interface velocity, as well as the types and concentrations of point defects produced at the solidification front at different levels of undercooling, are taken as input parameters for the continuum-level formulation of kinetics of solidification and point defects, Eqs. (2.12-2.18), complemented to the general framework of the continuum thermal model, enabling simulations of laser interactions with silicon and investigation of the laser-induced modifications of surface microstructure, of which the results are reported in the next two sections.

3.3 Formation of amorphous structure by short pulse laser irradiation

Based on the results of atomistic simulations discussed in Section 3.2, advanced continuum model of short pulse laser interaction with silicon, fully accounting the propagation of crystal-liquid interface under conditions of overheating/undercooling and formation of stable amorphous structure, is developed in this section. The irradiation conditions leading to the amorphization of strongly undercooled liquid is investigated and used to interpret different surface morphologies of amorphous structure observed in experiments. The computational setup and parameters for the continuum simulations of laser melting and solidification of silicon target are discussed in Section 3.3.1. The effect of laser parameters, *i.e.*, laser fluence, pulse duration, spot size, and wavelength, on the formation of amorphous structure is explored through 1D simulations in Section 3.3.2. In Section 3.3.3, 2D simulations based on the cylindrical coordinates are performed to address the process of laser-induced phase transformations on the scale of whole laser spot and understand the mechanisms responsible for the modification of surface morphology. The computational results are summarized in Section 3.3.4.

3.3.1 Computational Setup

Continuum-level description of the laser-induced melting and resolidification at the experimental time- and length-scales is based on the general framework of the thermal model discussed in Section 2.2. The temperature and phase state evolutions in the irradiated target are evaluated by solving Eqs. (2.10) and (2.12). The system is represented by a 10 μm-thick silicon wafer and has cylindrical symmetry in 2D simulations. This depth is used to avoid notable change of temperature at the bottom of the wafer. To ensure no significant change of temperature at the side of the system in 2D simulations, the radius of the silicon wafer, R_{Si}, is chosen according to the laser spot diameter D_L, which is defined as the full width at 1/e^2 height of the radial Gaussian profile of the laser beam. In this work, R_{Si} = 30 μm for D_L = 5 μm; R_{Si} = 300 μm for D_L = 10 μm, 30μm, and 50 μm; and R_{Si} = 500 μm for D_L = 70 μm. The system is set at 300 K initially with adiabatic boundary conditions applied at the bottom and side of the wafer. The simulations are performed at different incident fluences in the irradiation regime of melting and resolidification, for a range of laser pulse durations from 30 ps to 100 ps.

Three values of laser wavelength in the continuum simulation are chosen as 355 nm, 532 nm, and 1064 nm, with the corresponding reflectivity of solid and liquid given in Refs. 160-163. The laser intensity attenuates exponentially with depth under the surface following the Beer-Lambert law, with the optical absorption depth determined in experiments.[164-166] The melting temperature T_m = 1687 K, enthalpy of melting $\Delta H(T_m)$ = 50.2 kJ/mol, boiling temperature T_b = 3505 K, and density ρ = 2320 kg/m^3 are taken as the experimental values.[167-169] The thermal conductivity K_{th} is implemented as a function of temperature for both crystal[170] and liquid[171] silicon. The temperature dependence of heat capacity C_P is fitted based on experimental measurements for crystal[172], liquid[173,174], and amorphous[175] phases.

3.3.2 1D simulations of the effect of laser parameters on amorphization

The time evolution of the temperature at the crystal-liquid/amorphous interface and the depth of the interface are plotted in Figure 10 and Figure 11, respectively, with comparison of the results obtained at different laser fluences and pulse durations. The laser energy deposition on the silicon wafer leads to a rapid heating of the surface region. When the surface temperature exceeds the equilibrium melting temperature, T_m, the crystal at the target surface transforms into liquid and the melting front propagates deep into the target, as illustrated in Figure 11. When the surface region is highly overheated by rapid energy deposition, significant homogeneous nucleation of liquid takes place in addition to heterogeneous melting. The melting front is cooled after laser pulse and its velocity decreases with decreasing level of overheating. Once cooled below the melting temperature, the melting front stops propagating and the melting turns into the epitaxial crystal growth. During resolidification, the crystal-liquid interface moves back to the surface, with the velocity determined by Eq. (2.12). When the interface is cooled below the amorphous transition temperature T_g=1200 K, the atomic rearrangements become too sluggish for the advancement of the solidification front as discussed in Section 3.2. As a result, the advancement of the crystal-liquid interface stops, leading to the formation of stable amorphous phase from the remaining undercooled liquid in the surface region of the irradiated target.

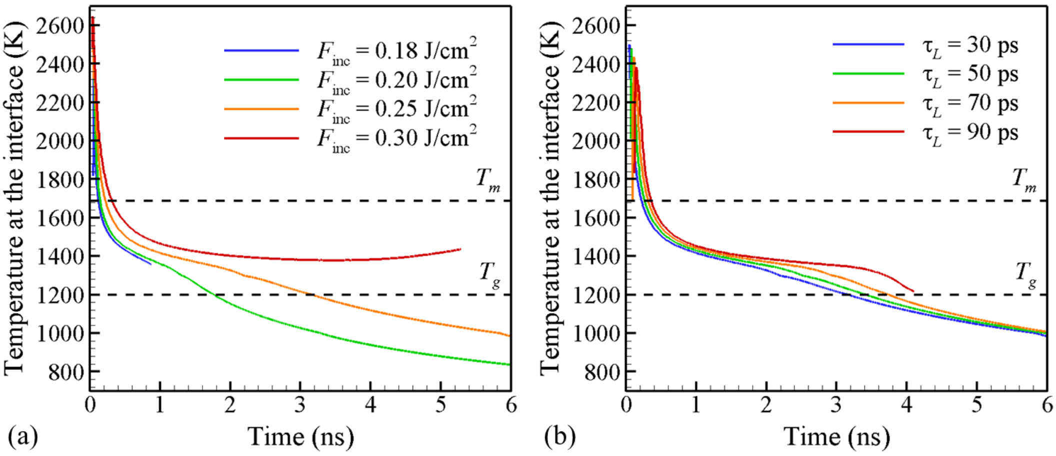

Figure 10. Time evolution of the temperature at the crystal-liquid/amorphous interface for 1D simulations of 30 ps laser irradiation at different incident fluences (a), and for 1D simulations performed at various pulse durations and laser incident fluence of 0.25 J/cm^2 (b). The laser wavelength is 532 nm. T_m and T_g mark the melting temperature (1687 K) and glass transition temperature (1200 K), respectively. The termination of some profiles indicates the complete crystal regrowth with the solidification front reaching the target surface.

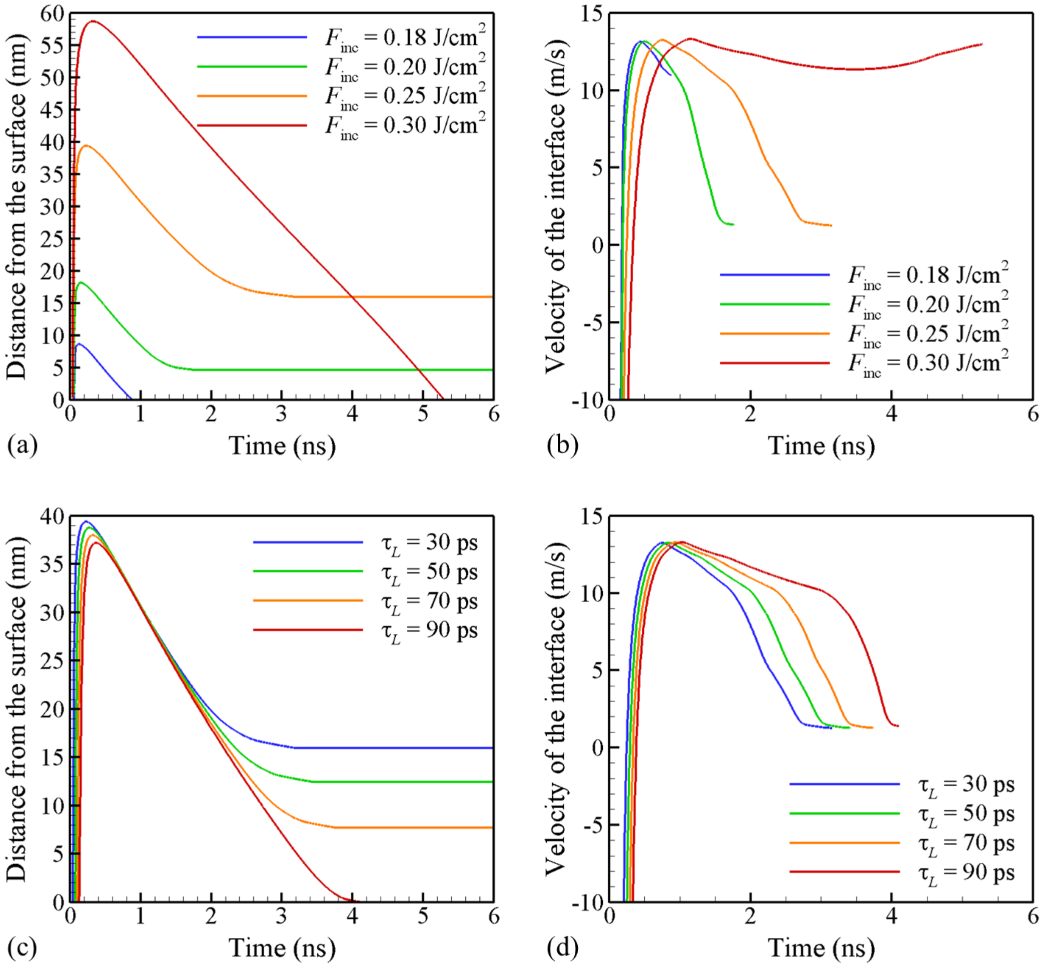

Figure 11. Time evolution of the depth and velocity of the crystal-liquid/amorphous interface for 1D simulations of 30 ps laser irradiation at different incident fluences (a,b), and for 1D simulations performed at various pulse durations and an incident fluence of 0.25 J/cm^2 (c,d). In (b,d), the velocity of the interface is shown until the completion of solidification (either through epitaxial growth of crystal to the surface, or freezing of the remaining undercooled liquid into amorphous structure). The positive velocity indicates solidification and the negative value refers to melting. The scale of the velocity is chosen to clearly show the propagation velocity of the solidification front. The laser wavelength is 532 nm.

The effect of laser fluence on the processes of melting and resolidification induced by 30 ps laser irradiation is illustrated in Figure 10a and Figure 11a. In the simulation performed at $F_{\text{inc}} =$ 0.18 J/cm^2, slightly above the melting threshold of 0.15 J/cm^2, a surface layer of ~ 9 nm thickness is melted rapidly by laser irradiation and is completely resolidified after ~ 0.8 ns through epitaxial crystal growth. Increasing the laser fluence also increases the maximum melting depth, thus allowing more time for the interface to be cooled down before complete resolidification. As a result, amorphization can appear upon strong undercooling of the interface below T_g at higher fluence, which is demonstrated by the formation of 4.6 nm and 16 nm thick amorphous regions at $F_{\mathrm{inc}} =$ 0.2 J/cm^2 and $F_{\mathrm{inc}} =$ 0.25 J/cm^2, respectively, as illustrated in Figure 11a. The temperature profiles in Figure 10a show that the cooling rate at the crystal/liquid interface during resolidification decreases with increasing laser fluence, and the interface temperature even increases due to release of latent heat at high fluence of 0.3 J/cm^2. With decreasing cooling rate, it takes longer time for the interface to reach the amorphous transition temperature, leading to the suppressed formation of amorphous structure at high laser fluence. The amorphization process may even be avoided when the interface temperature keeps staying at elevated levels above T_g during resolidification, as revealed in the simulation at $F_{\mathrm{inc}} =$ 0.3 J/cm^2. The effect of laser pulse duration on amorphization is investigated in the simulations performed at the incident fluence of 0.25 J/cm^2. Due to decreasing cooling rate at the crystal-liquid interface with increasing pulse duration, Figure 10b, the thickness of amorphous region decreases as illustrated in Figure 11c.

The comprehensive effect of laser fluence and pulse duration on the thickness of amorphous region is summarized in Figure 12a. According to the discussions above, two threshold fluences, F_a^{low} and F_a^{high}, can be defined based on the generation and disappearance of amorphous region as the laser fluence increases. Below F_a^{low}, the melting depth is not large enough to ensure sufficient undercooling of the interface before the completion of epitaxial crystal growth. Above F_a^{high}, the low cooling rate prevents the interface to be cooled below the amorphous transition temperature. The amorphous structure can only be formed in a range of fluence between these two thresholds, where the thickness of amorphous region increases and then decreases with increasing laser fluence. This can be explained by the combined effects of maximum melting depth and cooling rate. The maximum melting depth increases with laser fluence and allows more time for cooling of the interface, while the cooling rate decreases with increasing laser fluence thus slowing down the cooling process at the interface to reach the amorphous transition temperature. At certain laser fluence, the amorphous layer reaches a maximum thickness, which significantly decreases with increasing laser pulse duration. The threshold fluences of amorphization depend on the laser pulse duration, as illustrated in Figure 12b, and the range between these fluences narrows down with increasing pulse duration. For laser pulses longer than 92 ps, no amorphous structure is expected.

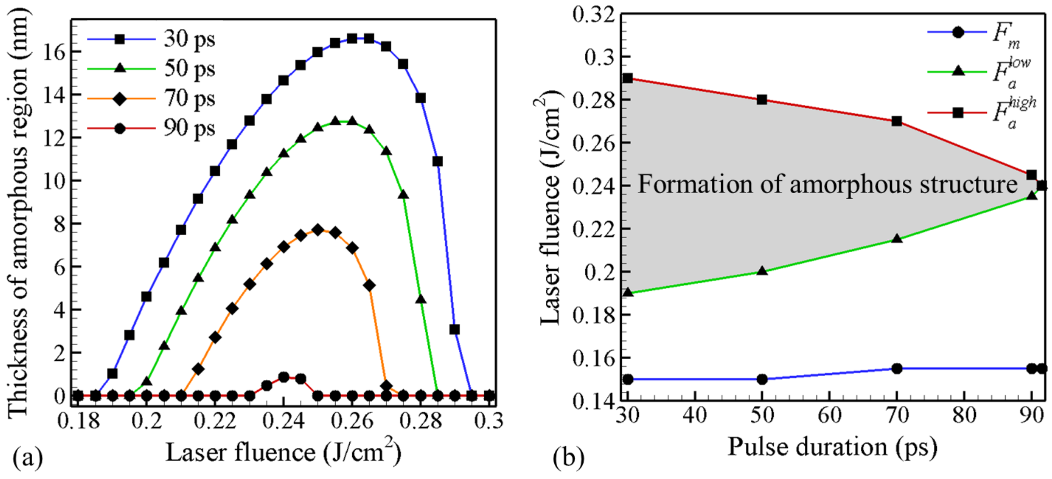

Figure 12. (a) The amorphous depth as a function of incident fluence predicted from continuum simulations of laser irradiation on Si performed with different pulse durations and wavelength of 532 nm. (b) The dependence of laser threshold fluences for generation of amorphous phase on the laser pulse duration. The amorphous region is only expected to be formed within the range of fluences between F_a^{low} and F_a^{high} (gray area). The resolution in fluence in the plots is 0.05 J/cm^2.

In order to evaluate the effect of laser wavelength on the formation of amorphous structure, the continuum simulations are also performed for laser wavelength of 355 nm and 1064 nm. The temperature dependence of the optical absorption depth for different laser wavelength is illustrated in Figure 13a. Above the melting temperature, T_m=1687 K, the target surface undergoes heterogeneous melting and the optical absorption depth immediately drops to the value of liquid silicon which is around 10 nm. While the optical absorption depth in liquid silicon is insensitive to laser wavelength, as shown in Figure 13a, the values for solid differ on orders of magnitudes, resulting in significant difference in the scale of laser energy deposition and initial temperature distribution. Decrease of the laser wavelength causes a substantial decrease in laser penetration depth and the buildup of stronger temperature gradient in the surface region of the Si target, thus leading to higher cooling rate during resolidification and easier formation of amorphous structure. This is demonstrated in Figure 13b, which shows that for 355 nm laser irradiation, amorphization can be realized for much longer laser pulse of hundreds of picoseconds even up to 1.44 ns and at wider range of fluences, compared with the results for 532 nm wavelength, Figure 12b. However, for the wavelength of 1064 nm, the penetration depth up to hundreds of micrometers creates almost uniform heating of the thin wafer, retaining the crystal-liquid interface around the melting temperature, well above the level required for the onset of amorphization until the solidification front reaches the surface of the target.

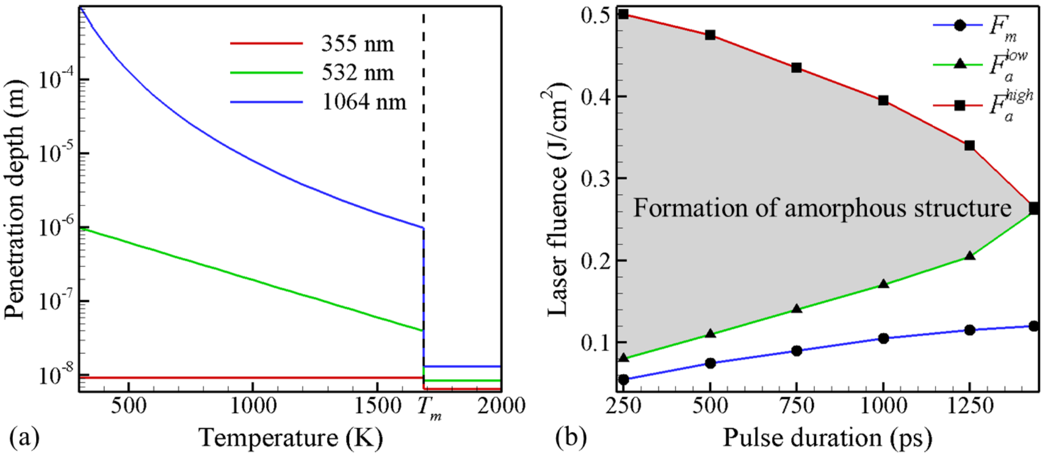

Figure 13. (a) Temperature dependence of the optical absorption depth in solid (below T_m) and in liquid (above T_m) silicon for different laser fluences. The data is taken from or calculated as a function of temperature following the functions provided in Refs. 164,166. (b) The dependence of laser threshold fluences for generation of amorphous phase on the laser pulse duration for a wavelength of 355 nm. The amorphous region is only expected to be formed within the range of fluences between F_a^{low} and F_a^{high} (gray area). The resolution in fluence in the plots is 0.05 J/cm^2.

3.3.3 2D simulations of formation of surface amorphous structure in different irradiation regimes

2D simulations provide the realistic description of the spatial propagation of crystal-liquid interface and morphology of amorphous region induced by a circular laser beam. Figures 14a and 15a show the contour plots of the volume fraction of amorphous structure after resolidification in simulations performed for a 30 ps laser pulse at incident flences of 0.25 J/cm^2 and 0.3 J/cm^2, respectively, with spot diameter of 50 μm. As discussed above, amorphous region can be formed when the local fluence within the laser spot lies in the range between two thresholds, F_a^{low} and F_a^{high}. This explains the formation of amorphous structure in the region of laser spot center in the simulation performed at $F_{\mathrm{inc}} =$ 0.25 J/cm^2. At the radial position larger than ~10 μm, as illustrated in Figure 14b, where the laser fluence along the Gaussian profile decreases below F_a^{low}, insufficient cooling at the interface before complete resolidification results in a region of single crystal structure. While at the center of the laser spot, *i.e.*, $|r| \leq$ 10 μm, the local fluence meets the criterion of formation of amorphous structure. The location of the value F_a^{low} along the radial laser beam profile determines the radius of amorphous region. In the simulation performed at $F_{\mathrm{inc}} =$ 0.3 J/cm^2, Figure 15b, the laser fluence in the vicinity of the laser spot center is higher than F_a^{high}, leading to insufficient cooling rate to induce amorphization. At the periphery of the laser beam where the local fluence drops below F_a^{high}, however, lower energy density deposited by the laser pulse results in a rapid undercooling of the molten region down to the amorphous transition temperature, contributing to the formation of a ring-shaped amorphous region surrounding the fully recrystallized central part of the laser spot. The inner and outer boundaries of the amorphous region are determined by the positions of F_a^{high} and F_a^{low} along the laser profile, respectively. The shape and scale of the amorphous regions analytically illustrated in Figures 14b and 15b have good agreement with the computational results in Figures 14a and 15a. The predicted effect of laser fluence on the formation of two different types of amorphous morphology is consistent with earlier experimental observations for silicon targets irradiated by a single 30 ps laser pulse[36] or by several 100 fs laser pulses.[130]

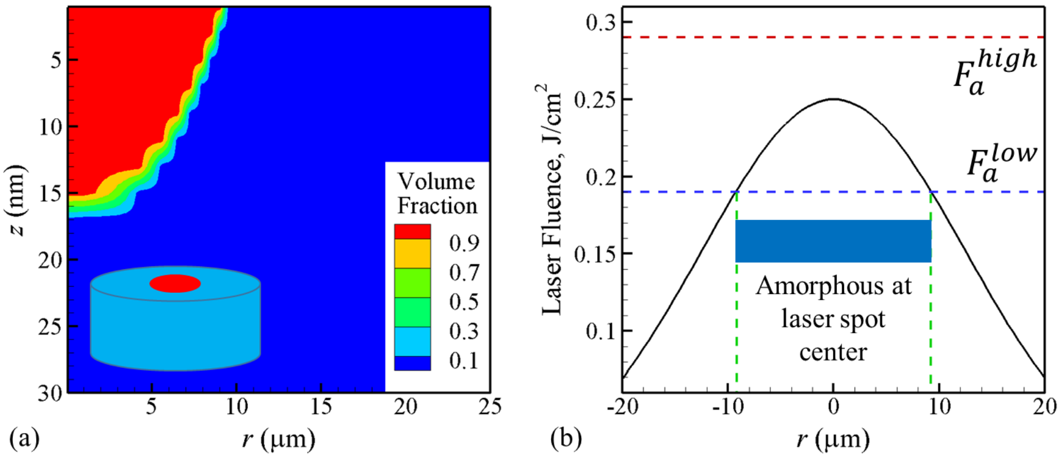

Figure 14. (a) Contour plot of volume fraction of amorphous phase in the Si target predicted from 2D continuum simulations of laser melting and resolidification at incident fluence of 0.25 J/cm^2. The laser wavelength is 532 nm, the pulse duration is 30 ps, and the spot diameter is 50 μm defined as the full width at 1/e^2 height of the Gaussian profile. The inset illustrates the morphology of the amorphous region marked by red. (b) Spatial Gaussian profile of a laser pulse with peak fluence of 0.25 J/cm^2 and spot diameter of 50 μm. The red and blue dashed lines represent the level of two thresholds of amorphization, F_a^{high} and F_a^{low}, respectively, which are obtained from Figure 12b. The blue band indicates the region where amorphous structure is formed.

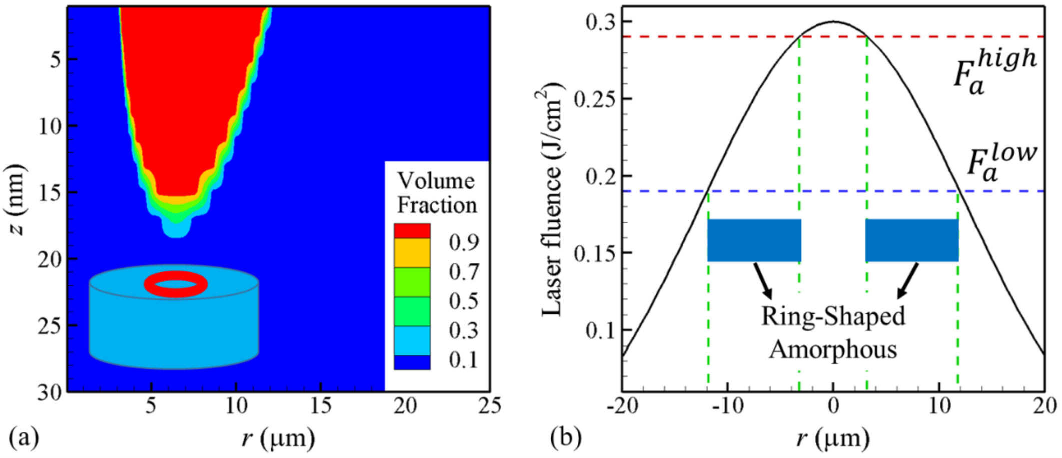

Figure 15. (a) Contour plot of volume fraction of amorphous phase in the Si target predicted from 2D continuum simulations of laser melting and resolidification at incident fluence of 0.3 J/cm^2. The laser wavelength is 532 nm, the pulse duration is 30 ps, and the spot diameter is 50 μm defined as the full width at 1/e^2 height of the Gaussian profile. The inset illustrates the morphology of the amorphous region marked by red. (b) Spatial Gaussian profile of a laser pulse with peak fluence of 0.3 J/cm^2 and spot diameter of 50 μm. The red and blue dashed lines represent the level of two thresholds of amorphization, F_a^{high} and F_a^{low}, respectively, which

are obtained from Figure 12b. The blue bands indicate the regions where amorphous structure is formed.

A series of simulations with different laser parameters are performed to study the dependence of the amorphous morphology on laser fluence, pulse duration, and spot size. Figure 16a shows a map of different types of morphologies of amorphous region as a function of laser fluence and pulse duration for a spot diameter of 70 μm. The amorphous morphologies with respect to laser fluence and spot diameter for the pulse duration of 30 ps are summarized in Figure 16b. In both figures, three regimes of laser-modified surface microstructure are identified: single crystal, amorphous region at the laser spot center and ring-shaped amorphous region. The lower and higher boundaries of the regime of amorphization at the laser spot center, as illustrated in Figure 16a, are consistent with the dependence of F_a^{low} and F_a^{high} on the pulse duration in Figure 12b, as expected according to the discussion above. When the laser spot diameter D_L is decreased less than 30 μm, as can be seen from Figure 16b, the boundary between the regimes of single crystal and amorphization at the laser spot center decreases with decreasing D_L, while the boundary between the regimes of amorphization at the laser spot center and ring-shaped amorphous region increases with decreasing D_L. The broadening of the regime of amorphization at the laser spot center with decreasing D_L is explained by the acceleration of cooling process at the crystal-liquid interface due to lateral thermal diffusion. The characteristic length of thermal diffusion $L_{th} = \sqrt{4D_{th}t}$, where $D_{th} = K_{th}/C_P$ is the thermal diffusivity, is calculated to be on the order of 10 μm for simulation of 10 ns. Therefore, for laser spot diameters larger than 30 μm which lead to ineffective lateral thermal diffusion, the lower and higher boundaries of the regime of amorphization at the laser spot center are nearly constant and follow the values of F_a^{low} and F_a^{high} predicted in 1D simulations, as marked by the dashed lines in Figure 16b. For laser pulse duration of 90 ps, however, the higher boundary predicted in 2D simulations does not match F_a^{high} until the laser spot diameter is larger than 70 μm. The effects of laser parameters on the amorphous morphologies shown in Figures

16a and b are similar in simulations performed for other spot diameters and pulse durations, respectively.

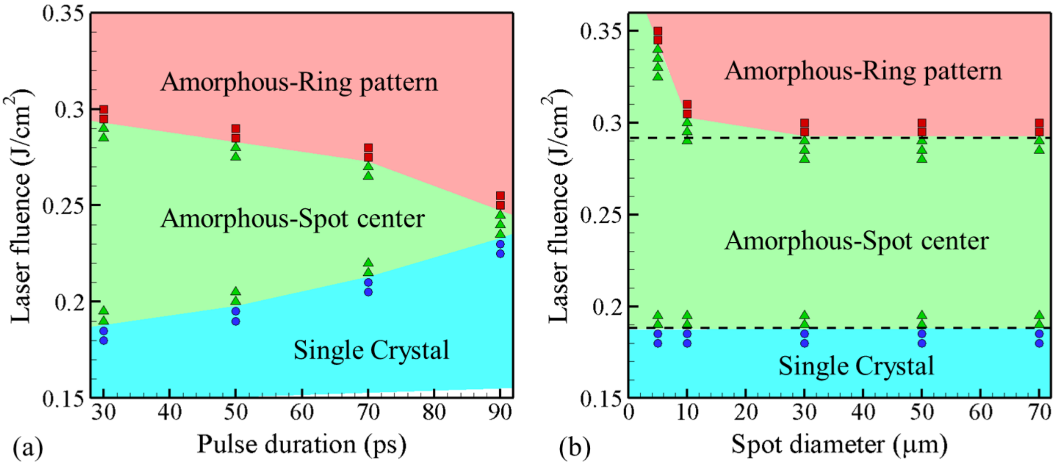

Figure 16. The map of regimes of final morphology of amorphous regions after resolidification depending on laser fluence and pulse duration for a laser spot diameter of 70 μm (a), and depending on laser fluence and spot diameter for the laser pulse duration of 30 ps (b). Each point represents one simulation with corresponding laser parameters. Blue circles correspond to conditions generating single crystal, green triangles correspond to amorphous region at the laser spot center and red squares correspond to ring-shaped amorphous region. To help visualize each regime, the single crystalline regime is colored by light blue, the regime of amorphization at laser spot center is colored by light green and the regime of ring-shaped amorphous region is colored by light red. The blank region in (a) corresponds to irradiation conditions below the melting threshold. The dashed lines in (b) correspond to the fluence thresholds for amorphization, F_a^{high} and F_a^{low}, predicted in 1D simulations.

3.3.4 Summary

Laser-induced melting, resolidification, and formation of amorphous structure in a silicon target are investigated by a series of 1D and 2D continuum simulations, complemented by the kinetics of crystal-liquid interface and conditions of amorphization predicted from the atomistic simulations. The effect of laser fluence, pulse duration, wavelength, and spot diameter on the formation of a stable amorphous region is evaluated.

1D simulations performed for a wide range of laser fluences and pulse durations reveal the decrease of cooling rate with increasing laser fluence or pulse duration, suppressing the formation of amorphous structure during resolidification. Two thresholds of fluence, between which the maximum melting depth and cooling rate are optimized to form amorphous region, are observed for each pulse duration. This range of laser fluence for amorphization narrows down with increasing pulse duration. Shorter laser wavelength with smaller optical penetration depth is demonstrated to facilitate the formation of amorphous structure, as a result of stronger temperature gradient and faster cooling rate.

2D simulations account for the lateral thermal diffusion and spatial propagation of the crystal-liquid interface. Three regimes of structural microstructures, single crystal, amorphous region at the laser spot center, and ring-shaped amorphous region, are identified with respect to laser fluence, pulse duration, and spot diameter. For each pulse duration or spot diameter, the boundary between the first two regimes corresponds to the lower threshold of fluence for amorphization, and the boundary between the second and third regimes corresponds to the higher threshold of fluence for amorphization. Decrease in either pulse duration or spot diameter leads to accelerated cooling rate at the crystal-liquid interface, contributing to the broadening of the regime of amorphous region at the laser spot center. Due to the limitation of effective thermal diffusion length, the boundaries between three regimes are nearly constant for laser spot diameters larger than 30 μm.

3.4 Generation and evolution of point defects in laser irradiated silicon

This section is divided into two main parts: First, based on the atomistic modeling of rapid propagation of the solidification front and the resulting formation of crystal defects under fixed levels of undercooling, which are discussed in Section 3.2, continuum simulations of laser interaction with silicon are performed to investigate the generation of point defects in the course of laser-induced melting and resolidification; Second, elimination of these point defects induced by laser processing is evaluated through continuum simulations of subsequent low power laser annealing below the melting threshold. The computational results will clarify the origin of laser-induced defects during various laser fabrication processes and suggest approaches for mitigating defects through control of laser parameter and post treatment, from which the manufacturing of high-efficiency devices will benefit. The computational system and parameters set for the continuum simulations are briefly discussed in Section 3.4.1. The laser-induced melting, resolidification, and generation of point defects in the surface region of the Si target on the experimental time- and length-scales are investigated in Section 3.4.2. The post annealing effects of the point defects by means of subsequent low power laser heating of the processed region is discussed in Section 3.4.3. The results and main conclusions are summarized in Section 3.4.4.

3.4.1 Computational setup

The continuum model of laser producing and removal of point defects is developed based on the general framework of thermal model, Eqs. (2.10-2.12), implemented by the continuum description of generation and evolution of point defects, Eqs. (2.13-2.18), as discussed in Section 2.2. The simulations of generation of point defects in the course of laser-induced melting and resolidification are performed for a Si wafer target irradiated by a 532 nm single laser pulse at a series of laser fluence ranging from 0.25 J/cm^2 to 0.7 J/cm^2, between the threshold of surface melting and onset of ablation. The laser beam has a Gaussian temporal and spatial profile with a pulse duration of 1 ns at full width at half maximum, and a spot diameter of 30 μm defined as full width at the 1/e^2 height. The system is discretized in 2D cylindrical coordinates, (r, z), and each cell has thickness of 8 nm and width of 100 nm. The radius and thickness of the Si wafer are chosen as 100 μm and 2 μm, respectively, to ensure no significant change of temperature at the edge or bottom of the target. The thermodynamic and optical properties of Si utilized in the continuum model are the same as described in Section 3.3.1.

To investigate the effect of laser annealing on eliminating the point defects, the laser-processed silicon target after the simulations of laser melting and resolidification, featuring high density of point defects in the surface region, is taken as the initial system and irradiated by subsequent low power lasers below the melting threshold. The pulse durations of the annealing laser are chosen for a wide range from 10 ns to 500 ns, and for the 50 ns laser pulse, simulations are also performed for double-pulse irradiation with 1 MHz repetition rate to evaluate the annealing effect of multiple pulses. To enable simulation of such long pulse duration, 1D continuum model is used and the initial concentration of point defects are taken from the values at the center of the processed target.

3.4.2 Generation of point defects in the course of laser-induced melting and resolidification

The capability of the continuum model to predict the distribution of point defects in a laser-processed Si target is exemplified in Figure 17, which shows the time evolutions of the concentrations of individual interstitials and individual vacancies produced in the surface region of the Si target irradiated by a 1 ns laser pulse at the incident fluence of 0.45 J/cm^2. Lase energy deposition results in a fast heating and melting of a surface region of the target, with the depth of melting reaching ~90 nm in the center of the laser spot. The laser heating and melting are followed by a rapid cooling and resolidification, as can be seen from the upwards movement of the crystal-liquid interface shown in Figure 17 by black lines. The solidification process proceeds through the epitaxial crystal regrowth, and the crystallization kinetics is described by Eq. (2.12) with parameters evaluated based on the results of atomistic simulations discussed in Section 3.2. In contrast to the simulations of picosecond laser irradiation discussed in the previous section, the irradiation by a longer, 1 ns, laser pulse reduces the temperature gradient and cooling rate, and does not result in the formation of amorphous phase. The undercooling in the vicinity of the solidification front, however, leads to the formation of distinct regions of strong supersaturation of both vacancies and interstitials in the parts that experience transient melting and resolidification. As illustrated in Figures 17a-h, substantial number of interstitials and vacancies are left behind the advancing solidification front, depending on the level of undercooling achieved at the crystal-liquid interface, as described by the source terms in Eqs. (2.13-2.14) and parameterized by the results from MD simulations discussed in Section 3.2. In Figure 17i, a smaller number of interstitials are observed closer to the surface region (the green part). This can be explained as that at later stage of the solidification process, the interfacial temperature increases due to release of the latent heat resulting in the reduced concentration of interstitials, which is discussed below. Moreover, it is interesting to find that the vacancies and interstitials can be eliminated by their diffusion to the target surface, which is regarded as the sink of point defects, as evident by the decrease of vacancy concentration at the surface in Figure 17j. This effect is not obvious in the interstitial distribution, due to significantly lower diffusion coefficient compared to vacancies.[108]

In order to investigate the effect of laser fluence on generation of point defects, the evolution of the temperature at the solid-liquid interface and the concentration of point defects averaged over the transiently melted region are shown in Figure 18. Figure 18b indicates a peak in defects concentration at the laser fluence of 0.4 J/cm^2, a fluence that provides conditions of maximum level of undercooling at the solidification front as illustrated in Figure 18a. The cooling rate at the solid-liquid interface in the beginning of the solidification process, as suggested in Figure 18a, is estimated as 2×10^{11} K/s under the irradiation conditions studied. At later stage, the temperature of the solidification front increased due to the release of latent heat, resulting in the maximum degree of undercooling at around 0.9 T_m. In this range of undercooling levels realized by the laser irradiation, according to Figure 7a, densities of both single interstitials and single vacancies are reduced with increasing temperature at the solidification front. At the laser fluences higher than 0.4 J/cm^2, the temperature at the solid-liquid interface is elevated due to slower cooling rate, resulting in decreased level of point defects. In contrast to the high-fluence irradiation, at fluences below 0.4 J/cm^2, the melting depth is significantly reduced so that complete solidification to the target surface occurs before the maximum undercooling at the solidification front is reached, thus suppressing further decrease of the interface temperature and leading to lower density of point defects.

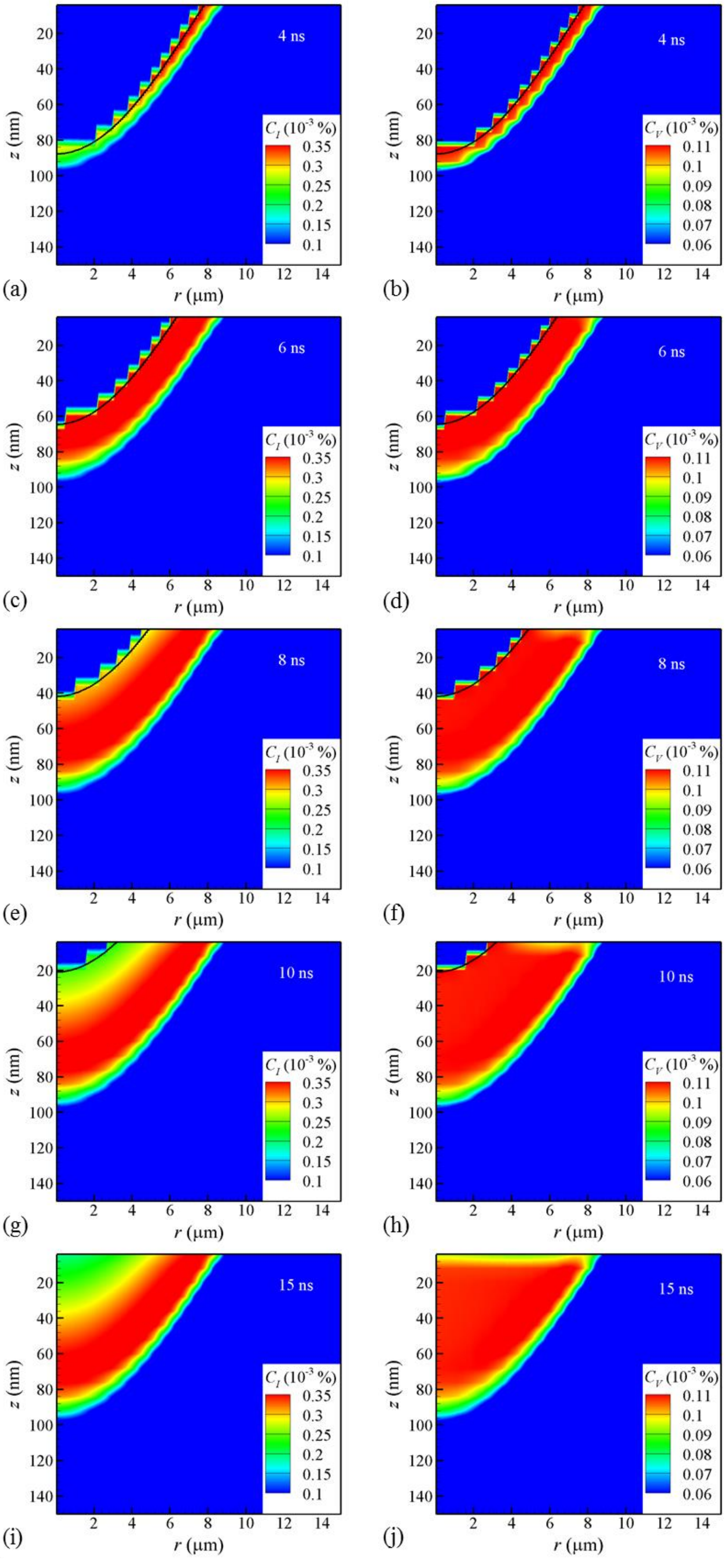

(a)
(b)
(c)
(d)
(e)
(f)
(g)
(h)
(i)
(j)
4 ns
6 ns
8 ns
10 ns
15 ns
z (nm)
r (μm)
20
40
60
80
100
120
140
2
4
6
8
10
12
14
C_I (10^{-3} %)
0.35
0.3
0.25
0.2
0.15
0.1
C_V (10^{-3} %)
0.11
0.1
0.09
0.08
0.07
0.06

Figure 17. Time evolutions of individual interstitials (left panel) and individual vacancies (right panel) during resolidification in a laser-melted Si wafer in the continuum simulation. The laser fluence is 0.45 J/cm^2, the pulse duration is 1 ns, and the spot diameter is 30 μm. The distributions of concentrations are expressed in atomic percent and shown at 4 ns (a,b), 6ns (c,d), 8 ns (e,f), 10 ns (g,h), and 15 ns (i,j) after laser irradiation. The black lines show the position of the crystal-liquid interface.

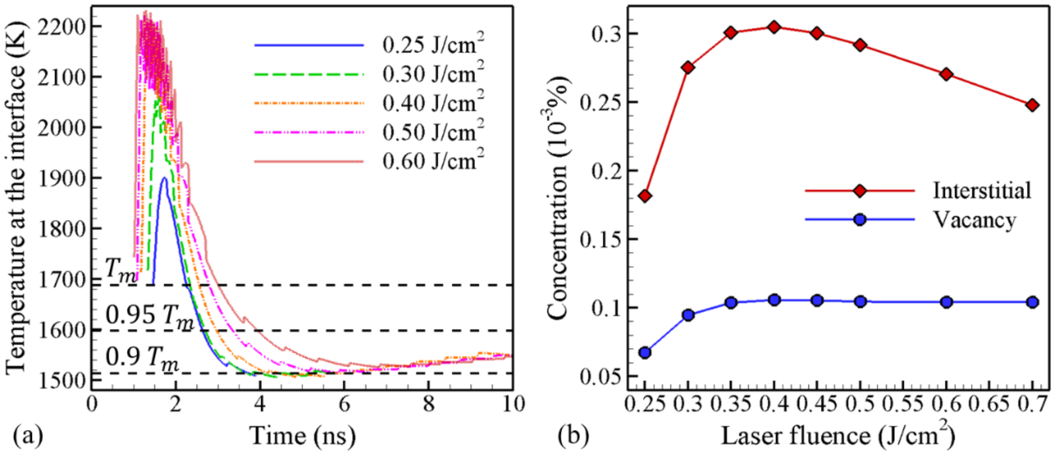

Figure 18. Predictions of time evolutions of the temperature at the crystal-liquid interface in the Si target at laser spot center (a), and average concentration of interstitials and vacancies in the laser-melted region (b), from continuum simulations performed at different laser fluences. The laser spot diameter is 30 μm and the pulse duration is 1 ns. In (a), the temperature profile ends when solidification is completed. The dashed lines indicate the undercooling level of T_m, 0.95 T_m, and 0.9 T_m. The concentration of vacancies in (b) takes both individual vacancies and di-vacancies into account.

The dependence of point defect concentration on laser fluence, and the observation of much higher density of interstitials than vacancies, predicted from continuum simulations have good agreements with the experimental results by our collaborator from the group of Prof. M. C. Gupta. Experimental measurements of the point defects are conducted using the attenuated total reflection (ART) analysis. Compared with unprocessed bare silicon wafer, three peaks at 960 cm^{-1}, 1120 cm^{-1}, and 2930 cm^{-1} are identified as oxygen-vacancy complex, interstitials, and hydrogen-vacancy complex, respectively, as shown in Figure 19a for a silicon target irradiated by 1 ns laser pulse at a fluence of 0.67 J/cm^2. The concentration of each type of point defect is quantitatively related to the integrated peak area of the associated ATR spectrum curve, which is calculated and plotted as a function of laser fluence in Figure 19b. Both interstitials and vacancy complexes exhibit the similar trend with laser fluence as computational predictions in Figure 18b, with the maximum concentration observed at ~0.67 J/cm^2.

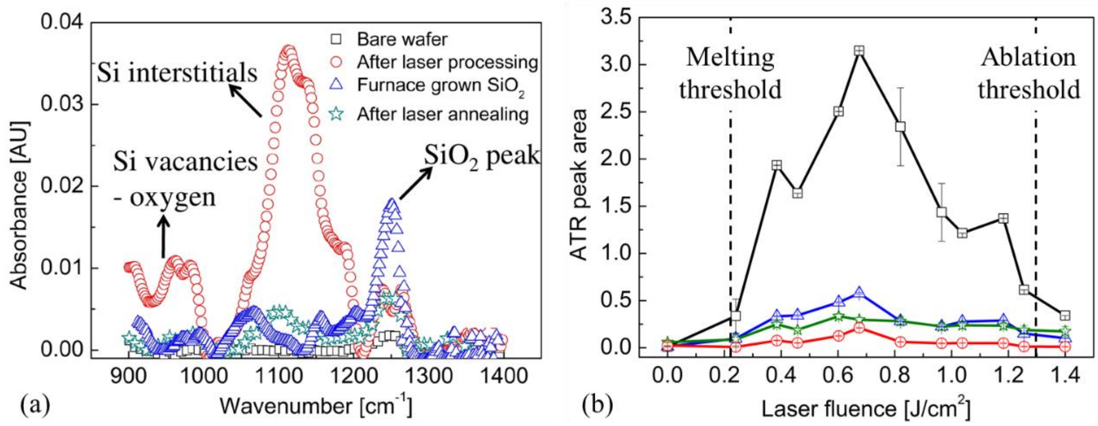

Figure 19. Laser generation of point defects revealed by ATR spectroscopy in experiments by Dr. Z. Sun from the group of Prof. M. C. Gupta. (a) Identification of laser-induced vacancies and interstitials in ATR spectra and comparison with SiO$_2$ peak. The laser-processed silicon sample was treated at 0.67 J/cm^2 fluence. (b) Laser-induced point-defect concentration, indicated by ATR point-defect peak area, as a function of laser fluence. The experimentally observed melting threshold, 0.22 J/cm^2, and ablation threshold, 1.3 J/cm^2, are represented by the dashed lines.

3.4.3 Simulation of post annealing effect on laser-induced point defects

High density of vacancies and interstitials generated by laser melting and resolidification can be reduced through post-annealing by subsequent laser pulses below the melting threshold. The low power laser irradiation provides reheating of the surface region modified by the processing laser close to the melting temperature, significantly enhancing the recombination rates of the point defects, *i.e.*, as described by Eqs. (2.16-2.18), and facilitating their diffusion to the free surface or deep into bulk of the system. For example, as shown in Figure 20a, heating above 1200 K results in a substantial increase of the mobility of point defects that can cause diffusion of tens of nanometers (comparable to the scale of the laser-modified region) within hundreds of nanoseconds. Figure 20b shows the evolution of the surface temperature of the 1D Si system irradiated by different laser pulses. The pulse duration, τ_L, of the annealing laser is much longer than that of the processing laser, 1 ns, to ensure sufficient time at elevated temperature for the diffusion and recombination of the point defects. As shown in Figure 20b, the thermal window experienced by the surface can be elongated by increasing the pulse duration or the number of pulses. At higher fluence or under multi-pulse irradiation, the average temperature that can be achieved during the laser pulse is increased, leading to faster diffusion and recombination of point defects. Therefore, the level of point defects after laser annealing is expected to be reduced by using longer, multi-pulse laser at higher fluence below the melting threshold.

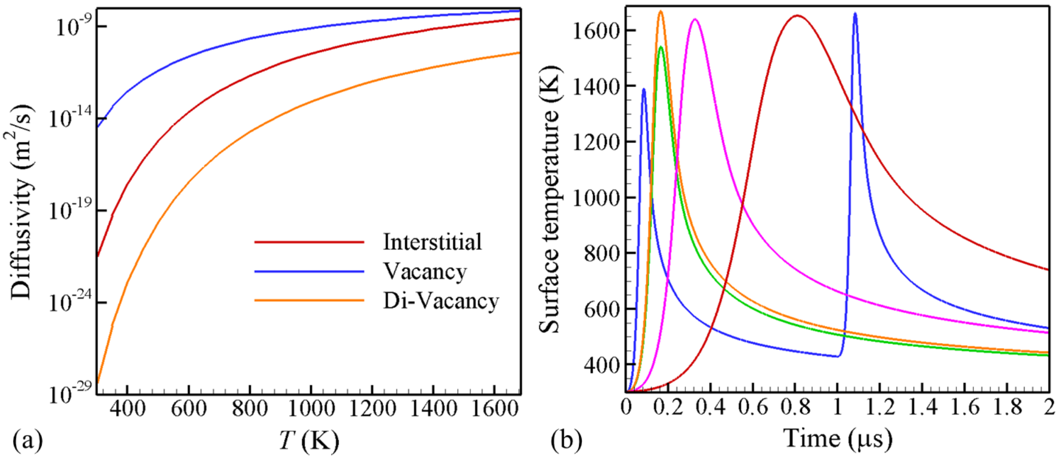

Figure 20. (a) Diffusivity of interstitials, vacancies, and di-vacancies as a function of temperature, adapted from the data reported in Refs. 108,109. (b) Temporal evolution of the surface temperature predicted from 1D continuum simulations of the Si target irradiated by different laser pulses. The pulse duration and incident fluence are labeled. The blue line corresponds to a two-pulse irradiation with repetition rate of 1 MHz.

The effects of laser fluence, pulse duration, and number of pulses on laser annealing are evaluated through a series of continuum simulations of evolution of point defects, which are generated in the course of laser melting and resolidification, *e.g.*, from the simulation of a 1 ns laser pulse irradiation at 0.45 J/cm^2 in Section 3.4.2, by subsequent low power annealing laser pulses, and the results are illustrated in Figure 21. As discussed above, the concentrations of both interstitials and vacancies (including di-vacancies that count for 2 vacancies) after laser annealing are decreased for longer pulse duration, higher fluence, and multi-pulse irradiation. Substantial reduction of the point defects to the equilibrium concentration at melting temperature can be achieved for a 500 ns laser pulse irradiation slightly below the melting threshold. Typically, efficient elimination of point defects can be achieved in experiments using microsecond laser pulse for annealing.

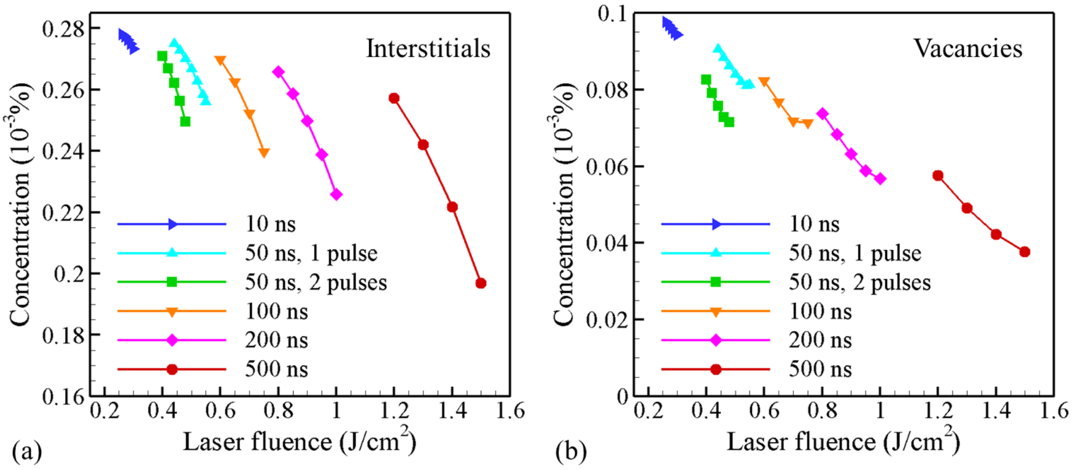

Figure 21. Predictions of average concentrations of interstitials (a) and vacancies (b) accounting for both individual vacancies and di-vacancies from 1D simulation of laser annealing. The initial concentrations are taken from the concentration distribution along the laser spot center from the 2D simulation at 40 ns after irradiation of a 0.45 J/cm^2 laser pulse. The concentrations are averaged over the melted depth along the laser spot center predicted in the 2D simulation.

3.4.4 Summary

Parameterized by the types and concentrations of point defects produced at the solidification front predicted from atomistic simulations, an advanced continuum model is developed to quantitatively describe the generation and evolution of interstitials and vacancies in the surface region of a Si target by laser irradiation within the entire laser spot and on a long time-scale. Laser-induced melting and resolidification results in the generation of supersaturated interstitials and vacancies distributed in the transiently melted and resolidified region. The average concentration of point defects in this region depends on laser fluence, and a pronounced maximum value is observed at 0.4 J/cm^2, under which condition the maximum undercooling in the vicinity of the crystal-liquid interface is achieved at 0.9 T_m. The laser-induced point defects can be mitigated by subsequent low power laser heating below the melting threshold, and the efficiency of point defects elimination is evaluated through continuum simulations of laser annealing performed for a wide range of laser parameters. The computational results suggest that laser-induced point defects can be minimized through tailoring laser-processing parameters, or can be efficiently reduced by subsequent microsecond laser annealing. The effect of laser parameters on the generation and evolution of point defects is validated by experimental measurements, and provides a general guidance in choice of experimental conditions for improving the device performance.

4. Computational study of laser-induced generation of crystal defects in metals

4.1 Introduction

Rapid solidification of metals under conditions of deep undercooling below the equilibrium melting temperature is a process of general fundamental importance in materials science, and also has direct practical relevance for a variety of material applications, ranging from high energy particle bombardment[176,177] to short pulse laser processing.[19,20,29,62,63] Ultrashort time and high degree of localization of energy deposition, achieved within an electronically excited ion track[178] or a thin surface layer of a target irradiated by a femtosecond or picosecond laser pulse,[179] can produce very steep temperature gradients and cooling rates reaching the levels of ~10^{11}-10^{13} K/s.[23,29] Resolidification of transiently melted material can be kinetically inhibited under conditions of such extreme quenching, thus bringing the molten material into a state of deep undercooling or even the amorphous state. While the direct measurement of the degree of undercooling is not possible in experiments, the estimations based on solution of heat transfer equation[19,33] and the results of MD simulations[19,21,23] suggest that the surface of the irradiated target can be undercooled down to 0.9-0.6 T_m by the end of the solidification process.

The rapid propagation of the solidification front under conditions of strong undercooling can result in the generation of highly non-equilibrium defect configurations, as discussed for silicon in the previous section, and would directly impact the damage accumulation in extreme radiation environments.[56,177,180,181] A number of electron backscatter diffraction studies have reported the presence of high densities of dislocations[14,15,16,17,18] and twin boundaries[13,19] in laser-processed metal targets. However, there have been limited experimental studies probing the movement of solidification front and evolution of the microstructure. The confinement of the rapid solidification and structural modification within the small sizes of collision cascades produced by high energy particle bombardment or within a thin surface region of the laser-irradiated target also brings challenge to *ex-situ* characterization of the irradiation-induced crystal defects.

A reliable physical interpretation of the experimental evidence of the laser-induced generation of crystal defects can be provided by atomistic modeling. Indeed, the ability of atomistic simulations to provide insights into the mechanisms responsible for surface nanocrystallization,[20,23,24,25] growth twining,[19] emission of dislocations,[26,52,53] and strong vacancy supersaturation[21,52,53] has been demonstrated in modeling of laser interactions with one-component Cr, Ag, and Ni targets. MD simulations of solidification performed for pure metal[182] and alloy[183] systems under conditions of fixed undercooling also reveal the formation of high density of vacancies, exceeding the equilibrium value at melting temperature, in the solidified region. The supersaturated vacancies are found to be produced at the solid-liquid interface during fast solidification process and trapped by the rapidly propagating solidification front,[182,184] leading to a strong correlation between the solidification velocity and vacancy concentration.

In the study, the atomistic modeling is extended to binary Ni-based solid-solution alloys and is focused on evaluation of the effect of chemical disorder on the generation and evolution of crystal defects in targets undergoing rapid melting and resolidification. The composition of three binary alloys used in this study, $Ni_{50}Fe_{50}$, $Ni_{80}Fe_{20}$, and $Ni_{80}Cr_{20}$, is selected to ensure that the alloys remain in the chemically disordered state under regular cooling conditions.[185,186] The binary single-phase solid-solution alloys can serve as model systems for investigation of the implications of chemical disorder on the behavior and properties of an emerging class of multicomponent solid-solution alloys that exhibit enhanced mechanical characteristics[187] and radiation damage resistance,[188] making them promising candidate materials for nuclear energy applications. For Ni-based solid-solution alloys, in particular, the site-to-site random variation of local chemical environments and corresponding lattice distortions have been shown to result in the suppression, as compared to pure Ni, of damage accumulation under high-energy particle irradiation[176,177,180,188-192].

Although the atomistic simulations of the displacement cascades generated by high-energy particle bombardment have provided important information on the sensitivity of the defect generation to the alloy composition, [176,177,180] the relatively small sizes of the individual collision cascades and rapid quenching in the regions of the energy deposition make it difficult to establish direct links between the characteristics of radiational damage, energetics and mobility of individual defects, and the evolution of thermodynamic conditions in the irradiated material. In contrast, the laser irradiation can create energy densities comparable to those in the high-energy ion tracks in much larger regions of the irradiated targets, thus providing more reliable statistical information on the structural response of the material to the strong excitation. Moreover, the thermodynamic parameters and structural transformations are evolving slower and in a more regular manner in laser-material interaction as compared to those in the high-energy particle bombardment, thus enabling more detailed analysis of the connections between the rapidly changing thermodynamic conditions, non-equilibrium phase transformations, and the generation of crystal defects.

As a prominent feature in the region transiently melted by laser irradiation, the generation of supersaturated vacancies is investigated and explained through the assistance of a systematic study of solidification under well-controlled conditions of undercooling and pressure, where the vacancy formation during the epitaxial crystal growth are investigated for bcc Cr, fcc Ni and Ni-based alloys, establishing dependences of the solidification kinetics and vacancy densities on the degree of undercooling, pressure, crystal structure, and crystallographic orientations for different materials, and providing atomic-level insights into the key processes responsible for the generation of vacancies at the propagating solidification front.

4.2 Laser-induced melting and resolidification, and generation of crystal defects in Ni and Ni-based binary solid-solution alloys

In this section, atomistic simulations of short pulse laser irradiation on Ni and

Ni-based solid-solution alloys ($Ni_{50}Fe_{50}$, $Ni_{80}Fe_{20}$, and $Ni_{80}Cr_{20}$) are performed to investigate the mechanisms of generation of vacancies, dislocations, stacking faults, and twin boundaries in the course of laser-induced melting and resolidification. The computational setup for the atomistic modeling and its parameterization for Ni-Fe and Ni-Cr single-phase solid-solution alloys are briefly described in Section 4.2.1. The results of atomistic simulations of the laser-induced melting and rapid solidification are reported in Section 4.2.2. The mechanisms responsible for the generation of crystal defects in the transiently melted and resolidified region are discussed in Section 4.2.3. The computational predictions on the laser-induced phase and structural transformations in Ni and Ni-based alloys are summarized in Section 4.2.4.

4.2.1 Computational Setup

The TTM-MD model for the laser interaction with metal targets has been described in Section 2.1, and here only the computational setup and parameters used in the simulations of laser irradiation on Ni and Ni-based alloys are outlined. The electron temperature dependences of the electron-phonon coupling factor and electron heat capacity for Ni and $Ni_{50}Fe_{50}$ are reported in Refs. 87,89,90. The dependences for $Ni_{80}Fe_{20}$ and $Ni_{80}Cr_{20}$ are evaluated in a similar manner, and all data sets are provided in tabulated forms in Ref. 193. The dependence of electron-phonon coupling on lattice temperature is not considered since such effect is negligible for lattice temperatures around and above the Debye temperature,[194] which are the conditions achieved in present simulations. The electron heat capacity C_e and electron-phonon coupling G for all materials are plotted as a function of electron temperature T_e in Figure 22. While the electron temperature dependences of electron heat capacities are similar, the decay of electron-phono coupling with increasing electron temperature is much slower in the Ni-based alloys as compared to pure Ni, which can be attributed to smearing of the sharp spike of the electron density of states near the Fermi level in Ni as a result of alloying with Fe or Cr.[90]

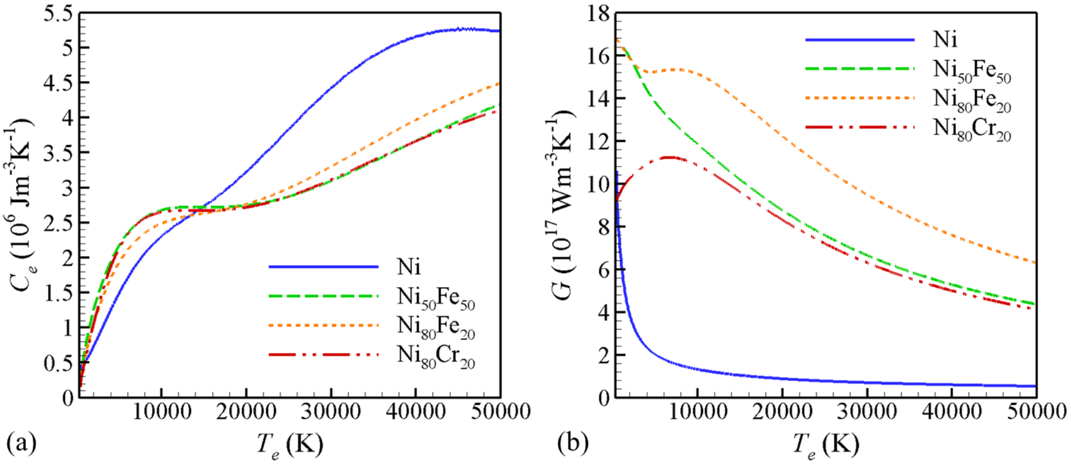

Figure 22. Electron temperature dependence of electron heat capacity C_e (a) and electron-phonon coupling factor G (b) calculated for Ni, $Ni_{50}Fe_{50}$, $Ni_{80}Fe_{20}$, and $Ni_{80}Cr_{20}$. The tabulated data is provided in Ref. 193.

The electron thermal conductivity is described by the Drude model relationship, Eqs. (2.4-2.5) in Section 2.1. The values of coefficient A, 1.4×10^6 K^{-2}s^{-1}, 1.36×10^6 K^{-2}s^{-1}, 1.37×10^6 K^{-2}s^{-1}, and 1.52×10^6 K^{-2}s^{-1} for Ni, $Ni_{50}Fe_{50}$, $Ni_{80}Fe_{20}$, and $Ni_{80}Cr_{20}$, respectively, are estimated following the approach suggested in Ref. 91. The values of coefficient B are fitted to the results of experimental measurements of thermal conductivity as a function of temperature and phase state under condition of electron-phonon thermal equilibrium, *i.e.*, $T_e = T_l$. For solid Ni, the thermal conductivity as a function of temperature is taken from Ref. 195, and a constant value of 60 Wm^{-1}K^{-1} is assumed for the liquid phase Ni. For solid $Ni_{50}Fe_{50}$ and $Ni_{80}Fe_{20}$, the temperature dependence of the thermal conductivity up to 1100 K is taken from Ref. 196. Above 1100 K, linear extrapolations of experimental data to T_m are used. The thermal conductivities of the alloys can also be reasonably well approximated by Wiedemann-Franz relationship, $k_e = LT/\rho_e$, where ρ_e is electrical resistivity and $L = 2.45 \times 10^{-8}$ WΩK^{-2} is the Lorenz number. Using the data on temperature dependent electrical resistivities for both solid and liquid alloys[197] and correcting by the difference between k_e extrapolated from experimental data in Ref. 196 and predicted by the Wiedemann-Franz law for solid alloys at T_m, the thermal conductivities of liquid alloys at T_m are estimated as 32.74 Wm^{-1}K^{-1} for $Ni_{50}Fe_{50}$ and

32.46 $Wm^{-1}K^{-1}$ for $Ni_{80}Fe_{20}$. For solid $Ni_{80}Cr_{20}$, k_e at temperature range of $300\ \mathrm{K} \leq T \leq 1100\ \mathrm{K}$ is taken from Ref. 198 and is extended to T_m using a linear coefficient obtained in Ref. 199 based on the Wiedemann-Franz law. The thermal conductivity of liquid $Ni_{80}Cr_{20}$, 40.8 $Wm^{-1}K^{-1}$, is estimated by taking k_e for solid $Ni_{80}Cr_{20}$ at T_m and subtracting the difference between the solid and liquid phase k_e reported in Ref. 199. The temperature dependences of thermal conductivities of solid Ni and three Ni-based solid solution alloys are plotted in Figure 23, where the Ni-base alloys exhibit significantly lower levels of thermal conductivity. The data shown in Figure 23 is in a good quantitative agreement with the results of recent experimental measurements reported in Ref. 200. The thermal conductivities of superheated solids are taken as k_e at T_m and are shown up to 1.25 T_m.

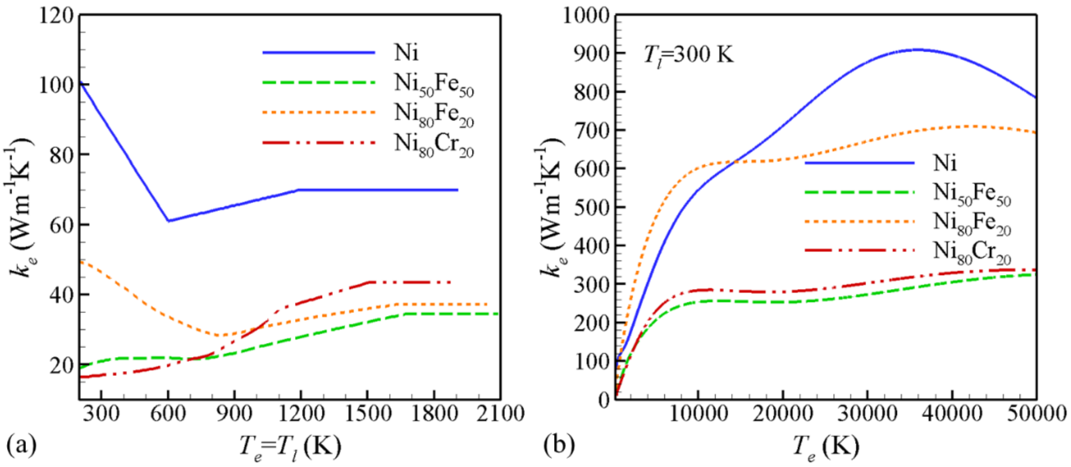

Figure 23. Temperature dependences of thermal conductivities of solid Ni, $Ni_{50}Fe_{50}$, $Ni_{80}Fe_{20}$, and $Ni_{80}Cr_{20}$. Temperature dependences under conditions of electron-phonon equilibrium, $T_e = T_l$, is shown in (a) and the ones of electronically-excited materials at a constant $T_l = 300$ K are shown in (b). In (a), constant values of thermal conductivity equal to the ones at T_m are assumed for superheated solids, *i.e.*, at $T > T_m$, and are shown up to 1.25 T_m.

The interatomic interactions in the MD part of the TTM-MD model for the Ni and Ni-based alloys are described by the EAM potential developed by Bonny *et al.*[201] for low temperature structural and elastic properties as well as the energies of crystal defects. A set of high temperature thermophysical properties that are relevant to the conditions realized in the simulations of laser-induced melting and resolidification are tested in collaboration with C. Wu and M. V. Shugaev.[54] The melting temperatures are estimated from a series of simulations performed for the solid-liquid coexistence systems under well-controlled temperature and zero pressure conditions. The melting temperature, determined as the value where the velocity of the solid-liquid interface reaches zero, is given as 1530 K for Ni, about 11% below the experimental value of 1728 K, [202] and 1680 K for $Ni_{50}Fe_{50}$, close to the experimental value of 1703 K.[203] The melting temperatures of $Ni_{80}Fe_{20}$ and $Ni_{80}Cr_{20}$ are calculated to be 1635 K and 1510 K, respectively. The surface tension, γ, is calculated with the test-area method[204] and plotted in Figure 24a as a function of temperature. Compared with the experimental value of 1.77 J/m^2 at melting temperature (1728 K), [205] Bonny EAM potential significantly underestimates the surface tension, which results in the much lower threshold fluence for cavitation and spallation as compared to the earlier simulations performed for Ni with Johnson EAM[27] and Mishin EAM[19] potentials. The temperature dependences of the lattice heat capacity, C_l, are calculated from series of constant pressure-constant temperature MD simulations, fitted to fourth-order polynomial, and plotted in Figure 24b. At 300 K, the heat capacity predicted from Bonny EAM Ni is 3.83×10^6 Jm^{-3}K^{-1}, agreeing well with the experimental value of 3.95×10^6 Jm^{-3}K^{-1}.[202] In summary, despite the underestimation of the surface tension, the Bonny EAM potential is found to reproduce reasonably well the thermodynamic parameters such as the melting temperature and stacking fault energy. Therefore, this potential is suitable for computational investigation of the generation of crystal defects in the process of transient melting and resolidification.

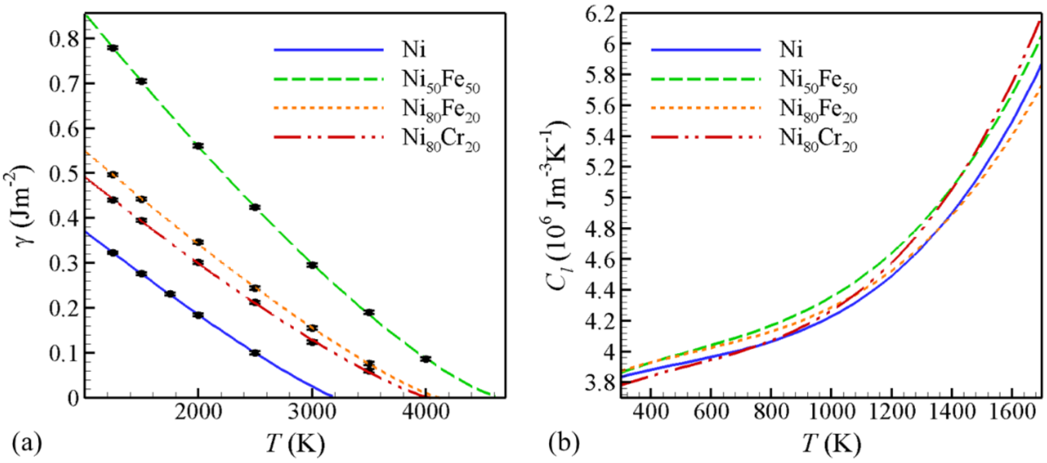

Figure 24. Temperature dependence of surface tension of liquid (a) and heat capacity of solid (b) Ni, $Ni_{50}Fe_{50}$, $Ni_{80}Fe_{20}$, and $Ni_{80}Cr_{20}$. The black points in (a) are the results of MD simulations as well as the error bars that are smaller than the size of each point.

The depth of the surface parts of the targets represented with atomistic resolution is 70 nm, and the initial MD systems have the face-centered cubic (fcc) crystal structure and (001) orientation of the free surface. The disordered Ni-based single phase solid-solution systems are prepared by occupying randomly selected lattice sites with Fe and Cr atoms, respectively, for the Ni-Fe and Ni-Cr alloys. Two sets of TTM-MD simulations are performed for each system with different computational size. The small-scale simulations, with lateral dimension of $7\ \text{nm} \times 7\ \text{nm}$, are aimed at establishing the threshold fluences delineating transitions between different regimes of the material response to the laser irradiation. Once the fluence regimes are established, one large-scale TTM-MD simulation, with lateral size of $100\ \text{nm} \times 100\ \text{nm}$ that corresponds to about 65 million atoms in the MD part of the computational domain, is performed for each target composition to provide microscopic information of the laser-induced generation of crystal defects. The laser parameters in the large-scale simulations are chosen based on the results of small-scale simulations, so that the irradiation conditions lead to a transient melting and resolidifiation of a ~20 nm deep region of the target. Periodic boundary conditions are applied in the lateral directions parallel to the surface of the targets for all TTM-MD simulations.

At the bottom of the MD part of the computational domain, a dynamic pressure-transmitting boundary condition[93,94] is applied to mimic the nonreflective propagation of the laser-induced pressure waves into the bulk of the target. In the deeper part of the target, below the bottom boundary of the MD region, the TTM equations for both lattice and electron temperatures are solved on a grid extending down to the depth of 2 μm, which ensures a negligible change in the electron and lattice temperatures at the bottom of the computational domain on the simulated timescales.

Before applying laser irradiation, all systems are pre-equilibrated at 300 K. The laser irradiation is represented through the source term formularized as in Eq. (2.3), describing the absorption of laser energy by conduction band electrons. The absorbed laser fluence F_{abs} is used in the discussion of the simulation results, due to the complex dependence of the reflectivity R on the temperature and microstructure of the irradiated surface. The optical absorption depth is approximated as 14.5 nm, taken based on the value of absorption coefficient of pure Ni and a laser wavelength of 800 nm.[206] The laser pulse duration τ_L is 50 fs in all small-scale simulations and either 100 fs or 50 ps in the large-scale simulations. The small-scale simulations are performed at absorbed laser fluences ranging from 200 to 600 J/m^2, while the irradiation conditions in the large-scale simulations are chosen to ensure the simulations are in the melting and resolidification regime.

4.2.2 Small-scale simulations of melting and resolidification, subsurface cavitation, and spallation of materials by laser irradiation at different fluences

In order to enable a direct comparison of laser-induced rapid melting and resolidification in Ni and Ni-based solid solution alloys and investigate the effect of the chemical disorder on generation of crystal defects, the irradiation conditions are selected to produce transient melting and resolidification of similar depth of regions in all four targets considered in this work. Based on the results of four series of computationally-inexpensive small-scale simulations performed for each material and for a broad range of laser fluences, different regimes of the material response to the laser irradiation, namely, melting and resolidification, subsurface cavitation, and spallation, are identified and summarized in Table 1, and the threshold fluences delineating transitions between these regimes are established.

Table 1. Distinct physical regimes of the response of Ni and Ni-based solid-solution alloy targets to the irradiation by 50 fs laser pulses at F_{abs} ranging from 200 to 600 J/m^2 predicted in small-scale TTM-MD simulations.

Fluence (J/m^2)	200	300	400	500	600
Ni	No melting	No melting	No melting	Melting and resolidification	Subsurface cavitation
$Ni_{50}Fe_{50}$	No melting	Melting and resolidification	Subsurface cavitation	Spallation	Spallation

$Ni_{80}Fe_{20}$	No melting	Melting and resolidification	Spallation	Spallation	Spallation
$Ni_{80}Cr_{20}$	No melting	Melting and resolidification	Spallation	Spallation	Spallation

The material response to laser irradiation identified in the small-scale simulations is following the sequence of the regimes established in earlier computational studies, for example, Refs. 24, 27, and 84. For pure Ni, the threshold for surface melting is found to be between 400 and 500 J/m^2, which is consistent with the melting threshold identified in simulations[19] performed with Mishin EAM potential[207] but higher than the melting threshold of 360 J/m^2 reported in Ref. 27 for Johnson EAM Ni[208], which significantly underestimates the melting temperature of Ni.[27] As the fluence increases to 600 J/m^2, the relaxation of the laser-induced stresses generated in the surface region of the Ni target under conditions of stress confinement[8,11] results in the transient appearance and collapse of voids in a subsurface region of the target. Further increase of the laser fluence leads to the coalescence of voids and ejection of a top liquid layer in the process commonly called spallation.[23,27,84] The threshold fluences for surface melting and spallation predicted in the simulations are much closer to each other than those in earlier simulations reported for Ni.[19,27] The early onset of void nucleation and spallation can be related to the substantial underestimation, with respect to experimental values, of the surface tension by the Bonny EAM potential as described in Section 4.2.1. The low surface tension reduced the energy cost for the subsurface cavitation and spallation, thus narrowing the range of fluences where the effect of the laser irradiation is limited to the melting and resolidification. This range of fluences, however, is still sufficient for investigation of the generation of crystal defects at the solidification front.

As discussed in Section 4.2.1, the intrinsic chemical disorder in the Ni-based alloys leads to stronger electron-phonon coupling and lower thermal conductivity as compared to pure Ni, Figure 22 and 23, implying faster electron-phonon equilibration and more localized heating of the surface region of the target. As a result, the melting threshold is significantly reduced for all Ni-based alloys, down to 200-300 J/m^2 as compared to 400-500 J/m^2 for pure Ni. Moreover, the faster and more localized lattice heating in the alloys results in the buildup of stronger compressive stresses and unloading tensile waves, causing the appearance of subsurface voids (cavitation) and onset of spallation at lower fluences. In the simulations performed at 400 J/m^2, the subsurface cavitation is followed by the collapse of the voids in $Ni_{50}Fe_{50}$ target, while in the $Ni_{80}Fe_{20}$ and $Ni_{80}Cr_{20}$ targets the voids grow, coalesce, and percolate, leading to the spallation of a liquid layer. This difference can be explained by the noticeably higher surface tension in $Ni_{50}Fe_{50}$ as compared to the other two alloys, see Figure 24a in Section 4.2.1.

4.2.3 Large-scale simulations of laser-induced melting and resolidification

In this work, the goal is to investigate the generation of crystal defects in the course of laser-induced melting and resolidification. Therefore, the irradiation conditions for the large-scale simulations are chosen to avoid spallation and to ensure similar maximum melting depth in targets of all four compositions, based on the results of small-scale simulations described in Section 4.2.2. For Ni and $Ni_{50}Fe_{50}$ targets, the pulse duration of 100 fs is used, and the absorbed fluences of 500 J/m^2 and 400 J/m^2 are selected, respectively, to melting surface regions down to ~20 nm while staying below the spallation thresholds. The transient appearance and collapse of voids in $Ni_{50}Fe_{50}$ at 400 J/m^2 takes place in the molten region before the arrival of the solidification front and does not affect the generation of crystal defects. For $Ni_{80}Fe_{20}$ and $Ni_{80}Cr_{20}$ alloy targets irradiation with 50 or 100 fs laser pulses, the spallation occurs before the desired melting depth is reached. Therefore, the large-scale simulations for these two targets are performed with longer 50 ps laser pulses at an absorbed fluence of 400 J/m^2, which produces melting depth similar to that in the other two simulations. The longer pulse duration allows for a partial relaxation of the thermoelastic stresses during the laser heating, significantly reduces the strength of the unloading tensile wave, and prevents spallation.

Four large-scale simulations for Ni, $Ni_{50}Fe_{50}$, $Ni_{80}Fe_{20}$, and $Ni_{80}Cr_{20}$ targets are performed under irradiation conditions described above, and the corresponding spatial and temporal evolutions of lattice temperature, pressure, and density are shown in Figure 25. Laser excitation of conduction band electrons followed by the electron-phonon equilibration leads to the temperature increase in the surface regions of the irradiated targets. As discussed above, the stronger electron-phonon coupling in the alloys leads to the confinement of the initial lattice heating in much shallower surface regions of the targets, as can be seen from the temperature contour plots. This stronger confinement of the initial energy deposition explains why substantially lower laser fluences are required for producing melting depth in the alloy targets similar to that in Ni.

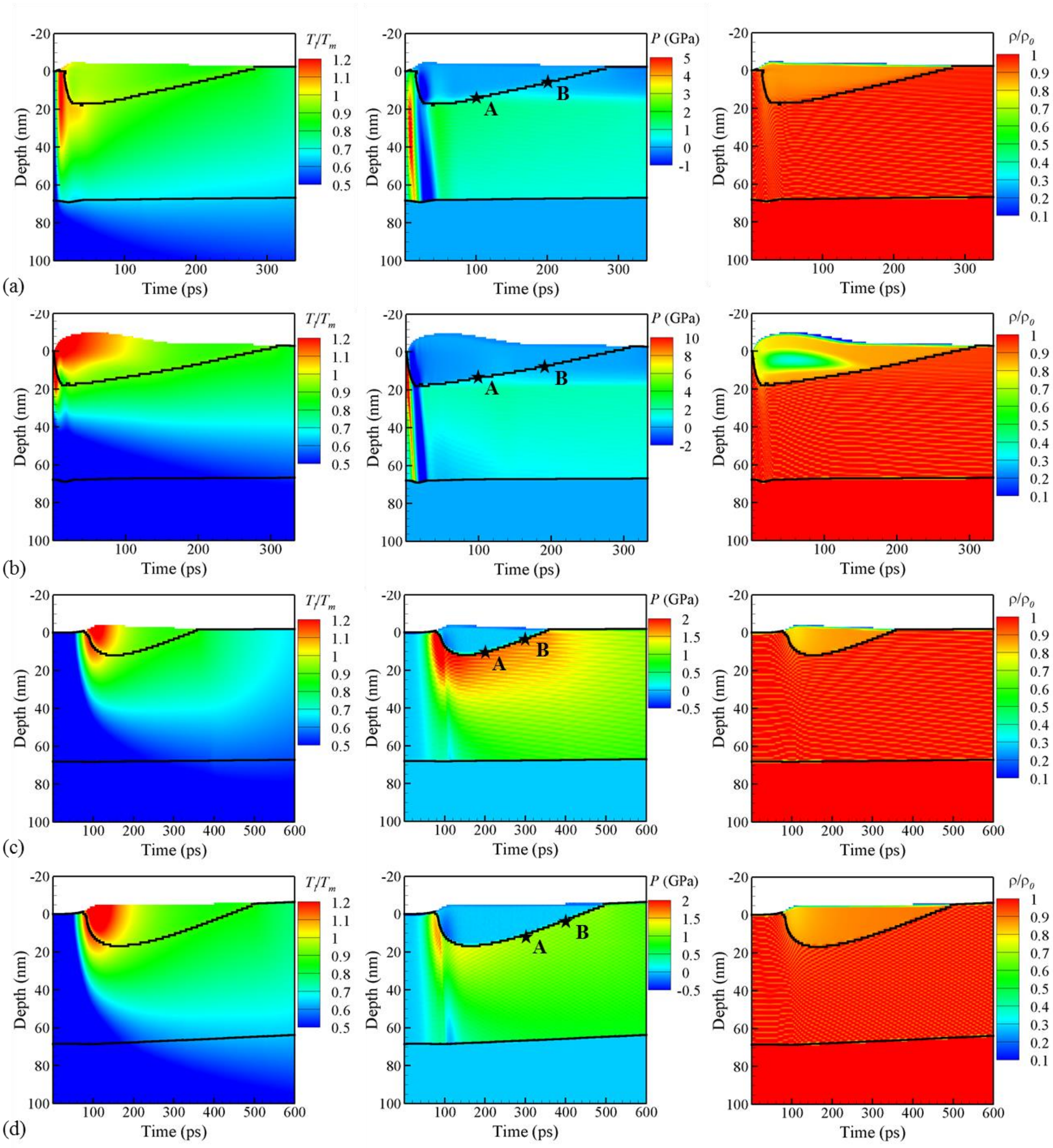

Figure 25. Contour plots of the spatial and temporal evolution of lattice temperature, pressure, and density in the surface regions of Ni (a), $Ni_{50}Fe_{50}$ (b), $Ni_{80}Cr_{20}$ (c), and $Ni_{80}Cr_{20}$ (d) targets irradiated in the regime of melting and resolidification. The temperature scale is normalized by the equilibrium melting temperature, T_m, which is different for each target material and is given in Section 4.2.1. The black solid lines near the surface of the targets show the movement of the crystal-liquid interface, and the black lines in the lower parts of the contour plots show the location of the nonreflecting boundary applied at the bottom of the MD part of the computational domain. The black stars marked by letters "A" and "B" show the moments of time for which interface roughness is evaluated and provided in Table 2. The irradiation conditions are $\tau_L = 100$ fs and $F_{\text{abs}} = 500$ J/m^2 for Ni (a), $\tau_L = 100$ fs and $F_{\text{abs}} = 400$ J/m^2 for $Ni_{50}Fe_{50}$ (b), and $\tau_L = 50$ ps and $F_{\text{abs}} = 400$ J/m^2 for $Ni_{80}Fe_{20}$ and $Ni_{80}Cr_{20}$ (c,d).

The temperature of the lattice in the surface region quickly exceeds the melting temperatures of the target materials, leading to rapid melting of the surface regions of the irradiated targets. For targets irradiated by 100 fs laser pulses, the surface is heated up to 1.2 T_m by 10 ps in Ni and by 1.2 ps in $Ni_{50}Fe_{50}$, again reflecting the effects of stronger electron-phonon coupling in the alloy. As soon as this critical level of superheating is reached, rapid homogeneous melting of about 18 nm deep surface layer takes place in both targets. For $Ni_{80}Fe_{20}$ and $Ni_{80}Cr_{20}$ targets, the heating is slower and is controlled by the rate of the laser energy deposition rather than the electron-phonon coupling ($\tau_L = 50$ ps is more than 10 times longer than the characteristic time of electron-phonon equilibration, τ_{e-ph}). As a result, the melting starts from the surface when the surface temperature exceeds T_m at ~75 ps, that is around the time when the intensity of the Gaussian laser pulse reaches its maximum, and the melting front accelerates as more energy is deposited during the second half of the laser pulse. Because of the kinetic constraints on the melting front propagation,[209] the crystal lattice below the molten material is superheated up to 1.17-1.19 T_m before the arrival of the melting front, which propagates to the maximum depth of 12 nm and 17 nm in the $Ni_{80}Fe_{20}$ and $Ni_{80}Cr_{20}$ targets, respectively.

The local temperature at the crystal-liquid interface drops below T_m, and the melting tuns into solidification at ~50 ps after the start of the simulation for Ni, at ~20 ps for $Ni_{50}Fe_{50}$, at ~150 ps for $Ni_{80}Fe_{20}$, and at ~165 ps for $Ni_{80}Cr_{20}$. The solidification velocity increases up to the maximum levels of 70-90 m/s as the temperature of the interface decreases down to the maximum undercooling of 0.9 T_m reached by the end of the resolidification process in all simulations. As can be seen from the temperature contour plots, the release of the latent heat of the melting increases the local temperature at the solidification front and reduces the level of undercooling with respect to the maximum one reached at the molten surface, ~0.85-0.87 T_m. Overall, as can be seen from the temperature contour plots and the black lines showing the progression of the crystal-liquid interfaces, the heating, melting, cooling, and epitaxial resolidification proceed in a qualitatively similar manner in all four simulations.

In the simulations performed with $\tau_L = 100$ fs $< \tau_{e-ph}$, the time of lattice heating is defined not by τ_L but by the time of the energy transfer from the hot electrons to the lattice, τ_{e-ph}. For both pure Ni and $Ni_{50}Fe_{50}$, τ_{e-ph} is shorter than the characteristic time for the mechanical relaxation (expansion) of the heated volume, $\tau_s \sim L_p/C_s$, the time needed to initiate a collective motion of atoms or molecules within the absorbing volume. Here, L_p is the laser penetration depth and C_s is the speed of sound in the irradiated material. In this case, the laser heating takes place under nearly constant volume conditions, leading to the generation of high thermoelastic stresses in the surface regions of the targets, as can be seen from the pressure contour plots in Figures 25a and b. In general, when the characteristic time of laser energy deposition defined by the pulse duration or the electron-phonon coupling time, whichever is longer, is less than that for the mechanical relaxation, a condition of so-called inertial stress confinement is achieved, where the inability of material to expand during the time of laser heating results in the buildup of strong compressive stresses in the surface region of the target. In each of the two simulations, the relaxation of the laser-induced compressive stresses drives the strong compressive pressure wave deep into the bulk of the target and induces an unloading tensile wave from the free surface that follows the compressive component. The compressive and tensile components of the pressure wave propagate without any noticeable reflection from the boundary separating the MD and continuum parts of the model. After the laser-induced pressure wave leaves the surface area of the target, zero pressure establishes in the molten region, while the residual thermoelastic stresses, which cannot relax by uniaxial expansion of the crystal lattice in the direction normal to the surface, remain in the crystalline part of the target.[27] These quasi-static compressive stresses, however, are relaxed in the top parts of the resolidified regions of the targets due to the generation of high density of crystal defects, as discussed in the next section.

Interestingly, the magnitudes of the compressive and tensile components of the stress wave generated in the $Ni_{50}Fe_{50}$ target are substantially higher than those in the pure Ni target, even though the absorbed fluence of 400 J/m^2 applied to the alloy target is 20% lower than that used in the simulation of pure Ni target. This observation can be related to the stronger electron-phonon coupling in the alloy, leading to a smaller τ_{e-ph} and a more abrupt heating of the lattice. The increased magnitude of the tensile unloading wave is sufficient for inducing cavitation in the subsurface overheated molted part of the target, which is apparent in the density plot shown in Figure 25b and proceeds through the nucleation and growth of subsurface voids. The voids collapse later as illustrated in Figure 25b, because of the surface tension prior to the arrival of the solidification front and do not affect the microstructure of the resolidified region. At higher fluence, the formation and growth of multiple subsurface voids may lead to eventual separation and ejection of liquid surface layers or large droplets from the bulk of the target, called photomechanical spallation[8,12,210-213] that is observed in the small-scale simulations of Ni-based alloys as summarized in Table 1. Note that the cavitation occurs in $Ni_{50}Fe_{50}$ alloy and not in pure Ni despite of the lower surface tension of the latter (See Figure 24a in Section 4.2.1), which is expected to facilitate the cavitation and spallation. This observation highlights the dominant role of the increased electron-phonon coupling and stronger stress confinement in defining the conditions for the generation of subsurface voids.

In the simulations performed for $Ni_{80}Fe_{20}$ and $Ni_{80}Cr_{20}$ alloys with longer pulse duration $\tau_L = 50$ ps $> \tau_{e-ph}$, the time of the lattice heating is defined by τ_L rather than τ_{e-ph}. Thus, despite of the strong electron-phonon coupling in the alloys, the condition for the stress confinement is not realized, and the thermoelstic stresses associated with the laser heating are largely relaxed during the laser energy deposition, as can be seen from much lower levels of pressure in Figures 25c,d as compared to those in Figures 25a,b. No subsurface voids are generated in these simulations, and the response to the laser irradiation is limited to melting and resolidification of the surface regions of the targets.

4.2.4 Generation of crystal defects in the course of laser-induced melting and resolidification

The visual picture of the laser-induced melting and resolidification is provided by four series of snapshots of the top 30 nm deep surface layers of the Ni, $Ni_{50}Fe_{50}$, $Ni_{80}Fe_{20}$, and $Ni_{80}Cr_{20}$ targets shown in Figure 26. The local structural environment is determined for each atom with a structure identification method developed in Refs. 214-216, all atoms with local fcc structure are blanked, and only the molten regions and crystal defects are shown in Figure 26. The transient appearance of the molten surface regions shown by blue color in Figure 26 is consistent with the discussion of the melting and resolidification processes based on the contour plots provided in the previous sections. The microstructures of the resolidified surface regions in Ni and $Ni_{50}Fe_{50}$ targets irradiated by 100 fs laser pulses feature high density of vacancies, dislocations, stacking faults, and twin boundaries, with the latter two types of defects being particularly abundant in the $Ni_{50}Fe_{50}$ target. In contrast, the defects produced in $Ni_{80}Fe_{20}$ and $Ni_{80}Cr_{20}$ targets irradiated by longer 50 ps laser pulses are largely limited to vacancies and vacancy clusters, with only a few small dislocation loops observed in the $Ni_{80}Cr_{20}$ target.

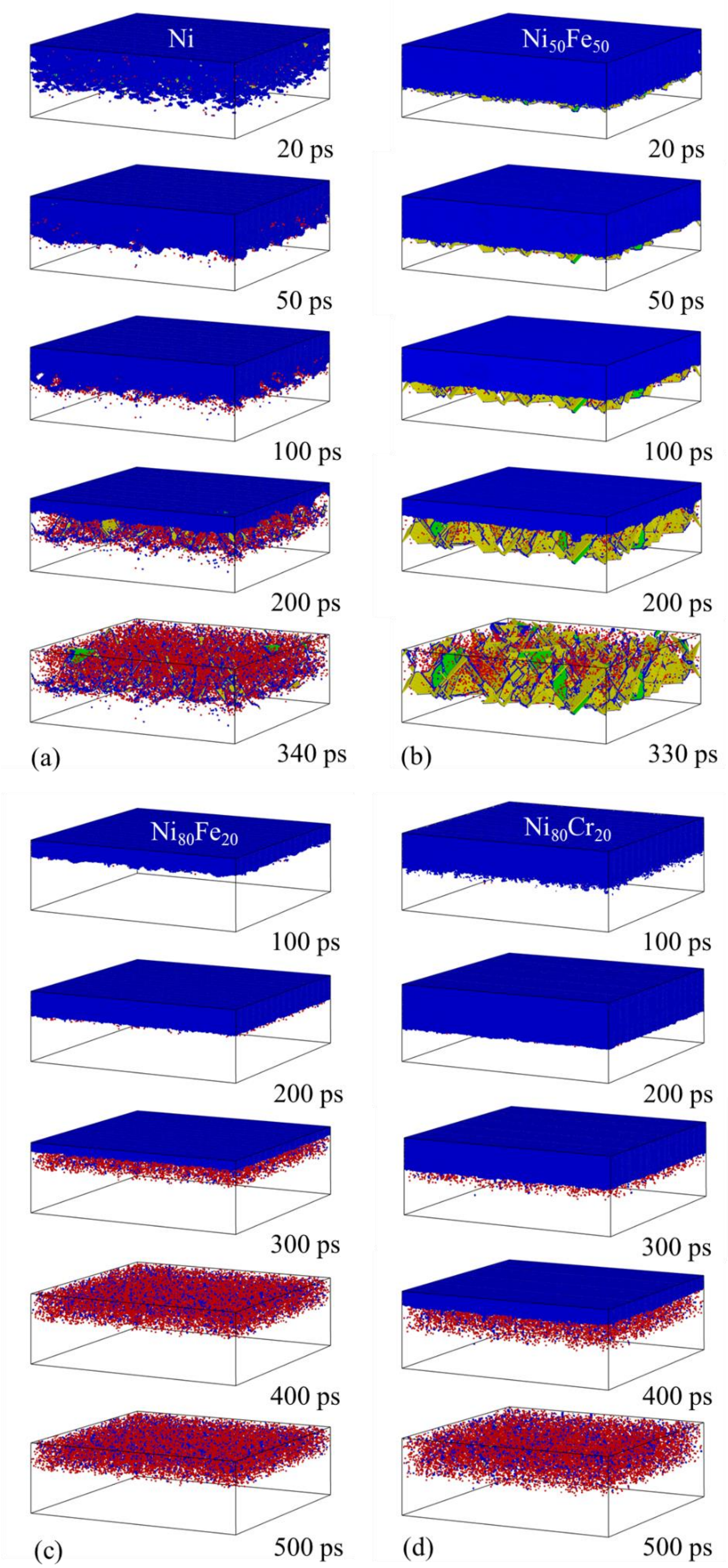
Ni
20 ps
50 ps
100 ps
200 ps
(a)
340 ps
Ni50Fe50
20 ps
50 ps
100 ps
200 ps
(b)
330 ps
Ni80Fe20
100 ps
200 ps
300 ps
400 ps
(c)
500 ps
Ni80Cr20
100 ps
200 ps
300 ps
400 ps
(d)
500 ps

Figure 26. Snapshots of the surface regions of Ni (a), $Ni_{50}Fe_{50}$ (b), $Ni_{80}Fe_{20}$ (c), and $Ni_{80}Cr_{20}$ (d) targets irradiated in the regime of melting and resolidification. Only the top 30 nm thick surface regions of the irradiated targets are shown in the snapshots. The atoms with local fcc structure are blanked to expose the defect structures. The remaining atoms are colored by their local structural environment so that blue color corresponds to atoms that belong to the liquid phase or make up dislocation cores, atoms surrounding vacancies are colored red, stacking faults are colored yellow, and twin boundaries are colored green.

The generation of dislocations, stacking faults and twin boundaries are found to be sensitive to both the target composition and irradiation conditions. Starting from the simulation performed for the pure Ni target, the formation of several twin boundaries (green) and stacking faults (yellow) outlined by Shockley partial dislocations can be seen in the last snapshot in Figure 26a and an enlarged top view of the final configuration shown in Figure 27a. The generation of the partial dislocations can be related to the roughness of the crystal-liquid interface formed by the end of the rapid melting process. The unloading tensile wave, produced due to the dynamic relaxation of the laser-induced stresses, passes through the melting front at ~20 ps, Figure 25a, reduces the crystal stability against melting,[6] and facilitates the homogenous nucleation of liquid regions in the superheated crystal, Figure 26a. As a result, the molten layer formed by 50 ps is separated from the crystalline bulk of the target by a mushy zone where nanoscale crystalline and molten region are mixed. The following solidification process starts from a rough interface and results in the formation of Frank partial dislocations upon folding of deep troughs that produces areas with missing atomic planes incorporated into the growing crystal. Frank partials split into various combinations of stair rod and Shockley partials connected to the solidification front and extending in the course of solidification. The total density of dislocations is estimated as 2.9×10^{16} m^{-2}. In addition to the dislocations, the formation of growth twins is activated on several (111) facets of the rough solidification front advancing in (001) direction when the temperature at the front drops below the critical level required for the onset of growth twining.[19]

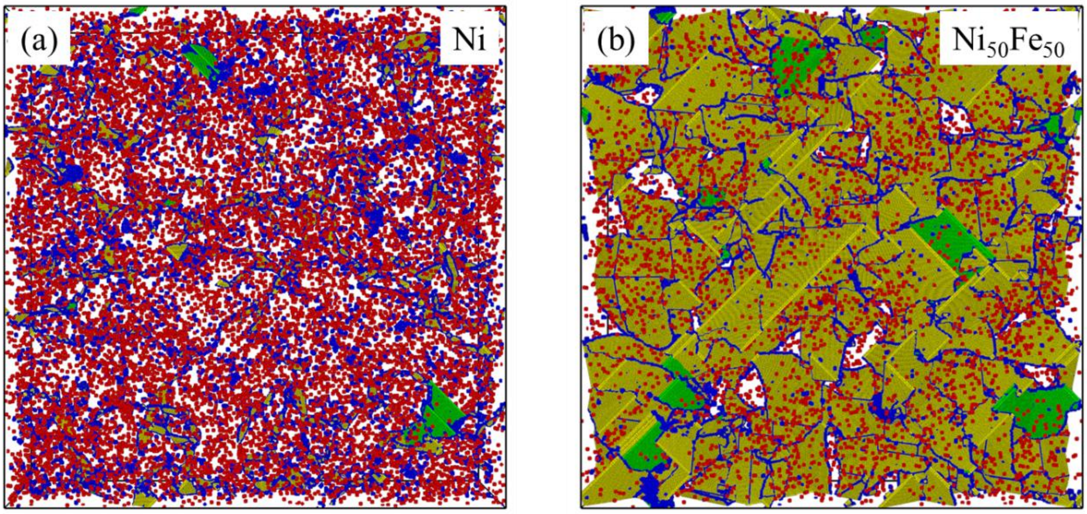

Figure 27. Top view of the crystal defects generated in the surface regions of Ni (a) and $Ni_{50}Fe_{50}$ (b) targets by the laser-induced melting and resolidification. The snapshots are shown for times of 340 and 330 ps after the laser irradiation of Ni and $Ni_{50}Fe_{50}$, respectively. All atoms with the fcc local crystal structure are blanked and the same coloring scheme as in Figure 26 is used.

The defect configuration generated in the $Ni_{50}Fe_{50}$ target is visually very different from the one discussed above for pure Ni and features much higher density of dislocations and stacking faults, Figures 26b and 27b. The density of the dislocations is calculated as around 5.12×10^{16} m^{-2}, with majority part contributed from Shockley partial and stair-rod dislocations. The formation of the stacking faults can be related to the emission of numerous partial dislocations from the crystal-liquid interface at the end of melting process, when strong tensile wave passes through the interface, Figure 25b. As discussed in previous sections, the higher strength of the electron-phonon coupling in the alloy as compared to pure Ni is responsible for the generation of stronger stress wave, which, in turn, generates the resolved shear stresses that are sufficient for the dislocation emission. The Shockley partial dislocations emitted from the melting front leave behind stacking faults that can be seen as earlier as 20 ps after the laser pulse in the snapshots shown in Figure 26b. The interaction of Shockley partials with each other leads to the formation of immobile stair-rod dislocation segments (Lomer-Cottrell and Hirth locks), which prevent further propagation of dislocations into the bulk of the crystal as well as their retraction to the crystal-liquid interface. Calculations of the stacking fault energies predicted by the Bonny EAM potential[201] yielded the value that is approximately two times lower for $Ni_{50}Fe_{50}$ than for Ni. The lower value of the stacking fault energy in the alloy agrees with predictions of thermodynamic calculations[217] and can be related to the suppression of the emission of trailing dislocations from the crystal-liquid interface, leading to the retainment of the large area stacking faults connecting the stair-rod dislocations to the melting/solidification front. The partial dislocations and the corresponding stacking faults are extended towards the surface during the solidification process, forming a continuous dislocation network in the resolidified part of the target, Figure 27b.

No dislocations are identified in the resolidified region of the $Ni_{80}Fe_{20}$ target, and only a few small dislocation loops are observed in the $Ni_{80}Cr_{20}$ target. The latter dislocation loops are formed during the resolidification by the same mechanism as the one discussed above for the Ni target. To understand the virtual absence of dislocations in these two alloys, the roughness of the crystal-liquid interface is analyzed. The targets are divided into small $0.4 \times 0.4 \times 0.4$ nm^3 cells each containing 4-6 atoms, and the cells located at the crystal-liquid interface are identified based on the local atomic structure. The standard deviations of the depth of the interfacial cells are calculated for Ni, $Ni_{50}Fe_{50}$, $Ni_{80}Fe_{20}$, and $Ni_{80}Cr_{20}$ targets and are summarized in Table 2. The calculations of the interface roughness are performed for two moments of time during resolidification for each target: 100 and 200 ps for Ni and $Ni_{50}Fe_{50}$, 200 and 300 ps for $Ni_{80}Fe_{20}$, and 300 and 400 ps for $Ni_{80}Cr_{20}$, as marked by stars in the pressure contour plots shown in Figure 25. The results shown in Table 2 reveal that the crystal-liquid interface is much rougher in the Ni target irradiated by a 100 fs laser pulse as compared to the two targets irradiated by longer 50 ps laser pulses, which is consistent with visual analysis of the corresponding snapshots in Figure 26. As mentioned above, high interface roughness is the prerequisite for the formation of dislocations through folding of deep troughs at the interface, and the low values of the interface roughness calculated for $Ni_{80}Fe_{20}$ and $Ni_{80}Cr_{20}$ alloys are consistent with low densities (or absence) of the dislocations in Figures 26c and d. Note that although the interface roughness in $Ni_{80}Cr_{20}$ is similar to that of $Ni_{80}Fe_{20}$, a small number of dislocation loops are generated in the

$Ni_{80}Cr_{20}$ target while no dislocations are found in the resolidified $Ni_{80}Fe_{20}$ target. This observation can be explained by the lower stacking fault energy in $Ni_{80}Cr_{20}$,[201,217] which makes it easier for loops of partial dislocations enclosing the stacking faults to form. The interface roughness in the $Ni_{50}Fe_{50}$ target is much lower than that in the pure Ni target due to faster and more localized heating, which leads to a rapid melting of the surface region before the arrival of the unloading tensile wave. In this case, the interaction of the unloading wave with the melting front results in the emission of partial dislocations rather than homogeneous nucleation of liquid phase regions below the crystal-liquid interface observed for Ni.

Table 2. Roughness of the solidification front in the large-scale simulations of laser-induced melting and resolidification of Ni, $Ni_{50}Fe_{50}$, $Ni_{80}Fe_{20}$, and $Ni_{80}Cr_{20}$ targets that are evaluated for times marked by stars and labeled as "A" and "B" in Figure 25. The roughness is calculated as standard deviation of the local depth of the interface below the target surface and listed in the units of Angstrom.

Time	Ni	$Ni_{50}Fe_{50}$	$Ni_{80}Fe_{20}$	$Ni_{80}Cr_{20}$
A	23.58	4.01	3.01	3.40
B	13.88	4.81	3.36	3.26

Another prominent feature of the microstructure formed by the laser-induced melting and resolidification is the presence of high density of vacancies in the resolidified parts of the targets as shown in Figure 26. An even clearer view of the vacancies is provided in Figure 28, where all defects except vacancies are blanked, and the single vacancies, di-vacancies, and larger clusters of vacancies are colored blue, green, and red, respectively. The visual analysis of Figure 28 suggests that while high vacancy concentrations are produced in all four targets, the generation of vacancies is strongly suppressed in $Ni_{50}Fe_{50}$ as compared to other targets. This observation is quantified in Figure 29, where the corresponding spatial distributions of vacancies within the irradiated targets are shown. As compared to Ni, where the vacancy concentration in the resolidified region is ~0.1%, the vacancy concentration is reduced by a factor of ~5, down to ~0.02%, in $Ni_{50}Fe_{50}$. This large suppression of the vacancy generation, however, is not observed in $Ni_{80}Fe_{20}$ and $Ni_{80}Cr_{20}$ alloys, where the vacancy concentrations of about 0.15% and 0.1% are observed, respectively. The explanation for the pronounced density of vacancies in the $Ni_{80}Fe_{20}$ and $Ni_{80}Cr_{20}$ targets irradiated by 50 ps laser pulse is provided in Section 4.3.2. Analysis of the temperature dependence of the vacancy mobility indicates that it takes more than 10 ns for a vacancy diffusion length to reach 1 nm at a temperature of 0.8 T_m, which is above the temperature of the surface region at the end of the simulations. Given the ultrafast cooling rate, on the order of 10^{12} K/s at the time of complete resolidification, and the exponential dependence of the mobility of vacancies on temperature, the high concentration of vacancies generated in the surface regions of the targets can be expected to be "frozen in" and remain after cooling down to the ambient temperature.

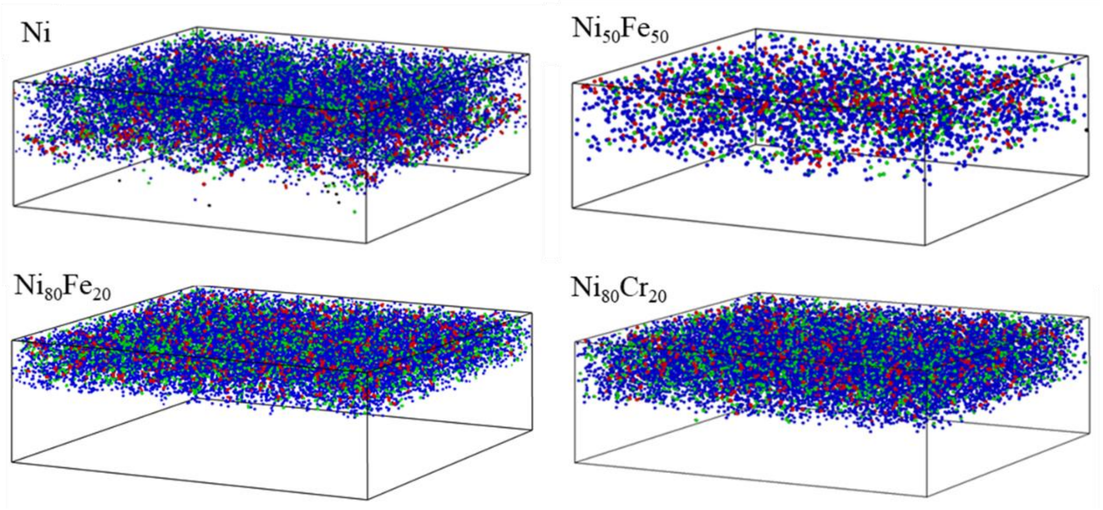

Figure 28. Final snapshots of atomic configurations generated by the end of the resolidification process (340 ps for Ni and $Ni_{50}Fe_{50}$, 500 ps for $Ni_{80}Fe_{20}$, and $Ni_{80}Cr_{20}$), where only the vacancies and vacancy clusters are shown. The atoms surrounding individual vacancies, di-vacancies, and large vacancy clusters are colored by blue, green, and red, respectively.

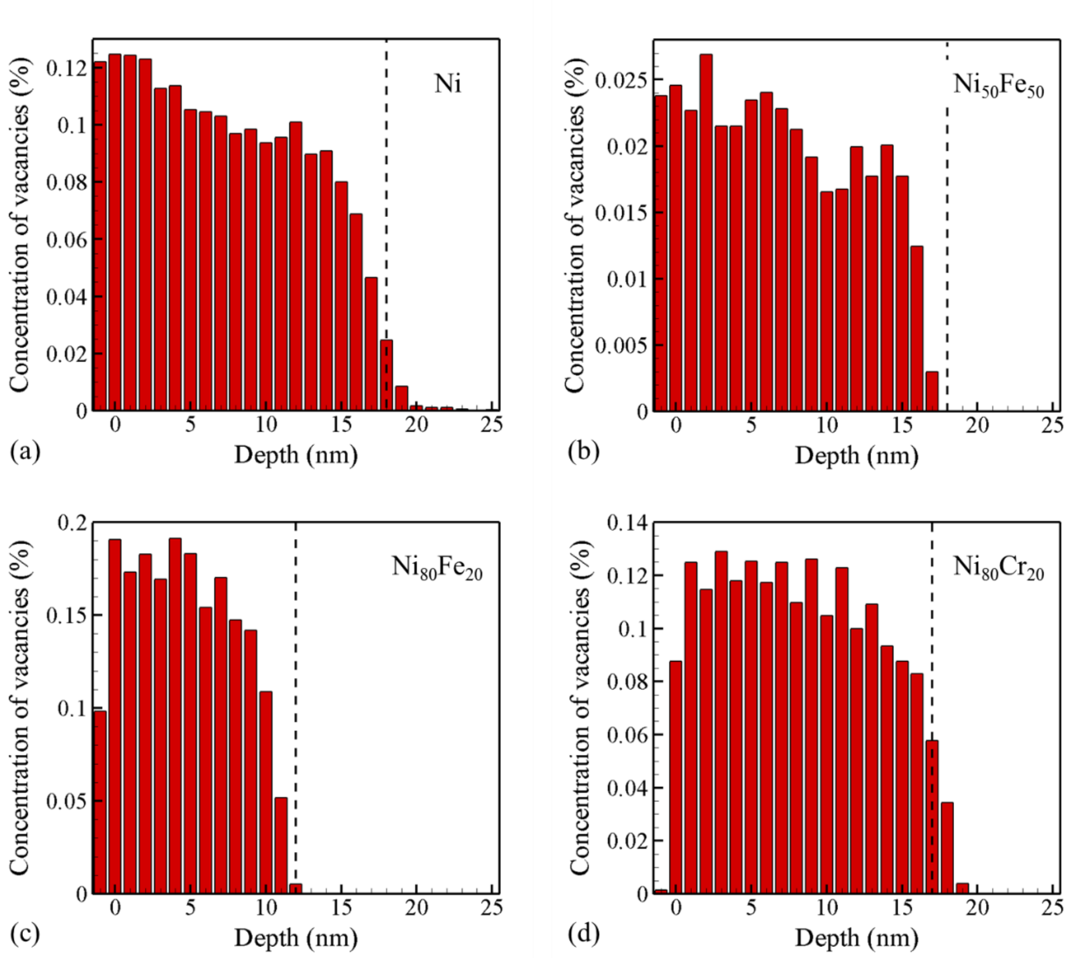

Figure 29. Distribution of vacancy concentration with respect to the depth under irradiated surface for Ni (a), $Ni_{50}Fe_{50}$ (b), $Ni_{80}Fe_{20}$ (c), and $Ni_{80}Cr_{20}$ (d) targets. The dashed lines mark the maximum melting depth reached after the laser irradiation. The vacancy concentrations account for single vacancies and di-vacancies (counted as two vacancies), but not larger vacancy clusters.

Another unexpected result related to the vacancy generation in the alloy systems is revealed in the analysis of the local composition in the immediate vicinity of the vacancies. Assuming a random distribution of atoms of different type in the solid-solution alloys, the probability of having k Ni atoms among the 12 atoms constituting the first neighbor shell of a vacancy site is given by the following equation:

$$F_k = \frac{12!}{k!(12-k)!} p^k (1-p)^{12-k}, \tag{4.1}$$

where p is the probability of a lattice site to be occupied by Ni atom, which is equal to 0.5 for the $Ni_{50}Fe_{50}$ alloy and 0.8 for both $Ni_{80}Fe_{20}$ and $Ni_{80}Cr_{20}$ alloys. The distributions calculated for the atomic configurations generated in the TTM-MD simulations for Ni-Fe alloy targets and shown in the form of the histograms in Figures 30a and b exhibit a pronounced shift towards lower number of Ni atoms with respect to the random distribution of different types of atoms given by Eq. (4.1). The peaks of the histograms shown in Figures 30a and b are shifted from 6 to 5 and from 10 to 9 Ni atoms, respectively, indicating the preference for vacancies to be surrounded by Fe atoms. The frequency histogram calculated for Ni atoms within the first vacancy neighbor shell for $Ni_{80}Cr_{20}$ alloy, Figure 30c, however, coincides with the distribution given by Eq. (4.1).

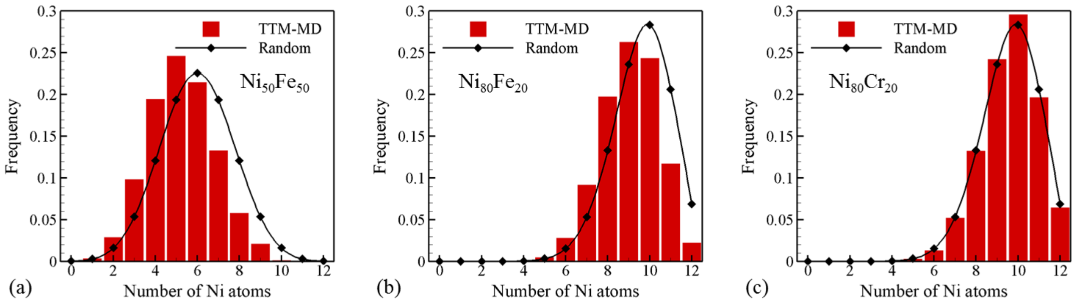

Figure 30. Distribution of the number of Ni atoms in the first nearest neighbor shell of individual vacancies generated by the end of the resolidification process in the TTM-MD simulations of laser irradiation of $Ni_{50}Fe_{50}$ (a), $Ni_{80}Fe_{20}$ (b), and $Ni_{80}Cr_{20}$ (c) alloys. The black lines show the distributions expected for a random arrangement of atoms given by Eq. (4.1).

4.2.5 Summary

The short-pulse laser induced generation of crystal defects, including vacancies, dislocations, stacking faults, and twin boundaries, in Ni and Ni-based binary solid-solution alloys are investigated in large-scale TTM-MD simulations performed in the irradiation regime of melting and resolidification. The intrinsic chemical disorder in the single-phase concentrated solid-solution alloys reduces the thermal conductivity and strengthens electron-phonon coupling with respect to pure Ni, leading to faster and more localized heating of the surface regions of the irradiated targets. As a result, the laser fluence thresholds for melting and spallation are significantly reduced, the magnitude of the laser-induced stresses increases, and the separation between the two thresholds shrinks in the alloy targets.

The microstructure of the resolidified surface regions in the Ni and $Ni_{50}Fe_{50}$

targets irradiated by 100 fs laser pulses is found to be strongly affected by the dynamic relaxation of the laser-induced stresses, which leads to the generation of a strong unloading tensile wave that interacts with the melting front and facilitates the formation of high densities of partial dislocations in the surface regions of the irradiated targets. In Ni, the tensile wave passes through the melting front, reduces the crystal stability against melting, and triggers homogeneous nucleation of new liquid regions in the superheated crystal. As a result, the crystal-liquid interface formed by the end of the melting process has a rough shape, and the resolidification proceeding from such interface yields a high density of dislocations connected to the solidification front and extending toward the surface in the course of the solidification.

In $Ni_{50}Fe_{50}$ target, numerous Shockley partial dislocations are directly emitted from the crystal-liquid interface at the end of the melting processes, when a strong unloading wave passes through the interface. The interaction of Shockley partials with each other leads to the formation of immobile stair-rod dislocation segments, which prevent the retraction of the dislocations to the crystal-liquid interface. The partial dislocations and the corresponding stacking faults are extended toward the surface during the solidification process, forming a continuous dislocation network in the resolidified part of the target.

In $Ni_{80}Fe_{20}$ and $Ni_{80}Cr_{20}$ targets irradiated by longer 50 ps laser pulses, the laser-induced thermoelastic stresses are much lower, and neither the melting front roughening nor dislocation emission is observed in the simulations. As a result, the solidification proceeds through the propagation of a smooth crystal-liquid interface, which yields no dislocations in $Ni_{80}Fe_{20}$ and only a small number of dislocation loops in $Ni_{80}Cr_{20}$. The levels of undercooling at the solidification front are similar to the values reached in the Ni and $Ni_{50}Fe_{50}$ targets irradiated by 100 fs laser pulses. The difference in the microstructure, therefore, is mainly related to the differences in laser-induced stresses and material properties.

One prominent feature of the microstructure formed in the surface regions of the irradiated targets is the generation of very high vacancy concentrations exceeding the equilibrium values at the melting temperature by about an order of magnitude. In all targets, the supersaturated vacancies are only observed in the regions that experienced transient melting and resolidification. Therefore, in order to explain the high density of vacancies generated in the course of laser-induced melting and solidification, the unexpected sensitivity of the vacancy concentration to the target composition, and the deviation of the first atomic neighbor surrounding the individual vacancies from the chemical disorder environment, additional series of simulations of solidification under conditions of fixed undercooling below the equilibrium melting temperature are performed, as reported in the next Section.

4.3 Atomistic simulations of vacancy formation at solidification front at fixed level of undercooling

The physical interpretation of the high levels of vacancy supersaturation produced by the laser-induced melting and resolidification as well as the suppression of vacancy generation in the $Ni_{50}Fe_{50}$ alloy, predicted in the TTM-MD simulations in the previous section, can be assisted by considering the results of MD simulations of solidification occurring at fixed levels of undercooling and pressure below the equilibrium melting temperature. The computational setup for the MD simulations, the method of calculating the equilibrium vacancy concentration, which is used to assess the level of vacancy supersaturation resulted from rapid solidification, and the approach to estimate the vacancy mobility, are described in Section 4.3.1. In Section 4.3.2, the mechanisms of vacancy generation at the solidification front for the Ni and Ni-based alloys, as well as the suppression of vacancies in the solid-solute alloys are revealed from MD simulations, which is related to the results of the TTM-MD simulations discussed in Section 4.2.4. A detailed, atomistic-level investigation of the process of vacancy formation at the solidification front in bcc and fcc metals, as well as a comprehensive study of the dependence of solidification kinetics and vacancy density on undercooling level, material properties, and crystalline orientation of the crystal-liquid interface, are presented in Section 4.3.3. The generation of vacancies in the course of rapid solidification proceeding under well-controlled pressure and temperature conditions predicted from MD simulations is summarized in 4.3.4.

4.3.1 Computational setup and methods

The MD simulations of solidification under conditions of constant pressure and undercooling levels are performed for crystal-liquid coexistence systems of bcc Cr and fcc Ni and Ni-based solid-solute alloys ($Ni_{50}Fe_{50}$, $Ni_{80}Fe_{20}$, and $Ni_{80}Cr_{20}$). The computational system is created by combining two liquid parts with a fcc crystal, as schematically illustrated in Figure 31a, and periodic boundary conditions are applied in all three directions, forming a system where a solid slab is surrounded by molten material. The fcc crystal is oriented so that its [001] direction is aligned with the longest axis of the combined system. The parts of the combined system are pre-equilibrated at a desired temperature and zero pressure. The liquid subsystem is prepared in a constant pressure simulation, where a crystal is first heated above the limit of its thermodynamic stability against the onset of homogeneous melting, ~1.2-1.3 T_m,[7,218,219] leading to the rapid melting of the whole system. The molten material is then cooled down to the desired temperature, below T_m. The undercooled liquid remains in the metastable state because of the absence of any nucleation sites and relatively slow rate of homogeneous nucleation of new crystallites at moderate levels of undercooling. After the combined systems are prepared, the solidification simulations are performed at a range of fixed temperature and pressure conditions. The crystal-liquid coexistence systems are subdivided into 2-4 nm thick slices along the [001] direction, and the temperature is controlled through the Berendsen thermostat algorithm[220] applied to each slice independently. This slice-by-slice temperature control eliminates the appearance of temperature spikes near the advancing solidification fronts due to the release of the latent heat of meting, and enables simulation of the solidification at a well-controlled temperature of the crystal-liquid interface. In both the preparation of the liquid part of the system and the solidification simulations, the pressure control is done through the Berendsen barostat algorithm[220] applied along the z-axis of the system only, with sizes of the systems along the x and y directions fixed at values that correspond to a crystal equilibrated at desired temperature and pressure. This enables combination of the liquid and crystalline parts of the system at the same preparation stage and eliminates the appearance of anisotropic lattice distortions in the simulations of solidification. The solidification velocities are then calculated by tracking the movement of the two crystal-liquid interfaces, and the defects generated in the parts of the system where the solidification takes place in the steady-state regime are analyzed.

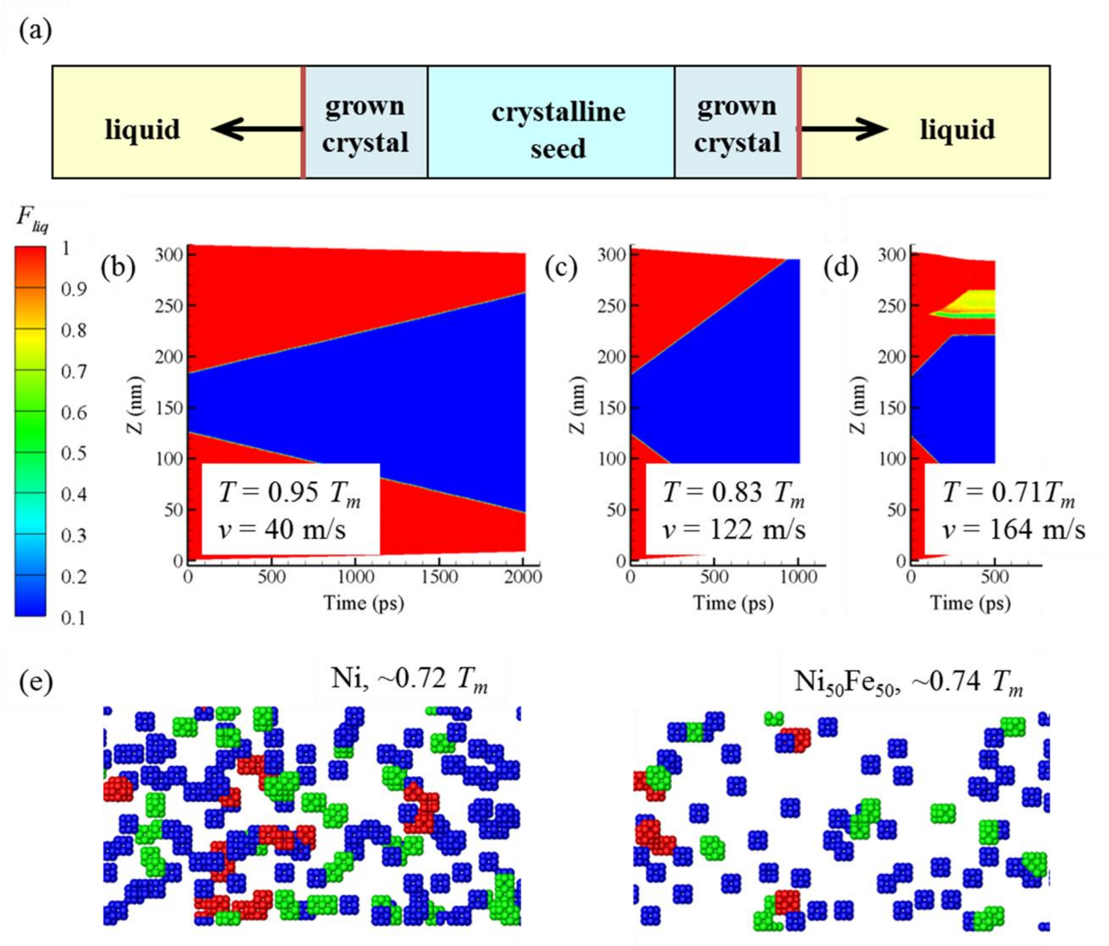

Figure 31. Analysis of the generation of vacancies in MD simulations of the solidification front propagation. (a) Schematic illustration of the computational setup used for simulation of solidification under conditions of constant temperature and pressure. (b-d) Contour plots depicting the evolution of the fraction of liquid phase in MD simulations performed for the $Ni_{50}Fe_{50}$ system at temperatures of 0.95 T_m, 0.83 T_m, and 0.71 T_m, respectively. The computational system has a dimension of $7\ \text{nm} \times 7\ \text{nm} \times 300\ \text{nm}$ (1.28 million atoms), consisting of a 60 nm long fcc crystal surrounded by a 120 nm long liquid part on each side along z axis. The values of the solidification front velocities calculated from the rates of advancement of the crystal regions (blue) into the molten parts of the system (red) are provided on the plots. (e) Parts of the solidified regions produced in simulations of Ni and $Ni_{50}Fe_{50}$ systems. The atoms surrounding individual vacancies, di-vacancies, and vacancy clusters are colored by blue, green, and red colors, respectively.

The interatomic interactions in the Ni and Ni-based alloys are described by the Bonny EAM potential,[201] and the interatomic interactions in the Cr system are described by the EAM potential developed by Johnson *et al.*[208] which predicts the melting temperature of 2366 K. The effects of crystallographic orientations of the solidification front on the generation of vacancies are investigated for the Cr system with (001), (011), and (111) orientations along z axis, which is normal to the initial crystal-liquid interface. In order to study the effect of interatomic interactions on the generation of crystal defects, the Johnson EAM potential is also used for the simulations of fcc Ni system and the results are compared with that of MD simulations performed with the Bonny EAM potential[201], as well as other forms of EAM potential suggested by Foiles, Baskes and Daw (FBD) [221] and Mishin[207], respectively. The melting temperatures calculated for Johnson, Mishin, and Bonny EAM potentials are 1445 K, 1701 K, and 1530 K, respectively. The FBD EAM potential gives the best approximation of melting temperature, 1719 K, compared with the experimental value of 1728 K.[202]

To investigate the effect of lateral stress on the generation of vacancies, additional MD simulations of solidification under controlled temperature and pressure conditions are performed for the crystal-liquid coexistence systems of Ni, $Ni_{50}Fe_{50}$, and $Ni_{80}Fe_{20}$. Under each degree of undercooling, instead of fixing the lateral size of the systems along the x and y directions at values that corresponds to the equilibrated crystal at zero pressure, for different lateral sizes are selected and kept as 0.98, 0.99, 1.01, and 1.02 of the equilibrium values for each system, thus creating conditions of lateral tensile and compressive strain of 1% and 2%. The pressure along z-axis of the crystal-liquid coexistence system is controlled at zero. The temperature, lattice parameter, as well as calculated lateral stress of each system with fixed lateral strain are summarized in Table 3.

Table 3. Parameters for the simulations of solidification in the crystal-liquid coexistence systems of Ni, $Ni_{50}Fe_{50}$, and $Ni_{80}Fe_{20}$. T is the temperature at which the simulation is controlled, a_0 is the equilibrium lattice parameter of the crystal under conditions of corresponding temperature and zero pressure, and σ is the lateral stress calculated for each system with lateral strain ε.

Material	T (K)	T/T_m	α_0 (Å)	σ (GPa)			
				$\varepsilon = -2\%$	$\varepsilon = -1\%$	$\varepsilon = 1\%$	$\varepsilon = 2\%$
Ni	1100	0.72	3.543	-2.97	-1.62	1.91	4.15
	1400	0.92	3.5619	-2.22	-1.27	1.6	3.54
$Ni_{50}Fe_{50}$	1250	0.74	3.5403	-2.72	-1.58	2.02	4.42
	1550	0.92	3.5676	-1.67	-1.01	1.4	3.16
$Ni_{80}Fe_{20}$	1200	0.73	3.539	-3	-1.68	2.06	4.47
	1500	0.92	3.5611	-2.08	-1.22	1.59	3.55

To calculate the vacancy mobility of each Ni-based disordered binary solid-solution alloy, small cubic systems with $10 \times 10 \times 10$ fcc unit cells thus containing 4000 lattice sites are created. One vacancy site is pre-incorporated at the center of the system, and the remaining 3999 lattice sites are randomly assigned with an atomic type according to the alloy composition. To be specific, 2000 Ni atoms and 1999 Fe atoms are assigned in the $Ni_{50}Fe_{50}$ system, and 3200 Ni atoms and 799 Fe or Cr atoms are assigned in the $Ni_{80}Fe_{20}$ or $Ni_{80}Cr_{20}$ system. The MD simulations are performed by controlling each system at a range of fixed undercooling levels from ~0.7 T_m to ~0.99 T_m with 50 K increment. The lattice parameter of each system is chosen as the equilibrium value under the condition of controlled temperature and zero pressure.

For a solid system with vacancy concentration, C_V, defined as the fraction of vacant sites over all lattice sites, the vacancy mobility, D_V, can be derived from the equation $D_V = D/C_V$, where D is the self-diffusion coefficient of atoms calculated from the Einstein relation

$$D = \frac{R^2(t)}{6t}. \tag{4.2}$$

$R^2(t)$ is the average mean square displacement of all atoms at time *t*. The MD simulations are performed at different levels of temperature for 6 ns, and the position of atom i, $\vec{r}_i(t)$, are recorded every 1 ps during the simulation. The mean square displacement from time t_1 to time t_2 is calculated as $R^2(t_2 - t_1) = \frac{\sum_{i=1}^{n}[\vec{r}_i(t_2) - \vec{r}_i(t_1)]}{n}$, where $n = 3999$ is the number of atoms of the system with one pre-implemented vacancy. To reduce the statistical fluctuations, the simulation time is divided into periods of 500 ps so that the beginning time τ_k for each period k is changing as 0 ps, 1 ps, … 5500 ps. Therefore, the average of the mean square displacement for the 500 ps period can be calculated as

$$\tilde{R}(t) = \frac{\sum_{k=0}^{5500}\sum_{i=1}^{n}[\vec{r}_i(\tau_k + t) - \vec{r}_i(\tau_k)]}{5501 \cdot n}, \ 0 \leq t \leq 500. \quad (4.3)$$

Linear fitting of $\tilde{R}(t)$ as a function of t according to Eq. (4.2) gives the coefficient of self-diffusion D, and the vacancy diffusivity in this system consisting of one vacancy over 4000 lattice sites can be calculated as $D_V = D/C_V = D \cdot 4000$.

In order to assess the significance level of the concentration of vacancies generated at the rapidly propagating solidification front, the equilibrium values of vacancy concentration as a function of temperature are estimated based on the Arrhenius expression:

$$C_V^{eq} = \exp\left(-\frac{G_f(T)}{k_B T}\right), \quad (4.4)$$

where $G_f(T) = H_f(T) - TS_f(T)$ is the change of Gibbs free energy associated with forming a vacancy. The vacancy formation enthalpy $H_f(T)$ is calculated by our collaborator Dr. M. V. Shugaev from the group of Prof. L. V. Zhigilei in a series of constant pressure and temperature (NPT) simulations as the enthalpy difference between systems with and without vacancies. The obtained temperature dependence of enthalpy of vacancy formation is fitted to the following equation

$$H_f = H_f^0 + AT^2 + Be^{-C/T}, \quad (4.5)$$

as shown by the red lines in Figure 32. Based on the fitting parameters H_f^0, A, B, and C, which are summarized in Table 4, the entropy and free energy of vacancy formation can be expressed in the following forms:

$$G = -T\int \frac{H(T)dT}{T^2}\ ,\ S = -\left(\frac{\partial G}{\partial T}\right)_P, \tag{4.6}$$

$$S_f = S_f^0 + 2AT + B(T^{-1} + C^{-1})e^{-C/T}, \tag{4.7}$$

$$G_f = H_f^0 - TS_f^0 - AT^2 - \frac{BT}{C}e^{-C/T}. \tag{4.8}$$

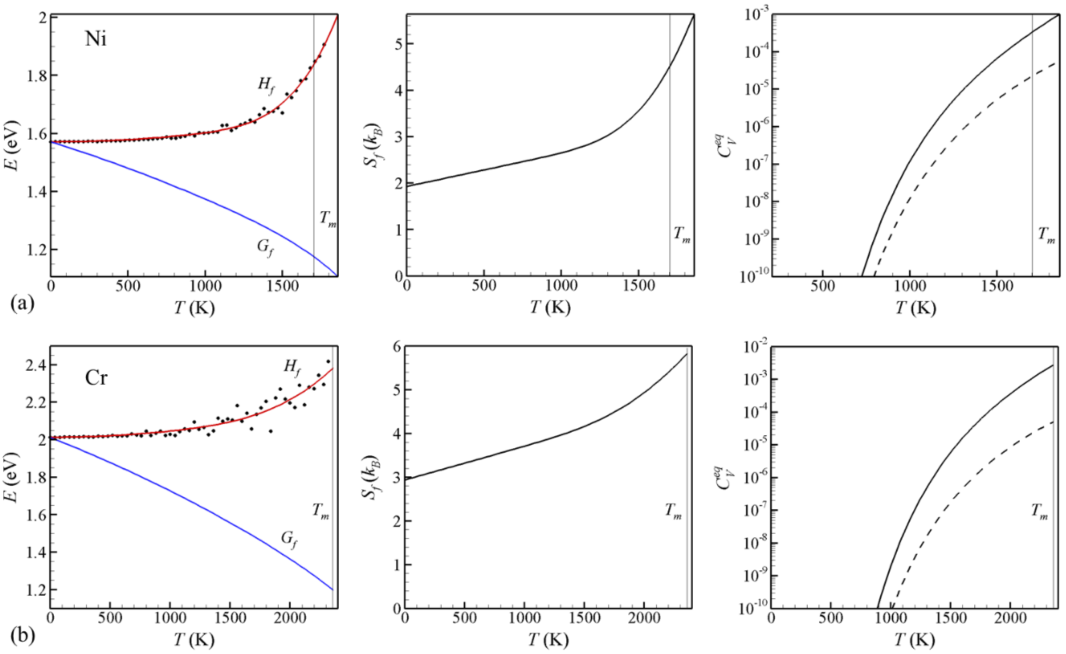

Figure 32. The enthalpy, free energy, entropy of vacancy formation, and the equilibrium concentration of vacancies at different temperatures for Ni system described by Mishin EAM potential[207] (a) and Cr system described by Johnson EAM potential[208] (b). The concentration of vacancies predicted based only on the enthalpy of vacancy formation at 0 K, H_f^0, is shown by the dashed lines. The fitting parameters are summarized in Table 4. The results are obtained by Dr. M. V. Shugaev from the group of Prof. L. V. Zhigilei.

Table 4. Fitting parameters for Eqs. (4.4-4.8) and the equilibrium concentration of vacancies at melting temperature, $C_V^{eq}(T_m)$, predicted from the MD simulations for Ni and Cr systems described by Mishin[207] and Johnson[208] EAM potentials, respectively. All parameters except $C_V^{eq}(T_m)$ are calculated by Dr. M. V. Shugaev from the group of Prof. L. V. Zhigilei.

	H_f^0 (eV)	S_f^0 (k_B)	A (eV/K^2)	B (eV)	C (K)	$C_V^{eq}(T_m)$
Ni	1.57	1.93	3.06×10^{-8}	306	12690	3.3×10^{-4}
Cr	2.01	2.94	3.33×10^{-8}	48.4	13140	2.9×10^{-3}

Since Eq. (4.5) is written in a form that does not account for the temperature dependence of entropy near 0K, calculation of entropy following this function with the condition of zero entropy at 0K may lead to a notable deviation from the value obtained by an appropriate approximation of the low temperature behavior, which is challenging and requires a lot of complex considerations. Therefore, a parameter S_f^0 is introduced in Eqs. (4.7-4.8) to address this difference. The value of S_f^0 can be estimated from the equilibrium concentration of vacancies at melting temperature, $C_V^{eq}(T_m)$, calculated by MD simulations. The simulations are performed for a large crystal system with thickness of 10 nm initially prepared at the melting temperature T_m. Periodic boundary conditions are applied on the lateral dimensions so the system can be regarded as an infinitely large thin film with two free surfaces along z axis. A certain number of vacancies are uniformly incorporated in the system at the beginning of the simulation, and since the free surfaces act as sources and sinks of vacancies, the equilibrium concentration of vacancies at T_m will finally be achieved in the system by vacancy diffusion to/from the free surfaces. The evolution of the vacancy concentration, $C_V(z,t)$, in the system can be calculated by solving the Fick's law

$$\frac{\partial C_V(z,t)}{\partial t} = D_V \frac{\partial^2 C_V(z,t)}{\partial z^2}, \tag{4.9}$$

with the boundary conditions

$$C_V(z,0) = C_0, \tag{4.10}$$

$$C_V(0,t) = C_V(L,t) = C_V^{eq}(T_m). \tag{4.11}$$

Here, D_V is the vacancy diffusivity, C_0 is the initial vacancy concentration implemented in the system, and L is a parameter fitted from MD simulations, which is equivalent to the distance between two sources/sinks of vacancies where the concentration is constant as $C_V^{eq}(T_m)$. The value of L is typically less than the thickness of the film considering that heterogeneous melting will occur initially at the free surface due to fluctuations, and the crystal-liquid interface cannot be regarded as an ideal boundary described by Eq. (4.11) due to its complex structure. The general solution of Eqs. (4.9-4.11) can be derived as

$$C_V(z,t) = C_0 + \frac{C_V^{eq}(T_m) - C_0}{2 - \operatorname{erf}\left(\frac{L}{\sqrt{4D_V t}}\right)} \left[2 - \operatorname{erf}\left(\frac{z}{\sqrt{4D_V t}}\right) - \operatorname{erf}\left(\frac{L-z}{\sqrt{4D_V t}}\right)\right]. \tag{4.12}$$

The MD simulations are performed for the Cr and Ni systems pre-incorporated with vacancies at $C_0 \approx 0.4\%$ and 0.08%, respectively, the values corresponding to the non-equilibrium density of vacancies generated at the solidification front at ~0.9 T_m as discussed in Section 4.3.3. The time evolutions of vacancy concentration in the systems, as shown in Figure 33, are plotted and used to fit Eq. (4.12), yielding the fitting parameters of $C_V^{eq}(T_m) = 0.031\%$, $L = 5.7$ nm for Ni described by Mishin EAM potential,[207] and $C_V^{eq}(T_m) = 0.285\%$, $L = 4.1$ nm for Cr described by Johnson EAM potential.[208] Due to much smaller value of vacancy mobility of Ni than Cr, the time required to achieve equilibrium vacancy concentration in the Cr system, ~6 ns, is several times shorter than that for the Ni system, more than 20 ns. To examine the effect of C_0 on the computational results, additional MD simulation is also performed for the Cr system with an initially perfect system, $C_0 = 0$. The results are shown in Figure 33c, and the fitted parameters, $C_V^{eq}(T_m) = 0.292\%$, $L = 4$ nm, is consistent with the values obtained with $C_0 = 0.4\%$.

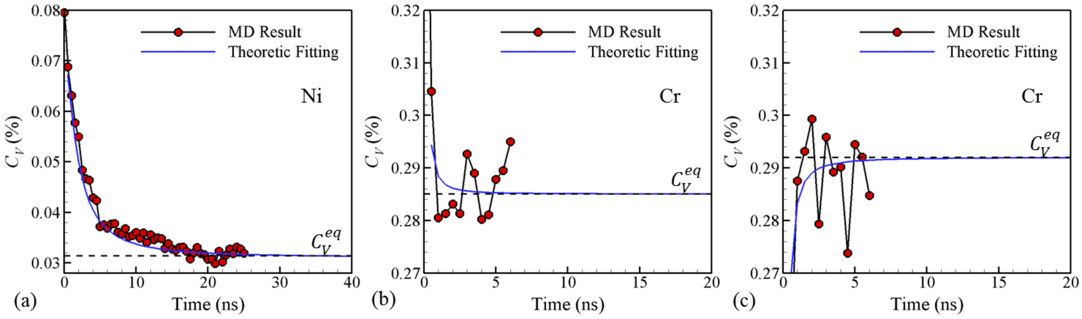

Figure 33. Time evolution of vacancy concentration predicted in the MD simulations of a 10 nm thick film performed at T_m for the Ni system described by the Mishin EAM potential[207] with $C_0 = 0.073\%$ (a), as well as the Cr system described by the Johnson EAM potential[208] with $C_0 = 0.4\%$ (b) and $C_0 = 0$ (c). The blue lines are fitted from MD results (red circles) based on Eq. (4.12) and the fitting parameters are given in the text. The dashed lines indicate the level of equilibrium vacancy concentration at melting temperature, of which the values are given in the text.

The value of $C_V^{eq}(T_m)$ is applied in Eq. (4.4) along with H_f at T_m obtained from Eq. (4.5), to calculate the entropy of vacancy formation at melting temperature, thus the parameter S_f^0 can be estimated from Eq. (4.7), giving the values of $S_f^0 = 4.53$

k_B for Ni, $S_f^0 = 5.86$ k_B for Cr with $C_0 = 0.4\%$, and $S_f^0 = 5.88$ k_B for Cr with $C_0 = 0$. After determination of all the parameters in Eqs. (4.5-4.8), the equilibrium vacancy concentration is calculated as a function of temperature from Eq. (4.4), as plotted in Figure 32.

4.3.2 Generation of vacancies during solidification under conditions of fixed temperature and pressure in Ni and Ni-based alloys

Four series of MD simulations of solidification are performed for Ni, $Ni_{50}Fe_{50}$, $Ni_{80}Fe_{20}$, and $Ni_{80}Cr_{20}$ systems under conditions of zero pressure and a range of undercooling levels. As illustrated by the contour plots depicting the local fraction of the liquid phase, Figures 31b-d, a crystalline seed with two (001) crystal-liquid interfaces grows epitaxially and the steady-state propagation of the two solidification fronts proceeds with a constant velocity defined by the undercooling level maintained through the system. The local fraction of liquid phase, F_{liq}, is determined based on calculation of local order parameter[82,222] that identifies atoms with local surroundings characteristic of liquid or crystalline phases. When the undercooling approaches a critical level of ~30% below T_m, the homogeneous nucleation of new crystallites inside the strongly undercooled liquid is observed in addition to the epitaxial propagation of the melting fronts, as exemplified by the emergence of a new region with nonzero fraction of crystalline atoms inside the liquid phase region in a simulation performed at 0.71 T_m, Figure 31d. The onset of homogeneous nucleation of new crystallites has been observed at similar levels of undercooling in earlier simulations of laser melting and resolidification performed for Foiles-Baskes-Daw EAM Ag,[232425] and at a deeper undercooling of ~0.60 T_m for Johnson EAM Ni.[20] To avoid the effect of the homogeneous nucleation of new crystallites on the analysis of the vacancy formation at the solidification front, only the results obtained at temperatures ranging from 0.98-0.99 T_m down to the threshold for the onset of the homogenous nucleation are used in the analysis. Two representative atomic configurations showing the presence of vacancies, di-vacancies, and vacancy clusters in the solidified region of Ni and $Ni_{50}Fe_{50}$ systems are provided in Figure 31e. The vacancies are counted and the vacancy concentrations are calculated for the atomic configurations generated at different levels of undercooling.

The solidification velocities and the average concentrations of vacancies in the solidified parts of the four systems predicted in the simulations are plotted as functions of temperature in Figures 34a and c. The solidification front velocities are similar in Ni, $Ni_{50}Fe_{50}$ and $Ni_{80}Fe_{20}$, while a reduced velocity is observed for the $Ni_{80}Cr_{20}$ alloy, Figure 34a. At 0.9 T_m, *i.e.*, the maximum undercooling achieved by the end of the solidification process in TTM-MD simulations of laser-induced melting and resolidification discussed in Section 4.2.3, the solidification velocity is ~80 m/s for Ni and Ni-Fe systems and ~70 m/s for the $Ni_{80}Cr_{20}$ alloy, which agrees with the maximum velocities of the resolidification front in the TTM-MD simulations.

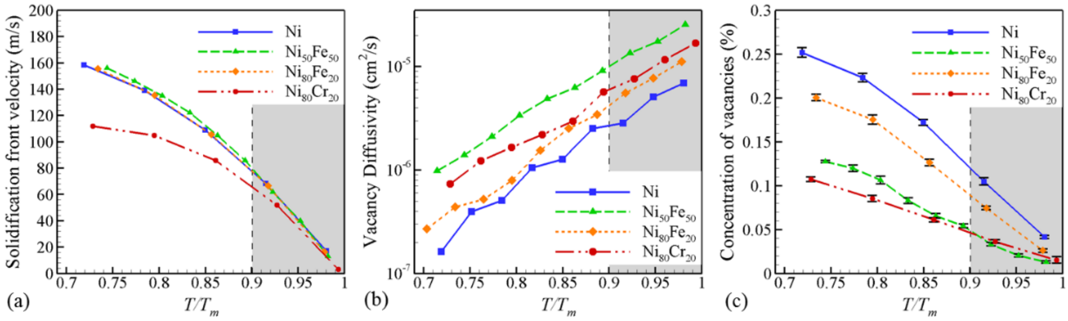

Figure 34. Temperature dependence of solidification velocity (a), vacancy mobility (b), and concentration of vacancies (c) for Ni, $Ni_{50}Fe_{50}$, $Ni_{80}Fe_{20}$, and $Ni_{80}Cr_{20}$ systems. Data in (a) and (c) are predicted from MD simulations of solidification performed under conditions of fixed undercooling levels below the equilibrium melting temperature and zero pressure. Results in (b) are computed from MD simulations of diffusion of one vacancy in solid system under constant temperature and zero pressure. The gray zone indicates the range of temperatures observed in TTM-MD simulations of laser-induced melting and resolidification discussed in Section 4.2.3.

The comparison of Figures 34a and c reveals similarity of the temperature dependences of the solidification front velocity and vacancy concentration, both exhibiting increase with decreasing temperature. The acceleration of the solidification velocity with increased undercooling can be attributed to the rapid increase in the thermodynamic driving force for crystallization. Indeed, close to linear increase of the solidification front velocities up to a maximum level ~100 m/s followed by a saturation with increasing undercooling has been reported in earlier MD simulations[223] and supported by experimental measurements.[31] The increase in the vacancy concentration, however, looks surprising from the first sight, as the thermodynamic driving force for the generation of vacancies is decreasing exponentially with decreasing temperature. The generation of vacancies, therefore, can only be explained by peculiarities of the kinetics of the increasingly rapid growth of the crystal at lower temperatures: The vacancies are essentially generated as “errors” in the process of building the crystal structure at the solidification front rapidly advancing under conditions of strong undercooling below the equilibrium melting temperature of the material. The increase of the interface velocity with increasing undercooling, Figure 34a, reduces the time available for atomic rearrangements needed to correct these “errors” and results in trapping of increased number of vacancies behind the propagating solidification front.

While the vacancy concentrations predicted for different material systems exhibit qualitatively similar dependencies on the level of undercooling, Figure 34c, the plots also demonstrate an obvious suppression of the vacancy generation in the three alloy systems with respect to pure Ni. At all levels of undercooling, the vacancy concentration decreases with addition of Fe, from pure Ni to $Ni_{80}Fe_{20}$ and to $Ni_{50}Fe_{50}$. The addition of Cr has even stronger effect on the vacancy concentration, with $Ni_{80}Cr_{20}$ exhibiting the lowest vacancy concentrations out of the four systems below 0.9 T_m. The reduced vacancy density with increased Fe concentration in the Ni-Fe alloys cannot be explained by the effect of solidification velocities, which are similar for the Ni, $Ni_{50}Fe_{50}$, and $Ni_{80}Fe_{20}$ systems as shown in Figure 34a. However, the suppression of vacancy generation by adding Fe in the Ni-Fe alloys can be related to the enhanced mobility of the vacancies as reflected in the plot of vacancy diffusion coefficient as a function of undercooling levels, Figure 34b, which is consistent with previous study.[224] Higher vacancy mobility may facilitate the diffusion of vacancies into the liquid parts, resulting in less vacancy concentration remained in the solidified region.[184] Moreover, the mobility of vacancies decreases exponentially with temperature decrease, thus preventing the vacancies from escaping to the liquid, and reinforcing the effect of increasing vacancy concentration with the degree of undercooling in addition to the increase of solidification velocity. The combined effect of solidification velocity and vacancy mobility can also explain the difference in vacancy concentration between $Ni_{50}Fe_{50}$ and $Ni_{80}Cr_{20}$ alloys. Above 0.9 T_m, where the solidification velocities are similar, the higher level of vacancy concentration in $Ni_{80}Cr_{20}$ is attributed to lower vacancy mobility than in the $Ni_{50}Fe_{50}$ system. Below 0.9 T_m, the substantially decreased solidification velocity in $Ni_{80}Cr_{20}$ system offsets the effect of vacancy mobility and is responsible for the reduced vacancy concentration compared to the $Ni_{50}Fe_{50}$ system.

The reduced concentrations of vacancies in the alloy systems are consistent with the results of TTM-MD simulations for Ni and $Ni_{50}Fe_{50}$, where levels of the vacancy concentration in the resolidified regions, Figures 29a and b, are close to the ones obtained in the constant temperature and zero pressure simulations, Figure 34c. The suppression of vacancy generation, however, is not observed in the laser irradiated $Ni_{80}Fe_{20}$ and $Ni_{80}Cr_{20}$ targets, Figures 29c and d, where the average vacancy concentration in the resolidified regions is 1.5-2 times higher than the levels one would expect based on the results of the constant temperature simulations. Specially, the vacancy concentration in the laser-irradiated $Ni_{80}Fe_{20}$, Figure 29c, is the highest among the four targets and exceeds that in the pure Ni target. This apparent contradiction can be explained by the presence of substantial residual compressive stresses in the resolidified regions of $Ni_{80}Fe_{20}$ and $Ni_{80}Cr_{20}$ targets, which is shown in the pressure contour plots shown in Figures 25c and d. These thermoelastic stresses cannot relax through the uniaxial expansion of the target in the direction normal to the surface and will remain in the surface region of the target until it cools down to the ambient temperature. Meanwhile, as discussed in Section 4.2, in Ni and $Ni_{50}Fe_{50}$ targets the residual lateral stresses are relaxed by the high density of dislocations and, as a result, the vacancy concentrations in the resolidified regions are in accord with the predictions of zero pressure simulations performed at comparable levels of undercooling.

To demonstrate the effect of the residual lateral stress on the generation of vacancies during solidification, MD simulations of solidification as described in

Section 4.3.1 are performed at different levels of lateral stress as summarized in Table 3. The dependence of vacancy concentration generated at the crystal-liquid interface on different undercooling and stress levels are shown in Figure 35a. At fixed lateral stress, vacancy concentration generated at deeper undercooling, 0.92 T_m, is higher than the value obtained at lower level of undercooling, ~0.72-0.74 T_m. This observation is consistent with the result obtained at zero pressure, Figure 34c, and can be explained by the combined effect of faster propagation of solidification front and lower vacancy mobility at higher undercooling level. Interestingly, the vacancy concentration exhibits positive dependence with lateral stress, showing the suppression of vacancy generation under tensile lateral stress and higher vacancy density under higher lateral compression. The formation of vacancies creates local tensile environment, and compressive lateral stress may help counteract this effect and decrease the vacancy formation energy, thus fostering the generation of vacancies. At 2% lateral strain, significant compressive stress around 3-4 GPa as listed in Table 3 leads to the emission of dislocations and formation of stacking faults. Figure 35b shows an example of solidification process under 0.92 T_m and 2% strain in the $Ni_{80}Fe_{20}$ system. The blue region corresponds to liquid, and the middle region colored in red corresponds to crystal in which the lateral stress cannot be relaxed through uniaxial expansion. The pressure plotted in Figure 35b, $P = \frac{P_x+P_y+P_z}{3}$, can be estimated as $\frac{2}{3}P_{x/y}$ since the pressure along z direction is controlled at zero during simulation and the lateral pressure $P_{x/y} \approx P_x \approx P_y$. Therefore, the lateral stress of 3.55 GPa as listed in Table 3 due to 2% strain results in 2.37 GPa of pressure in Figure 35b. The generation of dislocations and stacking faults begins at the crystal-liquid interface at around 300 ps, which propagates deep into the crystal and can relax the lateral stress. To obtain a reliable result of vacancy concentration generated under certain lateral stress, the structural analysis is only performed for this system at 200 ps, before the onset of generation of dislocations and stacking faults. The small size of solidified region for analysis substantially increases the standard deviation of vacancy concentration, and the results for ~0.72-0.74 T_m at 2% strain are not shown in Figure 35a due to the statistical inaccuracy. However, the positive correlation between the lateral stress and vacancy concentration is obvious, and the suppression of vacancy generation in the Ni-based alloys compared with pure Ni under the same undercooling and lateral stress is demonstrated.

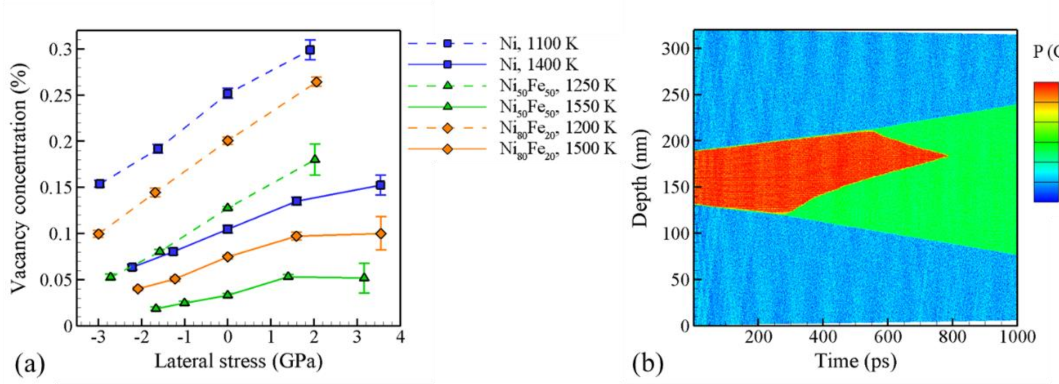

Figure 35. (a) Vacancy concentration predicted from MD simulations of solidification under conditions of fixed undercooling level and latera stress. Blue squares, green triangles, and yellow diamonds are obtained for Ni, $Ni_{50}Fe_{50}$, and $Ni_{80}Fe_{20}$ systems, respectively. Dashed lines correspond to the undercooling level of ~0.72-0.74 T_m, while solid lines correspond to the undercooling level of 0.92 T_m. Parameters of the simulations are summarized in detail in Table 3. (b) Contour plots of the spatial and temporal evolution of pressure in the $Ni_{80}Fe_{20}$ target at 0.92 T_m and 2% lateral compressive strain. The blue regions correspond to liquid, the red region corresponds to crystal under 2% lateral compressive strain, and the green region corresponds to crystal with relaxed lateral stress due to the emission of dislocations and formation of stacking faults.

Finally, the deviation from the chemical disorder around the individual vacancies observed for the Ni-Fe alloy targets in the TTM-MD simulations, Figures 36a and b, is confirmed in the MD simulations of solidification occurring under conditions of fixed undercooling. The analysis of the first atomic shells surrounding the vacancy sites in the alloy systems reveals the preference for vacancy sites to be surrounded by Fe atoms in the $Ni_{50}Fe_{50}$ and $Ni_{80}Fe_{20}$ systems, as reflected in the pronounced shift of the distributions calculated in MD simulations to the left with respect to the binomial distributions given by Eq. (4.1), Figures 36a and b. The appearance of atomic-scale chemical heterogeneities in the immediate vicinity of the vacancy sites is also apparent from the average numbers of Ni atoms present in the first neighbor shells of the vacancies listed in Table 5. The number of Ni atoms is substantially reduced with respect to the values that correspond to the random mixing in the Ni-Fe alloy systems, 6 Ni neighbors for 50 at.% Ni and 9.6 Ni neighbors for 80 at.% Ni alloys. In contrast, the vacancy configurations do not exhibit any noticeable deviation from the random mixing of the two components in the $Ni_{80}Cr_{20}$ alloy, Figure 36c and Table 5. This observation is consistent with the results of the TTM-MD simulation of melting and resolidification of a Ni-Cr alloy target discussed in Section 4.2.4, Figure 30c. A detailed computational analysis of the energetics of different vacancy configuration is performed and will be discussed in Section 4.4 to explain the observed preferable composition of the first neighbor shell of a vacancy site.

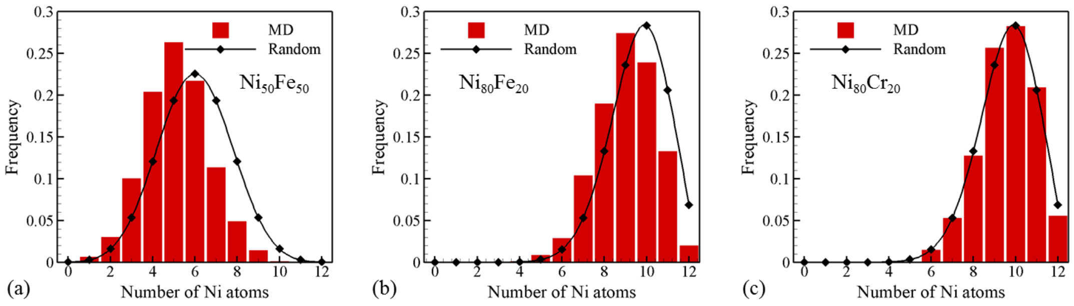

Figure 36. Distribution of the number of Ni atoms in the first nearest neighbor shell of individual vacancies generated in the MD simulations of solidification process proceeding at ~0.72-0.74 T_m and zero pressure in $Ni_{50}Fe_{50}$ (a), $Ni_{80}Fe_{20}$ (b), and $Ni_{80}Cr_{20}$ (c) systems. The black lines show the distributions expected for a random arrangement of atoms given by Eq. (4.1).

Table 5. Average number of Ni atoms in the first neighbor shells of individual vacancies expected for a random arrangement of atoms of different types in the alloys, predicted in the TTM-MD simulations of laser-induced melting and resolidification, and calculated in MD simulations of solidification performed at a fixed temperature of ~0.72-0.74 T_m.

	$Ni_{50}Fe_{50}$	$Ni_{80}Fe_{20}$	$Ni_{80}Cr_{20}$
Random	6.00	9.60	9.60
TTM-MD	5.25	9.06	9.59
MD	5.13	9.04	9.59

4.3.3 Processes responsible for the generation of vacancies in fcc Ni and bcc Cr systems

The previous section has demonstrated the generation of high density of vacancies at the rapidly advancing solidification front under fixed temperature and pressure conditions. In order to understand the key processes responsible for this phenomenon, as well as the factors that can affect the significance level of vacancies, detailed computational studies of vacancy formation at the solidification front are extended to fcc Ni that is described by different interatomic potentials and a bcc Cr system. MD simulations of well-controlled solidification of the Ni and Cr coexistence systems are performed at a series of undercooling levels ranging from 0.95 T_m to 0.1 T_m for Cr and from 0.95 T_m to 0.01 T_m for Ni, respectively, with the interatomic interactions described by Johnson EAM potential.[208] The simulations for the Ni system are performed by our collaborators, Dr. M. V. Shugaev and Dr. E. T. Karim from the group of Prof. L. V. Zhigilei. The dimension of the computational system of Cr in the lateral direction is 17 nm, and the lateral size of 28 nm is used for Ni system. Due to the onset of rapid homogeneous solidification at strong undercooling below ~0.65-0.7 T_m, as exemplified in the Section 4.3.2 for Ni-based solid-solution alloys and illustrated in Figure 31, that does not allow study of the heterogeneous propagation of solidification front, a series of simulations for the Ni system are performed with smaller lateral size, 5nm, to decrease the probability of solid seeds nucleation at the time scale of the simulation. The computational results of Ni system with 28 nm lateral size are only reported for simulations performed above 0.6 T_m. The solidification velocities are calculated by tracking the movement of the two crystal-liquid interfaces, and the concentration of vacancies is evaluated as the average fraction of unoccupied lattice sites on each crystalline plane. Figure 37 summaries the solidification velocity and concentration of vacancies generated in the solidified region as a function of undercooling level. As shown in Figures 37a and c, the solidification velocity and vacancy concentration are not sensitive to the choice of lateral dimensions. In both Ni and Cr systems, the dependence of the kinetics of the solidification front on temperature can be divided into two regimes. In the high temperature region extending from the melting temperature T_m to ~0.7 T_m for Ni and ~0.75 T_m for Cr, the solidification velocity increases with degrees of undercooling and reaches the maximum velocity of ~165 m/s at 0.7 T_m and ~140 m/s at 0.75 T_m in the Ni and Cr systems, respectively. At temperatures below the equilibrium melting point, T_m, the free energy of the solid phase is lower than that of the liquid, establishing a driving force for the transformation from liquid to solid. This thermodynamic driving force increases rapidly with undercooling levels, thus increasing the velocity of the solidification front. In the low temperature region, computational predictions of the dependence of solidification front velocity on the degree of undercooling reveal distinct trends between two metals. For bcc Cr, a decrease of the solidification velocity with increasing undercooling down to zero at ~0.1 T_m is observed. In contrast, a plateau where the solidification velocity remains between ~164-176 m/s is extended down to 0.05 T_m for fcc Ni, and eventually the velocity decreases from 167 m/s to 137 m/s with decreasing temperature from 0.05 T_m to 0.01 T_m. The different behaviors of solidification velocity in the low temperature regime between bcc and fcc metals are also observed in Ref. 223.

The kinetic description of the velocity of solidification front, on the atomic-level mechanisms, can be related to the difference between the rates of atomic migration from the liquid to the crystal and from the crystal to the liquid at the crystal-liquid interface. At high temperature, the Wilson-Frenkel expression is suggested to account for the effect of the thermodynamic driving force on the velocity of crystal growth:[99]

$$V(T) = V_0^h \exp\left(-\frac{E_a^h}{k_B T}\right)\left[1 - \exp\left(-\frac{\Delta G(T)}{k_B T}\right)\right], \tag{4.13}$$

essentially the same as the formula in Eq. (2.12). $\Delta G(T)$ is the difference in the free energies of solid and liquid phases depending on temperature, E_a^h is the activation energy associated with the mobility of atoms in liquid phase, k_B is the Boltzmann constant, and V_0^h is a constant that depends on the interatomic spacing, the frequency for the atomic vibrations, and the average thermal velocity of atoms in liquid. At moderate deviations from the equilibrium melting temperature T_m, $\Delta G(T)$ can be approximated as $\Delta G(T) \approx \Delta H_m(T_m - T)/T_m$, where ΔH_m is the latent heat of melting at T_m. In the low temperature regime, the kinetic processes at the solidification front are primarily limited by the atomic mobility in the liquid phase, leading to the formula associated with a simple Arrhenius temperature dependence:[223]

$$V(T) = V_0^l \exp\left(-\frac{E_a^l}{k_B T}\right). \tag{4.14}$$

The solidification velocities predicted from the MD simulations at temperatures in the range of $0.6\,T_m < T < T_m$ and $T < 0.6\,T_m$ are fitted to Eqs. (4.13) and (4.14), respectively, and the fitting parameters are listed in Table 6. As shown in Figures 37a and b, application of the two equations plotted by the solid and dashed red lines in the high and low temperature regimes, respectively, provides a good description of the temperature dependence of the velocity of solidification front for both Ni and Cr materials.

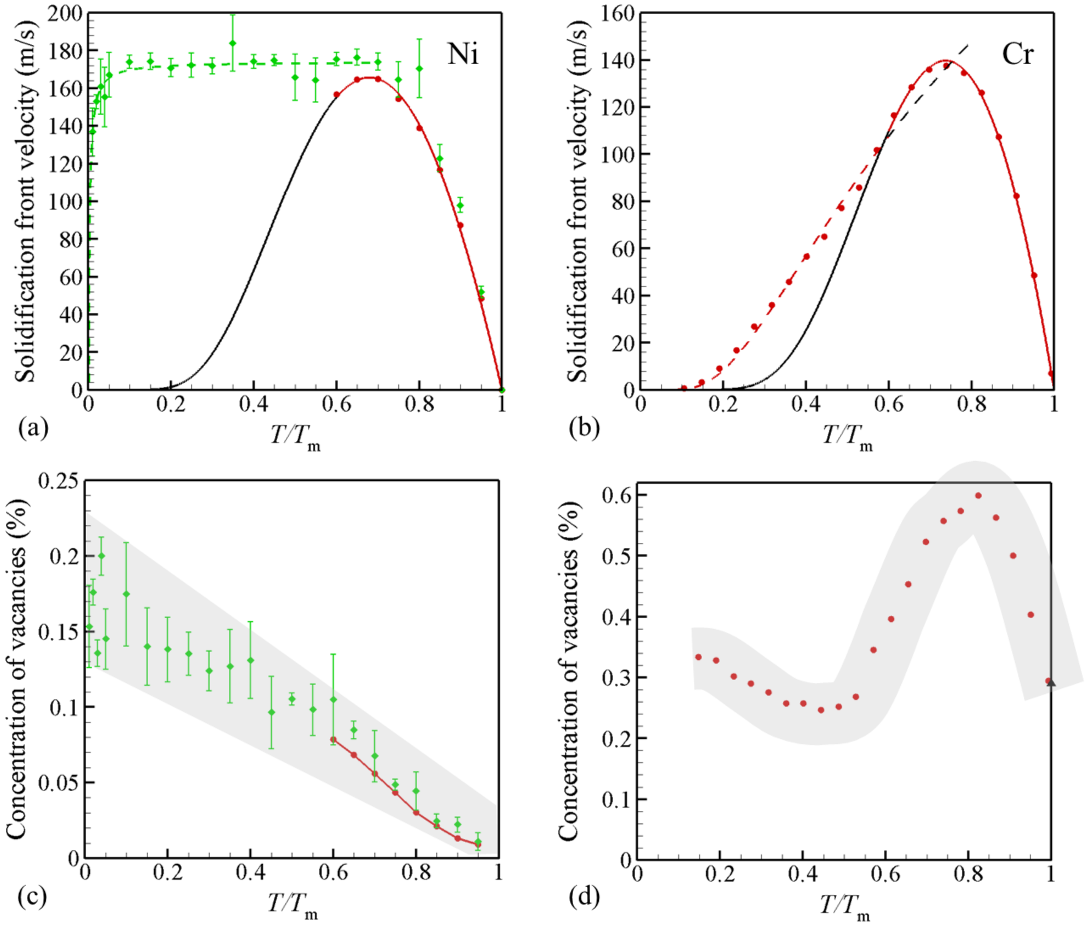

Figure 37. Velocities of solidification front and concentrations of vacancies in solidified parts of Ni (a,c) and Cr (b,d) systems predicted in MD simulations performed at different levels of

undercooling below the equilibrium melting temperature. Red circles represent the results predicted from the simulations performed for large-scale systems with lateral size of 28 nm for Ni and 17 nm for Cr, while green diamonds show results for small-scale Ni systems with lateral size of 5 nm. For small-scale simulations, the error bars represent the standard deviations obtained by rerunning simulations three times for the same undercooling, each starting at different initial conditions. For large-scale simulations, the error bars are comparable to the size of the symbol of each data point and are not shown. The solid and dashed lines in (a,b) show the predictions of Eqs. (4.13) and (4.14), respectively, with parameters provided in Table 6. The red parts of the curves correspond to the parts of the data sets where the equations provide a good description of the MD results, while the parts where the equations do not match the results of the simulations are colored black. The black triangle in (d) is the predicted equilibrium concentration of vacancies at T_m, $C_V^{eq}(T_m)$, as discussed in Section 4.3.1. The gray areas in (c,d) serve as guidance to the eye to depict the different dependences of vacancy concentration on undercooling for Ni and Cr, respectively. Data in (a,c) are obtained from MD simulations performed by Dr. M. V. Shugaev and Dr. E. T. Karim from the group of Prof. L. V. Zhigilei.

Table 6. The parameters in Eqs. (4.13) and (4.14) fitted to describe the dependence of velocity of solid-liquid interface on the level of undercooling in the high temperature region and low temperature region, respectively. The interatomic interactions in Ni and Cr systems are described by Johnson EAM potential.[208] The latent heat of melting calculated for this potential is 0.150 eV for Ni and 0.234 eV for Cr.

	V_0^h (m/s)	E_a^h (eV)	V_0^l (m/s)	E_a^l (eV)
Ni	3848	0.195	174	0.320×10^{-3}
Cr	9066	0.464	384	0.156

In the solidified region, large number of vacancies are observed and the dependences of vacancy concentration on the degree of undercooling for Cr and Ni are illustrated in Figures 37c and d. In the Cr system, the atomic percentage of vacancies increases with decreasing temperature from 0.29% near T_m to around 0.6% at 0.8 T_m followed by a rapid drop down to ~0.27% at around 0.53 T_m. Further increase of the level of undercooling leads to moderate rise of the vacancy to 0.33% at 0.15 T_m. Comparison of these values with $C_V^{eq}(T)$ presented in Figure 37 confirms that the rapid propagation of solidification front produces the vacancy density than can exceed the equilibrium value by orders of magnitude. Meanwhile, in the vicinity of the melting temperature, due to extremely small velocity of solidification front and high mobility of vacancies, the vacancy concentration is reduced towards the equilibrium value at melting temperature. In the Ni system, however, the vacancy concentration experiences a nearly monotonous increase from 9.05×10^{-3}% at 0.95 T_m to the maximum value of

~0.17% at 0.1 T_m. To provide a clear picture of the different trends in the relation between the concentration of vacancies and degree of undercooling predicted from the MD simulations of Ni and Cr systems, the data points in Figures 37c and d are visually guided by gray areas highlighting the general temperature dependence of vacancy concentrations.

In order to understand the mechanism of vacancy generation and the correlation of vacancy concentration with the undercooling level and solidification velocity, the atomic rearrangements at the propagating solidification front are investigated in detail. Figure 38 is prepared by our collaborator, Dr. E. T. Karim from the group of Prof. L. V. Zhigilei, and illustrates the atomic configurations at the solid-liquid interface obtained from atomistic simulations of Cr coexistence system described by Johnson EAM potential[208] at constant temperature 0.5 T_m. The system is divided into layers parallel to the lateral directions, so that each layer in the solid part corresponds to one crystal atomic plane, and the atoms are colored according to the identification number of the atomic planes they are associated with. The system is quenched to 0 K to reduce the thermal noise in the atomic configurations. Figure 38a represents a side view of the region of solid-liquid interface along [010] direction at the time of 102 ps, and Figure 38b tracks the atomic movements in four interfacial planes during the following 9.5 ps until they are solidified in bcc crystal structure. The atoms that came from or are going to move to another plane are marked by circular ribbons and ribbons with crosses, respectively, colored according to the plane of origin or the new atomic plane. For example, from 102 ps to 104 ps, 8 atoms originally from plane 240 jumped to plane 239 to occupy the lattice sites. At 102 ps, these atoms in plane 240 are labeled by ribbons with crosses in green color that is associated with their new position, plane 239; and at 104 ps, the same atoms moved to plane 239 are encircled by yellow ribbons denoting their origin from plane 240.

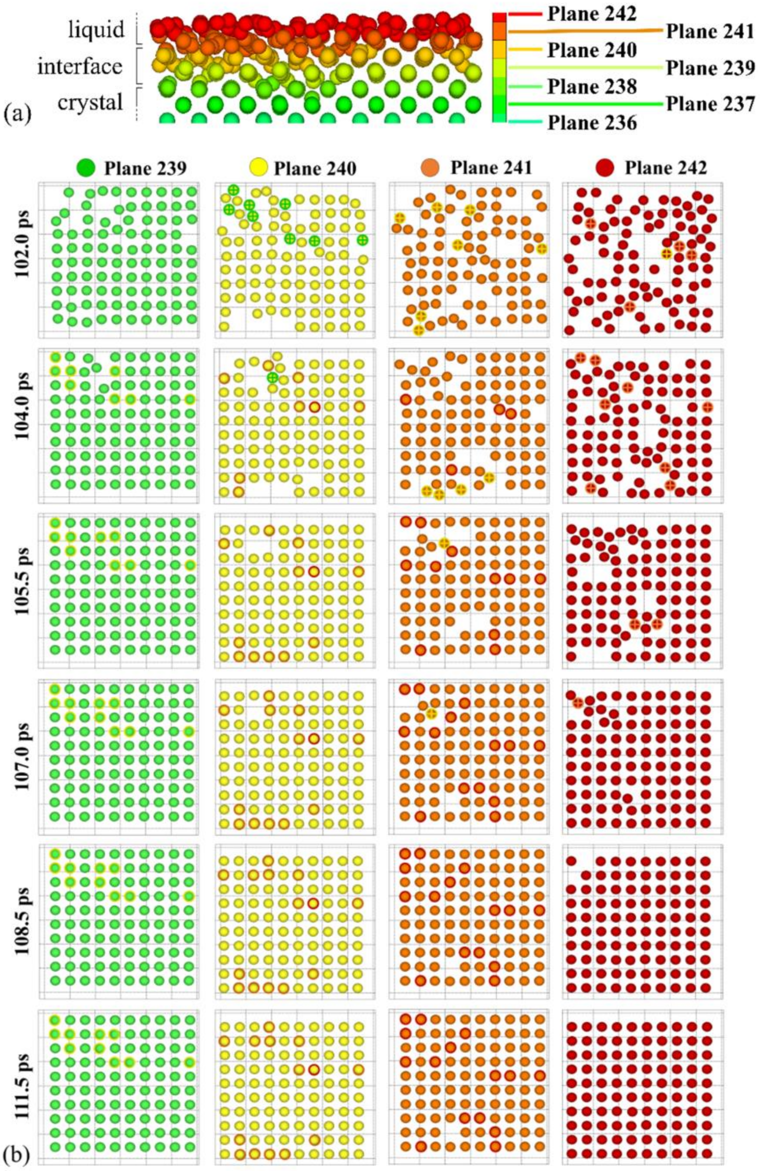

Figure 38. Close up view of four atomic planes that, at a time of 102 ps, include liquid-like plane 242, interfacial region (planes 241 and 240), and largely crystalline plane 239 in a simulation performed for Cr with Johnson EAM potential at $T = 0.50T_m$. The side view of the planes is shown for 102 ps in (a). The atoms are colored according to the atomic planes they are associated with. The atoms with circular ribbons are the ones that came from a different plane during the time span illustrated in the figure, and the color of the ribbons corresponds to their plane of origin. The atoms marked by circular ribbons with crosses are the ones that are going to move to another atomic plane at the next moment of time shown in the figure, and the color of the ribbons and crosses represents the color of their new atomic plane. The atomic configuration is quenched to 0 K in order to reduce the thermal noise in atomic positions. The results are provided by Dr. E. T. Karim from the group of Prof. L. V. Zhigilei.

Figure 38b provides a detailed picture of atomic rearrangements during the process of solidification and reveals the mechanisms of generation of vacancies. At time 102 ps, plane 239 has almost crystalline structure, plane 242 corresponds to the liquid phase, while planes 240 and 241 are associated with interfacial region. During the following 9.5 ps, crystal structure in the interfacial region is gradually built up through atomic jumps from liquid to the lattice sites, which is stabilized by the thermodynamic driving force for crystallization, resulting in the movement of the solid-liquid interface in the course of solidification. Since the liquid phase of metals has lower density and more “open” structure than solid, a large number of vacant sites are formed at the advancing solidification front, which can be filled by atoms jumping from upper planes with higher index in the direction opposite to the crystal growth. This scenario is opposite to the case in silicon system as discussed in Section 3.2.3, where larger number of interstitials than vacancies are observed at small undercooling levels, due to a larger density of Si liquid than solid. After passed by the solidification front, the remaining vacant sites become vacancies trapped in the solidified region. For example, at the time of 102 ps, plane 240 includes 97 atoms, corresponding to 3 vacancies. During the following 2 ps, the atoms in plane 240 rearrange themselves forming crystal structure; meanwhile, 8 atoms marked by green ribbons with cross jump to plane 239; 7 atoms from plane 241 and 1 atom from plane 242 diffuse from the liquid side of the interface to plane 240, as denoted as atoms with orange and red ribbons at the time of 104 ps. During the period between 104 ps and 105.5 ps, 1 atoms in plane 240 move to plane 239 and the vacancy sites in plane 240 are occupied by 4 atoms jumping from plane 241. As a result, from 102 ps to 105.5 ps, a total number of 9 atoms in plane 240 diffuse to plane 239, together with 2 atoms diffusing from plane 240 to plane 238 (not shown here), and 12 atoms are moved from plane 241 to plane 240, leading to the annihilation of one vacancy site. The remaining two vacancies in plane 240 are consequently occupied by atoms from plane 241 within the time span between 105.5 ps and 108.5 ps, resulting in the formation of a perfect crystal plane.

This scenario of vacancy generation and annihilation is demonstrated from the correlation between concentration of vacancies and solidification front in Figure 37. Based on the atomic-level analysis of solidification process, we hypothesize that the movement of the crystal-liquid interface is controlled by the rearrangement of the atoms from the liquid to solid phases where the liquid part acts as the source and sink for the defects.[225] At high temperature for both Cr and Ni systems the velocity of solidification is low that enables sufficient time for atomic rearrangement at the crystal-liquid interface and allows atoms occupying the correct lattice sites and vacancies diffusing to the liquid, leading to reduction of vacancy concentrations. Meanwhile, in the undercooling range where solidification velocity remains around a high constant level in Ni, the plateau in Figure 37a, the increase of vacancy concentration trapped by solidification front with increasing undercooling is explained by the drop of atomic mobility that suppresses the escape of vacancies to the liquid. The combined effect of the velocity of solidification front and vacancy mobility on the vacancy concentration also well explain the suppression of vacancy generation in the Ni-based alloys compared to pure Ni, as discussed in Section 4.3.2.

The sensitivity of the temperature dependence of solidification velocity and its correlation with vacancy generation to the choice of interatomic interaction potentials are tested through MD simulations of solidification under well-controlled conditions for Ni, performed with the FBD,[221] Mishin,[207] and Bonny[201] EAM potentials. As shown in Figure 39, where the concentrations of vacancies generated in the solidified region as a function of undercooling predicted from different EAM potentials are compared, the vacancy concentration predicted from FBD EAM potential has a good agreement with the result obtained from Mishin EAM potential, while the Bonny EAM potential predicts higher concentration of vacancy, reaching more than 0.3% at 0.7 T_m. Note that the vacancy concentration in Figures 37, 39 and 40 are calculated based on the average number of missing atoms in the solidified region, accounting for not only single vacancies and di-vacancies but also larger vacancy clusters. Due to the existence of vacancy clusters, *e.g.*, Figure 28, the vacancy concentration computed for Bonny EAM potential in Figure 39 is larger than the values shown in Figure 34c, especially at strong undercooling. For Mishin EAM potential, the vacancy concentration close to the melting temperature approaches to the level of $C_V^{eq}(T_m) =$ 0.031% calculated in

Section 4.3.1. The lowest level of vacancy concentration is observed in the simulation performed with Johnson EAM potential, showing that the vacancy concentration is less than 0.08% in the temperature range from 0.65 T_m to the melting temperature. The different concentrations of vacancies may be attributed to the difference in vacancy formation energy predicted as 1.63 eV,[221] 1.57 eV[207], 1.70 eV[226], and 1.48 eV from FBD, Mishin, Johnson, and Bonny EAM potential, respectively, where smaller formation energy provides lower barrier for generation of vacancies thus leading to higher vacancy density. In addition, the difference in the melting temperature predicted from different potentials, which results in different actual temperature conditions during solidification even at the identical nominal undercooling level, may also affect the concentration of vacancies. Despite of the quantitative difference in vacancy concentration, a common trend is observed for all four potentials that the density of vacancies increases gradually with the degree of undercooling, thus demonstrating a general picture of the generation of vacancies depending on temperature regardless of the choice of the interatomic interaction for the same material.

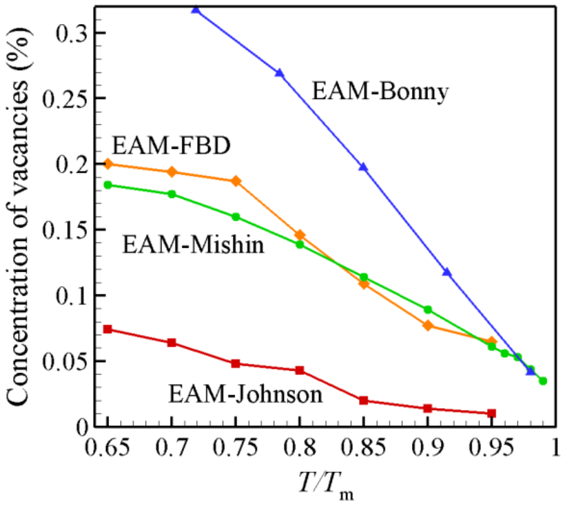

Figure 39. Concentration of vacancies generated during solidification as a function of the undercooling level predicted in MD simulations for crystal-liquid coexistence systems of Ni described by different EAM potentials developed by Johnson,[208] Foiles-Baskes-Daw,[221] Mishin,[207] and Bonny[202]. The simulations for Johnson and FBD potential are performed by Dr. E. T. Karim, the simulations for Mishin potential are performed by Dr. M. V. Shugaev, from the group of Prof. L. V. Zhigilei. The data for Bonny potential is adapted from Figure 34c and vacancy clusters are counted.

The generation of vacancies during solidification is also investigated for different crystallographic orientations of in the Cr solid-liquid coexistence systems. MD simulations are performed for three, (001), (011), and (111), low index orientations of the solid-liquid interface under controlled undercooling above the threshold of homogeneous crystallization, and the temperature dependences of vacancy concentration and solidification velocity are shown in Figure 40. At temperature above 0.85 T_m, the vacancy concentrations are similar for all three interface orientations and increase with undercooling level. At temperature below 0.85 T_m, vacancy concentration generated at the (001) interface during solidification is less than that generated at the (011) and (111) oriented interfaces. As shown in Figure 40b, the solidification front with (001) orientation moves faster than the interfaces with (011) and (111) orientations, but has the maximum velocity only up to 17% higher than the values for the other two orientations. The values of vacancy concentration and solidification velocity at different conditions of temperature and interface orientation are summarized in Table 7. The velocities of solidification front depending on temperature are fitted by Eq. (4.13), with the fitting parameters summarized in Table 8.

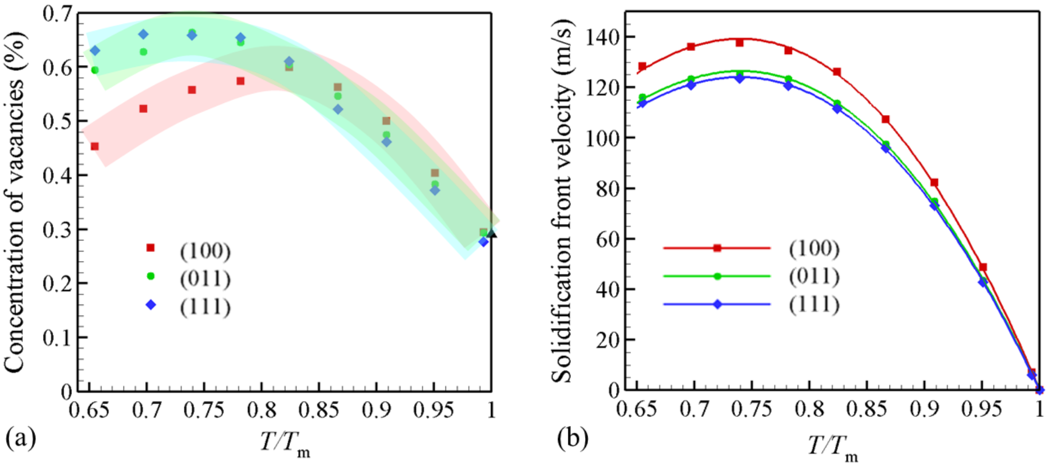

Figure 40. (a) The concentration of vacancies generated during resolidification and (b) corresponding velocity of the solid-liquid interface predicted by MD simulations of Cr system described by Johnson interatomic potential[208] at different levels of undercooling. The velocities are fitted to Eq. (4.13). Three low-index (001), (011), and (111) orientations of the solid-liquid interface are considered. The data presented in (a) and parameters of fitted curves in (b) are summarized in Tables 7 and 8.

Table 7. The velocity of solid-liquid interface and the concentration of vacancies produced in a series of atomistic coexistence simulations of Cr system with (001), (011), and (111) crystallographic orientations of solidification front at different level of undercooling. The interatomic interactions are described by Johnson EAM potential.[208]

	T/T_m	0.99	0.95	0.91	0.87	0.82	0.78	0.74	0.7	0.65
(001)	V (m/s)	7	48.7	82.4	107.3	126.2	134.5	137.6	136	128.5
	C_V (%)	0.294	0.404	0.5	0.563	0.599	0.574	0.558	0.523	0.453
(011)	V (m/s)	6.2	43.5	75	97.6	113.6	123.4	125.4	123.4	116.1
	C_V (%)	0.293	0.384	0.475	0.546	0.605	0.645	0.664	0.628	0.594
(111)	V (m/s)	6	42.8	73	95.8	111.5	120.7	123.5	120.9	113.9
	C_V (%)	0.277	0.372	0.461	0.522	0.611	0.654	0.658	0.661	0.63

Table 8. The parameters of Eq. (4.13) fitted to describe the dependence of velocity of solid-liquid interface on the level of undercooling in the Cr system with (001), (011), and (111) crystallographic orientations of solidification front. The interatomic interactions are described by Johnson EAM potential,[208] which predicts the heat of fusion as 0.234 eV.

	(001)	(011)	(111)
V_0^h (m/s)	9438	8604	8381
E_a^h (eV)	0.470	0.471	0.470

4.3.4 Summary

On the basis of the results of MD simulations of solidification occurring at fixed levels of undercooling and in the absence of mechanical stresses performed for bcc Cr, fcc Ni and Ni-based solid-solution alloys, the mechanisms responsible for the generation of supersaturated vacancies at the propagating solidification front are revealed and strongly correlated with the temperature dependence of the velocity of the solidification front and vacancy mobility. The vacancies are generated as “errors” in the process of building the crystal structure at the solidification front, and the sharp drop in mobility of the vacancies and the increase in the solidification front velocity with increasing undercooling diminish the chances for the vacancies to escape to the liquid phase.

Despite the qualitatively similar dependences on the levels of undercooling, the vacancy generation in the $Ni_{50}Fe_{50}$, $Ni_{80}Fe_{20}$, and $Ni_{80}Cr_{20}$ alloy systems is found to be strongly suppressed with respect to pure Ni. In particular, atomistic calculations of vacancy mobility show enhanced vacancy diffusion by adding Fe element in the Ni-Fe alloys, leading to higher chance for vacancies to escape to the liquid and less vacancies left in the solid. The reduced concentration of vacancies in the $Ni_{80}Cr_{20}$ alloy compared to Ni is interpreted as a result of combined effect of higher vacancy mobility as well as lower solidification velocity, the latter leads to diminished vacancy trapping behind the advancing solidification front. The effect of lateral stress on the generation of vacancies is also studied in the MD simulations of solidification of crystal-liquid coexistence systems under controlled conditions. Lateral compression results in increased concentration of vacancies compared to the value corresponding to zero pressure, which explains the high vacancy density observed in the laser-irradiated alloy targets with residual lateral stress discussed in Section 4.2.3. Under the same condition of undercooling and lateral stress, the strong suppression of vacancy concentration in the Ni-base solid-solution alloys compared to pure Ni is demonstrated.

Comprehensive studies of solidification for bcc Cr and fcc Ni systems fixed at a broad range of undercooling levels reveal a general picture of the rapid propagation of solidification front and formation of vacancies. The dependence of solidification velocity on the levels of undercooling can be divided into two regimes. In high temperature regime, the velocity of crystal-liquid interface increases with the degree of undercooling, which is attributed to the increased driving force of phase transformation from liquid to crystal. In low temperature regime, the exponential decrease of atomic mobility with increasing undercooling level prevails the increase of the thermodynamic driving force and leads to monotonous decrease of solidification velocity in Cr as well as formation of a plateau of the solidification velocity in Ni. Detailed analysis of the generation of vacancy in the crystal-liquid interface region with atomic resolution supports the hypothesis that the vacancies are generated at the advancing solidification front as “errors” in the process of building the crystal structure, which are either occupied by atoms jumping from the liquid or finally trapped after passed by the solidification front. MD simulations performed for Ni with different EAM potentials indicate that the choice of interatomic interaction potentials may affect the values of vacancy concentration but does not change its general dependence on temperature, which is determined by the combined effects of temperature dependence of solidification velocity and atomic mobility. The effect of crystallographic orientations is also investigated for Cr as an example, showing a higher velocity of the solidification front with (001) orientation than the values computed for (011) and (111) oriented solidification fronts.

The combination of the TTM-MD simulations of laser-induced melting and resolidification (Section 4.2.3) with MD modeling of solidification occurring under well-controlled temperature and pressure conditions has provided important insights into the mechanisms of the generation of vacancies under conditions of strong thermal and mechanical nonequilibrium induced by a rapid energy deposition. For Ni and Ni-based alloys, the solidification velocity and vacancy concentration predicted from MD simulations have good agreement with the values calculated from TTM-MD simulations of laser-induced melting and resolidification in Section 4.2.3, suggesting the vacancy formation at the solidification front as the primary source of vacancies induced by laser irradiation.

4.4 Evolution of the first neighbor configuration of vacancies in Ni-base alloys

In Section 4.2.4 and Section 4.3.2, analysis of the configuration of the first neighbor shell surrounding the individual vacancies in Ni-based alloy systems reveals the preference of a Fe-rich local environment for vacancies, indicated by a shift of the distribution of the first neighbor shell composition to lower number of Ni atoms with respect to the distribution expected for random atomic arrangements in the disordered alloys, Figures 30 and 36. To fully understand the preferential vacancy configuration with Fe-rich first neighbor shells, a set of MD simulations are performed to investigate the formation energy and dynamic evolution of vacancies for $Ni_{50}Fe_{50}$, $Ni_{80}Fe_{20}$, and $Ni_{80}Cr_{20}$ systems. The computational setup and methods to calculate the vacancy formation energy are described in Section 4.4.1. The results from the MD simulations and the reasons explaining different neighboring chemical environment of vacancies in each alloy are discussed in Section 4.4.2. The main conclusions are summarized in Section 4.4.3.

4.4.1 Computational setup and methods

The vacancy formation energy is calculated through MD simulations of $Ni_{50}Fe_{50}$, $Ni_{80}Fe_{20}$, and $Ni_{80}Cr_{20}$ systems with Bonny EAM interatomic interactive potential.[201] Cubic systems with $10 \times 10 \times 10$ fcc unit cells pre-incorporated with one vacancy site at the center of the system, similar to the systems of calculation of vacancy mobility as described in Section 4.3.1, are created for each of the Ni-based solid-solution alloy. The lattice parameter equaling to the equilibrium value at 0 K and zero pressure is used for each system, and periodic boundary conditions are applied in all three directions.

To investigate the dependence of the formation energy of a vacancy on its first atomic shell, the atomic types of the 12 nearest neighbors surrounding the vacancy site are artificially switched to generate $2^{12} = 4096$ different configurations for the binary solid-solution alloys. For each first neighbor configuration, the system with one pre-incorporated vacancy is quenched at zero temperature for 1 ps and its internal energy is calculated as E_V. In the second step, vacancy site is occupied by a Ni atom while its first neighbor shell is fixed, generating a perfect crystal, and the quenching process is repeated to get the internal energy of the perfect system, E_{Ni}. The same procedure is then applied to get the internal energy associated with occupying the vacancy site with a Fe atom in the Ni-Fe alloys, E_{Fe}, or with a Cr atom in the Ni-Cr alloy, E_{Cr}. The internal energies, E_V, E_{Ni}, and E_{Fe} (E_{Cr}) are calculated for all 4096 first neighbor configurations. To obtain statistically reliable result, the simulations are performed for 20 independent systems with the same atomic composition but different initial random assignments of atomic types on the lattice sites. The atomic energy of each type of atoms E_a^X, where X can be Ni, Fe, and Cr, is calculated for perfect systems with ideal stoichiometric ratio and the results are averaged over 20 systems with different atomic arrangements. As a result, the formation energy of the vacancy associated with a missing X-type atom can be calculated as $E_f^X = E_V - E_X + E_a^X$.

The evolution of vacancy configurations is investigated through MD simulations of vacancy diffusion under controlled conditions of constant temperature and zero pressure. A $50\,nm \times 50\,nm \times 50\,nm$ large cubic system is generated for each binary solid-solution alloy. At the center of each $5\,nm \times 5\,nm \times 5\,nm$ sub-system, one lattice site is pre-defined as vacancy, generating $10 \times 10 \times 10 = 1000$ uniformly distributed vacancies in each system. The 5 nm space between two neighboring vacancies is chosen to avoid interaction between vacancies during simulation. The system is consisting of 13.499 million atoms which are assigned on the remaining lattice sites based on the atomic composition. MD simulations are performed for 400 ps at constant temperature of 1250 K, 1200 K, and 1100 K for $Ni_{50}Fe_{50}$, $Ni_{80}Fe_{20}$, and $Ni_{80}Cr_{20}$ systems (~0.72-0.74 T_m), respectively, and the configuration of each vacancy is analyzed by counting the number of different type of atoms in the first nearest neighbor shell. Periodic boundary conditions are applied along all three dimensions, and the size of the system is chosen as the values associated with a crystal equilibrated at the corresponding temperature and zero pressure.

4.4.2 Deviation of vacancy configuration from chemical disordering to energetic favorable local environment

The vacancy formation energy has been calculated in Ref. 190 and shown to be strongly dependent on vacancy configurations. To eliminate the effects of chemical environment outside the first neighbor shell, the formation energy in this work is calculated for each atomic arrangement in the first neighbor shell while fixing the type of atoms outside the first neighbor shell. Figure 41 shows the effect of number of Ni atoms in the first neighbor shell on the formation energy of Ni and Fe/Cr type vacancy averaged over 20 systems with different random atomic arrangements for each alloy, with the error bar showing the standard deviation of the mean value. Each data point in Figure 41 corresponds to one vacancy configuration. As shown in Figures 41a and b, the formation energies for both Ni and Fe type vacancies increase with the number of Ni atoms in the first neighbor shell surrounding the vacancy site, suggesting less energetically favorable configurations with more Ni atoms in the Ni-Fe alloys. However, a contrary trend is observed in the $Ni_{80}Cr_{20}$ alloy, Figure 41c, where the vacancy formation energies almost decrease with increasing Ni richness in the first neighbor shell of the vacancy site. The dependence of formation energy on the number of Ni atoms in the first neighbor shell is less significant in the $Ni_{80}Cr_{20}$ system than in the $Ni_{50}Fe_{50}$ and $Ni_{80}Fe_{20}$ systems. For example, the formation energy of Ni-type vacancy only decreases by 0.13 eV with the number of Ni atoms in the first neighbor shell increasing from 0 to 12, while an increase of 0.34-0.35 eV is observed in the Ni-Fe systems. In addition, the large spread of formation energy of vacancies with the same number of Ni atoms in the first neighbor shell in $Ni_{80}Cr_{20}$ system suggests that the formation energy is sensitive to the specific first neighbor atomic arrangements.

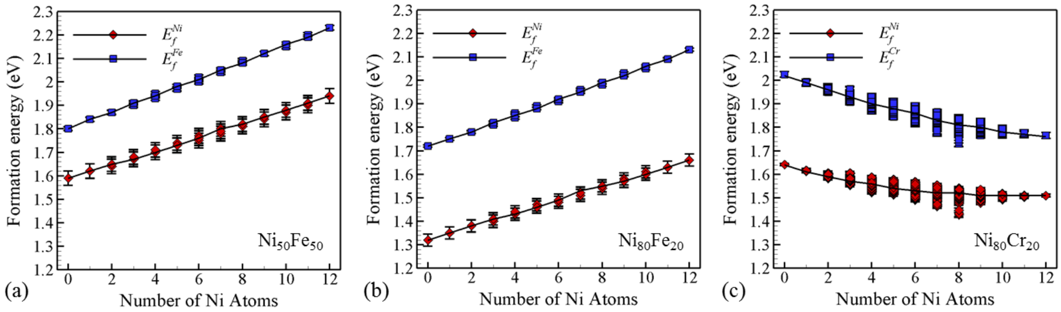

Figure 41. Formation energy of individual vacancies with different configurations in $Ni_{50}Fe_{50}$ (a), $Ni_{80}Fe_{20}$ (b), and $Ni_{80}Cr_{20}$ (c) systems. Red diamonds show the formation energy of vacancies with a missing Ni atom, and blue squares show the formation energy of vacancies with a missing Fe atom in (a) and (b) and with a missing Cr atom in (c). Each data point represents one certain arrangement of atoms in the first neighbor shell surrounding the individual vacancy site, and is plotted according to the number of Ni atoms in the first neighbor shell. The solid lines depict the formation energy averaged over all first neighbor configurations with the same number of Ni atoms. The error bars show the standard deviation of the mean calculated based on 20 simulations with different random atomic arrangements.

Based on the values of vacancy formation energy for different first neighbor configurations, the probability of having k Ni atoms among the 12 atoms constituting the first neighbor shell of a vacancy site, F_k, can be given by the following equation:

$$F_k = \frac{p^k \cdot (1-p)^{12-k} f_k}{\sum_{i=1}^{12} p^i \cdot (1-p)^{12-i} f_i}, \tag{4.15}$$

where

$$f_k = \sum_{j=1}^{n_k} \left[p \cdot \exp\left(\frac{-E_f^A(k,j)}{k_B T}\right) + (1-p) \cdot \exp\left(\frac{-E_f^B(k,j)}{k_B T}\right) \right]. \tag{4.16}$$

Here, A and B indicate two types of atoms in the binary alloy system, in this work, A is Ni while B is Fe in Ni-Fe systems and Cr in Ni-Cr system, and p is the probability of a lattice site to be occupied by A atom. $E_f^A(k,j)$ and $E_f^B(k,j)$ are the formation energies of vacancies corresponding to one missed A and one missed B atom at the vacancy site, respectively. k is the number of A atoms in the first neighbor shell of the vacancy site, and j indicates different arrangement of atoms in the first neighbor shell with fixed k. The value of j ranges from 1 to $n_k = \frac{12!}{k!(12-k)!}$, the total number of first atomic configurations with k atoms of type A and $(12-k)$ atoms of type B. Therefore, the numerator in Eq. (4.15) is the probability of finding k number of type A atoms within the 12 nearest neighbors of a vacancy site weighted by the formation energy, and the brackets in Eq. (4.16) can be regarded as the contribution to the energetic weight from configuration (k,j). If the vacancy formation energy is a constant $E_f^0 = E_f^X(i,j)$, where $X \in (A,B)$, $1 \le i \le 12$, and $1 \le j \le n_i$, Eq. (4.15) can be rewritten as

$$F_k = \frac{p^k \cdot (1-p)^{12-k} n_k \exp\left(-E_f^0/k_B T\right)}{\sum_{i=1}^{12} p^i \cdot (1-p)^{12-i} n_i \exp\left(-E_f^0/k_B T\right)} = n_k \cdot p^k \cdot (1-p)^{12-k}, \tag{4.17}$$

which is essentially the distribution expected for the random arrangement of atoms in disordered binary alloys, Eq. (4.1) in Section 4.2.4.

The distribution of number of Ni atoms in the first neighbor shell predicted from Eqs. (4.15) and (4.16) at ~0.72-0.74 T_m are shown as the red bars in Figure 42, compared with the results of MD simulation of solidification under controlled conditions at the same undercooling levels and zero pressure obtained from Figure 36 in Section 4.3.2, which are depicted by blue circles. The black lines are distributions predicted from Eq. (4.17) assuming no energetically favorable configuration exist. For vacancies generated at propagating solidification front predicted from MD simulations, the blue circles, a shift of the distribution to lower number of Ni atoms in the first neighbor shell with respect to the black lines is found in $Ni_{50}Fe_{50}$ and $Ni_{80}Fe_{20}$ alloys, Figures 42a and b. The results from MD simulations coincide with the histograms predicted from Eqs. (4.15) and (4.16), and can be explained by the energetic preference of vacancies to be surrounded by a Fe-rich environment, which is demonstrated by the decreasing formation energy of vacancies with less Ni atoms in the first neighbor shell, Figures 41a and b. However, the effect of atomic composition in the first neighbor shell of vacancy site is less noticeable in Ni$_{80}$Cr$_{20}$ alloy, Figure 41c, and the formation energy is strongly depending on how atoms are arranged with respect to each other. Therefore, Eqs. (4.15) and (4.16) predict no shift in the configuration of vacancies as expected from random mixing of Ni and Cr atoms in the Ni$_{80}$Cr$_{20}$ system, Figure 42c, which agrees well with the results from MD simulations. The deviation of local composition in the first neighbor shell of individual vacancies from the configuration expected for random arrangement of atoms in Ni-Fe alloys, where the number of Ni atoms in the first neighbor shell shifts towards lower value, is also confirmed in the results of TTM-MD simulations of laser-induced generation of vacancies, Figure 30 in Section 4.2.4.

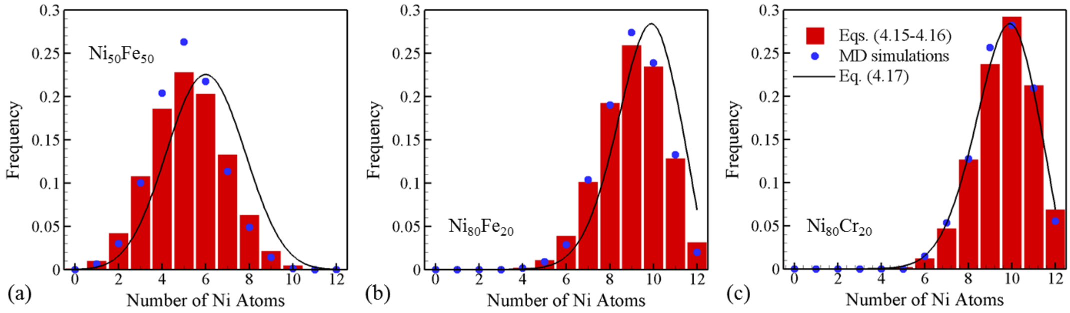

Figure 42. Distribution of the number of Ni atoms in the first neighbor shell of individual vacancies for Ni$_{50}$Fe$_{50}$ (a), Ni$_{80}$Fe$_{20}$ (b), and Ni$_{80}$Cr$_{20}$ (c) systems. Red bars are predicted distribution based on Eqs. (4.15) and (4.16) at ~0.72-0.74 T_m, blue circles are results from MD simulations of solidification process proceeded at the same undercooling and pressure conditions reported in Section 4.3.2. The black lines show the distributions expected for a random arrangement of atoms and given by Eq. (4.17)/Eq. (4.1).

In the course of crystal growth of the disordered single phase solid-solution alloys, the vacancies generated behind the rapidly solidification front should initially have chemical environment associated with random atomic arrangements. To understand how the energetic favorable configurations are formed, MD simulations of $50\ nm \times 50\ nm \times 50\ nm$ large cubic system with 1000 incorporated vacancies, as described in Section 4.4.1, are performed for Ni$_{50}$Fe$_{50}$, Ni$_{80}$Fe$_{20}$, and Ni$_{80}$Cr$_{20}$ systems controlled at fixed temperature of ~0.72-0.74 T_m. Figure 43 shows the distribution of number of Ni atoms in the first neighbor shells of the 1000 individual vacancies at different time of simulation, compared to the histograms predicted from Eqs. (4.15)-(4.16) and shown in Figure 42, which are calculated at the same temperature as the MD simulations. At the beginning of simulation, as shown by blue triangles, the vacancy configuration is determined by chemical disordering in the alloys and predicts the most frequent first neighbor composition with 6 Ni atoms in $Ni_{50}Fe_{50}$ and 10 Ni atoms in $Ni_{80}Fe_{20}$ and $Ni_{80}Cr_{20}$ alloys, as predicted from the distribution corresponding to random atomic arrangement, Eq. (4.17). During 0 ps-200 ps, the distributions in Ni-Fe alloys evolve by decreasing the frequency of Ni-rich first neighbor shells and increasing the frequency of Fe-rich first neighbor shells, resulting a shape closer to the histogram. By 300 ps, the peak of the of the distribution already shifts from 6 to 5 Ni atoms in $Ni_{50}Fe_{50}$ system and from 10 to 9 Ni atoms in $Ni_{80}Fe_{20}$ system, indicating the transition of vacancy configurations towards energetically preferable Fe-rich first neighbor environment. At 400 ps, the distribution further coincides with the prediction from Eqs. (4.15)-(4.16). However, the pronounced evolution of vacancy configurations is not observed in the $Ni_{80}Cr_{20}$ system, in which the distribution remained as initial random distribution. From Figure 34b, the vacancy mobility at ~0.72-0.74 T_m is assessed as 1.39×10^{-6} cm^2/s for $Ni_{50}Fe_{50}$, 4.38×10^{-7} cm^2/s for $Ni_{80}Fe_{20}$, and 7.34×10^{-7} cm^2/s for $Ni_{80}Cr_{20}$, respectively, giving the diffusion length $L = \sqrt{6D_v t}$ around 0.29 nm, 0.16 nm, and 0.21 nm for every 100 ps. From Table 3, the equilibrium lattice parameter at corresponding temperature and zero pressure is around 3.54 Å, predicting 2-4 jumps for each vacancy during 400 ps.

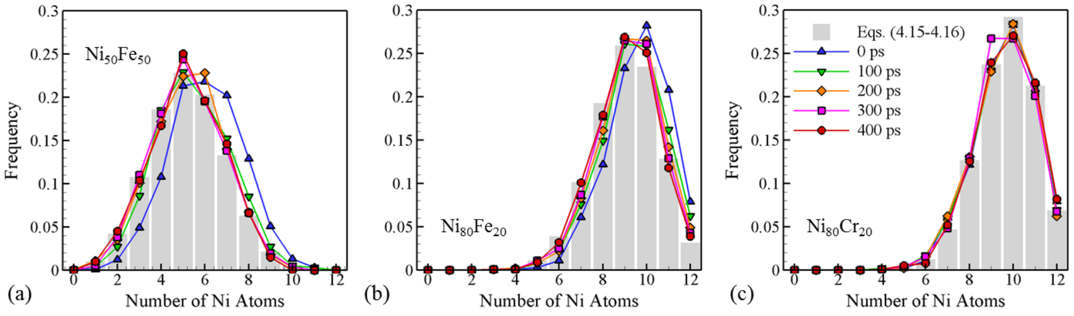

Figure 43. Evolution of distribution of the number of Ni atoms in the first nearest neighbor shell of individual vacancies for $Ni_{50}Fe_{50}$ (a), $Ni_{80}Fe_{20}$ (b), and $Ni_{80}Cr_{20}$ (c) systems. The results are predicted from MD simulations of disordered solid solution alloys with initially incorporated vacancies under conditions of fixed undercooling at ~0.72-0.74 T_m and zero pressure. Gray bars are predicted distributions based on Eqs. (4.15)-(4.16) at the same undercooling condition.

Figure 44 shows the evolution of vacancy configurations during the MD simulation by plotting the average number of Ni atoms in the first neighbor shell of the 1000 pre-incorporated individual vacancies. For $Ni_{50}Fe_{50}$ and $Ni_{80}Fe_{20}$ alloys, the composition of the immediate vicinity of vacancies decreases from the values expected for random atomic arrangements (6 for $Ni_{50}Fe_{50}$ and 9.6 for $Ni_{80}Fe_{20}$) towards a Fe-richer nearest neighboring environment during the first 200 ps, and converges to the levels predicted from Eqs. (4.15)-(4.16) shown by dashed lines by 400 ps. Since the most favorable vacancy configuration only requires the change of one Ni atom to Fe atom from the initial randomly arranged first neighbor shell, 2-4 jumps estimated for this time period is sufficient for vacancies to find the preferable local configuration. In contrast, the average number of Ni atoms in the first neighbor shell surrounding the vacancies does not exhibit the deviation from the level associated with random mixing of elements in the $Ni_{80}Cr_{20}$ disordered alloy.

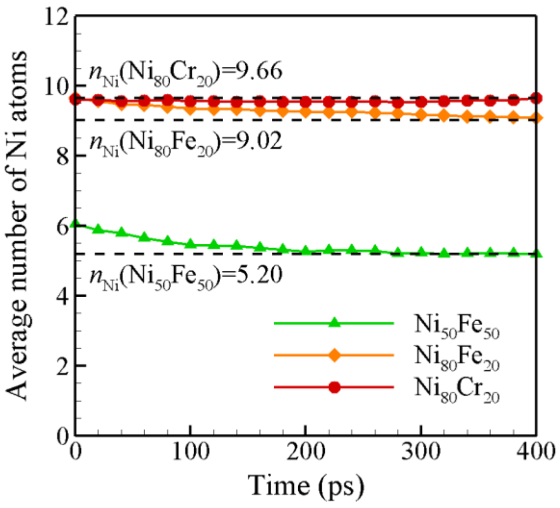

Figure 44. Evolution of average number of Ni atoms in the first neighbor shell of individual vacancies predicted from MD simulations of vacancy migration in $Ni_{50}Fe_{50}$, $Ni_{80}Fe_{20}$, and $Ni_{80}Cr_{20}$ alloys. The MD simulations are performed at a fixed temperature of ~0.72-0.74 T_m and zero pressure. The dashed lines show the expected value for distribution of vacancy configurations following Eqs. (4.15)-(4.16) at the same undercooling conditions.

4.4.3 Summary

In this section, the preference of vacancies for a Fe-rich local environment in the Ni-Fe disordered solid-solute alloys, predicted by both TTM-MD simulations of laser-induced melting and resolidification and MD simulations of solidification under well-controlled conditions, is demonstrated based on the theoretical analysis of the vacancy formation energy. MD calculations of the vacancy formation energy for each possible configuration of the first atomic shells reveal a pronounced energetic preference of vacancies to be surrounded by more Fe atoms. The distribution of number of Ni atoms in the nearest neighbor shell is predicted from theoretical equations of binomial distribution biased on vacancy formation energy, showing a shift towards lower number of Ni atoms with respect to the random distribution, which is consistent with the results from atomistic simulations. Even though addition of Fe significantly decreases the total vacancy concentration as compared to pure Ni, the atomic configurations with more Fe atoms surrounding the vacancy tend to be more stable. This observation is an example of how the crystal defects can produce atomic-scale chemical heterogeneities in the single phase concentrated solid-solution alloys. In the Ni-Cr alloy, however, the vacancy formation energy is not sensitive to the number of Ni atoms in the first neighbor shell, leading to a distribution of vacancy configuration similar to that expected for a completely random arrangement of atoms.

Large-scale MD simulations of vacancy migration performed at fixed undercooling conditions provide atomistic insights on the evolution of vacancy configuration. Despite of the immediate random chemical environment in the vicinity of the vacancies in the Ni-Fe alloys, either incorporated in a randomly arranged crystal system, or generated at the rapidly propagating solidification front, the following atomic jumps shift the vacancy environment towards the energetically favorable configurations with Fe-rich first neighbor shells within a few jumps.

5. Laser generation of microbumps on bilayer Ag-Cu thin films

5.1 Introduction

In previous sections, laser-induced phase and structural transformations are investigated in the regime of melting and resolidification. Laser irradiation at much higher fluence can trigger the onset of subsurface cavitation even material ejection, thus creating a wide variety of surface microstructure and morphologies, *i.e.*, random micro- and nanostructures,[13, 227, 228] subsurface voids and microcracks,[23,213, 229] and laser-induced periodic surface structures or “ripples”.[19,37,230-232] In addition, tightly-focused ultrafast laser interactions with metal films have been demonstrated to produce micro/nanobumps and frozen nanojets in a number of previous works.[233-240] By interference between multiple laser beams, the microbumps can be replicated into ordered arrays on the target surface, which bring unique properties to the material, such as superhydrophobicity[241,242], self-cleaning[243], enhanced tribological performance[244], and active and nonlinear optical response.[245]

While the ability of generating such micro/nanoscale surface features opens up a range of opportunities for practical applications, the processes responsible for the generation of microbumps are not yet fully understood. Possible mechanisms for the formation and rupturing of the microbumps are suggested as the Marangoni convection,[234,240] peeling and expansion of the film due to subsurface boiling and the vapor pressure released at the substrate-film interface,[233,236] as well as thermoelastic and plastic deformation of the film.[237,246] Due to the ultrafast, highly-nonequilibrium character of the laser-induced processes, the applicability of experiments or conventional hydrodynamic models on providing information for the material response to short pulse laser irradiation is limited. However, atomistic modeling provides attractive alternative opportunities to explore the formation of the frozen surface structures, without prior assumptions on the physical processes of interest. In particular, large-scale molecular dynamics simulations of thin Ni films irradiated by a single femtosecond pulse[20,247] have shown that the rapid localized laser heating and melting of the film takes place under partial inertial stress confinement,[10-12,27] leading to a buildup of compressive stresses. The relaxation of photomechanical stresses provides driving force of the initial upward acceleration of the melted film, which is followed by a delamination of the spalled layer from the substrate. Ejection of the spalled layer from the remaining target is elastically resisted from the colder parts of the film at periphery of the laser spot, leading to the eventual formation of a microbump.

Short pulse laser-induced generation of microbumps and nanojets have been widely investigated for Au,[47,48,234-237,240] Ag,[238,239,248] and Cu[239] films, even for silicon film irradiated by a nanosecond pulse,[249] and bulk glass targets covered by a polymer or water overlayer.[250,251] However, few works have been carried on the microbump formation on films composed of multi layers of different materials. The advantage of the multi-layered targets has been demonstrated in recent studies of the mechanisms of laser-induced ripple formation in a multi-pulse irradiation regime,[252] as well as nanostructuring by a single femtosecond X-ray vortex pulse.[253] Analysis of the elemental composition of the laser-processed surfaces and target cross-sections provides valuable information on the extent of melting and heat affected zones, and the results can be compared to the MD simulations. In this section, a combined experimental and computational study of the laser generation of microbumps is performed for the Ag-Cu bilayer films. The choice of the Ag-Cu system, a eutectic binary alloy with very limited solubility in the solid state, ensures that the observation of elemental mixing in the bumps would be an unequivocal indication of melting. An additional factor in choosing the Ag-Cu system is the large difference in the strength of the electron-phonon coupling factor between the two metals, allowing the exploration of the implications of the energy redistribution in the electronically excited state for the final morphology of the laser-generated surface structures.

5.2 Experimental observation of microbump formation on bilayer Ag-Cu thin films irradiated by femtosecond laser pulse

The experimental portion of this work is done by our collaborators from the group of Prof. W. Kautek. A detailed description of the experimental methods and results is given in Ref. 51, and here a brief summary of the results that are relevant to the discussion of computational results is provided. In experiments, Ag-Cu bilayer films are prepared by depositing a 50 nm-thick Ag film and a 50 nm-thick Cu film on a silica glass substrate, with either Ag on the top of Cu layer or Cu on the top of Ag layer. Laser pulses with a full width at half maximum duration of 60 fs at a central wavelength of 800 nm are irradiated on the bilayer film target under vacuum (10^{-2} mbar) environment, at fluences ranging from the level below the threshold of visible modification of the film to the value above complete breaching of the film. The modification and breaching thresholds are determined by optical microscopy, respectively, with the onset of irreversible morphological alteration without bump formation, and break of the bump and revealing of the underlying material. The threshold fluences of modification, bump formation, bump breaching, and jet formation for the Ag on Cu (Ag-Cu-SiO_2) and Cu on Ag (Cu-Ag-SiO_2) bilayer films are presented in Figure 45. The respective breached layer is denoted on the bump breaching data to indicate whether breaching took place in a mixed or in a single layer.

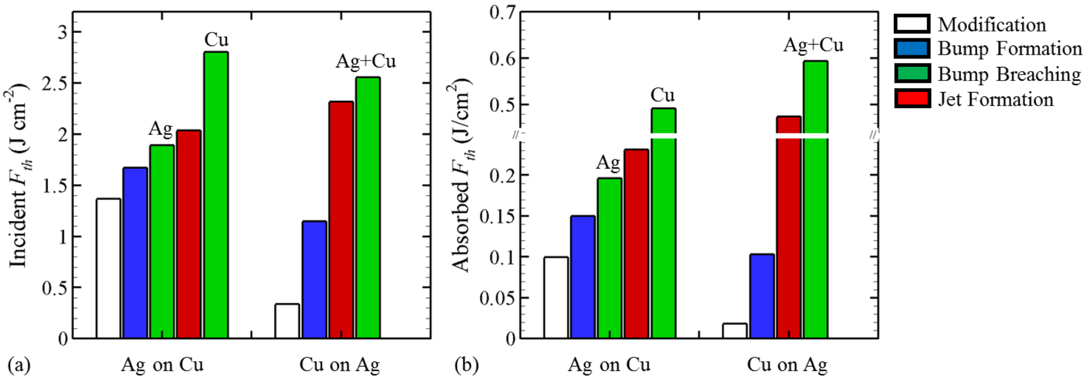

Figure 45. Threshold fluences for modification, bump formation, bump breaching, and jet formation observed in 60 fs laser irradiation of Ag-Cu bilayers. The breached layer is denoted on the corresponding column. The results are shown in terms of incident fluence (a) and absorbed fluence (b) calculated from the incident fluence by conversion discussed in Section 5.3.2.

Figure 46 shows the SEM images of surface microstructure of the Ag on Cu bilayer systems after irradiated by a 60 fs laser pulse at various fluences above the threshold of bump formation. Each SEM image is overlain with the results of the integrated Energy Dispersive X-ray Spectroscopy (EDX) analysis, where the horizontal axes are located along the scan lines. In Figure 46a, a microbump is formed and the EDX data detects only the presence of Ag, indicating that the escape depth of the X-ray radiation is below 50 nm. At higher fluence close to the threshold of Ag breaching, Figure 46b, the size of the microbump is substantially increased and the underlying Cu with atomic percentage of 10 at. % is observed, indicating that the thickness of the Ag bump is decreased. Above the breaching threshold, Figure 46c, the microbump breaks and reveals the underlying Cu layer detected by EDX with some remnant Ag around 10 at. %. Onset of nanojet formation with microbump of the underlying Cu layer is observed in Figure 46d, and the height of the nanojet increases with the laser fluence, Figure 46e. At sufficiently high fluence exceeding the breaching threshold for the underlying Cu layer, Figure 46f, a hole in the bilayer target is observed with neither Cu nor Ag signals and exposes the silica glass substrate.

In contrast to the Ag on Cu bilayer system, significantly different features of surface microstructure of the Cu on Ag irradiated target are shown by the SEM overlain with EDX data in Figure 47. Instead of formation of microbumps, the target surface exhibits a rough morphology, Figure 47a, featuring the ablation trace of the top Cu layer. This surface morphology becomes more apparent with increased laser fluence, Figure 47b, and reveals the underlying Ag layer, Figure 47c, as increasing amount of the overlaying Cu is ablated. Formation of the Ag bump is shown in Figures 47d and e, where substantial amount with around 25 at. % is present in the region of microbump. As shown in Figure 45, the range of fluences corresponding to surface modification below the threshold of bump formation, which is the difference in fluence between the white and blue bars, in the Cu on Ag target is much wider than that in the Ag on Cu target, indicating that a large fraction of the laser energy contributes to the heating and expulsion of the top part of the Cu layer. Complete breaching of the bilayer film is observed in Figure 47f. The interpretations of the differences in surface microstructure and threshold fluences for the Ag on Cu and the Cu on Ag bilayer systems are assisted by atomistic simulations and discussed in the following sections.

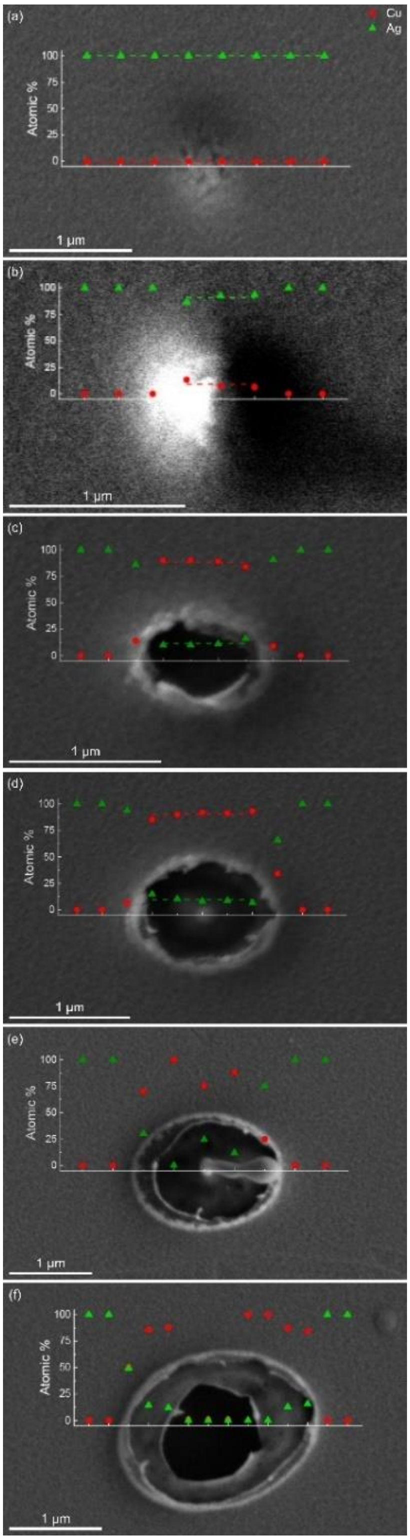

Figure 46. Scanning electron micrographs overlain with EDX line scans of the Ag on Cu bilayer target irradiated by a single 60 fs laser pulse at fluence of F_{inc}=1.73 J/cm^2, F_{abs}=0.16 J/cm^2 (a), F_{inc}=1.92 J/cm^2, F_{abs}=0.20 J/cm^2 (b), F_{inc}=2.00 J/cm^2, F_{abs}=0.22 J/cm^2 (c), F_{inc}=2.18 J/cm^2, F_{abs}=0.27 J/cm^2 (d), F_{inc}=2.70 J/cm^2, F_{abs}=0.45 J/cm^2 (e), and F_{inc}=3.16 J/cm^2, F_{abs}=0.66 J/cm^2 (f). The x-axes represent the EDX scan lines, green triangles and red dots show the atomic percentage of Ag and Cu, respectively, and dashed lines mark the average values of selected data points.

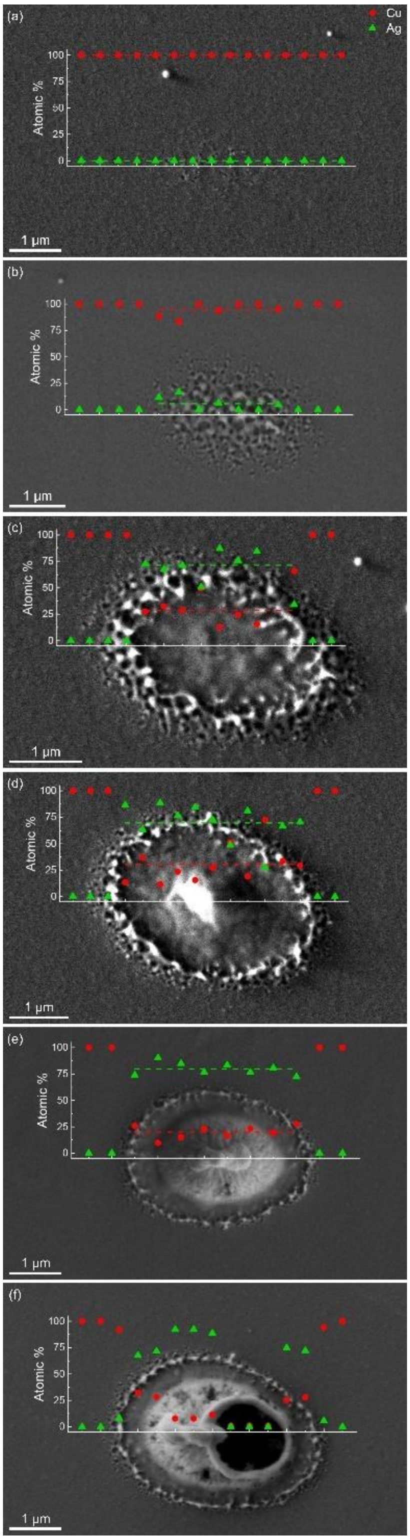

Figure 47. Scanning electron micrographs overlain with EDX line scans of the Cu on Ag bilayer target irradiated by a single 60 fs laser pulse at fluence of F_{inc}=0.48 J/cm^2, F_{abs}=0.03 J/cm^2 (a), F_{inc}=0.67 J/cm^2, F_{abs}=0.04 J/cm^2 (b), F_{inc}=1.05 J/cm^2, F_{abs}=0.09 J/cm^2 (c), F_{inc}=1.63 J/cm^2, F_{abs}=0.21 J/cm^2 (d), F_{inc}=2.41 J/cm^2, F_{abs}=0.52 J/cm^2 (e), and F_{inc}=2.81 J/cm^2, F_{abs}=0.73 J/cm^2 (f). The x-axes represent the EDX scan lines, green triangles and red dots show the atomic percentage of Ag and Cu, respectively, and dashed lines mark the average values of selected data points.

5.3 Computational study of the laser-induced material removal in the Ag-Cu bilayer systems responsible for the microbump formation

In this section, the mechanisms responsible for the femtosecond laser generation of microbumps on the Ag-Cu bilayer films are investigated through TTM-MD simulations. Considering the large laser spot size on the order of micrometer that is typically used in experiments, the complete description of the dynamic response of irradiated films to the laser energy deposition, leading to the formation of a microbump, is beyond the capabilities of atomistic MD method. Therefore, the simulations reported in this section are only focused on the processes occurring in the central part of the laser spot, and are aimed at investigating the thermodynamic driving forces responsible for the laser-induced material removal and redistribution. Although the simulations are not able to directly reproduce the laser-induced surface morphology of microbumps on the bilayer films, insights of the mechanisms responsible for the microbump formation are provided and used to interpret the experimental observations. The TTM-MD model developed for atomistic simulations of laser interaction with the Ag-Cu bilayer films deposited on a silica glass substrate, the parameters for the computational setup, as well as the TTM model to convert absorbed fluence used in simulations to incident fluence, are described in Section 5.3.1. The results of TTM-MD simulations of laser-induced material removal and its implications on formation of microbumps observed in experiments for Ag on Cu and Cu on Ag bilayer systems are reported in Sections 5.3.2 and 5.3.3, respectively. The laser energy redistribution in the Ag-Cu bilayer films, the relaxation of laser-induced thermoelastic stresses, the release of vapor at the interfacial region, and their implications on the modification of surface morphology, are summarized in Section 5.3.4.

5.3.1 Computational setup and methods

In order to obtain physical insights into the key processes responsible for the laser-induced modification of the surface morphologies on the Ag-Cu bilayer film targets, a series of TTM-MD simulations of laser irradiation on the Ag-Cu bilayer systems are performed, under irradiation conditions comparable to those used in the experiments. The combined TTM-MD model is described in Section 2.1.3, and the computational system is represented by a Ag-Cu bilayer film composed of a Ag and a Cu layer, both with the thickness of 50 nm, deposited on a silica glass substrate. The Ag and Cu solids have fcc crystal structure and the Ag-Cu interface is oriented along the (001) plane. The interatomic interactions in the MD part of the TTM-MD model are described by the embedded atom method (EAM) potential in the form suggested by Foiles, Baskes, and Daw (FBD)[221]. The potential functions are fitted to the sublimation energies, equilibrium lattice constants, elastic constants, and vacancy formation energies for pure metals. While for cross-interactions in dilute binary solid solutions, this potential is fitted to the heat of mixing. A cutoff function[254] is added to the potential, which brings the interaction energies and forces to zero at a cutoff distance of 5.5 Å. The melting temperatures of FBD EAM Ag and Cu, (1139 ± 2) K and (1288 ± 2) K, respectively, are evaluated in Ref. 22 and found to agree reasonably well with experimental values. [255] The critical temperatures estimated based on the test area method[256] calculation of the temperature dependence of the surface tension are (3380 ± 11) K and (5767 ± 39) K for the FBD EAM Ag and Cu, respectively. The lattice parameters predicted by the FBD EAM potential at 300 K under zero pressure are $a_{Ag} = 4.11$ Å and $a_{Cu} = 3.63$ Å. Despite of the overestimation compared with experimental values (4.09 Å and 3.61 Å for Ag and Cu, respectively),[257] the relative values of the lattice parameters and the corresponding misfit are similar for both MD results and experimental values at 300 K, $9\, a_{Cu} = 7.95\, a_{Ag}$, suggesting that the discrepancy between the computational and experimental lattice parameters does not affect the properties of the Cu-Ag interface.

The lateral size of the computational system is 6.54 nm × 6.54 nm, which corresponds to 18 unit cells for the Cu film and 16 slightly compressed unit cells for the Ag film, and periodic boundary conditions are applied in the lateral directions. Before applying laser irradiation, the combined Ag-Cu bilayer system with the silica substrate is equilibrated in MD simulation performed at 300 K for 250 ps. The misfit in the lattice parameters of Ag and Cu results in the formation of a semi-coherent interface with an array of misfit dislocations parallel to the <110> directions in the plane of the interface, as shown in Figure 48.

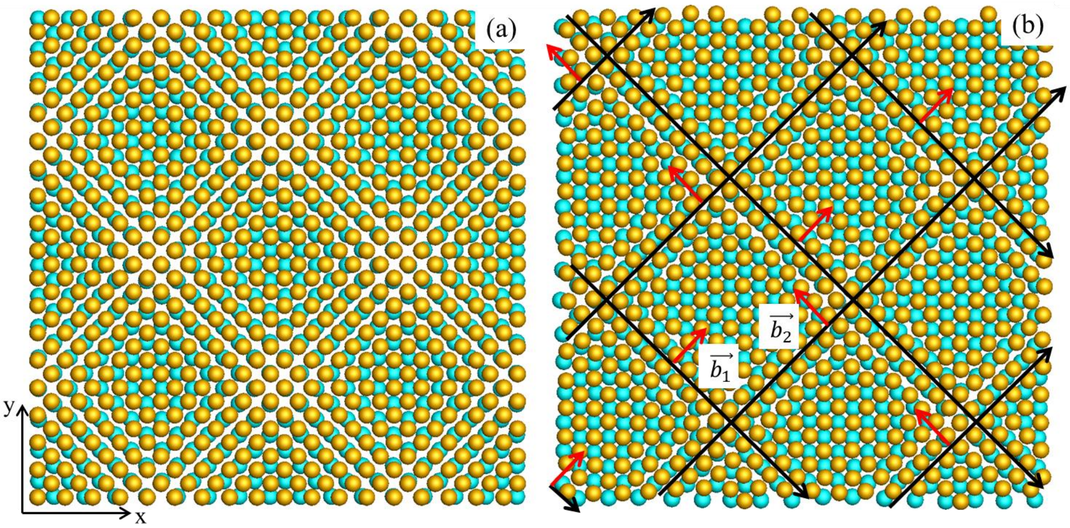

Figure 48. Atomic configuration of the Ag-Cu interface at initial time (a), and after equilibration at 300 K for 250 ps (b). Two atomic layers adjacent to the interface are shown, with Ag atoms colored in light blue and Cu atoms colored in yellow. The black arrows show the lines of misfit dislocations and the corresponding Burgers vectors, $\overrightarrow{b_1} = \frac{1}{2}[110]$ and $\overrightarrow{b_2} = \frac{1}{2}[\bar{1}10]$, are indicated by the red arrows.

Representation of the silica glass substrate with atomic resolution significantly increases the computational cost. For example, considering the characteristic length of thermal diffusion in fused silica, $L_{th} = \sqrt{2tk_{th}/c_V} \approx 39$ nm, where t ~ 500 ps is the timescale of simulations, k_{th} and c_V are thermal conductivity and heat capacity estimated as 1.38 $\mathrm{Wm^{-1}K^{-1}}$ and $3R$ = 9.15 $\mathrm{Jm^{-3}K^{-1}}$,[255] the computational size of the substrate should be comparable to the film thickness to avoid heat transfer through the bottom boundary of the silica substrate. Since we are only interested in the elastic response of the metal-silica interface to the thermal expansion and laser-induced pressure, and its implications on material removal, the silica glass substrate is described by a flat imaginary plane that interacts with the underlying metal layer, following the method described in Ref. 258. The interactions between the atoms of the underlying layer and the substrate are represented by the Lennard-Jones (LJ) potential parameterized to reproduce the experimental value of adhesion energy as well as the local stiffness of the interface under uniaxial compression. The work of adhesion for Ag-SiO_2 and Cu-SiO_2 interface is 0.43 N/m and 0.84 N/m, respectively[259]. The LJ parameter ε, which is the depth of the potential well and defines the energy scale of the potential, is fitted so that the energy of the metal-silica interface equals to the value determined by the equation $\gamma_{\mathrm{Ag(Cu)-SiO_2}} = \gamma_{\mathrm{Ag(Cu)}} + \gamma_{\mathrm{SiO_2}} - W_{adh}$, where W_{adh} is the work of adhesion, $\gamma_{\mathrm{SiO_2}}$ is the surface energy of silica substrate which equals to zero since it is represented by an imaginary plane, $\gamma_{\mathrm{Ag}} = 0.69$ J/m^2 and $\gamma_{\mathrm{Cu}} = 1.3$ J/m^2 are the surface energies of Ag and Cu, respectively, calculated for the EAM-FBD potential[221] used in this study. The other LJ parameter σ, the distance at which the interaction potential is zero, is chosen to reproduce the local stiffness to uniaxial compression. The local stiffness is defined by an arithmetic average of the elastic constants C_{11} between EAM-FBD metals, 124 GPa for Ag and 170 GPa for Cu,[221] and the fused silica, which is 77.6 Gpa.[255] The above fitting process yields the following parameters of the LJ potential: $\sigma = 2.951$ Å and $\varepsilon = 0.223$ eV for Ag-SiO_2 interaction and $\sigma = 4.693$ Å and $\varepsilon = 0.267$ eV for Cu-SiO_2 interaction. The displacement of the imaginary plane is controlled by the LJ forces acting on it from the atoms of the underlying metal layer, as well as an additional force matching the boundary condition that mimics the partial propagation of the laser-induced pressure wave through the metal-silica interface. The additional force, $\vec{F}_{add} = -SZ\vec{v}$, is proportional to the instantaneous velocity $\vec{v}$ of the imaginary plane and in the direction opposite to the movement. S is the surface area of the interface and Z is the acoustic impedance which can be calculated as $Z = \rho_{SiO_2} c_{SiO_2}$, where ρ_{SiO_2}=2.2 g/cm^3 and c_{SiO_2}=5900 m/s are the experimental values of density and speed of sound in fused silica.[255] The equation of motion for the imaginary plane is solved together with the integration of the equations of motion for all the atoms at each MD step, and the mass assigned to the imaginary plane is equal to the total mass of a single (001) atomic plane.

The laser energy deposition is described by the source term in Eq. (2.3), with pulse duration of $\tau_L = 60$ fs. The optical penetration depth L_{opt} for 800 nm laser wavelength, 13 nm for Cu and 12 nm for Ag, is combined with the ballistic penetration depth L_b, 15 nm for Cu and 53 nm for Ag, giving the effective range of laser energy deposition of $L_P = 28$ nm for Cu and 65 nm for Ag.[260] The temperature dependence of the electron thermal conductivity is described by Eqs. (2.4) and (2.5) in Section 2.1, and the values of the coefficient A are estimated as 2.66×10^6 $s^{-1}K^{-1}$ for Cu and 3.57×10^6 $s^{-1}K^{-1}$ for Ag, following the approach suggested in Ref. 91. The values of coefficient B, 2.41×10^{11} $s^{-1}K^{-1}$ for Cu and 1.12×10^{11} $s^{-1}K^{-1}$ for Ag are obtained by matching the experimentally determined thermal conductivity of solid Cu and Ag at the melting temperature, 330 $Wm^{-1}K^{-1}$ and 363 $Wm^{-1}K^{-1}$ for Cu and Ag, respectively. The effect of thermal boundary resistance on electron heat transfer across the interface between two metal layers has been investigated in time-resolved thermoreflectance experiments[261 - 263]. Although the experiments revealed sufficiently high thermal boundary resistance which may have practical implications on the electron heat transfer in nanoscale metal multilayers, all the values were measured in a narrow range of temperature around room temperature. Under short pulse laser irradiation at high fluence used in this study, however, electron temperature on the order of ten thousand Kelvin can be achieved. According to the electron diffuse mismatch model used to interpret the thermoreflectance data, the interface conductance increases linearly with the electron temperature, the electron temperature on the order of 10^4 K in the irradiation conditions in this section is expected to completely erase the effect of interface resistance and produce thermalization of electrons on a sub-picosecond timescale. This conclusion is consistent with the results of a recent study of the heat transfer in Au-Ni bilayer system with ultrafast X-ray diffraction,[264] where the stronger pump pulse produced electron temperature of thousands of Kelvin and the results are found to be incompatible with any significant electronic interface resistance between the two metal layers. Therefore, the thermal boundary resistance for the electronic energy transfer through the Ag-Cu interface is not considered in this model.

The TTM-MD simulations are performed at absorbed fluences ranging from 0.03 J/cm^2, which is slightly below the melting threshold, to 0.4 J/cm^2, where both Ag and Cu layers are removed from the substrate, which corresponds to the complete breaching of the bilayer films observed in experiments. To facilitate the comparison of the computational results with experimental observations, where the incident fluence is usually specified, the conversion between the absorbed fluence and incident fluence is established from a series of TTM simulations accounting for the electron temperature dependence of the reflectivity and optical absorption coefficient. The laser parameters such as wavelength and pulse duration, as well as the temperature dependences of electron-phonon coupling coefficient, electron heat capacity, and electron thermal conductivity are the same as in the TTM-MD model described above. Without atomistic description of the system, where all lattice properties are incorporated in the interatomic interactions potential, the lattice heat capacity is assumed to be constant and taken as 35.35 J mol^{-1} K^{-1} and 24.44 J mol^{-1} K^{-1} for Ag and Cu, respectively.[202]

The reflectivity and the optical absorption depth in the TTM simulations are determined by the complex permittivity ε that is parameterized based on the Lorentz-Drude model,[265]

$$\varepsilon = 1 - \frac{\Omega_P{}^2}{\omega(\omega - i\Gamma_0)} + \sum_{j=1}^{n_k} \frac{f_j \omega_P{}^2}{(\omega_j{}^2 - \omega^2) + i\omega\Gamma_j}, \tag{5.1}$$

where ω_P is the plasma frequency, which is 1.37×10^{16} Hz for Ag and 1.64×10^{16} Hz for Cu, ω is the angular laser frequency that is associated with the laser wavelength λ and light speed C through the relation $\omega = \frac{2\pi C}{\lambda}$, $\Omega_P = \sqrt{f_0}\omega_P$ is the plasma frequency associated with intraband transitions with oscillator strength f_0 and damping constant Γ_0, n_k is the number of oscillators that any oscillator j is associated with the frequency ω_j, strength f_j, and life time $1/\Gamma_j$. The complex permittivity is described as a function of temperature by replacing Γ_0 by an effective electron collision frequency, $\nu_{ef} = \min(\nu_e, \upsilon_c)$, where $\nu_e = 1/\tau_e = AT_e{}^2 + BT_l$ is the electronic collision frequency as defined in Eq. (2.5), and $\upsilon_c = (4\pi n_0/3)^{1/3}\sqrt{\nu_f{}^2 + k_B T_e/m_e}$ is the maximum critical electron collision frequency.[266] The coefficients A and B for Ag and Cu are given above, n_0 (5.74×10^{28} m^{-3} for Ag and 8.34×10^{28} m^{-3} for Cu) is the electron density, and v_f (1.39×10^6 m/s for Ag and 1.57×10^6 m/s for Cu) is the Fermi velocity. The reflectivity R and the optical absorption depth L_{opt} can be calculated from the following equations:

$$R = \left|\frac{\sqrt{\varepsilon}-1}{\sqrt{\varepsilon}+1}\right|^2, \tag{5.2}$$

$$L_{opt} = \frac{\lambda}{4\pi \mathrm{Im}(\sqrt{\varepsilon})}. \tag{5.3}$$

As described above, the effective range of laser energy deposition L_P is calculated as a combination of L_{opt} and a ballistic electron penetration depth L_b .In order to evaluate the sensitivity of calculated absorbed fluence to the assumed value of the ballistic penetration depth, the results obtained with a constant value of L_{b0} (15 nm for Cu and 53 nm for Ag) used in the TTM-MD model are compared with the ones where the ballistic range is estimated as the mean free path of the electrons, $L_b(T_e, T_l) = v_f/v_e$, which is a function of both electron and lattice temperatures. Figure 49 shows the values of reflectivity R, optical penetration depth L_{opt}, and ballistic penetration depth L_b for a broad range of electron temperatures T_e at a fixed lattice temperature of $T_l = 300$ K. The dependences of the optical properties, R and L_{opt}, on electron temperature are plotted in Figure 49a. The two assumptions of ballistic penetration depth, L_{b0} and $L_b(T_e, T_l)$ are illustrated in Figure 49b.

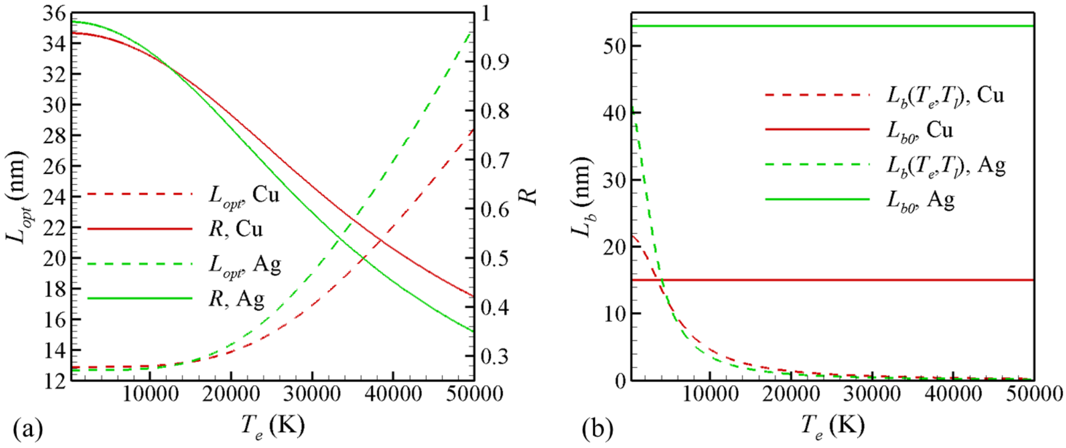

Figure 49. (a) The electron temperature dependence of reflectivity R and optical penetration depth L_{opt} calculated for Cu and Ag at a laser wavelength of 800 nm and a fixed lattice

temperature of 300 K. (b) Comparison of two assumptions for the ballistic penetration depth: a function of electron and lattice temperatures $L_b\,(T_e,\,T_l) = v_f/\nu_e$ with lattice temperature at 300 K, and a constant value L_{b0}, for Ag and Cu.

To build the relationship between the absorbed fluence and incident fluence, the TTM simulations are performed for bulk Cu and Ag systems irradiated by a 60 fs laser pulse with wavelength of 800 nm. Figure 50 shows the absorbed fluences calculated from a range of incident ones with two assumptions of the ballistic penetrating depth indicated in Figure 49b. Due to the ultrashort laser pulse duration and shallow optical penetration depth, the laser energy is expected to be rapidly deposited in the surface region of the target. For a bilayer system composed of 50-nm-thick layers, the optical properties of the bilayer system are largely defined by the properties of the top layer, since most of the laser energy is confined within the top layer during the laser pulse. Therefore, the absorbed fluence for a bilayer system can be expected to be close to that of a bulk system exposed to the same incident fluence, and the relationships between the incident fluence and absorbed fluence predicted for the Cu and Ag bulk system, Figure 50, can be used as reasonable approximation for the Cu on Ag and Ag on Cu bilayer systems investigated in the TTM-MD simulations.

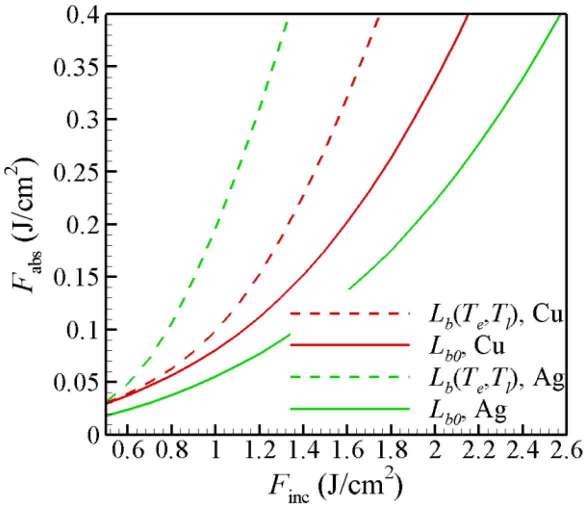

Figure 50. The relation between the incident fluence F_{inc} and absorbed fluence F_{abs} calculated for the bulk Ag and Cu targets. The laser beam has pulse duration $\tau_L =$ 60 fs and wavelength $\lambda =$ 800 nm. The results represented by solid and dashed lines are based on the assumptions of a constant value of L_{b0}, and a temperature dependent ballistic penetration depth $L_b\,(T_e,\,T_l)$, respectively.

The temperature dependence $L_b(T_e, T_l)$ is based on the assumption of electron equilibration within the characteristic time of a single scattering event. Since a single scattering event cannot be expected to result in the complete equilibration of the excited electron, this assumption can only be considered as a lower bound limit of the ballistic range, which results in overestimation of the surface heating, underestimation of surface reflectivity, and corresponding overestimation of absorbed fluence. At the threshold absorbed fluence for complete ablation of the bilayer film, ~ 0.4 J/cm^2 as predicted in the TTM-MD simulations, the incident fluence is estimated as 2.2 J/cm^2 for Cu and 2.6 J/cm^2 for Ag with constant values of L_{b0}, which is in a reasonably good agreement with the experimental values of 2.5 J/cm^2 for Cu on Ag bilayer and 2.8 J/cm^2 for Ag on Cu bilayer films, respectively, as shown in Figure 45. Therefore, the relations between the absorbed and incident fluence predicted with an assumption of constant L_{b0} (solid lines in Figure 50) are used as rough estimations for comparison of computational and experimental results.

5.3.2 TTM-MD simulations of laser-induced phase transformation and material ejection in the Ag on Cu bilayer film

A series of hybrid TTM-MD simulations are performed for the Ag on Cu double layer system under irradiation conditions comparable to those used in the experiments and the results are presented below. Due to the higher strength of the electron-phonon in Cu, as compared to Ag,[22,89] the redistribution of laser energy during the time of electron-phonon non-equilibrium may lead to the subsurface heating of the underlying Cu layer. This effect is illustrated in Figure 51, which shows the temporal evolution of temperature and pressure in the Ag on Cu bilayer system irradiated by a 60 fs laser pulse at F_{abs} = 0.05 J/cm^2. During laser excitation of the conduction band electrons, most of the deposited energy is confined within the top Ag layer, leading to a substantially higher electron temperature in the Ag layer generated by the end of the laser pulse, as shown in Figure 51c. The hot electrons in the Ag layer rapidly equilibrate with the electrons in the Cu layer, and the electron temperature equalizes within the two layers during the first 2 ps after the laser pulse. Nevertheless, as can be seen from Figures 51a and d, the lattice temperature in the bottom Cu layer increases faster than that in the Ag layer and reaches much higher maximum values. This behavior can be explained by more than twice stronger electron-phonon coupling in Cu as compared to

Ag at room temperature and even larger difference between the two materials in the electronically excited state, due to the stronger contribution of thermally excited d-band electrons in Cu.[22,89] As shown in Figure 51d, the equilibration between the electrons and phonons leads to the preferential heating of the Cu layer, and the difference in the lattice temperature within the two layers increases with time. By 6 ps, Figures 51a and d, subsurface heating of the Cu layer above the melting temperature firstly causes heterogeneous melting from the Cu-SiO_2 interface, followed by a rapid homogeneous melting of the whole layer when the temperature exceeds 2000 K. However, the overlaying Ag layer still retains its original crystalline structure with the temperature below 1000 K. A similar effect of subsurface heating in femtosecond laser interactions with layered targets has been predicted in TTM calculations performed for Au-Cr targets [267] and in TTM-MD simulations of Au-Cu[85] and Ag-Cu[22] targets. Experimentally, the electronic energy redistribution under conditions of electron-phonon non-equilibrium has been used to explain the results of time-resolved pump probe thermoreflectivity measurements performed for Au-Cr[268] and Au-Pt[269] layered systems. Another consequence of the rapid heating of the Cu layer is the generation of strong compressive pressure that reaches the level of 13 GPa just before the onset of the homogeneous melting of the layer, Figure 51b. As discussed below, the buildup of high pressure in the subsurface layer triggers complex dynamics of the pressure relaxation which, depending on irradiation conditions, may lead to the formation of internal voids, spallation of the film, or generation of a microbump by a tightly-focused laser beam.

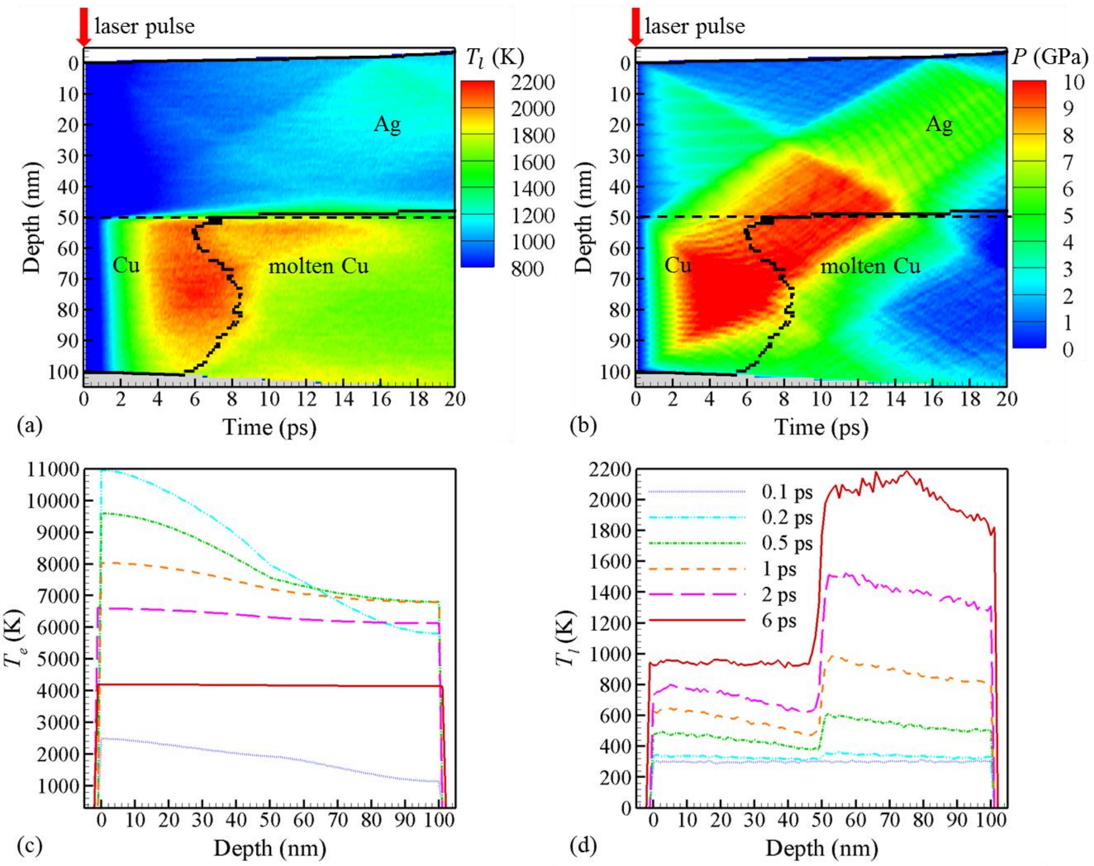

Figure 51. The results of the TTM-MD simulation of Ag on Cu bilayer system irradiated by a 60 fs laser pulse at an absorbed fluence of 0.05 J/m^2. The contour plots of spatial and temporal evolution of lattice temperature and pressure are shown in (a) and (b), respectively. The direction of the laser pulse is indicated by the red arrow. The dashed lines mark the location of the interface between the Ag and Cu layers, and the solid lines show the position of the solid-liquid interface. The gray regions represent the silica substrate. The distributions of electron and lattice temperature with respect to depth are plotted in (c) and (d), respectively. In (c,d), similar lines correspond to the same moments of time marked in (d).

Figure 52 shows the contour plots of the temporal and spatial evolution of the lattice temperature and pressure in the target irradiated at higher absorbed fluences of 0.1, 0.2, 0.3, and 0.4 J/cm^2. At absorbed fluence of 0.1 J/cm^2, the preferential subsurface heating and melting of the Cu substrate is apparent from Figure 52a, where the Cu layer can be seen to melt within several picoseconds following the laser excitation, while the lower part of the Ag layer remains solid up to about 20 ps. Similar to Figure 51b, the rapid heating and melting of the top part of the Cu layer leads to the generation of compressive stresses that drive compressive waves propagating into the overlaying Ag layer and towards the glass substrate. The complete reflection of the compressive wave from the top surface of the film and partial reflection from the substrate (the acoustic impedance of silica glass is less than half of that of Cu) result in the generation of tensile waves. These waves converge on the interface between the layers and create tensile stresses sufficient for delamination of the film into Ag and Cu parts, with the Ag layer further separating into several parts at later time. In contrast to the ejection of the Ag layer in the quasi one-dimensional TTM-MD simulation performed with a relatively small lateral size of the computational cell, under experimental conditions of irradiation by a tightly focused laser beam, the delaminated Ag layer can be expected to decelerate due to its interaction with the surrounding colder material at the periphery of the laser spot, leading to the formation of a Ag bump similar to that observed in Figures 46a and b. According to the TTM calculations discussed in Section 5.3.1, the absorbed fluence of 0.1 J/cm^2 is realized at about 1.4 J/cm^2 of incident fluence, which is comparable to the fluence producing the bump shown in Figure 46a.

At an absorbed fluence of 0.2 J/cm^2 (~1.9 J/cm^2 incident fluence), the temperature of Ag film is brought near the critical temperature (estimated as 3380 K for FBD EAM Ag), leading to an explosive decomposition and removal of the Ag film, Figure 52b. The temperature of the top part of the Cu layer also approaches the critical temperature (estimated as 5767 K for FBD EAM Cu) for a short time, but the decomposition of the Cu layer is suppressed by the pressure of the expanding plume produced by the explosive decomposition of the Ag layer. The ejection of the top Ag layer reveals the underlying Cu layer that can be expected to remain on the substrate. This scenario can be related to the experimentally observed breaching of Ag microbump, Figure 46c, at a fluence similar to that used in the simulation.

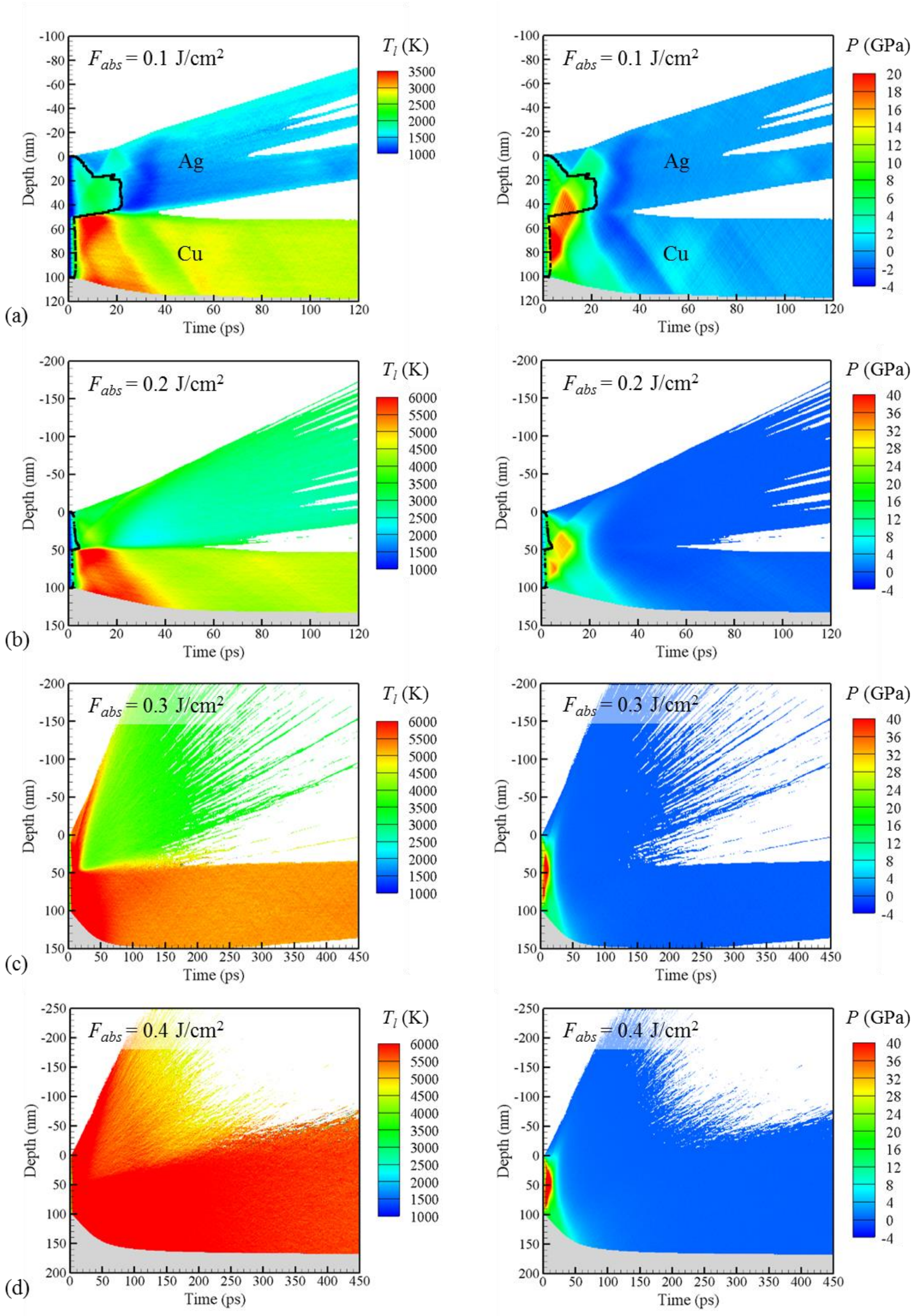

Figure 52. Spatial and temporal evolution of lattice temperature T_l and pressure P predicted in the TTM-MD simulations of Ag on Cu bilayer system irradiated by a 60 fs laser pulse at (a) F_{abs} = 0.1 J/cm^2, F_{inc} = 1.4 J/cm^2, (b) F_{abs} = 0.2 J/cm^2, F_{inc} = 1.9 J/cm^2, (c) F_{abs} = 0.3 J/cm^2, F_{inc} = 2.3 J/cm^2, (d) F_{abs} = 0.4 J/cm^2, F_{inc} = 2.6 J/cm^2. The black lines in (a,b) represent the solid-liquid interfaces which outline the solid parts of the film. The black lines are not shown in (c,d) where fast homogeneous melting is completed within ~4 ps. The gray regions represent the

silica substrate. Regions with relative atomic density ρ/ρ_0 of less than 0.07 are blanked, where ρ_0 is the density of Cu at 300 K

At a higher absorbed fluence of 0.3 J/cm^2 (~2.3 J/cm^2 incient fluence, Figure 52c), the pressure from the Ag layer undergoing the phase explosion can no longer suppress the separation of the Cu layer from the substrate. The temperature of the Cu layer at the time of its separation from the substrate (appearance of a white low-density region near the substrate at ~250 ps) remains close to the critical temperature, and the separation is driven by pressure from vapor released at the Cu-substrate interface. Nevertheless, the Cu layer retains its integrity during the simulation, suggesting that, similarly to the Ag layer in the simulation performed at F_{abs} = 0.1 J/cm^2, the deceleration due to the interaction of the layer with the surrounding colder material, as well as the Ag recoil vapor pressure from above, can prevent the ejection of the layer and lead to the formation of a Cu microbump and/or frozen nanojet similar to those shown in Figures 45d and e.

Finally, at an absorbed fluence of 0.4 J/cm^2 (~2.6 J/cm^2 incident fluence, Figure 52d), both Ag and Cu layers undergo an explosive decomposition into vapor and liquid droplets, leading to the complete removal of the bilayer film from the substrate. While the decomposition of the Cu layer into the mixture of vapor and small liquid droplets is difficult to see from the temperature and pressure contour plots shown in Figure 52, it is apparent in the corresponding density plot shown in Figure 53d discussed below. The fluence required for the complete film removal predicted in the simulations is in a good quantitative agreement with experimentally measured threshold fluence for Cu bump breaching, F_{inc} = 2.8 J/cm^2 (Figure 45) and the formation of a hole in the bilayer film (Figure 46f).

In order to facilitate the connection between the computational predictions and the experimental EDX line scans, the density and composition profiles calculated for systems obtained by the end of the TTM-MD simulations are plotted, along with the density contour plots, in Figure 53. The system is divided into 1 nm-thick slices along depth, and the normalized density ρ/ρ_0 is calculated by dividing the local density in each slice by the density of solid Cu at 300 K. The regions where ρ/ρ_0 is less than ~0.1 can be regarded as regions where only vapor and small clusters of atoms are present. The density and composition profiles in the right panels of Figure 53 are plotted in blue and red colors, respectively, and are calculated for the last moment of time shown in the contour plots in the left panels of Figure 53.

Below the threshold for the Ag layer breaching/removal, where the ejection of the Ag film from the center of the laser spot is expected to be suppressed by the interaction with surrounding colder regions, the EDX data mainly register Ag atoms but also detect a small fraction of Cu, Figure 46b. As can be seen from the right panel of Figure 53a, the mixing between the two layers is very limited at this fluence, and the Cu signal in Figure 46b is likely to be related to thinning of the Ag layer at the center of the laser spot during the microbump formation, which may allow the X-ray radiation to detect the underlying Cu layer. Above the Ag breaching threshold, as shown in the right panel of Figure 53b, the concentration of Ag mixed with the underlying Cu layer decreases from 20 at. % at a depth of 55 nm to zero at 60 nm, resulting in an average of about 10 at. % Ag in the surface region of remaining target, which agrees well with the results of experimental measurements, Figures 46c and d. Further increase in the laser fluence does not result in a substantial increase in the amount of Ag diffusing into the Cu layer, Figure 53c, although an additional deposition of Ag from the expanding plume is likely to occur at a later time and to result in an increased concentration of Ag that can be seen in Figure 46e. Finally, above the Cu breaching threshold, the whole system is disintegrated, as reflected by the rapid drop in density in the contour plot and the low values of density in the mixing region shown in Figure 53d. The material undergoing an explosive decomposition into vapor and small liquid droplets (on the timescale beyond the time of the simulation) is expected to be completely ablated away, resulting in the complete breaching of the film in the central part of the laser spot (Figure 46f). At the periphery of the laser spot, where the local fluence corresponds to the threshold for removal of the Ag layer only, the Cu layer with residual Ag can be seen.

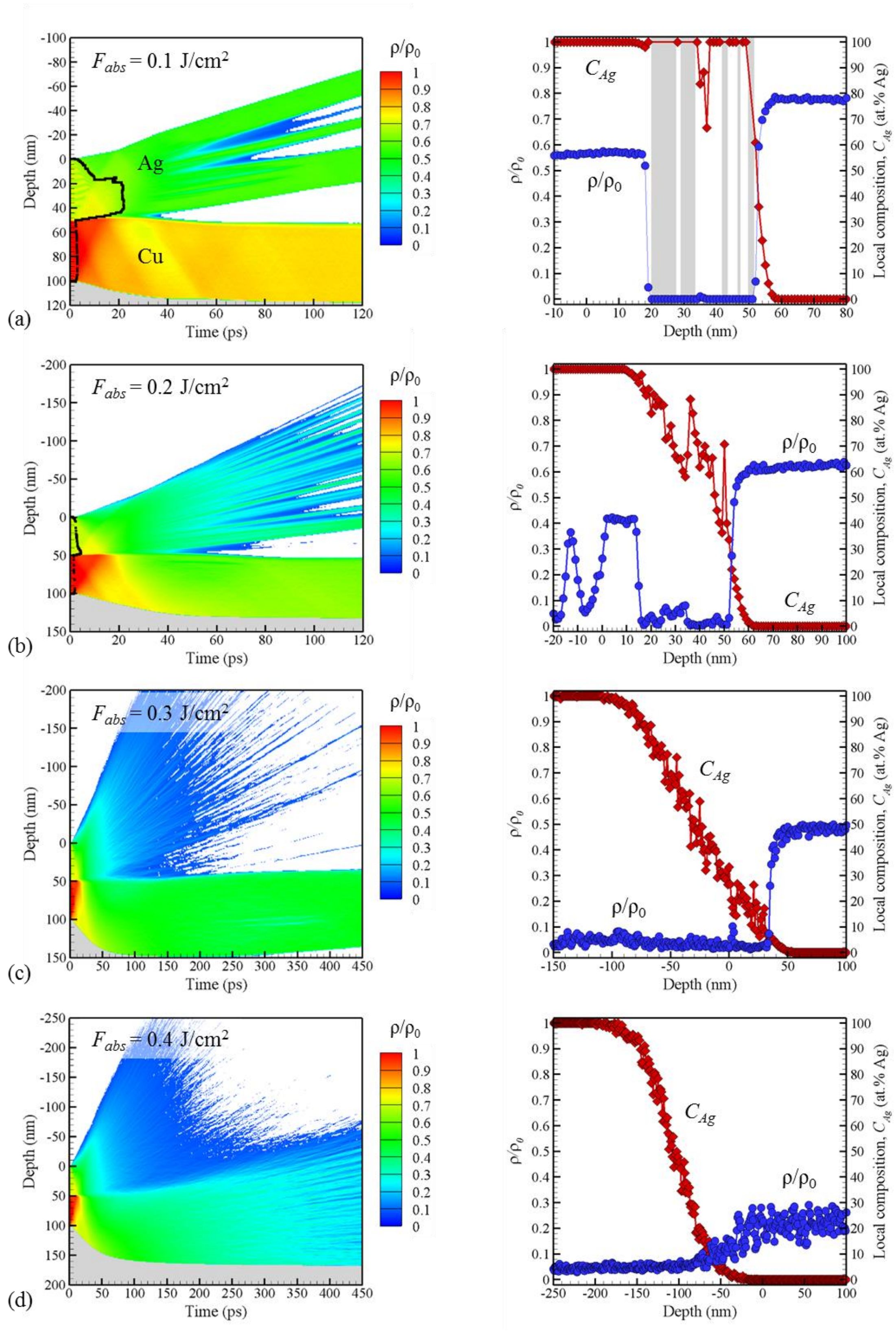

Figure 53. Spatial and temporal evolution of density normalized to the density of Cu at 300 K (left panels) and the distribution of normalized density and the elemental composition in the

mixing regions at the end of simulations (right panels) shown for the simulations illustrated by Figure 52. In the left panels, the regions where the normalized density is below 0.07 are blanked, the gray regions represent the silica substrate, and the black lines correspond to solid-liquid interfaces that outline the solid parts. In the right panel of (a), the gray areas show the regions of zero density, where the composition cannot be defined.

5.3.3 TTM-MD simulations of laser-induced phase transformation and material ejection in the Cu on Ag bilayer film

The results from TTM-MD simulations of laser irradiation on the Cu on Ag bilayer system are shown in Figure 54. As discussed before, Cu has significantly stronger electron-phonon coupling and shorter electron mean free path as compared to Ag, which contribute to the much faster thermalization of the excited electrons and stronger confinement of the deposited laser energy in the surface region of the Cu layer. The confinement of the deposited energy within the top part of the Cu layer can be seen in the temperature contour plots in Figures 54a and b. Note that the initial temperature evolution during the first 30 ps after the laser pulse is strongly affected by the dynamic relaxation of the laser-induced pressure (the propagation of the compressive and tensile components of the pressure wave produce strong transient heating and cooling of the material, respectively, by adiabatic compression and expansion[7,12]). However, the strong confinement of the deposited energy in the top part of the Cu layer is apparent from the large temperature differences between the Cu spalled layers, and is likely to result in a lower threshold of surface modification and damage, which explains the large ablation of Cu layer without bump formation as observed in experiments, Figure 47. As predicted in large-scale TTM-MD simulations of laser-induced photomechanical spallation,[84] the nucleation, growth, and coalescence of laser-induced subsurface voids leads to the formation of a transient foamy structure of interconnected liquid regions between the spalled layer and the remaining target. The fast cooling, resulted from the strong gradient of the deposited energy in the top part of the target, solidification, and break of this transient foamy structure is likely to be responsible for the characteristic rough morphology experimentally observed at the periphery of the (partially) ablated Cu layer in Figures 47b-f. The strong localization of the energy deposition in the top part of the Cu layer may also be related to the presence of a substantial amount of Cu, in excess of 20 at. %, revealed by the EDX analysis at relatively high laser fluences, in the regimes of microbump formation, Figures 47d and e, and even within the remnant bump material at fluences resulting in the breaching of the microbump, Figure 47f.

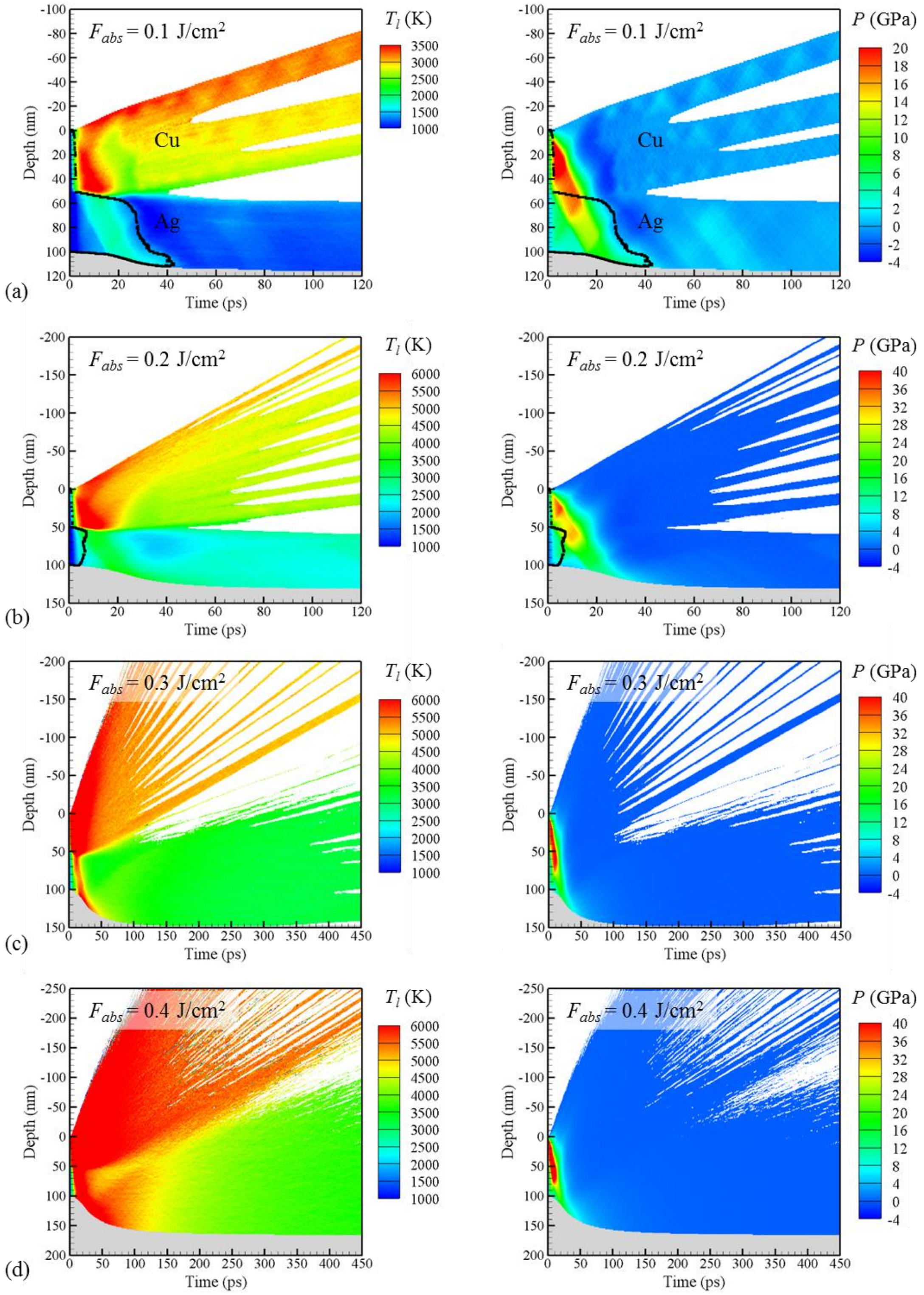

Figure 54. Spatial and temporal evolution of lattice temperature T_l and pressure P predicted in the TTM-MD simulations of Cu on Ag bilayer system irradiated by a 60 fs laser pulse at (a) F_{abs} = 0.1 J/cm^2, F_{inc} = 1.1 J/cm^2, (b) F_{abs} = 0.2 J/cm^2, F_{inc} = 1.6 J/cm^2, (c) F_{abs} = 0.3 J/cm^2, F_{inc} = 1.9 J/cm^2, (d) F_{abs} = 0.4 J/cm^2, F_{inc}=2.2 J/cm^2. The black lines in (a,b) represent the solid-liquid interfaces which outline the solid parts of the film. The black lines are not shown in (c,d) where fast homogeneous melting is completed within ~4 ps. The gray regions represent the silica substrate. Regions with relative atomic density ρ/ρ_0 of less than 0.07 are blanked, where ρ_0 is the density of Cu at 300 K.

The large difference between the threshold fluences of surface modification, microbump formation, microbump breaching, and nanojet formation in the Cu on Ag bilayer compared to the Ag on Cu system, as shown in Figure 45, can be related to the fact that a large fraction of the laser energy goes into the heating, explosive decomposition, and expulsion of the of the top part of the Cu layer. This can be seen from the results of TTM-MD simulations performed at all laser fluences, Figures 52 and 54. The recoil pressure exerted by the ablation of the top part of the Cu layer can further suppress the formation of the microbumps and nanojets in the underlying Ag laser. While the quasi one-dimensional TTM-MD simulations cannot fully capture the three-dimensional dynamics of the formation of microbumps and nanojets, the threshold fluences observed in experiments, Figures 45 and 47, are in a reasonable agreement with the computational predictions. At the absorbed fluence of 0.1 J/cm^2, the Cu layer disintegrates into three spalled layers, which are stabilized by the periodic boundary conditions applied in the lateral directions in the TTM-MD simulations. In experiments, however, the thin spalled layers with strongly confined thermal energy will eventually lose their integrity,[270] producing the rough surface morphology, similar to that in Figure 47c, through decomposition and rapid solidification. The absorbed fluence of 0.2 J/cm^2 is close to the conditions for partial spallation of the Ag layer which is more apparent at higher fluence, 0.3 J/cm^2, as can be seen from the transient appearance of voids or low-density region within the Ag layer in the density contour plot in Figures 55b and c. The partial spallation of the underlying layer can be related to the formation of microbump observed in experiments at the absorbed fluence of 0.21 J/cm^2, Figure 47d. An explosive disintegration of the Ag layer heated up to the critical temperature is predicted in the TTM-MD simulations for an absorbed fluence of 0.4

J/cm^2, Figures 54d and 55d, which is comparable to the film breaching threshold observed in experiments, $F_{abs} = 0.59$ J/cm^2 (Figure 45b).

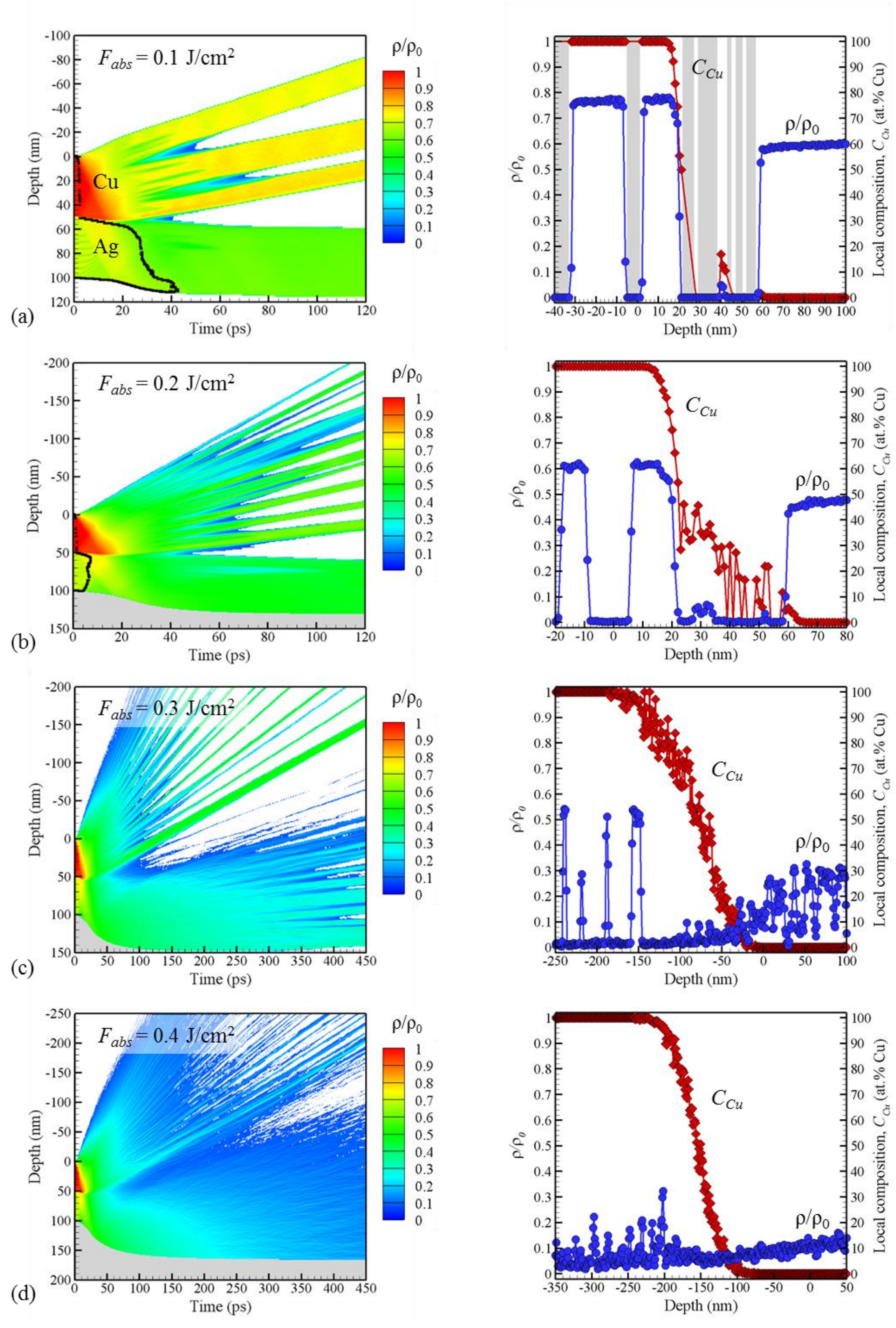

Figure 55. Spatial and temporal evolution of density normalized to the density of Cu at 300 K (left panels) and the distribution of normalized density and the elemental composition in the mixing regions at the end of simulations (right panels) shown for the simulations illustrated by Figure 54. In the left panels, the regions where the normalized density is below 0.07 are blanked, the gray regions represent the silica substrate, and the black lines correspond to solid-liquid interfaces that outline the solid parts. In the right panel of (a), the gray areas show the regions of zero density, where the composition cannot be defined.

5.3.4 Summary

In this section, TTM-MD simulations of the single-pulse femtosecond laser irradiation have been performed for the Ag-Cu bilayer films deposited on a glass substrate. The results from the simulations provide detailed information on the channels of energy redistribution and laser-induced phase transformations, and reveal the physical processes responsible for the laser-induced formation of microbumps. The computational predictions are related to the experimental observations, enabled by conversion of the incident laser fluence to the absorbed one based on a series of TTM simulations accounting for the electron temperature dependence of the reflectivity.

As demonstrated by the TTM-MD simulations, the energy redistribution in the bilayer system is largely defined by the difference in the strength of electron-phonon coupling between the two layers, and affects the values of threshold fluences for materials modification and the final surface morphology. In the Ag on Cu system, the stronger electron-phonon coupling of Cu results in the energy channeling from the top Ag layer to the underlying Cu layer during the time period of electron-phonon nonequilibrium, following the laser excitation of electrons in the Ag layer. The hot electrons of the Ag layer rapidly equilibrate with the electrons in the Cu layer, which in turn equilibrate with phonons, leading to the preferential heating and melting of the Cu layer. The formation of microbumps is found to occur at fluences exceeding the threshold for complete melting of the bilayer system, which is driven by the dynamic relaxation of the laser-induced compressive stress generated in the rapidly heated Cu layer. Further increase of the fluence leads to the complete removal of the top Ag layer and expulsion of the underlying Cu layer, the latter process is assisted by the release of vapor at the substrate-Cu interface due to the strong superheating of the molten Cu layer.

This may lead to the formation of a microbump or a nanojet observed in experiments.

In the case of Cu on Ag, a significantly lower effective depth of laser energy deposition and stronger electron-phonon coupling of Cu, as compared to Ag, lead to faster thermalization of the excited electrons and confinement of the deposited laser energy within the top part of the Cu layer. The energy confinement results in partial spallation of the Cu layer below the microbump formation threshold, leaving behind a characteristic frozen foamy surface morphology explained by the rapid cooling conditions created in this system. The surface structures formed at higher fluences mainly consist of Ag but still contain about 20 at. % of Cu.

Overall, in all systems the generation of microbumps is found to occur in the molten state and is driven by the dynamic relaxation of the laser-induced stresses, as well as the release of vapor at the substrate-metal interface at high fluences, when the molten material is strongly superheated close to the critical temperature. The resistance from the colder material at the periphery of the laser spot to the ejection of spalled layers, as well as the rapid solidification of the transiently molten structures, are largely defining the final shapes of laser-generated surface structures.

6. Large-scale simulation of femtosecond laser interaction with a Ag bulk target in the regime of phase explosion

6.1 Introduction

In the previous section, laser-induced collective ejection of the top layer or entire thin film, has been demonstrated in atomistic simulations of Ag-Cu bilayer films, leading to the formation and rupture of microbumps observed in experiments. Indeed, short pulse laser ablation of materials has been actively utilized in a broad range of practical applications, such as high precision cutting and drilling[86, 271, 272], surface microfabrication and processing[35,273-276], and generation of nano- and micrometer-sized particles[277-283].

One of the primary mechanisms of short pulse laser ablation is phase explosion, when strong laser energy deposition brings the surface region of the irradiated target beyond the limit of its thermodynamics stability, triggering an explosive decomposition of the overheated liquid into a mixture of vapor atoms and liquid droplets. A well-defined threshold fluence, where the transition from normal evaporation to phase explosion leads to a steep increase of material ejection rate, is observed in experiments.[38,39,40,41] Short pulse laser ablation can be also initiated at the fluence much lower than the phase explosion threshold,[284 - 286] which is attributed to the photomechanical effects driven by the relaxation of laser-induced stress under the conditions of stress confinement. The interaction of the thermoelastic compressive stress with free surface of the irradiated target leads to the formation of an unloading tensile wave propagating deep into the bulk target. The magnitude of the tensile stress increases with depth and laser fluence, and causes cavitation in a metastable liquid subsurface region or mechanical fracture/spallation of a brittle solid target. The coalescence of cavities or microcracks can lead to the mechanical disruption and ejection of large droplets or fractured solid fragments[8,285,287], resulting in the process of so-called photomechanical ablation or spallation.

Theoretical understanding of the material response to the fast laser excitation in the regime of ablation, including modification of the material properties by strong electronic excitation, fast non-equilibrium phase and structural transformations on target surface, and complex processes occurring in the ablation plume, is challenging and cannot be fully developed through direct experimental observations. MD simulations, which can provide atomic insights of the complex non-equilibrium processes during material ejection, have been applied in revealing the kinetics and mechanisms responsible for photomechanical spallation,[8,10,12,27,82-84,210-213,288,289] phase explosion,[8,10,27,43,83,84,290-304], and evolution of surface microstructures in the irradiated target.[24,26,228] In the regime of spallation, the relaxation of photomechanical stresses provides the driving force for the nucleation and growth of subsurface voids that leads to the formation of a foamy liquid structure interconnected by bridges and the separation of the spalled layer from the bulk of the target by coalescence and eventual percolation of multiple voids. In the regime of phase explosion, an explosive release of vapor, rather than the relaxation of photomechanical stresses, provides the main driving force for the collective ejection of the overheated surface region of the target. The elongation and eventual breakup of the liquid bridges connecting the ejected layers with the bulk target can contribute to the formation of complex surface morphology, featuring several nanospikes with a remarkable variability of the structural motifs. The high thermal conductivity of metals combined with the strong localization of the laser energy deposition result in high cooling rates. The processes of rapid solidification under conditions of deep undercooling play an important role in defining the shape and structure of the frozen nanospikes.

The characteristic sizes of the structural features (void, transient liquid filaments, droplets, nanospikes, *etc.*) generated in the course of laser can reach several tens or even hundreds of nanometers, which usually exceed the dimensions of computational systems commonly used in atomistic simulations. As a result, the periodic boundary conditions applied in the lateral directions cannot completely eliminate the effect of the finite size of the computational cell on simulation results, thus leaving the question on the sensitivity of the computational predictions to the size of the simulated systems open. In this section, a record-size TTM-MD simulation of laser ablation of a Ag bulk target is performed to provide reliable information on the characteristics of the ablation plume and the modification of surface morphology. A brief description of the computational setup used in the simulations is given in Section 6.2. The mechanisms responsible for the formation of the nanospikes and the processes that define their complex nanostructure are revealed in Section 6.3. The formation and evolution of the ablation plume, and the cluster distribution in the plume are analyzed in Section 6.4. In Section 6.5, the effect of finite lateral size of the system on computational predictions is discussed. The results of atomistic simulations of laser ablation in the regime of phase explosion and under conditions of stress confinement are summarized in Section 6.6.

6.2 Computational setup

The simulations of laser ablation of the bulk Ag target are performed with the TTM-MD method described in Section 2.1. The MD part of the computational system represents the top 300 nm surface region of a single crystal Ag target, enabling detailed analysis of the kinetics and mechanisms of the laser-induced phase and structural transformations, including melting and solidification, photomechanical generation of subsurface voids, hydrodynamic flow of liquid, and phase explosion, with atomic resolution. At the bottom of the MD domain, a dynamic pressure-transmitting boundary condition[93,94] is applied to allow nonreflecting propagation of the laser-induced pressure waves from the surface region to the bulk of the target. In the continuum part of the model, the TTM equation of electron temperature, Eq. (2.1), is solved on a 3D grid with the cell size of $4 \text{ nm} \times 4 \text{ nm} \times 2 \text{ nm}$ down to the depth of 3 μm. The smaller dimension of 2 nm in the direction normal to the target surface is used to provide adequate treatment of the strong electron temperature gradient generated by short laser pulse. The size of 3 μm for the TTM subsystem is chosen to ensure that no significant changes in the electron and lattice temperatures are observed at the bottom of the continuum region.

The initial Ag target has fcc structure with (001) surface orientation, and periodic boundary conditions are applied in the lateral directions. To provide realistic descriptions of the generation of subsurface voids and liquid droplets, the lateral size of the computational system is chosen as 400 nm, with the MD subsystem consisting of 2.8 billion atoms. To evaluate the effects of the finite lateral size applied with periodic boundary conditions on the computational predictions, the results of the large-scale simulation are compared with two additional simulations performed under the same irradiation conditions but with different lateral sizes, 20 nm and 100 nm, for the system.

The interatomic interactions between the Ag atoms are described by the FBD EAM potential.[221] Some properties predicted by this interatomic interaction potential, and the parameters used in the TTM equation for the electron temperature, are provided in the computational setup for the Ag-Cu bilayer system in Section 5.3.1. The threshold temperature of phase explosion at zero pressure is determined from a series of constant temperature and pressure simulations. In the simulations, a small cubic system consisting of 4000 atoms is firstly melted above ~1.2 T_m, followed by heating and equilibrating at 3050 K (~2.7 T_m). Later, the system is slowly heated with an increment of 10 K every 3 ns, until a sharp increase in the volume of the system is observed. Periodic boundary conditions are applied on all three directions and the pressure is controlled at zero. As shown in Figure 56, the onset of explosive decomposition of the system is manifested by the sharp increase in the volume around 3100 K, which is estimated as the threshold temperature for phase explosion. The value is ~8% lower than the critical temperature of 3380 K given in Section 5.3.1.

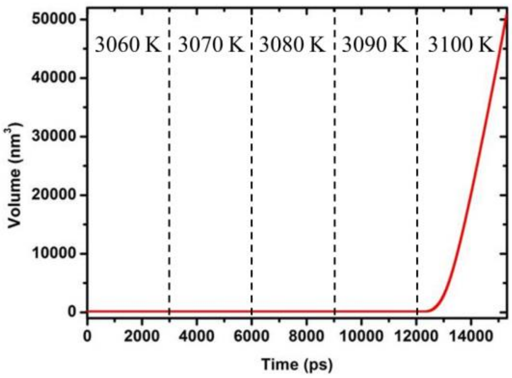

Figure 56. Temporal evolution of the volume of a cubic Ag system containing 4000 atoms in the MD simulations of slow heating. The initial temperature is 3050 K and from time 0, the temperature of the system is increased by 10 K and controlled at zero pressure for every 3 ns, as indicated by the simulation periods separated by dashed lines. The temperature controlled for the system during each period is noted.

The atomistic part of the system is pre-equilibrated at 300 K before applying the laser pulse. Laser energy deposition with uniform intensity along the lateral directions is represented by the source term Eq. (2.3), which assumes a Gaussian temporal profile and an exponential attenuation of laser intensity with depth under the surface (Beer-Lambert law). The laser pulse duration is 100 fs, much smaller than the characteristic time of mechanical relaxation of the heated volume, satisfying the conditions of stress confinement. The absorbed fluence is chosen as 3000 J/m^2, above the threshold of phase explosion.

6.3 Modification of the surface morphology by laser ablation in the regime of phase explosion

The response of the Ag bulk target to the 100 fs laser irradiation is illustrated in Figure 57 by contour plots showing the temporal and spatial evolution of the lattice temperature and pressure for the first 400 ps. As shown in Figure 57a, strong laser energy deposition leads to significant heating of the surface region of the Ag target over the threshold temperature for phase explosion, 3100 K. At such high temperature, the top part of the molten target becomes unstable and undergoes an explosive disintegration into a mixture of vapor and liquid droplets. This can be seen from the top part of the snapshots in Figure 58, where the explosive ablation of vapor atoms and small clusters (red color) are shown. The fast heating of the surface region under conditions of stress confinement leads to the buildup of high compressive stress, Figure 57b, which in turn relaxes by driving a compressive pressure wave deeper into the bulk of the target and inducing an unloading tensile wave from the free surface that follows the compressive component. The strength of the unloading tensile wave increases with depth, and reaches the maximum value of around -1.5 GPa at ~150 ps in the region close to the melting front. At the depth of 100-160 nm, where the liquid is strongly overheated, passing of the tensile pressure wave during 100-150 ps with negative stress around -1 GPa brings this metastable subsurface region across the stability limit against the onset of cavitation, leading to the nucleation and growth of large number of voids as can be seen in Figure 58.

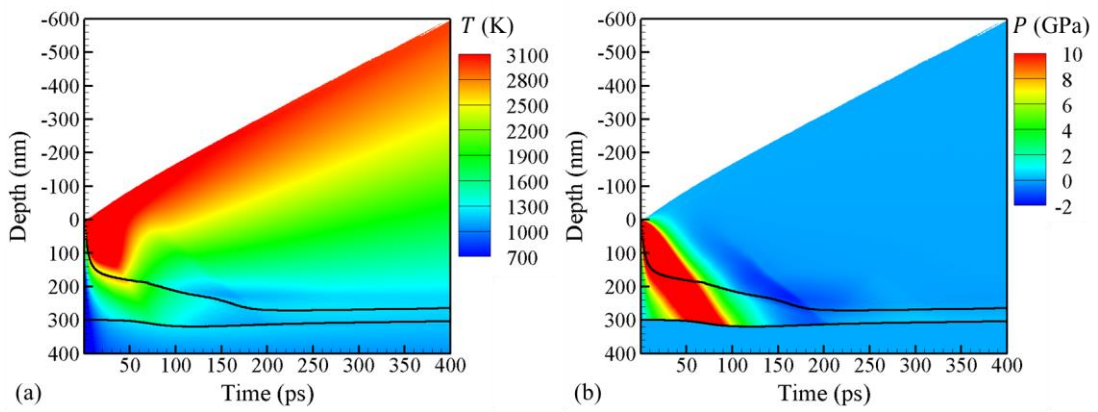

Figure 57. Contour plots of the spatial and temporal evolution of lattice temperature (a) and pressure (b) in the TTM-MD simulation of a Ag bulk target irradiated by a 100 fs laser pulse at an absorbed fluence of 3000 J/m^2. The black solid lines near the surface of the target show the movement of the crystal-liquid interface, and the black lines in the lower parts of the contour plots show the location of the nonreflecting boundary applied at the bottom of the MD part of the computational domain.

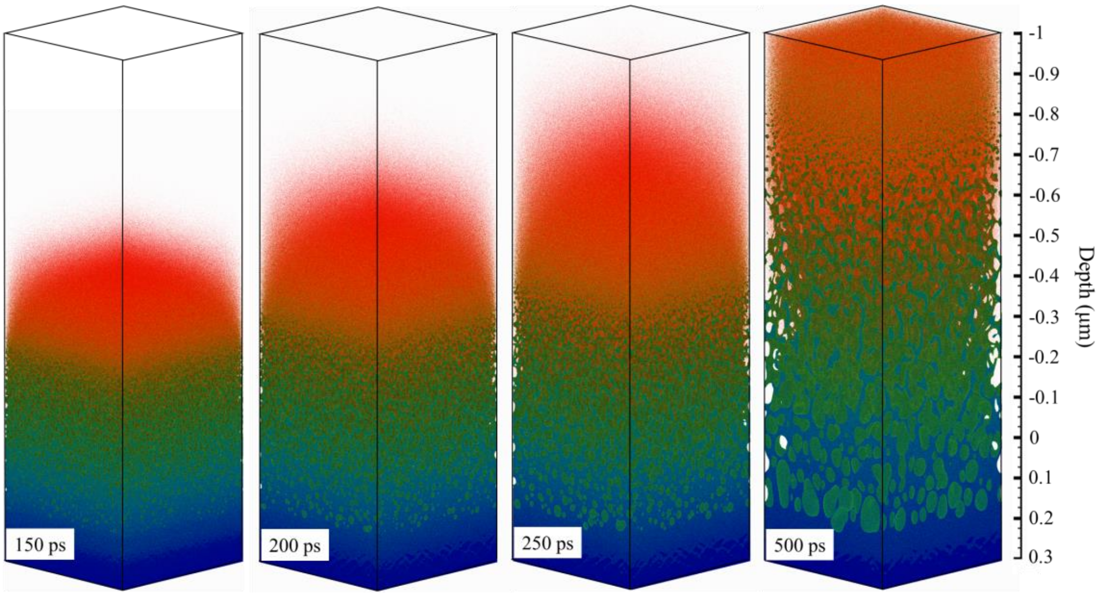

Figure 58. Snapshots of atomic configurations predicted in the TTM-MD simulation of a Ag bulk target irradiated by a 100 fs laser pulse at an absorbed fluence of 3000 J/m^2. The snapshots are shown for the time of 150 ps, 200 ps, 250 ps, and 500 ps after laser pulse. The atoms are colored according to their potential energies.

The growth and coalescence of the subsurface voids results in the formation of a complex structure of interconnected liquid bridges connecting the top liquid layers with the bulk of the target. As shown in Figure 59, the ejected liquid layers move away from the target at a velocity around 150 m/s, occurring concurrently with the elongation, shrinking, and breakdown of the liquid bridges. The breakdown of the liquid bridges starts from 2000 ps and is completed shortly after 5000 ps, resulting in the separation of the spalled liquid layers and formation of several nanospikes on the remaining target surface. Driven by minimization of the surface energy, the liquid droplets generated by disintegration of the interconnected liquid structure evolve into spherical nanoparticles with the size ranging from a few nanometers to tens of nanometers. The ejected liquid part, as shown at the time of 3500 ps, will disintegrate into several large droplets after sufficiently long time of evolution, which cannot be modeled due to the high computational cost of atomistic simulations. However, by counting the number of atoms in the lower part of the ejected layer outlined by the red dashed rectangle, estimated as ~0.38 billion atoms, we can expect that it will eventually evolve into a large spherical droplet with radius exceeding 120 nm. This value is comparable to the depth of material ejection on the surface of the irradiated target. The upper part of the spalled liquid layer, which contains ~0.25 billion atoms, starts to disintegrate during the simulation that will result in several large droplets with radius of tens of nanometers.

The dynamic evolution of the liquid bridges also has important implications on the thermal transport and the kinetics of solidification in the surface region of the target. Figure 60 illustrates the undercooling levels in the surface region of the target for a range of time from 4500 ps to 7000 ps after the laser pulse. The system is discretized into $2\,\text{nm} \times 2\,\text{nm} \times 2\text{nm}$ grid cells, and the local temperature of each cell is calculated based on the kinetic energy of atoms in that cell. The liquid bridges act as channels of conductive heat flow from the hot liquid spalled layer to the bulk of the target. After the breakdown of the bridges and formation of nanospike, as exemplified in the region outlined by black rectangle at the time of 5500 ps, complete termination of the heat flow results in rapid cooling of the top parts of the nanospike down below ~0.9 T_m. Further separation of the hot droplets from the nanospike during the following 1000 ps leads to a strong undercooling at the top of the remaining nanospike, as outlined by black rectangle at 6500 ps, below 0.65 T_m. Such high level of undercooling, as discussed for other metals in Section 4 and predicted for EAM Ag in earlier studies,[23,24] leads to the fast solidification of the remaining liquid region proceeding through homogenous nucleation and growth of new crystallites, thus determining the nanocrystalline structure and morphology of the frozen nanospikes as discussed below.

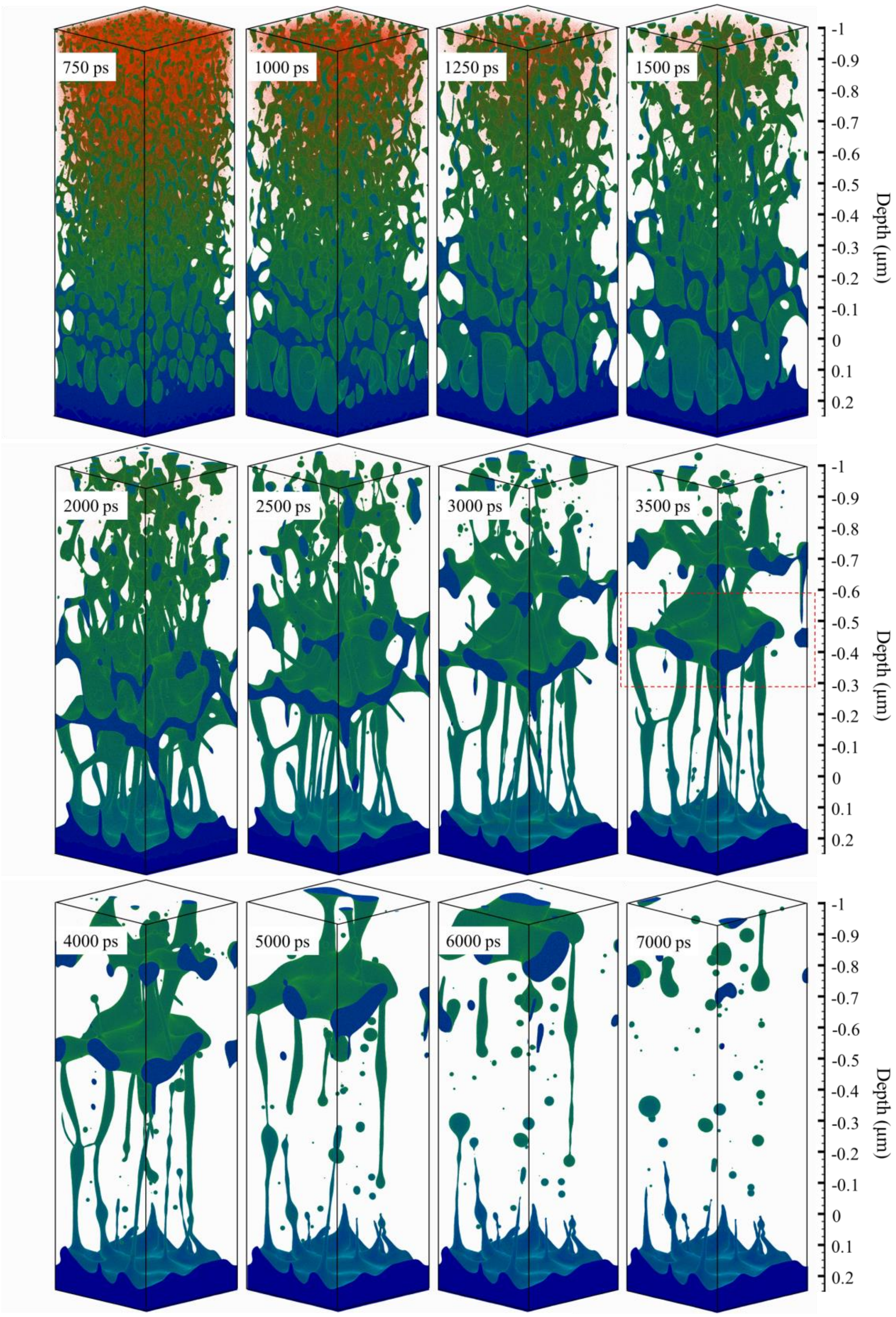

Figure 59. Snapshots of atomic configurations predicted in the TTM-MD simulation of a Ag bulk target irradiated by a 100 fs laser pulse at an absorbed fluence of 3000 J/m^2. The snapshots

are shown for a wide range of time to illustrate the evolution of the liquid structure near the target surface. The atoms are colored according to their potential energies.

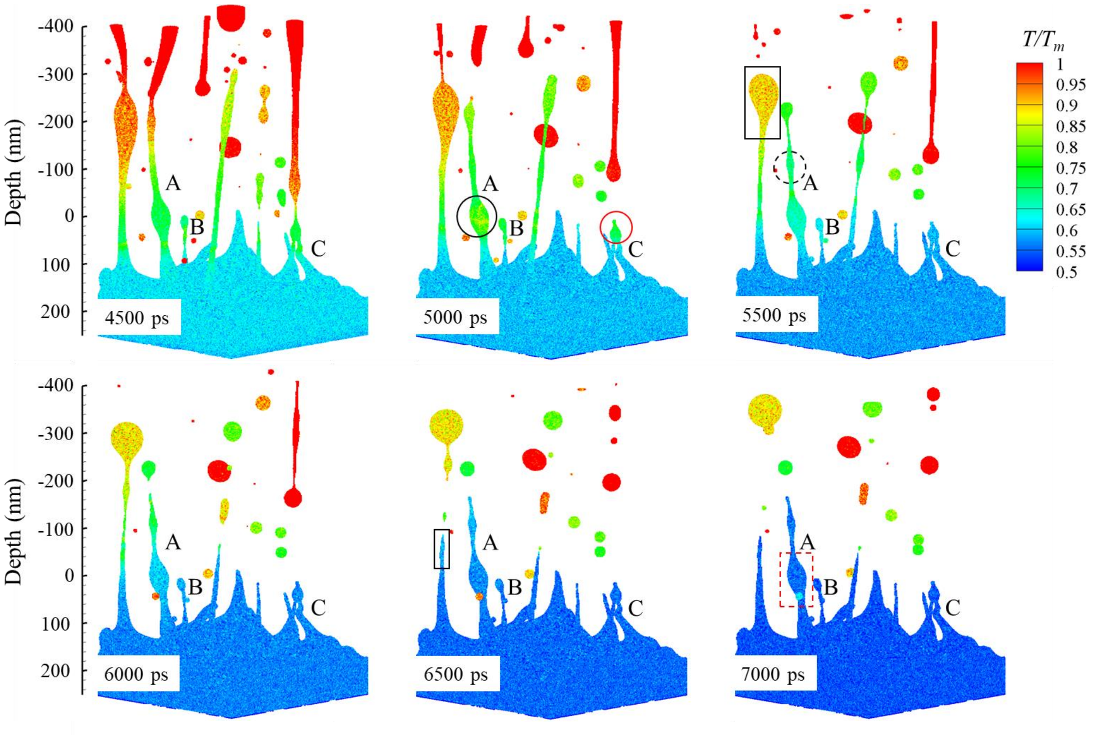

Figure 60. Snapshots of local temperature predicted in the TTM-MD simulation of a Ag bulk target irradiated by a 100 fs laser pulse at an absorbed fluence of 3000 J/m^2. The temperature is calculated for the $2\ \text{nm} \times 2\ \text{nm} \times 2\text{nm}$ grid cells of the system and normalized to the melting temperature. The cells with density lower than 0.88 ρ_0, where ρ_0 is the liquid density at melting temperature, are blanked. The black rectangles at the time of 5500 ps and 6500 ps outline the top regions of the nanospike illustrating the rapid cooling after breakdown of the liquid bridge. The red dashed rectangle outlines the region where a thick node is formed. The red and black circles at the time of 5000 ps mark the region of local temperature increase due to rapid solidification, as discussed in Figures 64 and 65, respectively. The dashed circle at the time of 5500 ps marks the region where sufficient undercooling level leads to the onset of homogeneous nucleation, as discussed in Figure 66. The formation of nanospikes marked as A, B, and C are discussed in the text.

As discussed above, the elongation, shrinking, and eventual breakdown of the liquid bridges lead to the formation of nanospikes. The shape of the nanospikes is defined by the dynamic evolution of the liquid bridges and the process of solidification. The surface morphology of the Ag target at the end of the simulation (7000 ps) is shown in Figure 61, featuring a total number of 9 nanospikes formed on the surface, with the length ranging from tens of nanometer to ~300 nm. Most of the nanospikes have a sharp tip, as expected from the shrinkage and breakdown of the liquid bridges, followed by prompt completion of the solidification process under conditions of strong undercooling. However, if the bridge breaks at a time when the majority of the nanospike still remains in liquid phase and the undercooling is not sufficiently high to induce homogeneous solidification, the shape of the nanospike could undergo a substantial evolution driven by the minimization of the surface energy. Indeed, the evolution of the top part of the broken liquid bridge into a spherical shape is observed on nanospike A marked in Figure 60 from 4500 ps to 5500 ps. The spherical head is then separated from the nanospike at ~6000 ps, forming a nanoparticle with a radius of ~30 nm. If the sphere is crystallized without separation from the nanospike, a spherical head instead of sharp tip of the nanospike can be observed, as shown on the top of spike B marked in Figure 60. Indeed, the spherical heads of the nanospikes are commonly observed in the experiments of laser ablation of different materials.[13,227,275]

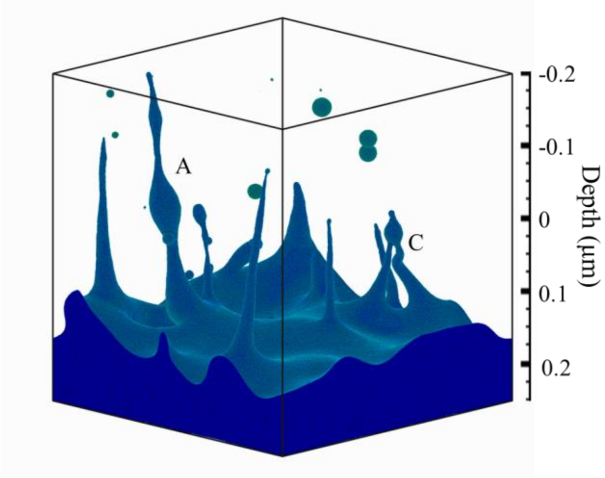

Figure 61. Snapshot showing the final surface morphology of the Ag target with lateral size of 400 nm, predicted from the TTM-MD simulation of ablation by a 100 fs laser pulse at an absorbed fluence of 3000 J/cm^2. A and C mark the same nanospikes as in Figure 60, for which the nanocrystalline structure is analyzed below.

A prominent feature of nanospike A is the formation of a thick node in the middle part of the nanospike, as marked by the red dashed rectangle in Figure 60 at the time of 7000 ps, which can be explained as a result of interactions between liquid bridges. As illustrated in Figure 62, a small nanospike is separated from the ejected liquid layer before 2500 ps, with the top part evolving into spherical shape. The bottom of this nanospike is connected with other two intertwined liquid bridges at the time of 2500 ps, and minimization of the surface energy drives the coalescence of the bridges with the nanospike during the following 500 ps. By 3250 ps, the head of the nanospike merges within the coarsened liquid bridge in the region outlined by the black rectangle, forming a node that tends to evolve into spherical shape, as shown in Figure 59 from 3500 ps to 7000 ps. Similar process of coalescence between two intertwined liquid bridges also leads to the large sphere at the top of nanospike C, as can be seen from 3500 ps to 5000 ps in Figure 59.

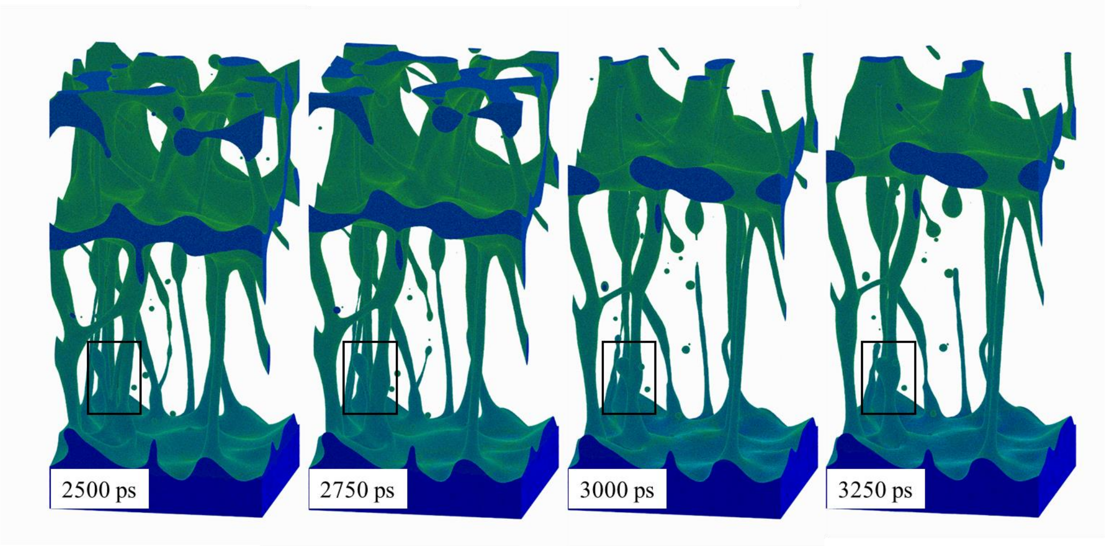

Figure 62. Snapshots illustrating the process responsible for the formation of a thick node in nanospike A as marked by the red dashed rectangle in Figure 60. The region where the small nanospike is coalesced with the liquid bridges is outlined by black rectangle. To provide a clear view of the merging process, the atomic configuration is shown along the direction that is different from Figures 60 and 61.

In order to understand the solidification process of the nanospikes and their nanocrystalline structure, the atomic configurations of the nanospikes A and C as marked in Figures 60 and 61 are analyzed and shown in Figures 63-66. The local structural environment is identified for each atom following a method suggested in Refs. 22 and 305, so that the liquid phase, crystal structure, and defects can be clearly identified. In Figures 63-66, the atoms with local hcp structure are colored in red, and yellow atoms are associated with fcc structure. Therefore, the twin boundaries and stacking faults are represented by the single and double red atomic layers on yellow background. Blue atoms correspond to the liquid phase, surfaces, dislocations, or grain boundaries surrounding the nanocrystalline grains.

At the base of nanospike C, Figure 63, solidification proceeds through epitaxial regrowth of the original single-crystal target before 4250 ps, which is manifested by the same crystal orientation with the bulk target. In the region outlined by the black rectangle, stacking faults on different {111} planes are observed, which can be related to the emission of partial dislocations from the crystal-liquid interface when strong tensile wave passes through, similar to the process discussed in Section 4.2.4 for short pulse laser-induced defects in $Ni_{50}Fe_{20}$ target. The stacking faults are left behind by the partial dislocations during the epitaxial crystal growth, and are terminated by emission of trailing dislocations from the solidification front or extended to the free surface. In other parts of the nanospike, a mixture of fcc-hcp structure is observed, which can be explained by the cross-nucleation of hcp {0001} layers on the structurally compatible {111} faces of growing fcc crystal. The high probability of nucleation of atomic layers with hcp stacking sequence on the {111} facets of the growing fcc crystal is related to the relatively low energies of coherent twin boundaries and stacking faults[306] as compared to the strong driving force for the solidification. Similar process of the cross-nucleation of the metastable hcp phase has been demonstrated in atomistic simulations of liquid Ag,[24] Cu,[307] as well as in Lennard-Jones liquids.[308,309]

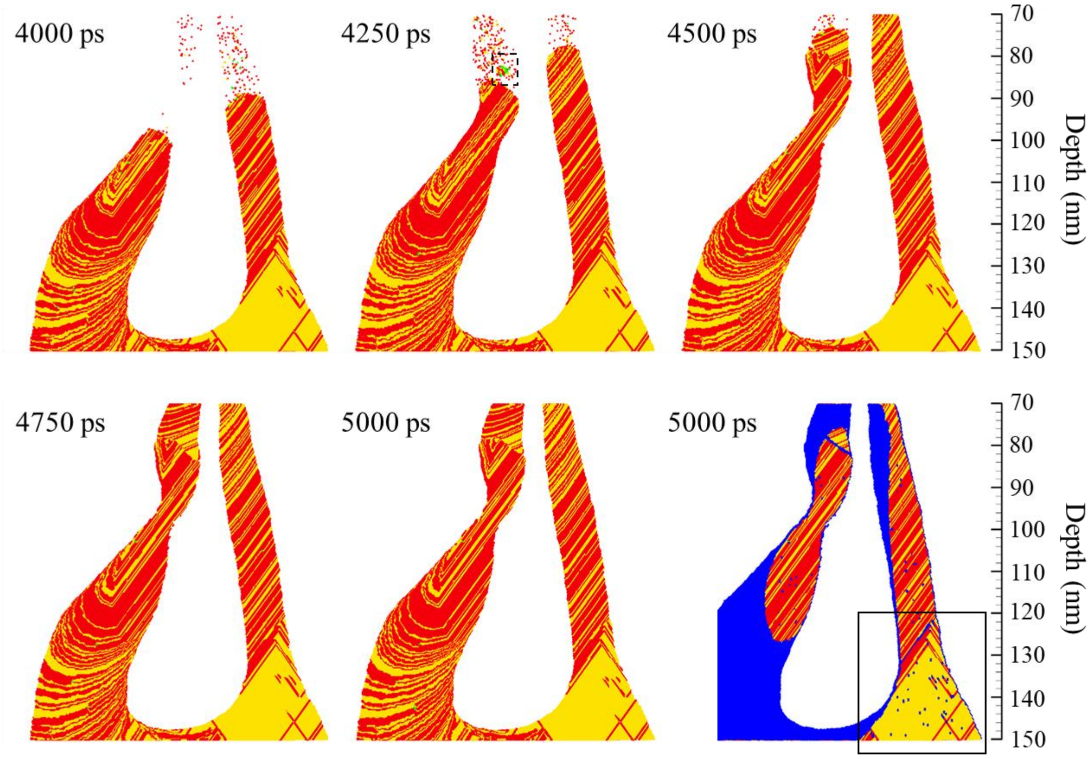

Figure 63. Snapshots illustrating the resolidification process in the lower part of spike C marked in Figures 60 and 61. To provide a clear view of the nanocrystalline structure and the

shape of the nanospike, the atomic configurations are shown for a 15 nm thin slice cut by (100) planes passing through the nanospike. The views of the cross sections are shown along the [110] direction. The atoms are colored according to their local structural environment,[22,305] so that the fcc and hcp atoms are colored yellow and red, respectively. The green color corresponds to atoms with bcc structure. The atoms that belong to the liquid phase, crystal defects (point defects, dislocations, or grain boundaries), or free surfaces are colored blue, which are blanked except for the last image to expose the process of homogenous crystallization. The dashed rectangle marks the nucleation of a crystallite at 4250 ps, and the solid rectangle at the time of 7000 ps outlines the region where stacking faults left behind the emitted partial dislocations during epitaxial crystal growth are formed.

The propagation of the solidification front at the base of nanospike C takes place under conditions of increasing undercooling of the remaining molten region. By the time of 4250 ps, the temperature of the liquid in the immediate vicinity of the solidification front drops below the level required for the onset of homogeneous nucleation, resulting in the appearance of one crystallite as marked by the dashed rectangle in Figure 63. This crystallite then grows and merges with the solidification front propagating through epitaxial regrowth of the substrate, by 4500 ps, locking the interface between the single crystal part of the target and the nanocrystalline region at the depth of ~80-85 nm.

In the top part of nanospike C, Figure 64, several crystal nuclei with random crystallographic orientations appear almost simultaneously at 4750 ps, followed by subsequent growth of the nuclei and the formation of a nanocrystalline structure. The cross-nucleation of hcp and fcc regions on close-packed faces of the growing crystallites is observed, resulting in a similar mixed fcc/hcp structure in each nanograin as in Figure 63. The release of the latent heat of solidification due to the homogenous nucleation and growth of new crystallites leads to a pronounced increase in the local temperature, thus retaining the top of nanospike C above 0.7 T_m, as shown by the red circle in Figure 60 at the time of 5000 ps.

In nanospike A, the homogeneous nucleation and growth of new crystallites in the strongly undercooled liquid region, forming the nanocrystalline structure, in the lower and upper part is illustrated in Figures 65 and 66, respectively. From 4750 to 5000 ps, the fast crystallization in the knob as shown in Figure 65 releases a large amount of latent heat, leading to the increase of local temperature up to 0.9 T_m, as shown in the region marked by the black circle in Figure 60 at the time of 5000 ps. As discussed above, the breakdown of the liquid bridge leads to fast cooling of the top part of the nanospike. As shown in the region marked by the dashed circle in Figure 60 at the time of 5500 ps, undercooling down to ~0.67 T_m is achieved, creating conditions for the homogeneous nucleation of a crystallite at the depth around -80 nm (80 nm above the initial target surface), Figure 66. The onset of homogeneous nucleation at this level of undercooling is also demonstrated in previous simulation.[24] After growing grains join together and form nanocrystalline structure, grain coarsening through disappearance of the small grains and growth of larger ones takes place, as illustrated in the regions outlined by the black rectangles in Figures 65 and 66, to minimize the interfacial and surface energy. Interestingly, at 6500 ps, a liquid droplet moves to the nanospike, followed by rapid cooling and crystallization, forming a spherical node with nanocrystalline structure on the nanospike.

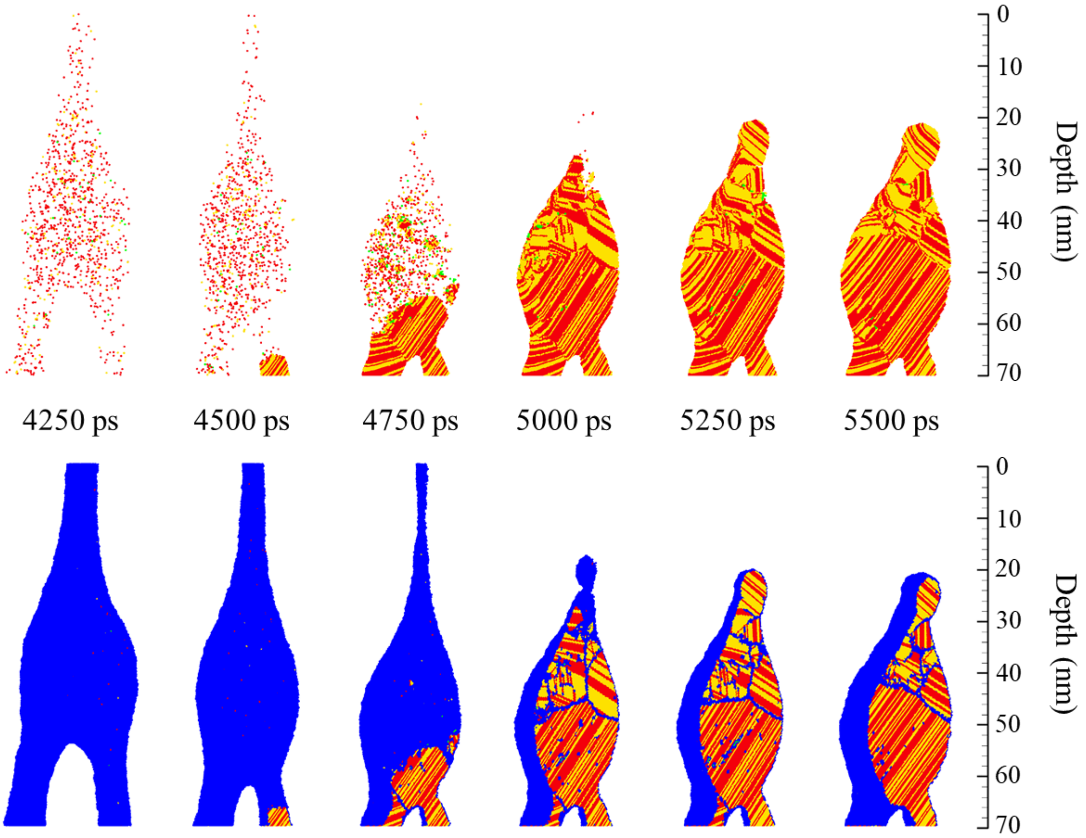

Figure 64. Snapshots illustrating the resolidification process in the upper part of spike C marked in Figures 60 and 61. The atomic configurations are shown for a 13 nm thin slice cut

by (100) planes passing through the nanospike, with the views of the cross sections along the [110] direction. The atoms are colored according to their local structural environment as in Figure 63. In the upper panel, the atoms that belong to the liquid phase, crystal defects, or free surfaces are blanked to expose the process of homogenous crystallization. In the lower panel, all atoms are shown so that the shape of the nanospike and grain boundaries are apparent.

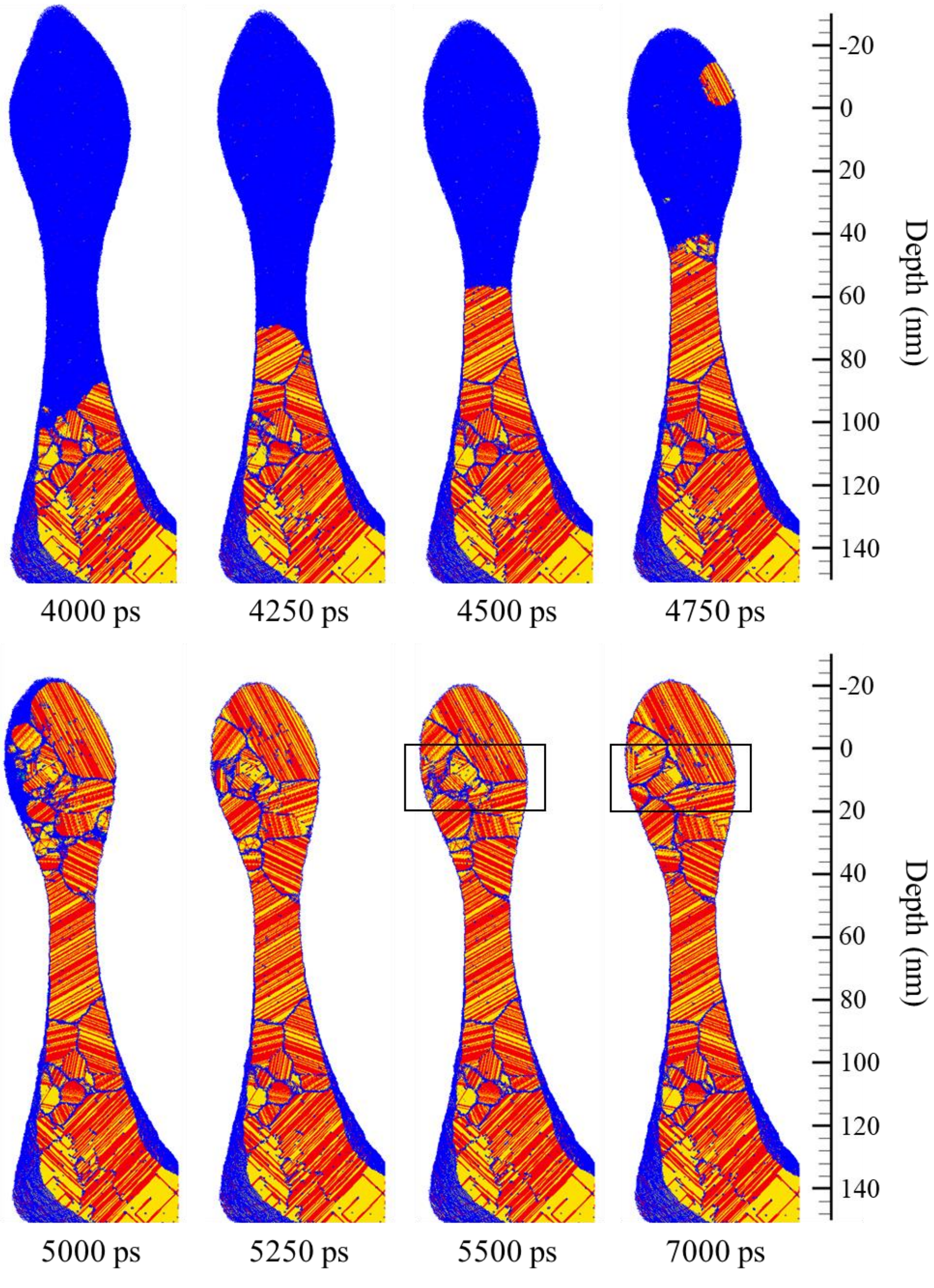

Figure 65. Snapshots illustrating the resolidification process in the lower part of spike A marked in Figures 60 and 61. The atomic configurations are shown for a 10 nm thin slice cut by (010) planes passing through the nanospike, with the views of the cross sections along the [010] direction. The atoms are colored according to their local structural environment as in Figure 63. The black rectangles mark the region where grain coarsening occur.

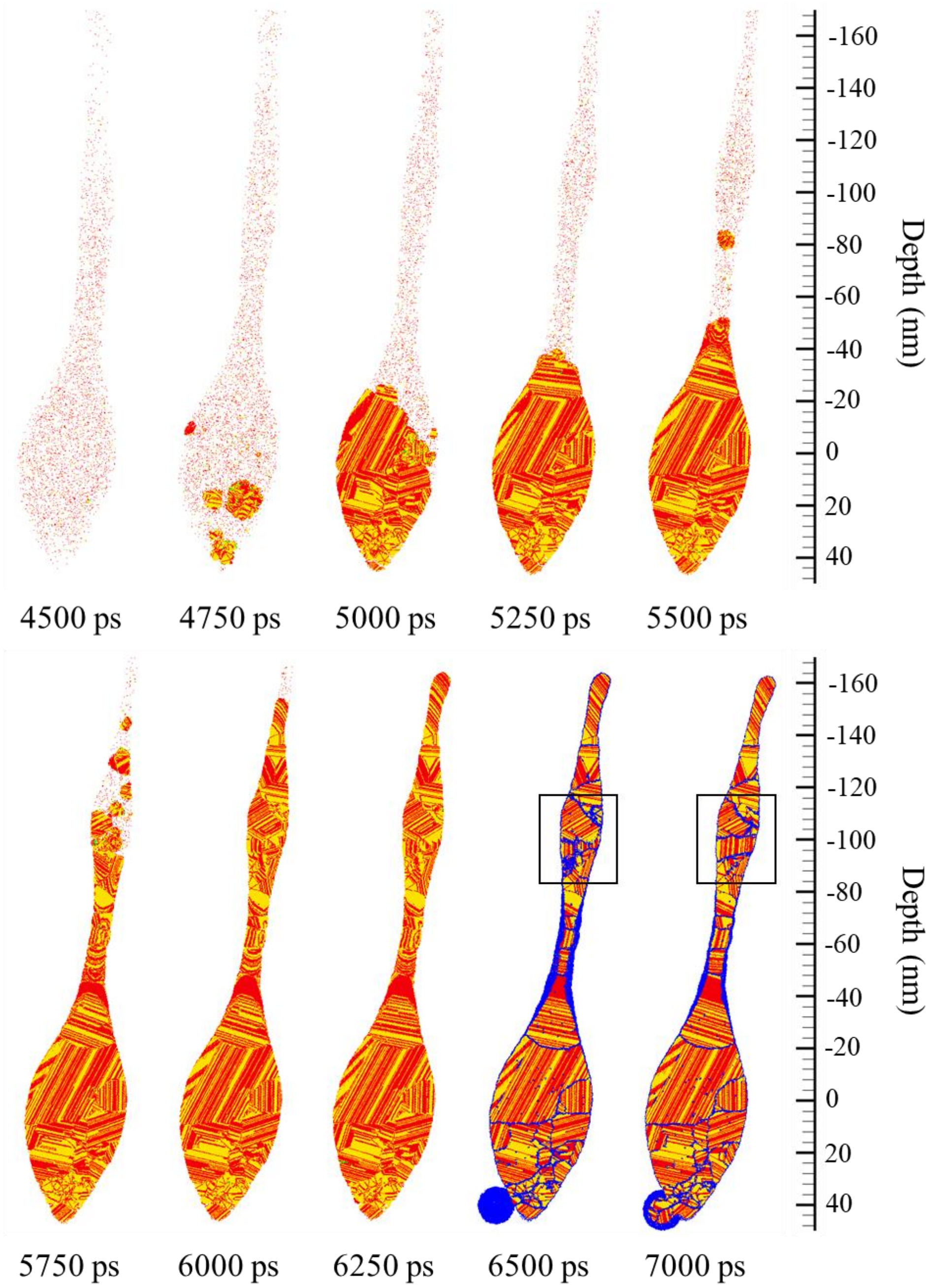

Figure 66. Snapshots illustrating the resolidification process in the upper part of spike A marked in Figures 60 and 61. The atomic configurations are shown for a 10 nm thin slice cut by (010) planes passing through the nanospike, with the views of the cross sections along the [010] direction. The atoms are colored according to their local structural environment as in Figure 63. The atoms that belong to the liquid phase, crystal defects, or free surfaces are blanked for the time from 4500 ps to 6250 ps. While all atoms are shown at the time of 6500 ps and 7000 ps to illustrate the grain coarsening in the region marked by the black rectangles.

6.4 Cluster distribution in the ablation plume generated by femtosecond laser ablation of the Ag target

As discussed in the previous section, laser heating of the Ag target in the regime of phase explosion leads to the decomposition of the surface region into vapor and clusters/droplets, forming a multi-component ablation plume expanding from the initial surface. Figures 67-69 show the snapshots for a broad range of distance from 0.15 μm below the original free surface up to 1.85 μm, 3.85 μm, and 5.85 μm above the surface at times of 600 ps, 1500 ps, and 3150 ps after laser irradiation, respectively. A hierarchical structure of the ablation plume exhibiting spatial segregation of clusters of different sizes in different positions is apparent: in the top part of the plume only vapor atoms and small clusters are observed, medium-size clusters are predominantly localized in the middle of the plume, and in the vicinity of the target surface, large clusters are formed through decomposition of the complex interconnected liquid structure and gradually develop into well-defined spherical liquid droplets.

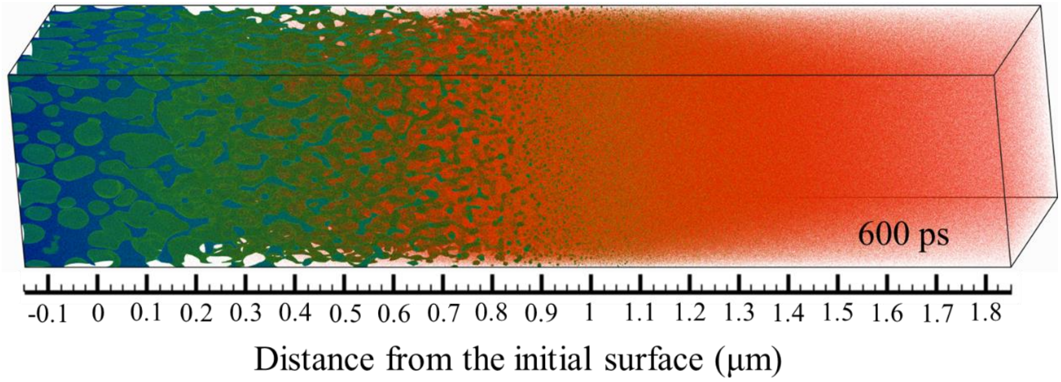

Figure 67. Atomic configuration of the ablation plume predicted in the large-scale TTM-MD simulation of laser ablation of a bulk Ag target irradiated by a 100 fs laser pulse at an absorbed fluence of 3000 J/m^2. The snapshot is plotted for a time of 600 ps after laser irradiation. The lateral dimension of the system is 400 nm. The atoms are colored according to their potential energies.

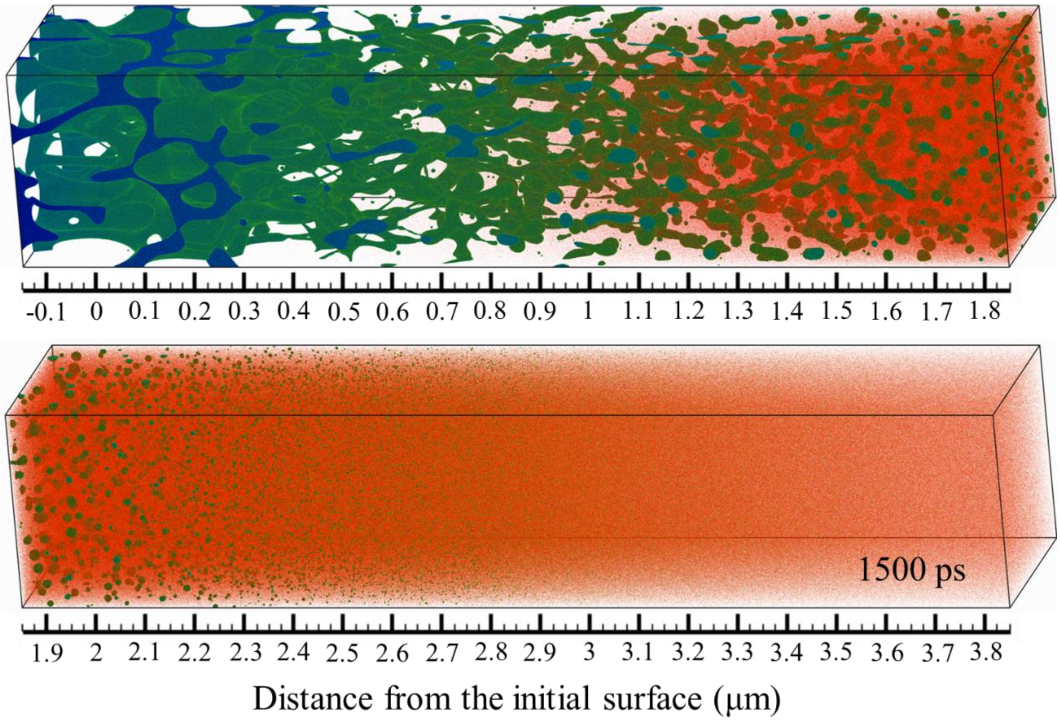

Figure 68. Atomic configuration of the ablation plume predicted in the large-scale TTM-MD simulation of laser ablation of a bulk Ag target irradiated by a 100 fs laser pulse at an absorbed fluence of 3000 J/m^2. The snapshot is plotted for a time of 1500 ps after laser irradiation, and is shown as a sequence of two consecutive fragments covering a range from 0.15 μm below the level of the initial surface of the target up to 3.85 μm above the surface to provide a broader view of the ablation plume. The lateral dimension of the system is 400 nm. The atoms are colored according to their potential energies.

Contour plots of the spatial density distribution of clusters of different sizes at 600 ps, 1500 ps, and 3150 ps after laser excitation, Figure 70, provide a detailed analysis of the dynamic evolution of the ablation plume. The large lateral computational size of 400 nm ensures a statistically adequate representation of the spatial distribution of medium and large clusters. Figures 70a,c,e show the distributions of individual atoms and clusters consisting of up to 1000 atoms, and Figures 70b,d,f show the distribution of all clusters and droplets in the ablation plume based on the values of their radius. The radius of each cluster is calculated according to the number of atoms, $R = \sqrt[3]{\frac{3N}{4\pi\rho_0}}$, where $\rho_0 = 51.95$ nm^{-3} is the number density of liquid Ag at the melting temperature, and N is the number of atoms in the cluster. Therefore, a cluster consisting of 1000 atoms has the radius of 1.66 nm. Each scattering point in Figures 70b,d,f is plotted by counting all clusters/droplets that have similar radius within a range of 0.5 nm difference. The distributions of individual atoms and small clusters consisting of less than 200 atoms have peaks at ~1 μm, ~2.4 μm, and ~6 μm from the initial surface, respectively, at 600 ps, 1500 ps, and 3150 ps after laser irradiation. The shape of the distributions characterizes a free expansion of the vapor atoms and small clusters in both directions away from the target and toward the target, the latter is resisted by the interconnected liquid structure and large droplets, as manifested by the asymmetric shape of the distribution with steeper lower profile, especially at 3150 ps. The spatial distribution of larger clusters and liquid droplets shift closer the target surface with increasing size. Liquid droplets consisting of more than 0.1 million atoms, which correspond to the radius larger than 7.7 nm, can only be found below 4.4 μm from the initial surface of the target.

The spatial segregation of clusters and droplets of different sizes in different parts of the ablation plume have also been observed in previous MD simulations[8,84,291,43,297,300,301] and combined MD-Direct Simulation Monte Carlo (DSMC) simulations[310 - 313] of laser ablation of metals and molecular systems. Computational predictions of the layered structure of the ablation plume are related to experimental results of plume imaging[300,310,314-318] and spatial- and time-resolved soft X-ray absorption spectroscopy probing[319,320], which reveal spitting of the plume into the fast vapor-phase component followed by slower nanoparticles. To describe the characteristic velocities and temperatures of the ejected vapor atoms and clusters/droplets in this work, the flow velocities in the direction normal to the target surface, as well as translational and internal temperatures calculated from the instantaneous atomic velocities are investigated.

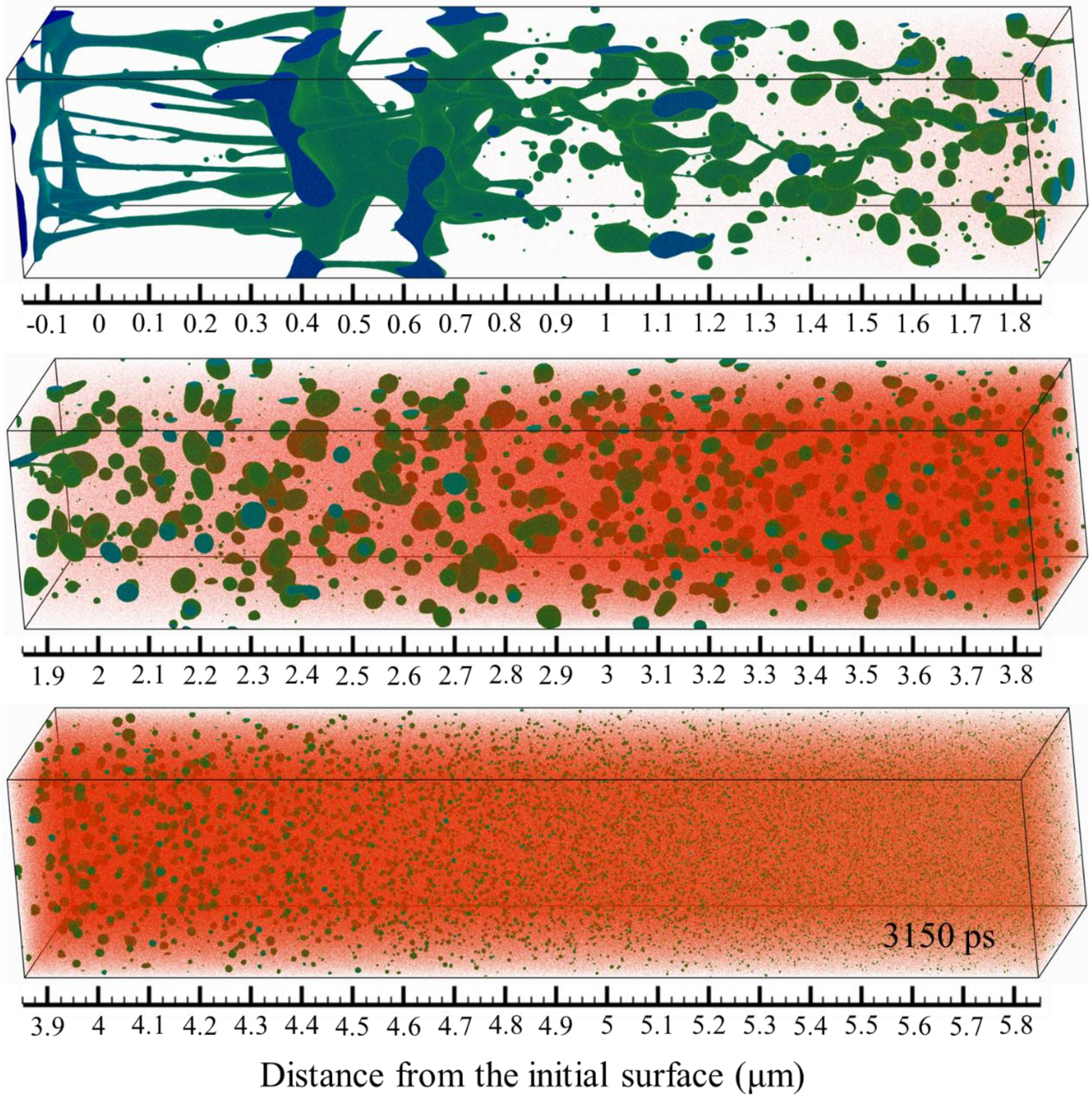

Figure 69. Atomic configuration of the ablation plume predicted in the large-scale TTM-MD simulation of laser ablation of a bulk Ag target irradiated by a 100 fs laser pulse at an absorbed fluence of 3000 J/m^2. The snapshot is plotted for a time of 3150 ps after laser irradiation, and is shown as a sequence of three consecutive fragments covering a range from 0.15 μm below the level of the initial surface of the target up to 5.85 μm above the surface to provide a broader view of the ablation plume. The lateral dimension of the system is 400 nm. The atoms are colored according to their potential energies.

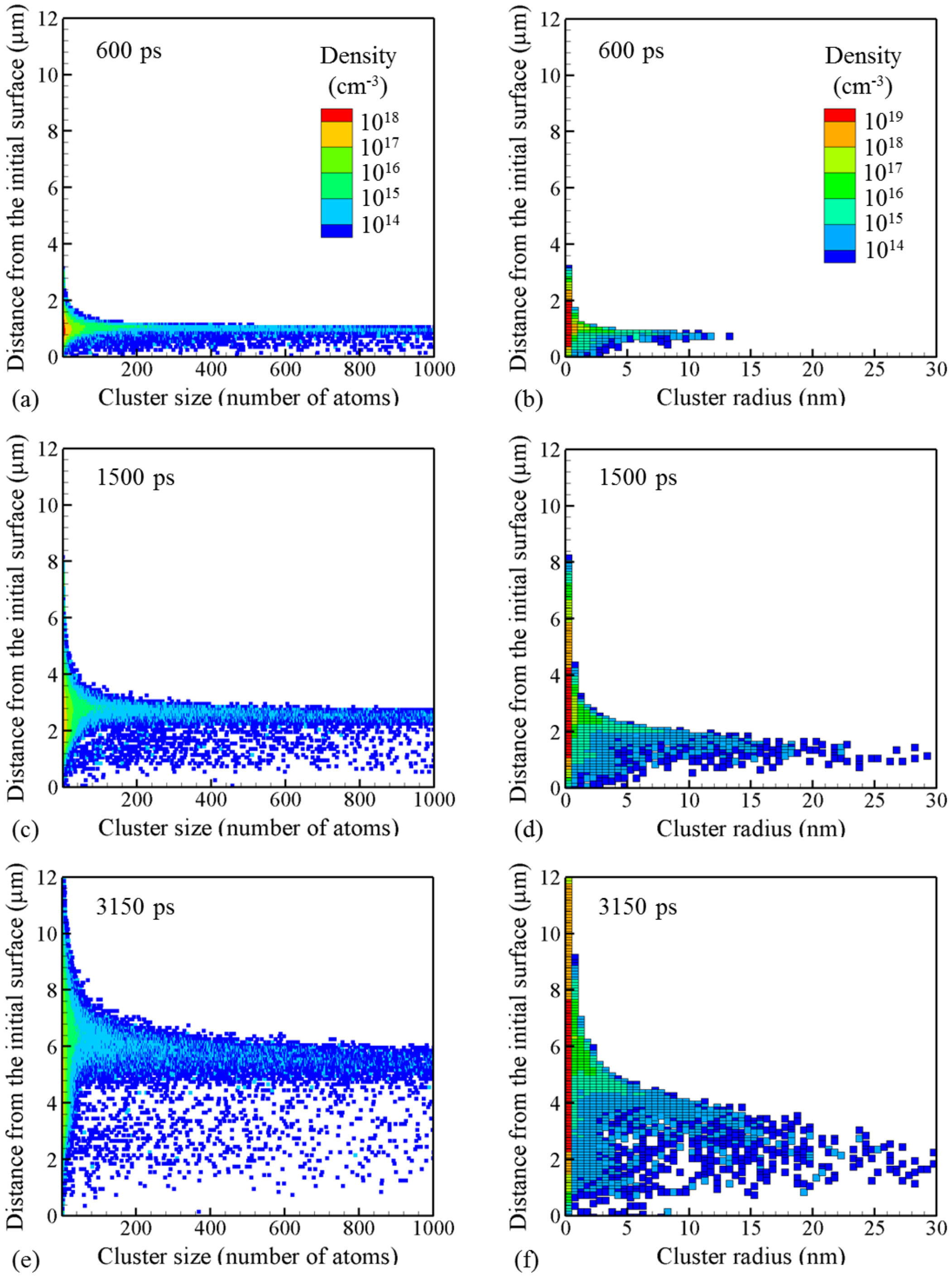

Figure 70. Density plots showing spatial and size distributions of clusters in the ablation plume at 600 ps (a, b), 1500 ps (c, d), and 3150 ps (e, f) after laser irradiation. The results are predicted from the large-scale TTM-MD simulation of laser ablation of a bulk Ag target with lateral dimension of 400 nm irradiated by a 100 fs laser pulse at an absorbed fluence of 3000 J/m^2. In (a,c,e), density distributions of individual atoms and clusters consisting of up to 1000 atoms with respect to the distance from the initial target surface are shown, and the color scale is shown in (a). In (b,d,f), density distributions are computed for all components of the plume, by

counting the clusters/droplets with similar radius within a 0.5 nm range of difference, and the color scale is shown in (b).

The flow velocity for different plume components at different distances from the surface is plotted in Figure 71. The vapor atoms at the top of the ablation plume expand with velocity exceeding 5500 m/s, whereas the maximum velocity of atomic clusters consisting of less than 25 atoms is ~3000 m/s. The maximum velocity of larger (26-1000 atoms) clusters is only achieved around 2000 m/s, and the flow velocity of large droplets containing more than 0.1 million atoms is below 1500 m/s. The flow velocity increases almost linearly with the distance from the surface, validating the characteristic of the free-expansion scenario mentioned above, that all components of the plume expand both in the direction of plume expansion and towards the target surface.

The thermal motions of the clusters are described through translational temperature and internal temperature, where the former is calculated from the radial components of the velocity of individual atoms and clusters which excludes the contribution from the flow velocity, while the latter is defined from the kinetic energy of the atomic motion in the clusters’ center of mass frame of reference. The equations for calculation of the translational and internal temperature, respectively, can be expressed as $T_{trans} = \frac{N m_{Ag}\left({v_x^c}^2 + {v_y^c}^2\right)}{2k_B}$ and $T_{int} = \frac{m_{Ag}\sum_{i=1}^{N}\left[\left(v_x^i - v_x^c\right)^2 + \left(v_y^i - v_y^c\right)^2 + \left(v_z^i - v_z^c\right)^2\right]}{3k_B(N-1)}$, where N is the number of atoms in the cluster, m_{Ag} is the mass of a single Ag atom, v_x^c, v_y^c and v_z^c are three components of the velocities of individual atoms or center of mass of clusters, v_x^i, v_y^i and v_z^i are three components of the velocity of atom *i* in the cluster, and $(N-1)$ in the equation for internal temperature is because that the translational degrees of freedom of the cluster’s center of mass should be excluded from the calculation of the kinetic energies. These two characteristic temperatures are plotted in Figure 72, by averaging over atoms and clusters located at different distances from the initial surface. As shown in Figure 72, the translational and internal temperatures for small clusters are on the same level, indicating that local thermal equilibration is achieved through collision with surrounding clusters and the spread of the radial velocities is associated with the thermal motion. The translational temperature for larger clusters (not shown here), however, are found to be significantly higher than their internal temperature, indicating that the collisions with surrounding smaller species in the plume are not sufficient for thermal equilibration. In fact, the high radial velocity reflects the dynamics of active hydrodynamic motion of the liquid material during the development of the ablation plume.[43] Despite of being ejected from the regions deeper under the surface, where the deposited laser energy and degree of overheating is less, the larger clusters in the plume also have on average substantially higher internal temperatures as compared to the smaller ones, as shown in Figures 72b,d,f. The lower temperature of the smaller clusters can be attributed to a more vigorous phase explosion and a fast expansion of the upper part of the plume where large fraction of the smaller clusters is located. These two factors provide significantly more efficient cooling channel, where the thermal energy is transformed to the potential energy of disintegration of the strongly overheated material and to the kinetic energy of the plume expansion, compared to the slower cooling of the larger clusters limited by normal evaporation. Significant variations of the translational and internal temperatures with distance from the initial surface are observed in Figure 72. The decrease of the temperature in the direction of flow of the plume in the range of 1-2 μm at 600 ps, 2-5 μm at 1500 ps, and 4-10 μm at 3150 ps can be explained by the adiabatic expansion of the plume. After reaching the minimum value, the temperature of small clusters starts to increase towards the front part of the expanding plume, which can be attributed to the lack of equilibration in this region where cluster-cluster collisions are rare due to low density of ejected species.

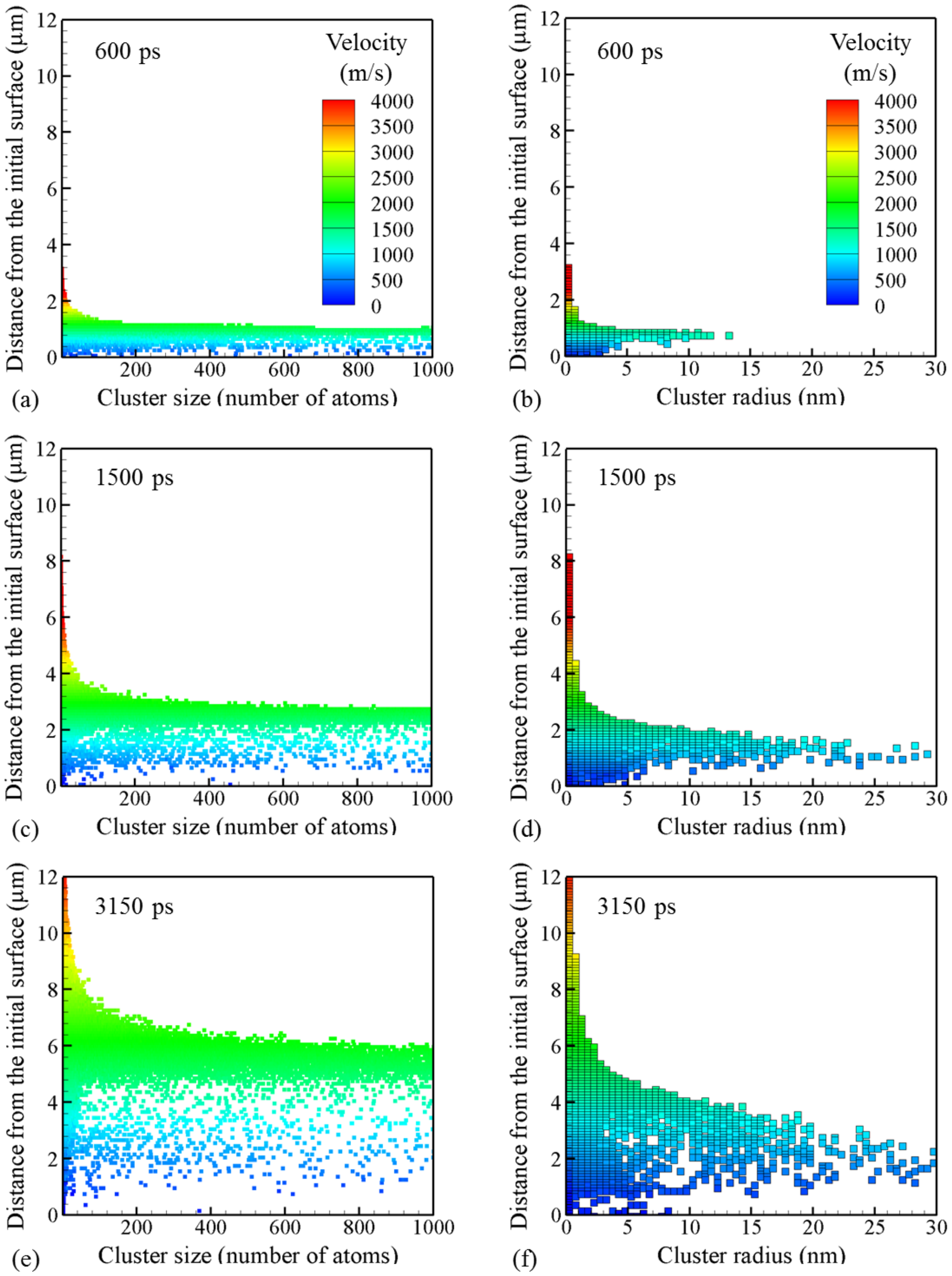

Figure 71. Flow velocity of different plume components in the direction normal to the irradiated target surface at 600 ps (a, b), 1500 ps (c, d), and 3150 ps (e, f) after laser irradiation. The results are predicted from the large-scale TTM-MD simulation of laser ablation of a bulk Ag target with lateral dimension of 400 nm irradiated by a 100 fs laser pulse at an absorbed fluence of 3000 J/m^2. In (a,c,e), flow velocities of individual atoms and clusters consisting of up to 1000 atoms with respect to the distance from the initial target surface are shown. In (b,d,f), flow velocities are computed for all components of the plume, by counting the clusters/droplets with similar radius within a 0.5 nm range of difference. The color scales are provided in (a,b).

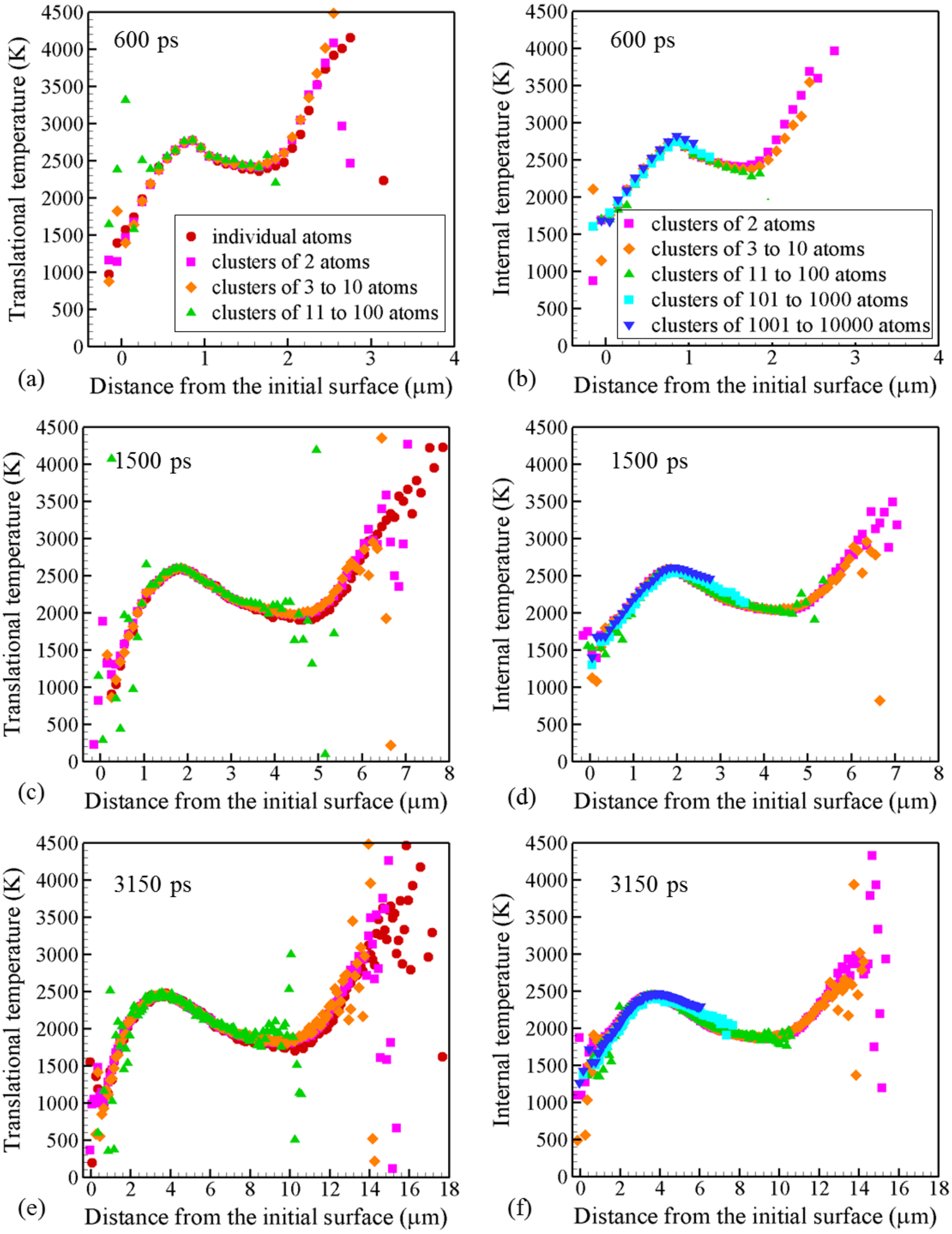

Figure 72. Translational (a,c,e) and internal (b,d,f) temperatures of different plume components as functions of the distance from the initial target surface. The translational temperature is calculated from the velocity components of the ejected atoms or clusters in the direction parallel to the irradiated surface. The internal temperature is calculated from the kinetic energies of atomic motion in the clusters' center of mass frame of reference. The results are predicted from the large-scale TTM-MD simulation of laser ablation of a bulk Ag target with lateral dimension of 400 nm irradiated by a 100 fs laser pulse at an absorbed fluence of 3000 J/m^2, and are shown for the time of 600 ps (a,b), 1500 ps (c,d), and 3150 ps (e,f) after the laser pulse.

In order to characterize the overall composition of the ablation plume, the probability distribution as a function of cluster size is plotted in Figure 73. Although the large lateral size of 400 nm ensures sufficient analysis of small- and medium-size clusters, larger droplets exceeding tens of nanometers are only observed occasionally and reliable statistical results cannot be obtained. To generate the probability distribution for all clusters, the following method is adopted: Assume k_1 number of clusters consisting of N_1 atoms are observed in the ablation plume, but no cluster is found with smaller size until N_0 or larger size up to N_2. The number of clusters consisting of N_0 and N_2 atoms is found as k_0 and k_2, respectively. The probability of finding a cluster with similar size as N_1, *e.g.*, $\frac{N_0+N_1}{2} < N \leq \frac{N_1+N_2}{2}$, where N is the number of atoms in this cluster, is assumed to be the same as the probability of finding the cluster containing N_1 number of atoms. Therefore, the probability of finding clusters in this size range, $\frac{N_0+N_1}{2} < N \leq \frac{N_1+N_2}{2}$, can be estimated as $P(N) = \frac{N_1}{\frac{N_1+N_2}{2} - \frac{N_0+N_1}{2}}$. Following this method, the cumulative probability for all clusters is equal to 1.

The probability distribution in Figure 73 is plotted in double-logarithmic scale, showing the decay of the probability to find clusters of increasing size that can be described by a power law, $p(N) \sim N^{-\tau}$, where the exponent τ is different for small and large clusters. Three regimes corresponding to atomic clusters consisting of 2-5 atoms, small clusters consisting of 6-25 atoms, and larger clusters and liquid droplets, respectively, are identified that each regime corresponds to a different power law exponent. In the regime of large clusters and liquid droplets, τ is fitted for the size range of 100 to 5×10^4 atoms, shown as the gray region in Figure 73. The power law dependence of the cluster yield distribution on cluster size has been predicted for the gas-liquid phase transition at the critical point[321] and for the fragmentation process[322-324]. However, the complex and highly non-equilibrium character of the laser ablation process makes it difficult to establish a direct link between any of the existing theoretical models and the results of present simulations, and to set a distinct threshold of cluster size for different regimes of fitting. Therefore, the power law fitting in Figure 73 is only used to provide a quantitative description of the cluster distribution. The existence of two values of exponents of power law for the cluster size distribution in the small- and large-size regimes suggests the different origins for different components of the ablation plume. The vapor-phase atoms and small clusters are explosively released in the strongly overheated material in the top part of the target, whereas larger clusters and liquid droplets are formed at later time as a result from disintegration and coarsening of the transient structure of interconnected liquid regions. Similar size distributions following the power law with different exponents for small and large clusters are also observed in previous atomistic simulation of laser ablation of metal target,[84] one-component molecular solid system,[43] and polymer solutions,[301,303,325] as well as cluster sputtering by ion or cluster bombardments,[326-328] where the values of the power law exponents for different regimes are close to the ones predicted in this work. Experiments of laser ablation of organic targets[325,329,330] also report the power law mass distribution with exponents semi-quantitatively consistent with computational results. The similar probability distribution functions of the cluster size revealed for different target materials and under a broad range or irradiation conditions highlight the general character of the ablation plume.

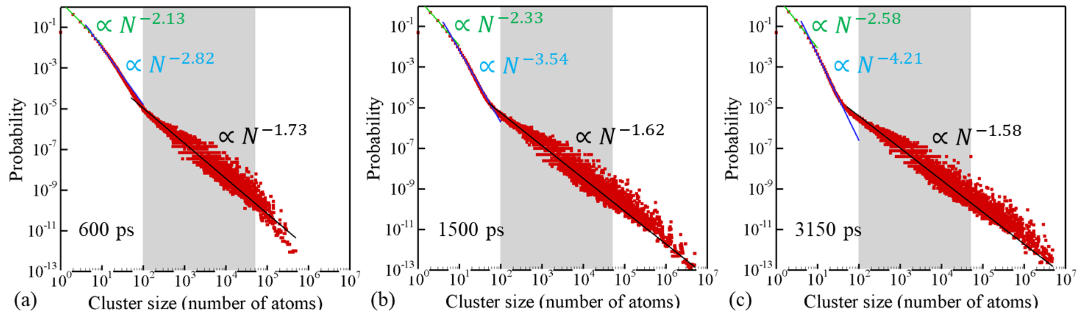

Figure 73. Cluster size distribution in the ablation plume generated at the time of 600 ps (a), 1500 ps (b), and 3150 ps (c) after laser irradiation. The results are predicted from the large-scale TTM-MD simulation of 100 fs laser pulse irradiation of a bulk Ag target at an absorbed fluence of 3000 J/m^2. The green, blue, and black lines are power law fittings of the data points in three regions that correspond to the 2-5 atom clusters, clusters consisting of 6-25 atoms, and larger clusters. The corresponding power-law dependences are indicated in the plots. The gray regions between 100 and 50000 atoms indicate the range of cluster size used for fitting in the large cluster regime.

The mass distributions of different plume components are plotted in Figure 74. The blue data points show the total mass for each size of cluster, calculated by multiplying the cluster size with the number of clusters found at this size. The red data points show the cumulative mass fraction as a function of cluster size, defined as the total number of atoms in clusters smaller than certain size divided by the total number of atoms in all clusters forming the ablation plume. The clusters consisting more than 5 million atoms, which account for more than 1 wt. % of the ablation plume and start to appear at 1500 ps, are not included in the calculation of mass fractions. Several of these super-large clusters can contribute up to 20 wt. % of the ablation plume and obscure the mass fraction of small- and medium-size clusters. The parallel blue data sets for mass of large clusters is resulted from the double-logarithm plot of total mass for each size of cluster depending on cluster size, so that the slope of the parallel datasets is 1 and the lowest dataset corresponds to cluster sizes at which only single cluster is found. At 600 ps, the vapor atoms and atomic clusters consisting of up to 100 atoms account for ~50 wt. % of the ablation plume, due to their significantly large number in the plume as shown in the probability distribution in Figure 73. After 1500 ps, the formation of large clusters and liquid droplets consisting of more than 10^5 atoms (corresponding diameter larger than 7.7 nm) through disintegration of the interconnected liquid structure predominantly contributes to the mass of the ablation plume (~ 70 wt. % at 1500 ps and ~80 wt. % at 3150 ps), as indicated by the abrupt increase of the cumulative mass fraction. The generation of large droplets is also manifested from the plot of total mass as a function of cluster size (blue data points), and by a decrease of the absolute value of the power law exponent in the regime of large cluster in Figure 73.

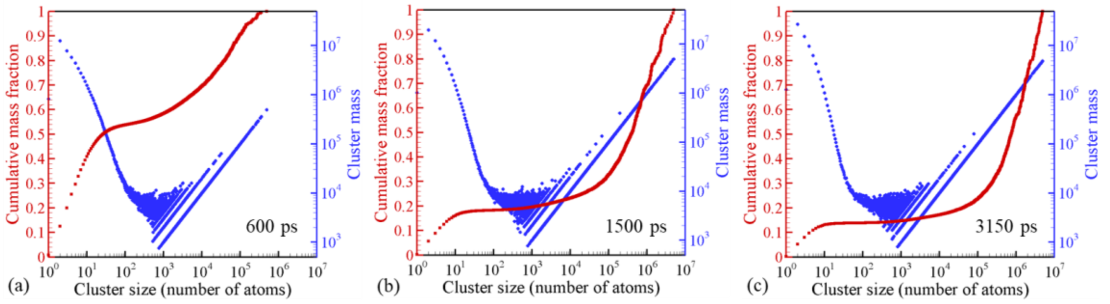

Figure 74. Mass fraction of different components in the ablation plume at the time of 600 ps (a), 1500 ps (b), and 3150 ps (c) after laser irradiation. The results are predicted from the large-scale TTM-MD simulation of 100 fs laser pulse irradiation of a bulk Ag target at an absorbed fluence of 3000 J/m^2. The blue data points illustrate the total number of atoms found for each cluster size. The red data points show the cumulative mass fraction, calculated by dividing the total number of atoms for clusters smaller than certain size by the total number of atoms in the ablation plume, as a function of cluster size. The super-large cluster consisting more than 5 million atoms (>1% mass fraction of the plume) and liquid regions that are connected to the bulk of the target are not included in the calculations.

6.5 Effect of computational size on the predictions of surface morphology and particle generation by laser ablation

The large-scale simulation performed for the system with a lateral size of 400 nm, although capable of providing reliable descriptions of the dynamics of the ablation plume and modification of surface morphology, comes with high computational cost. Smaller-scale simulations can save the computational resource, but their ability to fully capture some characteristics in the course of laser ablation, such as generation of large droplets exceeding 100 nm, and formation of several nanospikes with various shape and nanocrystalline structure, is limited by the size of the computational system. To find the optimized computational size, which requires reasonable computational time while enabling realistic representation of the laser-induced processes of interest, the sensitivity of computational predictions to the lateral size of the simulated system is investigated. The results from the large-scale simulation with 400 nm lateral dimension, as discussed in the previous two sections, are compared with results from two smaller-scale simulations performed for the same system but with lateral size of 20 nm and 100 nm under the same irradiation conditions.

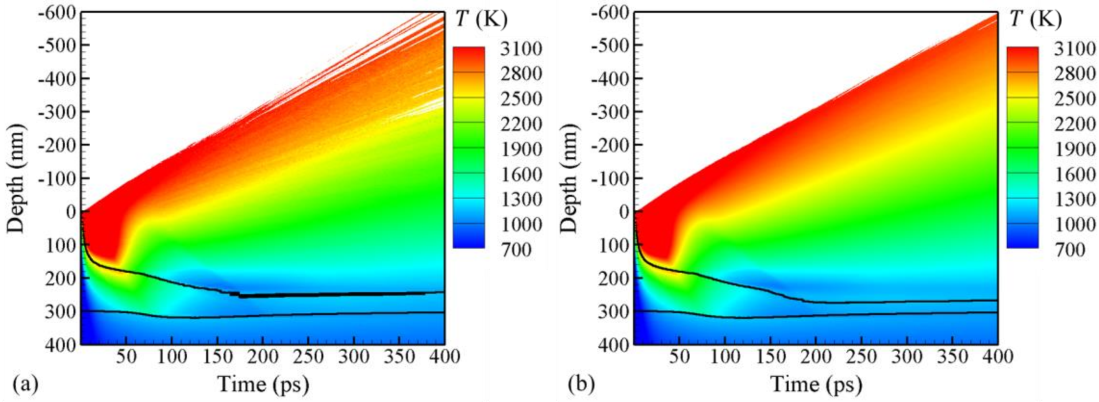

Figure 75. Contour plots of the spatial and temporal evolution of lattice temperature in TTM-MD simulations of a Ag bulk target with lateral size of 20 nm (a) and 100 nm (b), irradiated by a 100 fs laser pulse at an absorbed fluence of 3000 J/m^2. The black solid lines near the surface of the targets show the movement of the crystal-liquid interface, and the black lines in the lower parts of the contour plots show the location of the nonreflecting boundary applied at the bottom of the MD part of the computational domain.

The temporal and spatial evolutions of the lattice temperature in the smaller-scale simulations are shown in Figure 75, predicting similar superheating in the surface region of the target that leads to the onset of phase explosion. The explosive decomposition of the target surface into vapor and small clusters, forming the front of the ablation plume, is shown in the snapshots for the system with lateral size of 20 nm (Figure 76) and 100 nm (Figure 77). Due to the limited lateral size of 20 nm, the growth and coalescence of the subsurface voids are strongly affected by the periodic boundary conditions applied on lateral directions. Therefore, the breakdown of the liquid bridges connecting the spalled layers with the remaining target occurs at much earlier time of 600-700 ps, compared to the large system with 400 nm lateral size. The heat flow from the top liquid layer to the bulk of the target is hampered by the early disintegration of the spalled liquid part, leading to a smaller value of maximum melting depth, ~260 nm, compared to the value for the large system, ~270 nm. The ejected layers have thickness ranging from ~10 nm to ~40 nm and are stabilized by the periodic boundary conditions, whereas the spalled layers evolve into large spherical droplets as shown in Figure 59 for the large system.

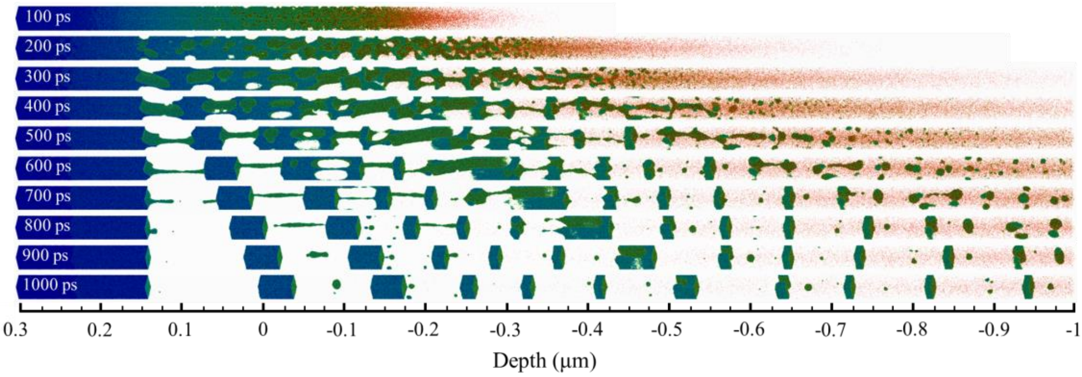

Figure 76. Snapshots of atomic configurations predicted in the TTM-MD simulation of laser ablation of a Ag bulk target with the lateral size of 20 nm. The laser pulse duration of 100 fs and the absorbed fluence of 3000 J/m^2 are the same as in Figure 59. The snapshots are shown for a wide range of time to illustrate the evolution of the liquid structure near the target surface. The atoms are colored according to their potential energies.

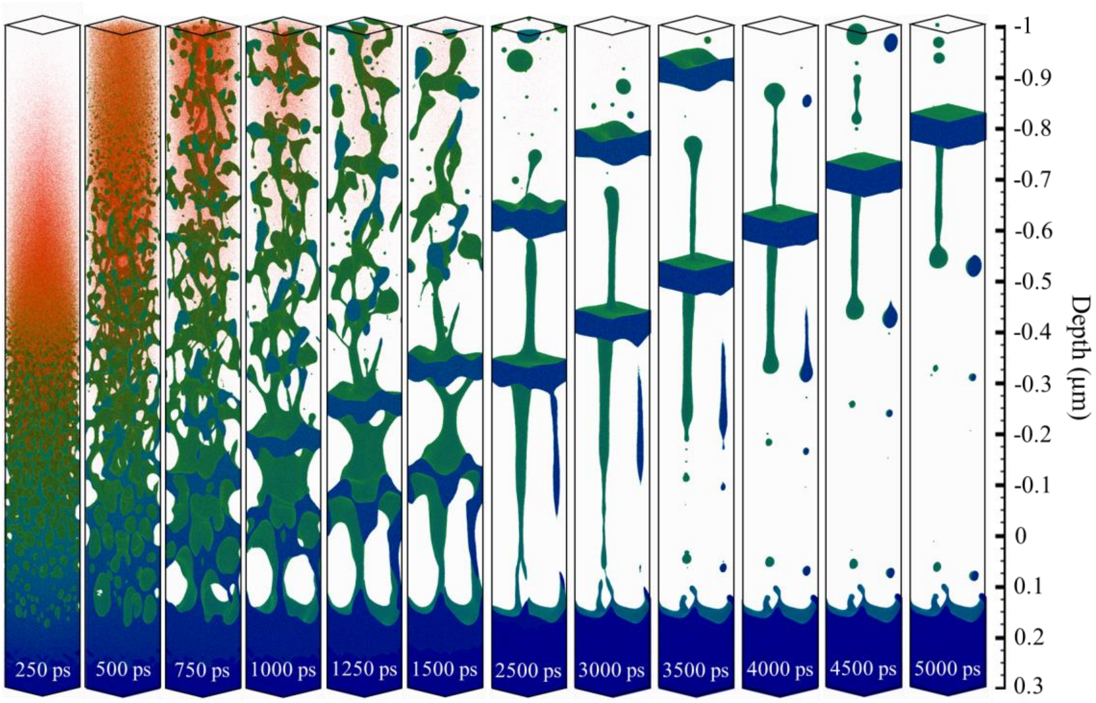

Figure 77. Snapshots of atomic configurations predicted in the TTM-MD simulation of laser ablation of a Ag bulk target with the lateral size of 100 nm. The laser pulse duration of 100 fs and the absorbed fluence of 3000 J/m^2 are the same as in Figure 59. The snapshots are shown for a wide range of time to illustrate the evolution of the liquid structure near the target surface. The atoms are colored according to their potential energies.

In Figure 77, the lateral size of 100 nm is comparable to the size of the large subsurface voids, enabling a reasonable representation of the dynamics of the interconnected liquid part and subsequent formation of two nanospikes on the target surface. The view of the nanospike is affected by the periodic boundary conditions applied on lateral directions in Figure 77. The observation of only ~10 nanospikes formed in the system with 400 nm lateral size and two nanospikes in the system with 100 nm lateral size indicates that the characteristic distance between the nanospikes is comparable to 100 nm. In this case, the simulation performed for the system with smaller size, *e.g.*, 20 nm as in Figure 76, can only predict a smooth surface. The stabilization of the ejected layer in the form of thin film, similar as in the system with 20 nm lateral size (Figure 76), suggests that a large droplet with size exceeding 100 nm can be expected from the spalled liquid layer by short pulse laser ablation.

The spatial and size distributions of clusters in the ablation plume generated from the systems with lateral sizes of 20 and 100 nm are shown in Figures 78 and 79, respectively. Generation of vapor atoms and small clusters containing less than 1000 atoms, which corresponding to a radius of ~1.66 nm, can be reliably described even by the lateral size of 20 nm, showing the similar density distribution as in Figure 70 predicted from the computational size of 400 nm. Note that in Figures 78 and 79, the resolution in density is 16 and 400 times smaller, respectively, compared to Figure 70, with detectable minimum density of 1×10^{15} cm^{-3} and 2.5×10^{16} cm^{-3} since the clusters are counted in a 100 nm-thick layer. For larger clusters/droplets with radius on the order of several even tens of nanometers, however, the lateral size of 20 nm is not sufficient to get statistically reliable information of their distributions. Although the cluster distribution predicted for the system size of 100 nm has a good agreement with the results from the system with lateral size of 400 nm, the comparable scale with the large clusters/droplets substantially limits its capability to provide statistically reliable representation of the composition and evolution of the ablation plume. Especially, for the large liquid droplet with radius exceeding 120 nm evolved from the ejected layer close to the target, only the simulation with 400 nm lateral size is able to eliminate the effect of periodic boundary conditions.

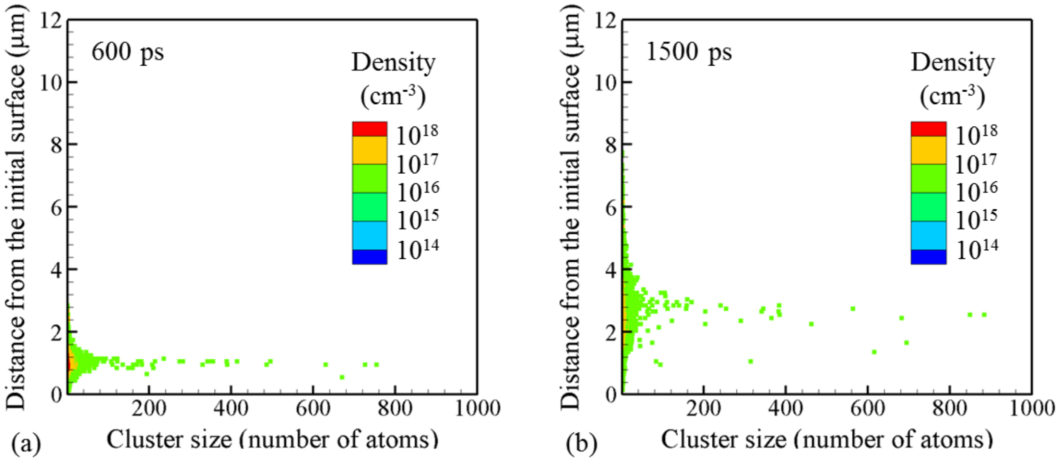

Figure 78. Density plots showing spatial and size distributions of clusters in the ablation plume at 600 ps (a) and 1500 ps (b) after laser irradiation. The results are predicted from the TTM-MD simulation of laser ablation of a bulk Ag target with lateral dimension of 20 nm irradiated by a 100 fs laser pulse at an absorbed fluence of 3000 J/m^2. The density distributions with respect to the distance from the initial target surface are shown for individual atoms and clusters consisting of up to 1000 atoms. To enable a clear comparison with the results from the larger-scale (400 nm) simulation, the color scales are the same as in Figure 70, but cluster density below 2.5×10^{16} cannot be resolved.

The probability distributions of clusters as a function of their size in the system with lateral sizes of 20 nm and 100 nm are plotted in Figures 80 and 81, respectively. The power law exponents for atomic clusters have good quantitative agreement with that predicted in the system with 400 nm size. However, the power law exponent predicted for large clusters, -1.65 at 600 ps and -1.09 at 1500 ps, generated in the system with 20 nm lateral size is smaller than the values obtained for other system sizes. This underestimation of the rate of probability decay of finding clusters with increasingly larger size, especially at the time of 1500 ps, can be related to the generation and stabilization of the numerous liquid spalled layers characteristic in the small system, where the periodic boundary conditions applied on the lateral directions play an important role. Indeed, the cluster distributions in the ablation plume are consistent for the system sizes of 100 nm and 400 nm.

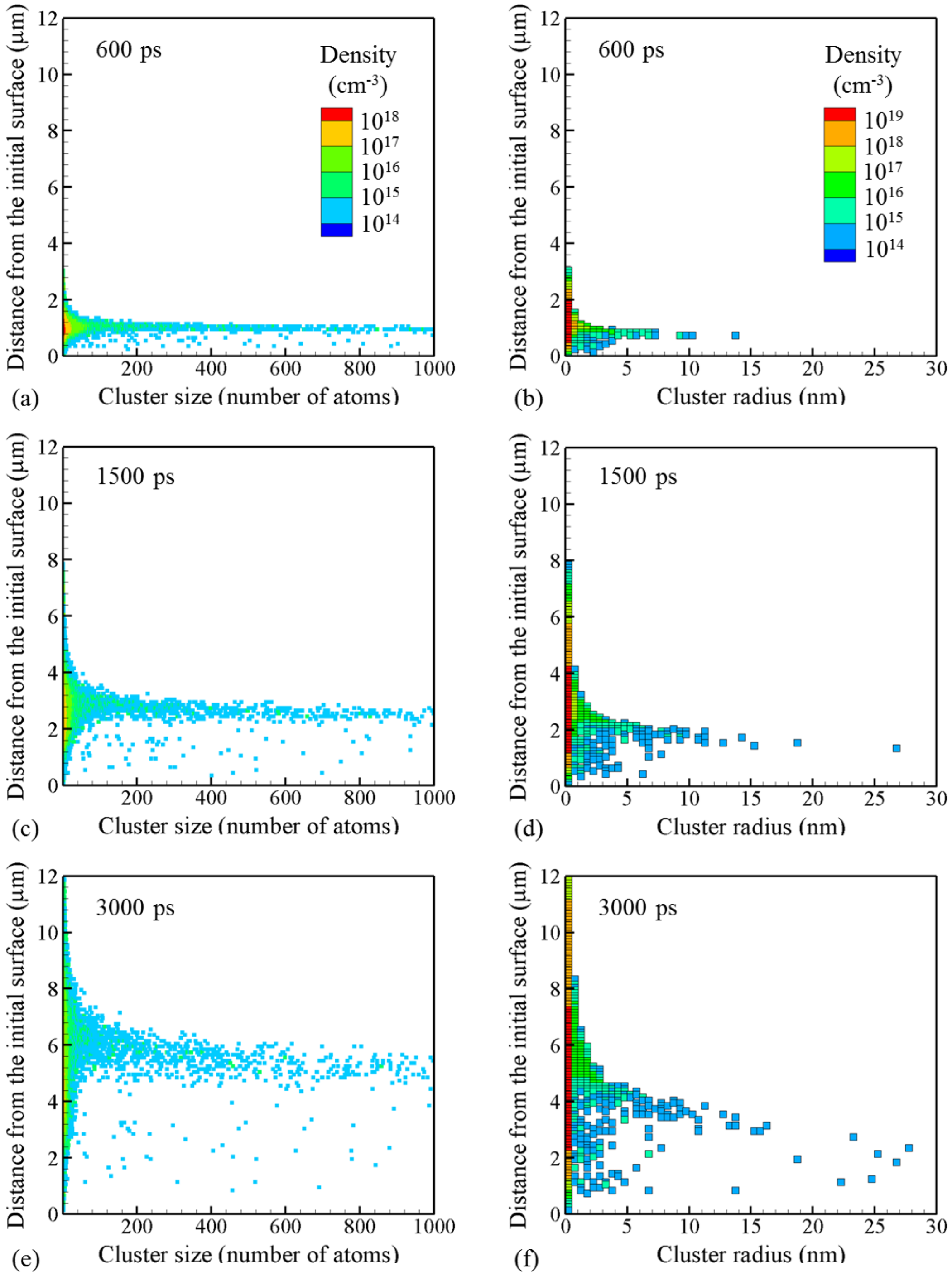

Figure 79. Density plots showing spatial and size distributions of clusters in the ablation plume at 600 ps (a, b), 1500 ps (c, d), and 3000 ps (e, f) after laser irradiation. The results are predicted from the TTM-MD simulation of laser ablation of a bulk Ag target with lateral dimension of 100 nm irradiated by a 100 fs laser pulse at an absorbed fluence of 3000 J/m^2. In (a,c,e), density distributions of individual atoms and clusters consisting of up to 1000 atoms with respect to the distance from the initial target surface are shown. In (b,d,f), density distributions are computed for all components of the plume, by counting the clusters/droplets with similar radius within a 0.5 nm range of difference. To enable a clear comparison with the results from the larger-scale

(400 nm) simulation, the color scales are the same as in Figure 70, but cluster density below 1×10^{15} cannot be resolved.

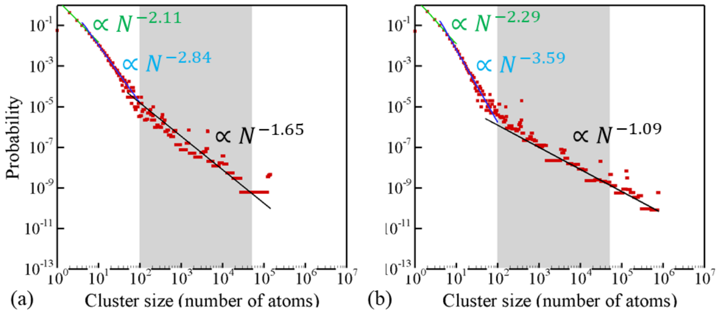

Figure 80. Cluster size distribution in the ablation plume generated at the time of 600 ps (a), 1500 ps (b), and 3000 ps (c) after laser irradiation. The results are predicted from the TTM-MD simulation of laser ablation of a bulk Ag target with lateral dimension of 20 nm. The laser pulse duration of 100 fs and the absorbed fluence of 3000 J/m^2 are the same as in Figure 73. The green, blue, and black lines are power law fittings of the data points in three regions that correspond to the 2-5 atom clusters, clusters consisting of 6-25 atoms, and larger clusters. The corresponding power-law dependences are indicated in the plots. The gray regions between 100 and 50000 atoms indicate the range of cluster size used for fitting in the large cluster regime.

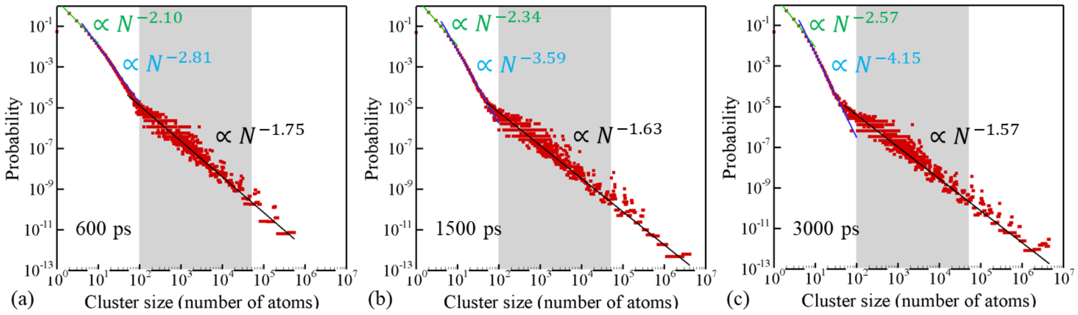

Figure 81. Cluster size distribution in the ablation plume generated at the time of 600 ps (a), 1500 ps (b), and 3000 ps (c) after laser irradiation. The results are predicted from the TTM-MD simulation of laser ablation of a bulk Ag target with lateral dimension of 100 nm. The laser pulse duration of 100 fs and the absorbed fluence of 3000 J/m^2 are the same as in Figure 73. The green, blue, and black lines are power law fittings of the data points in three regions that correspond to the 2-5 atom clusters, clusters consisting of 6-25 atoms, and larger clusters. The corresponding power-law dependences are indicated in the plots. The gray regions between 100 and 50000 atoms indicate the range of cluster size used for fitting in the large cluster regime.

6.6 Summary

In this section, a large-scale TTM-MD simulation with system size of 400 nm are performed for a Ag target irradiated by a femtosecond laser pulse in the regime of phase explosion. The computational results provide detailed information on the mechanisms responsible for the explosive decomposition of the target surface into mixture of vapor atoms and small clusters, ejection of larger liquid droplets, and the formation of frozen nanospikes. The short laser pulse duration creates conditions of stress confinement, where the relaxation of the laser-induced photomechanical stresses leads to the nucleation, growth, and coalescence of numerous voids in the melted subsurface region of the irradiated target, forming a complex structure of interconnected liquid. Further evolution of this transient liquid structure results in the formation, elongation, and eventual breakdown of multiple liquid bridges that produces a surface morphology with several nanospikes with length ranging from tens of nanometers to ~ 300 nm, as well as ejection of liquid layers that will evolve into large spherical droplets with diameter even exceeding ~240 nm. The high thermal conductivity combined with the strongly localized laser energy deposition leads to rapid cooling during the resolidification process following the laser heating and transient melting of the surface region of the target. In addition, the breakdown of the bridges by ~5.5 ns interrupts the connection between the remaining target and the top layer, which serves as the "heat reservoir" supporting the quasi-steady-state heat flow in the bridges, leading to fast cooling in the top part of the nanospikes. Rapid solidification proceeding under the conditions of strong undercooling involves competing processes of epitaxial regrowth of the crystal part of the bulk target, and homogeneous and growth of new crystallites, defining the complex nanocrystalline structure of the nanospikes. Investigation of the nanostructure of the frozen nanospikes reveals a high density of stacking faults, twins, and a mixed fcc/hcp structure produced from the cross-nucleation of hcp phase on the close-packed faces of the growing fcc crystallites.

Detailed analysis of the composition in the ablation plume uncovers a spatial segregation of clusters of different sizes, with only vapor atoms and small clusters present in the front of the plume that expand with velocity exceeding 3000 m/s. The medium-size clusters are distributed in the middle of the plume, with flow velocity of ~2000 m/s. Large droplets containing more than 0.1 million atoms are found closer to the bulk target with increasing size and move with velocity below 1500 m/s. The overall cluster composition of the ablation plume is characterized by cluster size distribution exhibiting power law exponents, which are different for different regimes of cluster size. This characteristic suggests different origins for the small and large clusters in laser ablation. The majority of individual atoms and small clusters are released in the explosive decomposition of strongly superheated surface region of the target. However, the large clusters and liquid droplets are formed as a result of disintegration and coarsening of the transient interconnected liquid structure. Despite of the small number of large clusters/droplets, they contribute a large fraction of the total mass of the ejected plume.

The sensitivity of computational predictions to the size of the system is examined by comparing the results from the large-scale simulations with two additional simulations performed for small lateral dimensions, $20\ \mathrm{nm} \times 20\ \mathrm{nm}$ and $100\ \mathrm{nm} \times 100\ \mathrm{nm}$, of the computational system. For the system with lateral size of 20 nm, which is much smaller than the characteristic sizes of the voids and ejected liquid droplets, various artificial size effects are resulted, such as easy spallation due to the self-interaction of large voids across the periodic boundary conditions, or layered structure of the ablation plume, where large droplet acquire the form of thin films rather than spherical droplets. Significantly limited size of this computational system, compared to the characteristic distance between the nanospikes (~100 nm), also prevents a realistic representation of the surface morphology. The composition of the ablation plume and modification of the surface morphology, predicted from the simulation for the large system with 400 nm lateral size, can be partially captured by the computational size of 100 nm, but lacking statistically sufficient information.

7. Summary of the dissertation

The rapid and highly localized energy deposition by short pulse laser irradiation have facilitated a number of applications for laser processing and fabrication of materials. Continuous advancement of the laser-based techniques, however, requires a fundamental understanding of the phase and structural transformations under the conditions of laser-induced strong electronic, thermodynamic, and mechanical nonequilibrium. In this dissertation, simulations of the materials response to laser pulse are performed for a broad range of irradiation conditions, from surface melting and resolidification to collective material ejection, providing physical insights into the processes responsible for laser-induced phase transformations, generation of crystal defects, and modification of the surface morphology. The computational studies are conducted by a hybrid TTM-MD model combining the classical molecular dynamics method with a continuum description of the laser interaction with the target, or by an advanced continuum model designed and parameterized based on the information from atomistic simulations. The key results obtained in this study are summarized below.

Multiscale modeling investigation of the effects of laser parameters on the production of point defects and amorphous structure in Si in the course of laser-induced melting and resolidification

First, the non-equilibrium phase and structural transformations under conditions of undercooling, which can contribute to the modification of microstructure in a laser processed Si target, are investigated in a series of atomistic simulations. A transition from the liquid phase to a low-density amorphous structure, manifested by remarkable changes in the structural and thermodynamic properties, is revealed at ~ 0.71 T_m. In the undercooling regime above the amorphous transition temperature, MD simulations of a crystal-liquid coexistence system predict the steady-state propagation of the solidification fronts with velocity depending on the undercooling level. At the rapidly advancing solidification front, formation of high density of vacancies, interstitials, dislocations, and twin boundaries is uncovered. Based on the results from MD simulations, a theoretical description of the temperature dependence of the crystal-liquid interface velocity and the concentration of different types of point defects (single interstitials, single vacancies, and di-vacancies) produced at the solidification front is developed. This information, combined with the threshold temperature for the formation of stable amorphous structure, are used to help design and parameterize an advanced continuum-level model that is capable of describing the kinetics of solidification and point defects in a laser processed Si target.

Based on the multiscale computational approach where atomistic simulations inform the large-scale continuum models, the irradiation regimes leading to the formation of amorphous region with different shapes in the surface region of a Si target are established. 1D continuum simulations are performed for different laser parameters, identifying the fluence thresholds for the onset of amorphous formation in the course laser laser-induced melting and resolidification. The range of fluence leading to the formation of amorphous structure broadens for shorter laser pulse or wavelength, which facilitates amorphization through faster cooling rate. The shape of the amorphous region formed in irradiated target surface, commonly observed in earlier experiments, is reproduced by 2D continuum simulations performed under a broad range of irradiation conditions on the experimental time- and length-scales. The mechanisms responsible for the formation of an amorphous region at the laser spot center, or a ring-shaped amorphous region are uncovered, and the effects of laser fluence, pulse duration, and spot diameter on the amorphous morphology are revealed.

Finally, informed by the types and concentrations of point defects produced at the solidification front from atomistic simulations, the ability of the advanced continuum model to provide quantitative description of the generation and evolution of point defects in laser irradiated Si target is demonstrated. Generation of high density of interstitials and vacancies in the transiently melted and resolidified surface region by nanosecond laser irradiation is revealed. The average concentration of both interstitials and vacancies in the resolidified region is found to be dependent on laser fluence, which is related to the MD prediction of the dependence of point defect density on undercooling levels that can be realized at the solidification front. The effect of fluence on the concentration of laser-induced point defects is validated by experimental measurements. Additional continuum simulations are performed by irradiating the laser-processed Si target with subsequent low power laser pulses below the melting threshold. The elimination of the laser-induced supersaturated point defects through post laser annealing, by providing sufficient heating for defects diffusion and recombination without conducting surface melting, is confirmed. The effect of laser parameters, including fluence, pulse duration, and number of pulses, on the mitigation of point defects is evaluated. This study provides guidance for controlling material microstructure and improving device performance through optimization of laser parameters as well as conditions of thermal annealing after laser processing.

Comprehensive study of the mechanisms responsible for the generation of crystal defects at the rapidly propagating solidification front

The mechanisms responsible for the generation of crystal defects, featuring high density of vacancies, dislocations, stacking faults, and twin boundaries, by short pulse laser irradiation in the regime of melting and solidification are revealed through large-scale TTM-MD simulations of Ni and Ni-based alloys ($Ni_{50}Fe_{50}$, $Ni_{80}Fe_{20}$, and $Ni_{80}Cr_{20}$). The decrease in the thermal conductivity and strengthening of the electron-phonon coupling due to the intrinsic chemical disorder in the Ni-based alloys, compared to pure Ni, are demonstrated to cause a more localized heating of the surface, stronger laser-induced stresses, and lower threshold of melting and spallation. The relaxation of laser-induced stresses, leading to the generation of a strong unloading tensile wave that interacts with the melting front, is found to play an important role in generation of dislocations. Indeed, two mechanisms of dislocation formation are uncovered from the large-scale TTM-MD simulations, suggesting that dislocations can be either formed during propagation of the rough solidification front (as demonstrated in the Ni target), or emitted at the crystal-liquid interface by the strong unloading tensile stress (as predicted in the $Ni_{50}Fe_{50}$ target).

The generation of high density of vacancies, exceeding the equilibrium values at the melting temperature by about an order of magnitude, in the course of laser-induce melting and resolidification is interpreted on the basis of MD simulations, where propagation of solidification fronts under well-controlled undercooling and pressure conditions is investigated. Detailed analysis of the vacancy behavior at the advancing crystal-liquid interface suggests that vacancies are generated as “errors” in the process of buildup of the crystal structure, which can either jump to the liquid or finally be trapped behind the solidification front. Thus, the concentration of vacancies is strongly correlated with the vacancy mobility and solidification velocity. A comprehensive, fundamental understanding of the vacancy formation at the propagating solidification front is developed through MD simulations for bcc Cr, fcc Ni and Ni-based alloys. The significance level of concentration of the non-equilibrium vacancies, and its dependence on material properties, crystallographic orientations of the solidification front, and temperature and pressure conditions are explored. For Ni and Ni-based alloys, the effect of undercooling level and lateral stress on the density of vacancies generated in the course of rapid solidification is revealed, and used to explain the results of TTM-MD simulations. The suppression of vacancy generation in the Ni-based alloys compared to pure Ni is confirmed, which is attributed to a combined effect of enhanced vacancy mobility and slower solidification velocity, validating their promising candidacy for nuclear energy applications.

Atomistic simulations enable detailed analysis of the atomic configuration of the vacancies generated in the Ni-based alloys. The preference of vacancies for a Fe-rich local environment in the Ni-Fe solid-solute alloys is shown in both TTM-MD simulations of the laser irradiated targets and MD simulations of the crystal-liquid coexistence systems. According to the MD predictions of the vacancy formation energy, which is calculated for each possible configuration of the first neighbor shell surrounding the vacancy site, a pronounced energetic preference of vacancies to be surrounded by more Fe atoms (less Ni atoms) is demonstrated. A theoretical equation for the distribution of number of Ni atoms in the first neighbor shell is developed, considering the binomial distribution biased on the vacancy formation energy, and well explains the results from the atomistic simulations. Furthermore, large-scale MD simulations of vacancy migration at fixed undercooling conditions are performed, providing a detailed analysis of the evolution of vacancy configuration from the random atomic arrangement to the energetically favorable Fe-rich environment. This study demonstrates an example of how the crystal defects can produce atomic-scale chemical heterogeneities in the single phase solid-solution alloys.

Atomistic simulations revealing the processes responsible for the laser-induced formation of microbumps on bilayer films observed in experiments

The experimental observations of microbump formation on Ag-Cu bilayer films deposited on a silica glass substrate irradiated by a femtosecond laser pulse are interpreted by atomistic simulations. The quasi one-dimensional TTM-MD simulations are performed aiming at providing physical insights into the thermodynamic driving force responsible for the laser-induced material removal and redistribution. In the Ag on Cu bilayer film, the confinement of the deposited energy in the underlying Cu layer, due to its much stronger electron-phonon coupling compared to Ag, leads to preferential heating and melting, and buildup of high compressive stress in the subsurface layer. The relaxation of the laser-induced compressive stresses provides driving force for the expulsion of the top Ag layer from the film target, by means of intra-layer cavitation and photomechanical spallation. The spallation of the Ag layer, which can be elastically resisted by the surrounding cold material at the periphery of the laser spot, is related to the formation of Ag microbumps observed in experiments. Further increase of the laser fluence leads to the onset of explosive decomposition of the Ag layer and expulsion of the underlying Cu layer, the latter process is assisted by the release of vapor at the substrate-Cu interface due to strong superheating near the critical temperature. The computational predictions of decomposition of the Ag layer, ejection, and eventually decomposition of the underlying Cu layer, with increasing laser fluence, coincide with the experimental observations of breaching of the Ag microbump, formation, and breaching of the Cu microbump, respectively.

In the Cu on Ag bilayer system, the rough surface morphology instead of formation of Cu microbumps is explained by partial spallation of the top Cu layer under conditions of strong confinement of the laser energy deposition. At high fluence, partial spallation and eventual explosive decomposition of the underlying Ag layer are related to the formation and breaching of Ag microbumps in experiments, respectively. While the quasi one-dimensional TTM-MD simulations cannot fully capture the three-dimensional dynamics of the formation of microbumps, computational predictions of the threshold fluences for microbump formation and breaching have a reasonable agreement with the experimental results.

Large-scale simulations of laser-induced generation of the ablation plume and modification of surface morphology in the regime of phase explosion

A record-size atomistic simulation of femtosecond laser ablation of a Ag target is performed in the regime of phase explosion, using a lateral size of 400 nm for the system consisting of 2.8 billion atoms. The large size of the computational system enables realistic representations of the liquid droplets generated in the ablation plume and the modification of surface morphology. Detailed analysis of the ablation plume reveals a spatial segregation of clusters and droplets of different sizes at different positions in the plume. Vapor atoms and small clusters in the front of the expanding plume are originated to an explosive decomposition of the target surface, which is melted and overheated to the temperature for phase explosion by sufficiently high laser energy deposition. The generation of large clusters and droplets is found as a result of hydrodynamic evolution of a transient interconnected liquid structure, which is attributed to the nucleation, growth, and coalescence of subsurface voids driven by the relaxation of laser-induced thermoelastic stresses.

The elongation, shrinking, and breakdown of the liquid bridges connecting the ejected layers with the bulk target leads to the formation of the surface nanospikes. Detailed analysis of the structure of the frozen nanospikes reveals nanocrystalline structure featuring high density of stacking faults, twin boundaries, and mixed region of hcp/fcc structure in each grain. The key processes defining the various shapes and nanocrystalline structures of the nanospikes, including hydrodynamic evolution of the liquid bridges, rapid solidification under conditions of strong undercooling, cross-nucleation of metastable hcp phase on close-packed faces of growing fcc crystallites, etc. are uncovered.

By comparing the results from the TTM-MD simulations performed for the system lateral sizes of 20 nm, 100 nm, and 400 nm, the sensitivity of computational predictions of the dynamics of ablation plume and modification of surface microstructure to the system size is examined. A characteristic scale of more than 100 nm is uncovered for the surface features induced by laser ablation, including the size of large liquid droplets and spacing between nanospikes. Strong size effects are revealed in the computational system with 20 nm lateral size, where several artificial characteristics, such as easy spallation of liquid layers and the layered structure of the ablation plume, are observed. The simulation performed with a system lateral size of 100 nm is demonstrated to be able to adequately describe the composition of the ablation plume and formation of nanospikes. However, the evolution of the spalled layer into a large liquid droplet with radius exceeding 120 nm (diameter exceeding 240 nm), as well as statistically sufficient analysis of the large clusters/droplets and the nanospikes, can only be realized in the system with 400 nm lateral size.

Effect of material properties on the laser-induced modification of surface microstructure/morphology

In this dissertation, computational studies of short pulse laser irradiation have been performed for a variety of materials including semiconductors, pure metals, and alloys. Some features of the modification of surface microstructure/morphology are revealed as general characteristics of the laser-induced non-equilibrium processes and can be generalized to other materials. In particular, formation of high density of point defects at the rapidly advancing solidification front has been demonstrated in Si, Cr, Ni, and Ni-based alloys, highlighting the general mechanism of the generation of supersaturated point defects in the course of laser-induced melting and resolidification.

Quantitative results on the types and concentrations of point defects, however, are strongly material dependent. For example, both interstitials and vacancies are observed in Si, whereas the metal systems only exhibit pronounced density of vacancies, which can be attributed to the difference in the density of liquid and crystal phases. In addition, the vacancy formation in the Ni-based alloys is significantly suppressed compared to pure Ni, which can be explained by a combined effect of higher vacancy mobility and, in the case of the Ni-Cr alloy, lower solidification velocity.

Although the evolution of the ejected plume and the formation of surface nanospikes induced by laser ablation in the regime of phase explosion have only been investigated in the Ag target, similar characters of the plume segregation effect, and the shape and nanocrystalline structure of the nanospikes have been revealed in earlier studies for other materials. The effect of materials properties such as surface energy and viscosity is manifested in the difference in the shapes, size, and spacing of the surface features.

Future directions

The continuum model for laser-induced formation of amorphous structure and generation of point defects, developed for Si in this dissertation, is limited to laser pulses longer than the characteristic time for electron-phonon coupling. For ultrashort pulse laser irradiation, as in the case of metal targets discussed in Sections 4-6, two temperature model accounting for the laser excitation of electrons, heat transfer by free carriers, and collision between electrons and phonons is required. In contrast to metals, laser interaction with semiconductors involves significantly more complex processes, such as laser excitation of valance band electrons, Auger recombination, ambipolar diffusion, and non-thermal phase transformations induced by strong excitation of electrons. Despite of various experimental works on the formation of amorphous phase by femtosecond or picosecond laser pulses, computational study of this process is limited. Based on the recently developed two temperature model, the melting, cooling, resolidification, and amorphization processes in the Si target irradiated by ultrashort laser pulses will be investigated.

The Ni-Fe alloy with ordered $L1_0$ structure has attractive magnetic properties. However, synthesis of the $L1_0$ ordered phase is challenging, since the driving force for the disordered A1-to-$L1_0$ ordering only exists at low temperature, where atomic rearrangements are significantly hindered. The generation of high density of vacancies in the surface region that experiences transient laser melting and resolidification, as discussed in Section 4, can substantially enhance atomic diffusion and may activate the ordering transformation at low temperature. This non-thermal activation of atomic rearrangements by laser-induced vacancies opens up new possibilities of forming $L1_0$ ordered phase. Atomistic simulations in this dissertation have revealed the preference of vacancies for a Fe-rich local configuration, indicating special paths for vacancy diffusion in the Ni-Fe alloys. To evaluate the feasibility of activating A1-to-$L1_0$ ordering transformation by vacancy-assisted atomic diffusion, the migration energy of vacancies, and the level of vacancy supersaturation required to induce ordering transformations within reasonable time period will be investigated.

Reference

[1] D. W. Bäuerle, Laser Processing and Chemistry (Springer-Varlag, Berlin, Heidelberg, 2000).

[2] R. Menzel, Photonics Linear and Nonlinear Interactions of Laser Light and Matter (Springer-Verlag, Berlin, Heidelberg, 2001).

[3] R. R. Gattass and E. Mazur, Femtosecond laser micromachining in transparent materials, *Nat. Photonics* **2**, 219-225 (2008).

[4] A. Y. Vorobyev and C. Guo, Direct femtosecond laser surface nano/microstructuring and its applications, *Laser Photonics Rev.* **7**, 385-407 (2013).

[5] M. V. Shugaev, C. Wu, O. Armbruster, A. Naghilou, N. Brouwer, D. S. Ivanov, T. J. -Y. Derrien, N. M. Bulgakova, W. Kautek, B. Rethfeld, and L. V. Zhigilei, Fundamentals of ultrafast laser-material interaction, *MRS Bull* **41**, 960-968 (2016).

[6] R. Rethfeld, K. Sokolowski-Tinten, and D. von der Linde, Ultrafast thermal melting of laser-excited solids by homogeneous nucleation, *Phys. Rev. B* **65**, 092103 (2002).

[7] D. S. Ivanov and L. V. Zhigilei, Effect of pressure relaxation on the mechanisms of short-pulse laser melting, *Phys. Rev. Lett.* **91**, 105701 (2003).

[8] I. Itzkan, D. Albagli, M. L. Dark, L. T. Perelman, C. von Rosenberg, and M. S. Feld, The thermoelastic basis of short pulsed laser ablation of biological tissue, *Proc. Natl. Acad. Sci. USA* **92**, 1960-1964 (1995).

[9] A. A. Oraevsky, S. L. Jacques, and F. K. Tittel, Mechanism of laser ablation for aqueous media irradiated under confined-stress conditions, *J. Appl. Phys.* **78**, 1281-1290 (1995).

[10] L. V. Zhigilei and B. J. Garrison, Microscopic mechanisms of laser ablation of organic solids in the thermal and stress confinement irradiation regimes, *J. Appl. Phys.* **88**, 1281-1298 (2000).

[11] G. Paltauf and P. E. Dyer, Photomechanical processes and effects in ablation, *Chem. Rev.* **103**, 487-518 (2003).

[12] E. Leveugle, D. S. Ivanov, and L. V. Zhigilei, Photomechanical spallation of molecular and metal targets: molecular dynamics study, *Appl. Phys. A* **79**, 1643-1655 (2004).

[13] J. V. Oboňa, V. Ocelík, J. C. Rao, J. Z. P. Skolski, G. R. B. E. Römer, A. J. Huis in ‘t Veld, and J. T. M. De Hosson, Modification of Cu surface with picosecond laser pulses, *Appl. Surf. Sci.* **303**, 118-124 (2014).

[14] A. Kumar and T. M. Pollock, Mapping of femtosecond laser-induced collateral damage by electron backscatter diffusion, *J. Appl. Phys.* **110**, 083114 (2011).

[15] X. Sedao, C. Maurice, F. Garrelie, J. -P. Colombier, S. Reynaud, R. Quey, G. Blanc, and F. Pigeon, Electron backscatter diffraction characterization of laser-induced periodic surface on nickel surface, *Appl. Surf. Sci.* **302**, 114-117 (2014).

[16] X. Sedao, C. Maurice, F. Garrelie, J. -P. Colombier, S. Reynaud, R. Quey, and F. Pigeon, Influence of crystal orientation on the formation of femtosecond laser-induced periodic surface structures and lattice defects accumulation, *Appl. Phys. Lett.* **104**,

171605 (2014).

[17] M. S. Titus, M. P. Echlin, P. Gumbsch, and T. M. Pollock, Dislocation injection in strontium titanate by femtosecond laser pulses, *J. Appl. Phys.* **118**, 075901 (2015).

[18] M. P. Echlin, M. S. Titus, M. Straw, P. Gumbsch, and T. M. Pollock, Materials response to glancing incidence femtosecond laser ablation, *Acta Mater.* **124**, 37-46 (2017).

[19] X. Sedao, M. V. Shugaev, C. Wu, T. Douillard, C. Esnouf, C. Maurice, S. Reynaud, F. Pigeon, F. Garrelie, L. V. Zhigilei, and J. -P. Colombier, Growth twinning and generation of high-frequency surface nanostructures in ultrafast laser-induced transient melting and resolidification, *ACS Nano* **10**, 6995-7007 (2016).

[20] D. S. Ivanov, Z. Lin, B. Rethfeld, G. M. O'Connor, T. J. Glynn, and L. V. Zhigilei, Nanocrystalline structure of nanobump generated by localized photo-excitation of metal film, *J. Appl. Phys.* **107**, 013519 (2010).

[21] Z. Lin, R. A. Johnson, and L. V. Zhigilei, Computational study of the generation of crystal defects in a bcc metal target irradiated by short laser pulses, *Phys. Rev. B* **77**, 214108 (2008).

[22] C. Wu, D. A. Thomas, Z. Lin, and L. V. Zhigilei, Runaway lattice-mismatched interface in an atomistic simulation of femtosecond laser irradiation of Ag film-Cu substrate system, *Appl. Phys. A* **104**, 781-792 (2011).

[23] C. Wu, M. S. Christensen, J. -M. Savolainen, P. Balling, and L. V. Zhigilei, Generation of subsurface voids and a nanocrystalline surface layer in femtosecond laser irradiation of a single crystal Ag target, *Phys. Rev. B* **91**, 035413 (2015)

[24] C. Wu and L. V. Zhigilei, Nanocrystalline and polyicosahedral structure of a nanospike generated on metal surface irradiated by a single femtosecond laser pulse, *J. Phys. Chem. C* **120**, 4438-4447 (2016).

[25] M. V. Shugaev, C. -Y. Shih, E. T. Karim, C. Wu, and L. V. Zhigilei, Generation of nanocrystalline surface layer in short pulse laser processing of metal targets under conditions of spatial confinement by solid or liquid overlayer, *Appl. Surf. Sci.* **417**, 54-63 (2017).

[26] M. V. Shugaev, I. Gnilitskyi, N. M. Bulgakova, and L. V. Zhigilei, Mechanism of single-pulse ablative generation of laser-induced periodic surface structures, *Phys. Rev. B* **96**, 205429 (2017).

[27] L. V. Zhigilei, Z. Lin, and D. S. Ivanov, Atomistic modeling of sort pulse laser ablation of metals: connections between melting, spallation, and phase explosion, *J. Phys. Chem. C* **113**, 11892-11906 (2009)

[28] W. H. Duff and L. V. Zhigilei, Computational study of cooling rates and recrystallization kinetics in short pulse laser quenching of metal targets, *J. Phys.: Conf. Ser.* **59**, 413-417 (2007).

[29] C. -J. Lin, F. Spaepen, and D. Turnbull, Picosecond pulsed laser-induced melting and glass formation in metals, *J. Non-Cryst. Solids*, **61-62**, 767-772 (1984).

[30] C. -J. Lin and F. Spaepen, Nickel-niobium alloys obtained by picosecond pulsed laser quenching, *Acta Metall.* **34**, 1367-1375 (1986).

[31] W. -L. Chan, R. S. Averback, D. G. Cahill, and Y. Ashkenazy, Solidification velocities in deeply undercooled silver, *Phys. Rev. Lett.* **102**, 095701 (2009).

[32] C. A. MacDonald, A. M. Malvezzi, and F. Spaepen, Picosecond time-resolved measurements of crystallization in noble metals, *J. Appl. Phys.* **65**, 129-136 (1989).

[33] M. B. Agranat, S. I. Ashitkov, V. E. Fortov, A. V. Kirillin, A. V. Kostanovskii, S. I. Anisimov, and P. S. Kondratenko, Use of optical anisotropy for study of ultrafast phase transformations at solid surfaces, *Appl. Phs. A* **69**, 637-640 (1999).

[34] J. Chen, W. -K. Chen, J. Tang, and P. M. Rentzepis, Time-resolved structural dynamics of thin metal films heated with femtosecond optical pulses, *Proc. Natl. Acad. Sci. USA*, **108**, 18887-18892 (2011).

[35] J. A. Alonso and J. M. López, Glass-forming ability in binary alloys produced by ion beam mixing and by laser quenching, *Mater. Lett.* **4**, 316-319 (1986).

[36] P. L. Liu, R. Yen, N. Bloembergen, and R. T. Hodgson, Picosecond laser-induced melting and resolidification morphology on Si, *Appl. Phys. Lett.* **34**, 864-866 (1979).

[37] J. Bonse, S. Baudach, J. Krüger, W. Kautek, and M. Lenzner, Femtosecond laser ablation of silicon-modification thresholds and morphology, *Appl. Phys. A* **74**, 19-25 (2002).

[38] K. H. Song and X. Xu, Explosive phase transformation in excimer laser ablation, *Appl. Surf. Sci.* **127-129**, 111-116 (1998).

[39] J. H. Yoo, S. H. Jeong, X. L. Mao, R. Greif, and R. E. Russo, Evidence for phase-explosion and generation of large particles during high power nanosecond laser ablation of silicon, *Appl. Phys. Lett.* **76**, 783-785 (2000).

[40] J. H. Yoo, S. H. Jeong, R. Greif, and R. E. Russo, Explosive change in crater properties during high power nanosecond laser ablation of silicon, *J. Appl. Phys.* **88**, 1638-1649 (2000).

[41] R. Kelly and A. Miotello, Does normal boiling exist due to laser-pulse or ion bombardment?, *J. Appl. Phys.* **87**, 3177-3179 (2000)

[42] N. M. Bulgakova and A. V. Bulgakov, Pulsed laser ablation of solids: transition from normal vaporization to phase explosion, *Appl. Phys. A* **73**, 199-208 (2001).

[43] L. V. Zhigilei, Dynamics of the plume formation and parameters of the ejected clusters in short-pulse laser ablation, *Appl. Phys. A* **76**, 339-350 (2003).

[44] Z. Lin, R. A. Johnson, and L. V. Zhigilei, Computational study of the generation of crystal defects in a bcc metal target irradiated by short laser pulses, *Phys. Rev. B.* **77**, 214108 (2008).

[45] G. D. Tsibidis, M. Barberoglou, P. A. Loukakos, E. Stratakis, and C. Fotakis, Dynamics of ripple formation on silicon surfaces by ultrashort laser pulses in subablation conditions, *Phys. Rev. B* **86**, 115316 (2012).

[46] G. D. Tsibidis, C. Fotakis, and E. Stratakis, From ripples to spikes: a hydrodynamical mechanism to interpret femtosecond laser-induced self-assembled structures, *Phys. Rev. B* **92**, 041405 (2015).

[47] D. Wortmann, J. Koch, M. Reininghaus, C. Unger, C. Hulverscheidt, D. Ivanov, and B. N. Chichkov, Experimental and theoretical investigation on fs-laser-induced nanostructure formation on thin gold films, *J. Laser Appl.* **24**, 042017 (2012).

[48] C. Unger, J. Koch, L. Overmeyer, and B. N. Chichkov, Time-resolved studies of femtosecond-laser induced melt dynamics, *Opt. Express* **20**, 24864-24872 (2012).

[49] Y. P. Meshcheryakov, M. V. Shugaev, T. Mattle, and T. Lippert, Role of thermal stresses on pulsed laser irradiation of thin films under conditions of microbump formation and nonvaporization forward transfer, *Appl. Phys. A* **113**, 521-529 (2013).

[50] X. W. Wang, A. A. Kuchmizhak, X. Li, S. Juokazis, O. B. Vitrik, Y. N. Kulchin, V. V. Zhakhovsky, P. A. Danilov, A. A. Ionin, S. I. Kudryashov, A. A. Rudenko, and N. A. Inogamov, Laser-induced translative hydrodynamic mass snalshots: noninvasive characterization and predictive modeling via mapping at nanoscale, *Phys. Rev. Appl.* **8**, 044016 (2017).

[51] A. Naghilou, M. He, J. S. Schubert, L. V. Zhigilei, and W. Kautek, Femtosecond laser generation of microbumps and nanojets on single and bilayer Cu/Ag thin films, *Phys. Chem. Chem. Phys.* **21**, 11846-11860 (2019).

[52] C. Wu, E. T. Karim, A. N. Volkov, and L. V. Zhigilei, Atomic movies of laser-induced structural and phase transformations from molecular dynamics simulations. In *Lasers in Materials Science*, Springer Series in Materials Science, Vol. **191**, Edited by M. Castillejo, P. M. Ossi, and L. V. Zhigilei (Springer International Publishing Switzerland, 2014), pp. 67-100.

[53] E. T. Karim, C. Wu, and L. V. Zhigilei, Molecular dynamics simulations of laser-materials interactions: General and material-specific mechanisms of material removal and generation of crystal defects, in *Fundamentals of Laser-Assisted Micro- and Nanotechnologies*, Springer Series in Materials Science, Vol. **195**, Edited by V. P. Veiko and V. I. Konov (Springer International publishing Switzerland, 2014), pp. 27-49.

[54] M. He, C. Wu, M. V. Shugaev, G. D. Samolyuk, and L. V. Zhigilei, Computational study of short-pulse laser-induced generation of crystal defects in Ni-based single-phase binary solid-solution alloys, *J. Phys. Chem. C* **123**, 2202-2215 (2019).

[55] Y. Jee, M. F. Becker, and R. M. Walser, Laser-induced damage on single-crystal metal surfaces, *J. Opt. Soc. Am. B* **5**, 648-659 (1988).

[56] P. T. Mannion, J. Magee, E. Coyne, G. M. O’Connor, and T. J. Glynn, The effect of damage accumulation behavior on ablation thresholds and damage morphology in ultrafast laser micro-machining of common metals in air, *Appl. Surf. Sci.* **233**, 275-287 (2004).

[57] S. E. Kirkwood, A. C. van Popta, Y. Y. Tsui, and R. Fedosejevs, Single and multiple shot near-infrared femtosecond laser pulse ablation thresholds of copper, *Appl. Phys. A* **81**, 729-735 (2005).

[58] J. Krüger, D. Dufft, R. Koter, and A. Hertwig, Femtosecond laser-induced damage of gold films, *Appl. Surf. Sci.* **253**, 7815-7819 (2007).

[59] G. Raciukaitis, M. Brikas, P. Gecys, and M. Gedvilas, Accumulation effects in laser ablation of metals with high-repetition-rate lasers, *Proc. SPIE* **7005**, 70052L (2008).

[60] N. Lasemi, U. Pacher, L. V. Zhigilei, O. Bomati-Miguel, R. Lahoz, and W. Kautek, Pulsed laser ablation and incubation of nickel, iron and tungsten in liquid and air, *Appl. Surf. Sci.* **433**, 772-779 (2018).

[61] O. Armbruster, A. Naghilou, M. Kitzler, and W. Kautek, Spot size and pulse number dependence of femtosecond laser ablation thresholds of silicon and stainless steel, *Appl. Surf. Sci.* **396**, 1736-1740 (2017).

[62] J. Ehrler, M. He, M. V. Shugaev, N. I. Polushkin, S. Wintz, V. Liersch, S. Cornelius, R. Hübner, K. Potzger, J. Lindner, J. Fassbender, A. A. Ünal, S. Valencia, F. Kronast, L. V. Zhigilei, and R. Bali, Laser-rewriteable ferromagnetism at thin-film surfaces, *ACS Appl. Mater. Interfaces* **10**, 15232-15239 (2018).

[63] N. I. Polushkin, V. Oliveira, R. Vilar, M. He, M. V. Shugaev, and L. V. Zhigilei, Phase-change magnetic memory: Rewritable ferromagnetism by laser quenching of chemical disorder in $Fe_{60}Al_{40}$ alloy, *Phys. Rev. Applied* **10**, 024023 (2018).

[64] B. J. Siwick, J. R. Dwyer, R. E. Jordan, and R. J. D. Miller, An atomic-level view of melting using femtosecond electron diffraction, *Science* **302**, 1382-1385 (2003).

[65] R. Ernstorfer, M. Harb, C. T. Hebeisen, G. Sciaini, T. Dartigalongue, and R. J. D. Miller, The formation of warm dense matter: experimental evidence for electronic bond hardening in gold, *Science* **323**, 1033-1037 (2009).

[66] S. Schäfer, W. Liang, and A. H. Zewail, Structural dynamics of nanoscale gold by ultrafast electron crystallography, *Chem. Phys. Lett.* **515**, 278-282 (2011).

[67] A. Barty, S. Boutet, M. J. Bogan, S. Hau-Riege, S. Marchesini, K. Sokolowski-Tinten, N. Stojanovic, R. Tobey, H. Ehrke, A. Cavalleri, S. Düsterer, M. Frank, S. Bajt, B. W. Woods, M. M. Seibert, J. Hajdu, R. Treusch, and H. N. Chapman, Ultrafast single-shot diffraction imaging of nanoscale dynamics, *Nat. Photonics* **2**, 415-419 (2008).

[68] E. S. Massaro, A. H. Hill, and E. M. Grumstrup, Super-resolution structured pump-probe microscopy, *ACS Photonics* **3**, 501-506 (2016).

[69] A. M. Lindenberg, S. L. Johnson, and D. A. Reis, Visualization of atomic-scale motions in materials via femtosecond X-ray scattering techniques, *Annu. Rev. Mater. Res.* **47**, 425-449 (2017).

[70] L. V. Zhigilei, Z. Lin, D. S. Ivanov, E. Leveugle, W. H. Duff, D. Thomas, C. Sevilla, and S. J. Guy, Atomic/molecular-level simulations of laser-materials interactions, in *Laser-Surface Interactions for New Materials Production: Tailoring Structure and Properties*, edited by A. Miotello and P. M. Ossi (Springer Verlag, New York, 2010), pp. 43-79.

[71] L. V. Zhigilei, A. N. Volkov, and A. M. Dongare, Computational study of nanomaterials: from large-scale atomistic simulations to mesoscopic modeling, in *Encyclopedia of Nanotechnology*, edited by B. Bhushan (Springer, Heidelberg, 2012), pp. 470-480.

[72] M. V. Shugaev, M. He, S. A. Lizunov, Y. Levy, T. J. -Y. Derrien, V. P. Zhukov, N. M. Bulgakova, and L. V. Zhigilei, Insights into laser-materials interaction through modeling on atomic and macroscopic scales, in *Advances in the Application of Lasers in Materials Science*, Springer Series in Materials Science, Vol. **274**, Edited by P. M. Ossi (Springer International Publishing Switzerland, 2018), pp. 107-148.

[73] K. Sokolowski-Tinten and D. von der Linde, Generation of dense electron-hole plasmas in silicon, *Phys. Rev. B* **61**, 2643-2650 (2000).

[74] J. Hohlfeld, S. S. Wellershoff, J. Güdde, U. Conrad, V. Jähnke, and E. Matthias, Electron and lattice dynamics following optical excitation of metals, *Chem. Phys.* **251**, 237-258 (2000).

[75] D. Frenkel and B. Snut, Understanding Molecular Simulation: From Algorithms to Applications (Academic Press, San Diego, 1996).

[76] D. Rapaport, The Art of Molecular Dynamics Simulation (Cambridge University Press, Cambridge, 2004).

[77] T. Kumagai, S. Izumi, S. Hara, and S. Sakai, Development of bond-order potentials that can reproduce the elastic constants and melting points of silicon for classical molecular dynamics simulation, *Comp. Mater. Sci.* **39**, 457-464 (2007).

[78] M. S. Daw and M. I. Baskes, Semiempirical, quantum mechanical calculation of hydrogen embrittlement in metals, *Phys. Rev. Lett.* **50**, 1285-1288 (1983).

[79] M. S. Daw and M. I. Baskes, Embedded-atom method: Derivation and application to impurities, surfaces, and other defects in metals, *Phys. Rev. B* **29**, 6443-6453 (1984).

[80] M. I. Kaganov, I. M. Lifshitz, and L. V. Tanatarov, Relaxation between electrons and the crystalline lattice, *Sov. Phys. JETP* **4**, 173-178 (1957).

[81] S. I. Anisimov, B. L. Kapeliovich, and T. L. Perel'man, Electron emission from metal surfaces exposed to ultrashort laser pulses, *Sov. Phys. JETP* **39**, 375-377 (1974).

[82] D. S. Ivanov and L. V. Zhigilei, Combined atomistic-continuum modeling of short-pulse melting and disintegration of metal films, *Phys. Rev. B* **68**, 064114 (2003).

[83] E. T. Karim, Z. Lin, and L. V. Zhigilei, Molecular dynamics study of femtosecond laser interactions with Cr targets, *AIP Conf. Proc.* **1464**, 280-293 (2012).

[84] C. Wu and L. V. Zhigilei, Microscopic mechanisms of laser spallation and ablation of metal targets from large-scale molecular dynamics simulations, *Appl. Phys. A* **114**, 11-32 (2014).

[85] D. A. Thomas, Z. Lin, L. V. Zhigilei, E. L. Gurevich, S. Kittel, and R. Hergenröder, Atomistic modeling of femtosecond laser-induced melting and atomic mixing in Au film-Cu substrate system, *Appl. Surf. Sci.* **255**, 9605-9612 (2009).

[86] S. -S. Wellershoff, J. Hohlfeld, J. Güdde, and E. Matthias, The role of electron-phonon coupling in femtosecond laser damage of metals, *Appl. Phys. A* **69**, S99-S107 (1999).

[87] N. M. Bulgakova and I. M. Bourakov, Phase explosion under ultrashort pulsed laser ablation: modeling with analysis of metastable state of melt, *Appl. Surf. Sci.* **197-198**, 41-44 (2002).

[88] Z. Lin and L. V. Zhigilei, Temperature dependences of the electron-phonon coupling, electron heat capacity and thermal conductivity in Ni under femtosecond laser irradiation, *Appl. Surf. Sci.* **253**, 6295-6300 (2007).

[89] Z. Lin, L. V. Zhigilei, and V. Celli, Electron-phonon coupling and electron heat capacity of matals under conditions of strong electron-phonon nonequilibrium, *Phys. Rev. B* **77**, 075133 (2008).

[90] G. D. Samolyuk, L. K. Béland, G. M. Stocks, and R. E. Stoller, Electron–phonon coupling in Ni-based binary alloys with application to displacement cascade modeling, *J. Phys.: Condens. Matter* **28**, 175501 (2016).

[91] R. H. M. Groeneveld, R. Sprik, and A. Lagendijk, Femtosecond spectroscopy of electron-electron and electron-phonon energy relaxation in Ag and Au, *Phys. Rev. B* **51**, 11433-11445 (1995).

[92] D. S. Ivanov and L. V. Zhigilei, Combined atomistic-continuum model for simulation of laser interaction with metals: Application in the calculation of melting

thresholds in Ni targets of varying thickness, *Appl. Phys. A* **79**, 977-981 (2004).

[93] L. V. Zhigilei and B. J. Garrison, Pressure waves in microscopic simulations of laser ablation, *Mater. Res. Soc. Symp. Proc.* **538**, 491-496 (1999).

[94] C. Schäfer, H. M. Urbassek, L. V. Zhigilei, and B. J. Garrison, Pressure-transmitting boundary conditions for molecular-dynamics simulations, *Comp. Mater. Sci.* **24**, 421-429 (2002).

[95] R. F. Wood, Macroscopic theory of pulsed-laser annealing. I. Thermal transport and melting, *Phys. Rev. B* **23**, 2923-2942 (1981).

[96] K. N. Vonatsos and D. I. Pantelis, Approximate solutions for the evaluation of the depth of laser-melted zones, *Appl. Phys. A* **80**, 885-889 (2005).

[97] I. H. Chowdhury and X. Xu, Heat transfer in femtosecond laser processing of metal, *Numer. Heat Transf. Part A Appl.* **44**, 219-232 (2003).

[98] V. V. Gupta, H. J. Song, and J. S. Im, Non-equilibrium two-dimensional model of excimer-laser melting and solidification of thin Si films on SiO_2, *MRS Proc.* **397**, 465-472 (1995).

[99] K. A. Jackson, The interface kinetics of crystal growth processes, *Interface Sci.* **10**, 159-169 (2002).

[100] H. Kisdarjono, A. T. Voutsas, and R. Solanki, Three-dimensional simulation of rapid melting and resolidification of thin films by excimer laser annealing, *J. Appl. Phys.* **94**, 4374-4381 (2003).

[101] D. Turnbull and J. C. Fisher, Rate of nucleation in condensed systems, *J. Chem. Phys.* **17**, 71-73 (1949).

[102] Y. Miyazawa and G. M. Pound, Homogeneous nucleation of crystalline gallium from liquid gallium, *J. Cryst. Crowth* **23**, 45-57 (1974).

[103] J. Farjas and P. Roura, Modification of the Kolmogorov-Johnson-Mehl-Avrami rate equation for non-isothermal experiments and its analytical solution, *Acta Mater.* **54**, 5573-5579 (2006).

[104] A. La Magna, V. Privitera, G. Fortunato, M. Cuscunà, B. G. Svensson, E. Monakhov, K. Kuitunen, J. Slotte, and F. Tuomisto, Vacancy generation in liquid phase epitaxy of Si, *Phys. Rev. B* **75**, 235201 (2007).

[105] T. Sinno, R. A. Brown, W. von Ammon, and E. Dornberger, Point defect dynamics and the oxidation-induced stacking-fault ring in Czochralski-grown silicon crystals, *J. Electrochem. Soc.* **145**, 302-318 (1998).

[106] R. A. Brown, D. Maroudas, and T. Sinno, Modelling point defect dynamics in the crystal growth of silicon, *J. Cryst. Growth* **137**, 12-25 (1994).

[107] E. Dornberger, T. Sinno, J. Esfandyari, J. Vanhellemont, R. A. Brown, and W. von Ammon, Proc. Electrochem. Soc. **98**, 170-187 (1998).

[108] T. Sinno, Z. K. Jiang, and R. A. Brown, Atomistic simulation of point defects in silicon at high temperature, *Appl. Phys. Lett.* **68**, 3028-3030 (1996).

[109] M. Mikelsen, E. V. Monakhov, G. Alfieri, B. S. Avset, and B. G. Svensson, Kinetics of divacancy annealing and divacancy-oxygen formation in oxygen-enriched high-purity silicon, *Phys. Rev. B* **72**, 195207 (2005).

[110] S. J. Eisele, T. C. Röder, J. R. Köhler, and J. H. Werner, 18.9% efficient full area laser doped silicon solar cell, *Appl. Phys. Lett.* **95**, 133501 (2009).

[111] M. Dahlinger, B. Bazer-Bachi, T. C. Röder, J. R. Köhler, R. Zapf-Gottwick, and J. H. Werner, Laser-doped back-contact solar cells, *IEEE J. Photovolt.* **5**, 812-818 (2015).

[112] M. Dahlinger, K. Carstens, E. Hoffmann, J. R. Köhler, R. Zapf-Gottwick, and J. H. Werner, 23.2% laser processed back contact solar cell: fabrication, characterization and modeling, *Prog. Photovolt.* **25**, 192-200 (2017).

[113] Z. Sun and M. C. Gupta, Laser annealing to enhance performance of all-laser-based silicon back contact solar cells, *Proc. 44th IEEE PVSC*, 937-939 (2011).

[114] V. V. Iyengar, B. K. Nayak, and M. C. Gupta, Optical properties of silicon light trapping structures for photovoltaics, *Sol. Energy Mater. Sol. Cells* **94**, 2251-2257 (2010).

[115] V. V. Iyengar, B. K. Nayak, K. L. More, H. M. Meyer Ⅲ, M. D. Biegalski, J. V. Li, and M. C. Gupta, Properties of ultrafast laser textured silicon for photovoltaics, *Sol. Energy Mater. Sol. Cells* **95**, 2745-2751 (2011).

[116] B. K. Nayak, V. V. Iyengar, and M. C. Gupta, Efficient light trapping in silicon solar cells by ultrafast-laser-induced self-assembled micro-nano structures, *Prog. Photovolt.* **19**, 631-639 (2011).

[117] E. Schneiderlochner, R. Preu, R. Ludemann, and S. W. Glunz, Laser-fired rear contacts for crystalline silicon solar cells, *Prog. Photovolt.* **10**, 29-34 (2002).

[118] L. Wang, D. E. Charlson, and M. C. Gupta, Silicon solar cells based on all-laser-transferred contacts, *Prog. Photovolt.* **23**, 61-68 (2015).

[119] U. Das, C. Thompson, U. Nsofor, Z. Sun, M. C. Gupta, and S. Hegedus, Effect of dielectric layers on laser-fired-contact performance in a-Si/c-Si heterojunction solar cells, *Proc. 7th IEEE WCPEC*, 2114-2117 (2018).

[120] K., Ohmer, Y. Weng, J. R. Köhler, H. P. Strunk, and J. H. Werner, Defect formation in silicon during laser doping, *IEEE J. Photovolt.* **1**, 183-186 (2011).

[121] Z. Sun and M. C. Gupta, Laser induced defects in silicon solar cells and laser annealing, *Proc. 43rd IEEE PVSC*, 713-716 (2016).

[122] Z. Sun and M. C. Gupta, Laser annealing of silicon surface defects for photovoltaic applications, *Surf. Sci.* **652**, 344-349 (2016).

[123] Z. Hameiri, T. Puzzer, L. Mai, A. B. Sproul, and S. R. Wenham, Laserinduced defects in laser doped solar cells, *Prog. Photovolt.* **19**, 391-405 (2011).

[124] Z. Sun and M. C. Gupta, A study of laser-induced surface defects in silicon and impact on electrical properties, *J. Appl. Phys.* **124**, 223103 (2018).

[125] J. Bonse, K. -W. Brzezinka, A. J. Meixner, Modifying single-crystalline silicon by femtosecond laser pulses: an analysis by micro Raman spectroscopy, scanning laser microscopy and atomic force microscopy, *Appl. Surf. Sci.* **221**, 215-230 (2004).

[126] J. Bonse, All-optical characterization of single femtosecond laser-pulse-induced amorphization in silicon, *Appl. Phys. A* **84**, 63-66 (2006).

[127] Y. Izawa, Y. Izawa, Y. Setsuhara, M. Hashida, M. Fujita, R. Sasaki, H. Nagai, and M. Yoshida, Ultrathin amorphous Si layer formation by femtosecond laser pulse

irradiation, *Appl. Phys. Lett.* **90**, 044107 (2007).

[128] Y. Izawa, S. Tokita, M. Fujita, M. Nakai, T. Norimatsu, and Y. Izawa, Ultrathin amorphization of single-crystal silicon by ultraviolet femtosecond laser pulse irradiation, *J. Appl. Phys.* **105**, 064909 (2009).

[129] T. H. R. Crawford, J. Yamanaka, G. A. Botton, and H. K. Haugen, High-resolution observations of an amorphous layer and subsurface damage formed by femtosecond laser irradiation of silicon, *J. Appl. Phys.* **103**, 053104 (2008).

[130] Y. Fuentes-Edfuf, M. Garcia-Lechuga, D. Puerto, C. Florian, A. Garcia-Leis, S. Sanchez-Cortes, J. Solis, and J. Siegel, Fabrication of amorphous micro-ring arrays in crystalline silicon using ultrashort laser pulses, *Appl. Phys. Lett.* **110**, 211602 (2017).

[131] J. M. Liu, R. Ren, H. Kurz, and N. Bloembergen, Phase transformation on and charged particle emission from a silicon crystal surface, induced by picosecond laser pulses, *Appl. Phys. Lett.* **39**, 755-757 (1981).

[132] J. A. Yater and M. O. Thompson, Orientation dependence of laser amorphization of crystal Si, *Phys. Rev. Lett.* **63**, 2088-2091 (1989).

[133] P. H. Bucksbaum and J. Bokor, Rapid melting and regrowth velocities in silicon heated by ultraviolet picosecond laser pulses, *Phys. Rev. Lett.* **53**, 182-185 (1984).

[134] Y. Weng, B. Kedjar, K. Ohmer, J. R. Köhler, J. H. Werner, and H. P. Strunk, Dislocation formation during laser processing of silicon solar cell materials, *Phys. Status Solidi C* **10**, 28-31 (2013).

[135] Z. Sun and M. C. Gupta, Laser processing of silicon for photovoltaics and structural phase transformation, *Appl. Surf. Sci.* **456**, 342-350 (2018).

[136] W. Li, S. Varlamov, J. Dore, and M. Green, Defect annealing in ultra-thin polycrystalline silicon films on glass: rapid thermal versus laser processing, *Mater. Lett.* **107**, 1-4 (2013).

[137] P. M. Fahey, P. B. Griffin, and J. D. Plummer, Point defects and dopant diffusion in silicon, *Rev. Mod. Phys.* **61**, 289-384 (1989).

[138] S. Goedecker, L. Billard, and T. Deutsch, A fourfold coordinated point defect in silicon, *Phys. Rev. Lett.* **88**, 235501 (2002).

[139] A. Alkauskas, M. D. McCluskey, and C. G. Van de Walle, Tutorial: defects in semiconductors-combining experiment and theory, *J. Appl. Phys.* **119**, 181101 (2016).

[140] P. Pellegrino, P. Lévêque, J. Lalita, and A. Hallén, Annealing kinetics of vacancy-related defects in low-dose MeV self-ion-implanted *n*-type silicon, *Phys. Rev. B* **64**, 195211 (2001).

[141] B. Hartiti, R. Schindler, A. Slaoui, B. Wagner, J. C. Muller, I. Reis, A. Eyer, and P. Siffert, Towards high-efficiency silicon solar cells by rapid thermal processing, *Prog. Photovolt.* **2**, 129-142 (1994).

[142] P. Doshi, J. Mejia, K. Tate, and A. Rohatgi, Modeling and characterization of high-efficiency silicon solar cells fabricated by rapid thermal processing, screen printing, and plasma-enhanced chemical vapor deposition, *IEEE Trans. Electron Devices* **44**, 1417-1424 (1997).

[143] P. Baeri and E. Rimini, Laser annealing of silicon, *Mater. Chem. Phys.* **46**, 169-177 (1996).

[144] Y. Qiu, F. Cristiano, K. Huet, F. Mazzamuto, G. Fisicaro, A. L. Magna, M. Quillec, N. Cherkashin, H. Wang, S. Duguay, and D. Blavette, Extended defects formation in nanosecond laser-annealed ion implanted silicon, *Nano Lett.* **14**, 1769-1775 (2014).

[145] J. Tersoff, Empirical interatomic potential for silicon with improved elastic properties, *Phys. Rev. B* **38**, 9902-9905 (1988).

[146] F. H. Stillinger and T. A. Weber, Computer simulation of local order in condensed phases of silicon, *Phys. Rev. B* **31**, 5262-5271 (1985).

[147] P. K. Schelling, Phase behavior and kinetics of a new bond-order potential for silicon, *Comp. Mater. Sci.* **44**, 274-279 (2008).

[148] S, Sastry and C. A. Angell, Liquid-liquid phase transition in supercooled silicon, *Nat. Mater.* **2**, 739-743 (2003).

[149] N. Jakse and A. Pasturel, Liquid-liquid phase transformation in silicon: evidence from first-principles molecular dynamics simulations, *Phys. Rev. Lett.* **99**, 205702 (2007).

[150] A. Hedler, S. L. Klaumünzer, and W. Wesch, Amorphous silicon exhibits a glass transition, *Nat. Mater.* **3**, 804-809 (2004).

[151] J. Godet, P. Hirel, S. Brochard, and L. Pizzagalli, Evidence of two plastic regimes controlled by dislocation nucleation in silicon nanostructures, *J. Appl. Phys.* **105**, 026104 (2009).

[152] M. Trempa, C. Reimann, J. Friedrich, G. Müller, and D. Oriwol, Mono-crystalline growth in directional solidification of silicon with different orientation and splitting of seed crystals, *J. Cryst. Growth* **351**, 131-140 (2012).

[153] V. A. Oliveira, B. Marie, C. Cayron, M. Marinova, M. G. Tsoutsouva, H. C. Silo, T. A. Lafford, J. Baruchel, G. Audoit, A. Grenier, T. N. Tran Thi, and D. Camel, Formation mechanism and properties of twinned structures in (111) seeded directionally solidified solar grade silicon, *Acta Mater.* **121**, 24-36 (2016).

[154] M. G. Tsoutsouva, T. Riberi-Béridot, G. Regula, G. Reinhart, J. Baruchel, F. Guittonneau, L. Barrallier, N. Mangelinck-Noël, *In situ* investigation of the structural defect generation and evolution during the directional solidification of <110> seeded growth Si, *Acta Mater.* **115**, 210-223 (2016).

[155] K. Fujiwara, K. Maeda, N. Usami, G. Sazaki, Y. Nose, and K. Nakajima, Formation mechanism of parallel twins related to Si-facetted dendrite growth, *Scr. Mater.* **57**, 81-84 (2007).

[156] T. Duffar and A. Nadri, On the twinning occurrence in bulk semiconductor crystal growth, *Scr. Mater.* **62**, 955-960 (2010).

[157] J. Pohl, M. Müller, A. Seidl, and K. Albe, Formation of parallel (111) twin boundaries in silicon growth from the melt explained by molecular dynamics simulations, *J. Cryst. Growth* **312**, 1411-1415 (2010).

[158] J. Pohl and K. Albe, Void formation in melt-grown silicon studied by molecular dynamics simulations: from grown-in faulted dislocation loops to vacancy clusters, *Appl. Phys. Lett.* **99**, 081910 (2011).

[159] N. Zhou, X. Wu, X. Wei, L. Zhou, Y. Wan, and D. Hu, A molecular dynamics study of nucleation of dislocation in growth of silicon from melt, *J. Cryst. Growth* **443**, 15-19 (2016).

[160] G. D. Ivlev and E. I. Gatskevich, Liquid phase reflectivity under conditions of laser-induced silicon melting, *Semiconductors* **34**, 759-762 (2000).

[161] K. M. Shvarev, B. A. Baum, and P. V. Gel'd, Optical properties of liquid silicon, *Sov. Phys. Solid State* **16**, 2111-2112 (1975).

[162] J. E. Moody and R. H. Hendel, Temperature profiles induced by a scanning cw laser beam, *J. Appl. Phys.* **53**, 4364-4371 (1982).

[163] K. G. Svantesson and N. G. Nilsson, Determination of the temperature dependence of the free carrier and interband absorption in silicon at 1.06 μm, *J. Phys. C* **12**, 3837-3842 (1979).

[164] G. E. Jellison Jr. and D. H. Lowndes, Measurements of the optical properties of liquid silicon and germanium using nanosecond time-resolved ellipsometry, *Appl. Phys. Lett.* **51**, 352-354 (1987).

[165] G. E. Jellison Jr. and F. A. Modine, Optical absorption of silicon between 1.6 and 4.7 eV at elevated temperature, *Appl. Phys. Lett.* **41**, 180-182 (1982).

[166] P. J. Chernek and J. A. Orson, A simple thermal response model for a p-doped silicon substrate irradiated by 1.06 and 1.32 micron lasers, *Proc. SPIE* **4679**, 186-197 (2002).

[167] P. D. Desai, Thermodynamic properties of iron and silicon, *J. Phys. Chem. Ref. Data* **15**, 967-983 (1986).

[168] NIST-Janaf Thermochemical Tables, *J. Phys. Chem. Ref. Data* **9**, 1881-1891 (1998).

[169] D. Bauerle, Laser Processing and Chemistry (Springer Press, Berlin, 2000).

[170] S. de Unamuno and E. Fogarassy, A thermal description of the melting of c- and a-silicon under pulsed excimer lasers, *Appl. Surf. Sci.* **36**, 1-11 (1989).

[171] R. F. Wood and J. E. Jellison Jr., Melting model of pulsed laser processing, in *Pulsed Laser Processing of Semiconductors*, Semiconductors and Semimetals, Vol. **23**, edited by R. F. Wood, C. W. White, and R. F. Young (Academic Press, Orlando, 1984)

[172] R. F. Wood and G. A. Geist, Modeling of nonequilibrium melting and solidification in laser-irradiated materials, *Phys. Rev. B* **34**, 2606-2620 (1986).

[173] Z. Zhou, S. Mukherjee, and W. K. Rhim, Measurement of thermophysical properties of molten silicon using an upgraded electrostatic levitator, *J. Cryst. Growth* **257**, 350-358 (2003).

[174] H. Kobatake, H. Fukuyama, T. Tsukada, and S. Awaji, Noncontact modulated laser calorimetry in a dc magnetic field for stable and supercooled liquid silicon, *Meas. Sci. Technol.* **21**, 025901 (2010).

[175] M. G. Grimaldi, P. Baeri, and M. A. Malvezzi, Melting temperature of unrelaxed amorphous silicon, *Phys. Rev. B* **44**, 1546-1553 (1991).

[176] M. W. Ullah, D. S. Aidhy, Y. Zhang, and W. J. Weber, Damage accumulation in ion-irradiated Ni-based concentrated solid-solution alloys, *Acta Mater.* **109**, 17-22 (2016).

[177] F. Granberg, K. Nordlund, M. W. Ullah, K. Jin, C. Lu, H. Bei, L. M. Wang, F. Djurabekova, W. J. Weber, and Y. Zhang, Mechanism of radiation damage reduction in equiatomic multicomponent single phase alloys, *Phys. Rev. Lett.* **116**, 135504 (2016).

[178] C. Trautmann, Mirco- and Nanoengineering with Ion Tracks, in *Ion Beams in Nanoscience and Technology*, R. Hellborg, H. J. Whitlow, and Y. Zhang (Editors), (Springer-Verlag Berlin Heidelberg, 2009) 369-387.

[179] M. V. Shugaev, C. Wu, O. Armbruster, A. Naghilou, N. Brouwer, D. S. Ivanov, T. J. -Y. Derrien, N. M. Bulgakova, W. Kautek, B. Rethfeld, and L. V. Zhigilei, Fundamentals of ultrafast laser-material interactions, *MRS Bull.* **41**, 960-968 (2016).

[180] L. K. Béland, C. Lu, Y. N. Osetskiy, G. D. Samolyuk, A. Caro, L. Wang, and R. E. Stoller, Features of primary damage by high energy displacement cascades in concentrated Ni-based alloys, *J. Appl. Phys.* **119**, 085901 (2016).

[181] D. Ashkenasi, M. Lorenz, R. Stoian, and A. Rosenfeld, Surface damage threshold and structuring of dielectrics using femtosecond laser pulses: the role of incubation, *Appl. Surf. Sci.* **150**, 101-106 (1999).

[182] H. Y. Zhang, F. Liu, Y. Yang, and D. Y. Sun, The molecular dynamics study of vacancy formation during solidification of pure metals, *Sci. Rep.* **7**, 10241 (2017).

[183] X. Q. Zheng, Y. Yang, Y. F. Gao, J. J. Hoyt, M. Asta, and D. Y. Sun, Disorder trapping during crystallization of the B2-ordered NiAl compound, *Phys. Rev. E* **85**, 041601 (2012).

[184] M. Hillert, M. Schwind, and M. Selleby, Trapping of vacancies by rapid solidification, *Acta Mater.* **50**, 3283-3291 (2002).

[185] N. Bordeaux, A. M. Montes-Arango, J. Liu, K. Barmak, and L. H. Lewis, Thermodynamic and kinetic parameters of the chemical order-disorder transformation in $L1_0$ FeNi (tetrataenite), *Acta Mater.* **103**, 608-615 (2016).

[186] J. Liu, L. J. Riddiford, C. Floristean, F. Goncalves-Neto, M. Rezaeeyazdi, L. H. Lewis, and K. Barmak, Kinetics of order-disorder transformation of $L1_2$ $FeNi_3$ in the Fe-Ni system, *J. Alloys Compd.* **689**, 593-598 (2016).

[187] Z. Wu, H. Bei, G. M. Pharr, and E. P. George, Temperature dependence of the mechanical properties of equiatomic solid solution alloys with face-centered cubic crystal structures, *Acta Mater.* **81**, 428-441 (2014).

[188] Y. Zhang, G. M. Stocks, K. Jin, C. Lu, H. Bei, B. C. Sales, L. Wang, L. K. Béland, R. E. Stoller, G. D. Samolyuk, M. Caro, A. Caro, and W. J. Weber, Influence of chemical disorder on energy dissipation and defect evolution in nickel and Ni-based concentrated solid-solution alloys, *Nat. Commun.* **6**, 8736 (2015).

[189] K. Jin, B. C. Sales, G. M. Stocks, G. D. Samolyuk, M. Daene, W. J. Weber, Y. Zhang, and H. Bei, Tailoring the physical properties of Ni-based single-phase equiatomic alloys by modifying the chemical complexity, *Sci. Rep.* **6,** 20159 (2016).

[190] S. Zhao, G. M. Stocks, and Y. Zhang, Defect energetics of concentrated solid-solution alloys from ab initio calculations: $Ni_{0.5}Co_{0.5}$, $Ni_{0.5}Fe_{0.5}$, $Ni_{0.8}Fe_{0.2}$ and $Ni_{0.8}Cr_{0.2}$, *Phys. Chem. Chem. Phys.* **18**, 24043-24056 (2016).

[191] K. Jin, W. Guo, C. Lu, M. W. Ullah, Y. Zhang, W. J. Weber, L. Wang, J. D. Poplawsky, and H. Bei, Effects of Fe concentration on the ion-irradiation induced defect evolution and hardening in Ni-Fe solid solution alloys, *Acta Mater.* **121**, 365-373 (2016).

[192] M. Jin, P. Cao, and M. P. Short, Thermodynamic mixing energy and heterogeneous diffusion uncover the mechanisms of radiation damage reduction in single-phase Ni-Fe alloys, *Acta Mater.* **147**, 16-23 (2018).

[193] http://www.faculty.virginia.edu/CompMat/electron-phonon-coupling/

[194] B. Y. Mueller and B. Rethfeld, Nonequilibrium electron-phonon coupling after ultrashort laser excitation of gold, *Appl. Surf. Sci.* **302**, 24-28 (2014).

[195] K. C. Mills, B. J. Monaghan, and B. J. Keene, Thermal conductivities of molten metals: Part 1 pure metals. *Int. Mater. Rev.* **41**, 209-242 (1996).

[196] C. Y. Ho, M. W. Ackerman, K. Y. Wu, S. G. Oh, and T. N. Havill, Thermal conductivity of ten selected binary alloy systems, *J. Phys. Chem. Ref. Data* **7**, 959-1177 (1978).

[197] C. Y. Ho, M. W. Ackerman, K. Y. Wu, T. N. Havill, R. H. Bogaard, R. A. Matula, S. G. Oh, and H. M. James, Electrical resistivity of ten selected binary alloy systems, *J. Phys. Chem. Ref. Data* **12**, 183-322 (1983).

[198] Y. Terada, K. Ohkubo, T. Mohri, and T. Suzuki, Thermal conductivity in nickel solid solutions, *J. Appl. Phys.* **81**, 2263-2268 (1997).

[199] T. Hüpf, C. Cagran, E. Kaschnitz, and G. Pottlacher, Thermophysical properties of $Ni_{80}Cr_{20}$, *Thermochimica Acta* **494**, 40-44 (2009)

[200] K. Jin, S. Mu, K. An, W. D. Porter, G. D. Samolyuk, G. M. Stocks, and H. Bei, Thermophysical properties of Ni-containing single-phase concentrated solid solution alloys, *Mater. Des.* **117**, 185-192 (2017).

[201] G. Bonny, D. Terentyev, R. C. Pasianot, S. Poncé, and A. Bakaev, Interatomic potential to study plasticity in stainless steels, the FeNiCr model alloy, *Modelling Simul. Mater. Sci. Eng.* **19**, 085008 (2011).

[202] J. R. Rumble (ed.), *Handbook of Chemistry and Physics*, 98 ed., (CRC Press, Boca Raton, 2017).

[203] Z. Wu, H. Bei, G. M. Pharr, and E. P. George, Temperature dependence of the mechanical properties of equiatomic solid solution alloys with face-centered cubic crystal structures, *Acta Mater.* **81**, 428-441 (2014).

[204] G. J. Gloor, G. Jackson, F. J. Blas, and E. de Miguel, Test-area simulation method for the direct determination of the interfacial tension of systems with continuous or discontinuous potentials, *J. Chem. Phys.* **123**, 134703 (2005).

[205] I. Egry, E. Ricci, R. Novakovic, and S. Ozawa, Surface tension of liquid metals and alloys – recent developments, *Adv. Colloid Interface Sci.* **159**, 198-212 (2010).

[206] S. Schäfer, W. Liang, and A. H. Zewail, Structural dynamics of nanoscale gold by ultrafast electron crystallography, *Chem. Phys. Lett.* **515**, 278-282 (2011).

[207] Y. Mishin, Atomistic modeling of the γ and γ'-phase of the Ni-Al system, *Acta Mater.* **52**, 1451-1467 (2004).

[208] X. W. Zhou, H. N. G. Wadley, R. A. Johnson, D. J. Larson, N. Tabat, A. Cerezo, A, K. Petford-Long, G. D. W. Smith, P. H. Clifton, R. L. Martens, and T. F. Kelly, Atomic scale structure of sputtered metal multilayers, *Acta Mater.* **49**, 4005-4015 (2001).

[209] D. S. Ivanov and L. V. Zhigilei, Kinetic limit of heterogeneous melting in metals, *Phys. Rev. Lett.* **98**, 195701 (2007).

[210] A. K. Upadhyay and H. M. Urbassek, Melting and fragmentation of ultra-thin metal films due to ultrafast laser irradiation: a molecular-dynamics study, *J. Phys. D:*

Appl. Phys. **38**, 2933-2941 (2005).

[211] A. K. Upadhyay, N. A. Inogamov, B. Rethfeld, and H. M. Urbassek, Ablation by ultrashort laser pulses: atomistic and thermodynamic analysis of the processes at the ablation threshold, *Phys. Rev. B* **78**, 045437 (2008).

[212] B. J. Demaske, V. V. Zhakhovsky, N. A. Inogamov, and I. I. Oleynik, Ablation and spallation of gold films irradiated by ultrashort laser pulses, *Phys. Rev. B* **82**, 064113 (2010).

[213] S. I. Ashitkov, N. A. Inogamov, V. V. Zhakhovskii, Y. N. Emirov, M. B. Agranat, I. I. Oleinik, S. I. Anisimov, and V. E. Fortov, Formation of nanocavities in the surface layer of an aluminum target irradiated by a femtosecond laser pulse, *JETP Lett.* **95**, 176-181 (2012).

[214] A. Stukowski, Structure identification methods for atomistic simulations of crystalline materials, *Modelling Simul. Mater. Sci. Eng.* **20**, 045021 (2012).

[215] A. Stukowski, V. V. Bulatov, and A. Arsenlis, Automated identification and indexing of dislocations in crystal interfaces, *Modelling Simul. Mater. Sci. Eng.* **20**, 085007 (2012).

[216] A. Stukowski and K. Albe, Extracting dislocations and non-dislocation crystal defects from atomistic simulation data, *Modelling Simul. Mater. Sci. Eng.* **18**, 085001 (2010).

[217] A. P. Miodownik, The calculation of stacking fault energies in Fe-Ni-Cr alloys, *CALPHAD: Comput. Coupling Phase Diagrams Thermochem.* **2**, 207-226 (1978).

[218] S.-N. Luo, T. J. Ahrens, T. Çağın, A. Strachan, W. A. Goddard, III, and D. C. Swift, Maximum superheating and undercooling: Systematics, molecular dynamics simulations, and dynamic experiments, *Phys. Rev. B* **68**, 134206 (2003).

[219] Z. Lin, E. Leveugle, E. M. Bringa, and L. V. Zhigilei, Molecular dynamics simulation of laser melting of nanocrystalline Au, *J. Phys. Chem. C* **114**, 5686-5699 (2010).

[220] H. J. C. Berendsen, J. P. M. Postma, W. F. van Gunsteren, A. DiNola, and J. R. Haak, Molecular dynamics with coupling to an external bath, *J. Chem. Phys.* **81**, 3684-3690 (1984).

[221] S. M. Foiles, M. I. Baskes, and M. S. Daw, Embedded-atom-method functions for the fcc metals Cu, Ag, Au, Ni, Pd, Pt, and their alloys, *Phys. Rev. B* **33**, 7983-7991 (1986).

[222] J. R. Morris and X. Song, The melting lines of model systems calculated from coexistence simulations, *J. Chem. Phys.* **116**, 9352-9358 (2002).

[223] Y. Ashkenazy and R. S. Averback, Kinetic stages in the crystallization of deeply undercooled body-centered-cubic and face-centered-cubic metals, *Acta Mater.* **58**, 524-530 (2010).

[224] S. Zhao, G. Velisa, H. Xue, H. Bei, W. J. Weber, and Y. Zhang, Suppression of vacancy cluster growth in concentrated solid solution alloys, *Acta Mater.* **125**, 231-237 (2017).

[225] K. Nordlund, and R.S. Averback, Role of self-interstitial atoms on the high temperature properties of metals, *Phys. Rev. Lett.* **80**, 4201-4204 (1998).

[226] R. A. Johnson, Alloy models with the embedded-atom method, *Phys. Rev. B* **39**, 12554 (1989).

[227] A. Y. Vorobyev and C. Guo, Enhanced absorptance of gold following multipulse femtosecond laser ablation, *Phys. Rev. B* **72**, 195422 (2005).

[228] A. Abou-Saleh, E. T. karim, C. Maurice, S. Reynaud, F. Pigeon, F. Garrelie, L. V. Zhigilei, and J. P. Colombier, Spallation-induced roughness promoting high spatial frequency nanostructure formation on Cr, *Appl. Phys. A* **124**, 308 (2018).

[229] J. -M. Savolainen, M. S. Christensen, and P. Balling, Material swelling as the first step in the ablation of metals by ultrashort laser pulses, *Phys. Rev. B* **84**, 193410 (2011).

[230] J. Reif, O. Varlamova, S. Uhlig, S. Varlamov, and M. Bestehorn, On the physics of self-organized nanostructure formation upon femtosecond laser ablation, *Appl. Phys. A* **117**, 179-184 (2014).

[231] R. D. Murphy, B. Torralva, D. P. Adams, and S. M. Yalisove, Polarization dependent formation of femtosecond laser-induced periodic surface structures near stepped features, *Appl. Phys. Lett.* **104**, 231117 (2014).

[232] J. Bonse, S. Höhm, S. V. Kirner, A. Rosenfeld, and J. Krüger, Laser-induced periodic surface structures – a scientific evergreen, *IEEE J. Sel. Top. Quantum Electron.* **23**, 109-123 (2017).

[233] Y. Nakata, T. Okada, and M. Maeda, Nano-sized hollow bump array generated by single femtosecond laser pulse, *Jpn. J. Appl. Phys.* **42**, L1452-L1454 (2003).

[234] F. Korte, J. Koch, and B. N. Chichkov, Formation of microbumps and nanojets on gold targets by femtosecond laser pulses, *Appl. Phys. A* **79**, 879-881 (2004).

[235] J. Koch, F. Korte, T. Bauer, C. Fallnich, A. Ostendorf, and B. N. Chichkov, Nanotexturing of gold films by femtosecond laser-induced melt dynamics, *Appl. Phys. A* **80**, 325-328 (2005).

[236] Y. Nakata, N. Miyanaga, and T. Okada, Effect of pulse width and fluence of femtosecond laser on the size of nanobump array, *Appl. Surf. Sci.* **253**, 6555-6557 (2007).

[237] Z. Guo, J. Feng, K. Zhou, Y. Xiao, S. Qu, and J. -H. Lee, The formation of different structures in the interaction between a single femtosecond laser pulse and a thin Au film, *Appl. Phys. A* **108**, 639-644 (2012).

[238] P. A. Danilov, E. A. Drozdova, A. A. Ionin, S. I. Kudryashov, S. B. Odinokov, A. A. Rudenko, V. I. Yurovskikh, and D. A. Zayarny, Single-shot front-side nanoscale femtosecond laser ablation of a thin silver film, *Appl. Phys. A* **117**, 981-985 (2014).

[239] A. I. Kuznetsov, C. Unger, J. Koch, and B. N. Chichkov, Laser-induced jet formation and droplet ejection from thin metal films, *Appl. Phys. A* **106**, 479-487 (2012).

[240] A. I. Kuznetsov, J. Koch, and B. N. Chichkov, Nanostructuring of thin gold films by femtosecond lasers, *Appl. Phys. A* **94**, 221-230 (2009).

[241] D. Jiang, P. Fan. D. Gong, J. Long, H. Zhang, and M. Zhong, High-temperature imprinting and superhydrophobicity of micro/nano surface structures on metals using molds fabricated by ultrafast laser ablation, *J. Mater. Process. Tech.* **236**, 56-63 (2016)

[242] S. -J. Kim, S. Lee, and S. -H. Hong, Hierarchical micro/nano-structured nanoimprinting stamp fabrication for superhydrophobic application, *Appl. Spectrosc.*

Rev. **51**, 636-645 (2016).

[243] H. Yu, J. Liu, X. Fan, W. Yan, L. Han, J. Han, X. Zhang, T. Hong, and Z. Liu, Bionic micro-nano-bump-structures with a good self-cleaning property: the growth of ZnO nanoarrays modified by polystyrene spheres, *Mater. Chem. Phys.* **170**, 52-61 (2016).

[244] J. Bonse, S. V. Kirner, M. Griepentrog, D. Spaltmann, and J. Krüger, Femtosecond laser texturing of surfaces for tribological application, *Materials* **11**, 801 (2018).

[245] S, Chang, X. Guo, and X. Ni, Optical metasurfaces: progress and applications, *Ann. Rev. Mater. Res.* **48**, 279-302 (2018).

[246] Y. P. Meshcheryakov and N. M. Bulgakova, Thermoelastic modeling of microbump and nanojet formation on nanosize gold films under femtosecond laser irradiation, *Appl. Phys. A* **82**, 363-368 (2006).

[247] D. S. Ivanov, B. Rethfeld, G. M. O'Connor, T. J. Glynn, A. N. Volkov, and L. V. Zhigilei, The mechanisms of nano-bump formation in femtosecond pulse laser nanostructuring of thin metal films, *Appl. Phys. A* **92**, 791-796 (2008).

[248] P. A. Danilov, D. A. Zayarny, A. A. Ionin, S. I. Kudryashov, T. T. H. Nguyen, A. A. Rudenko, I. N. Saraeva, A. A. Kuchmizhak, O. B. Vitrik, and Y. N. Kulchin, Structure and laser-fabrication mechanisms of microcones on silver films of variable thickness, *JETP Lett.* **103**, 549-552 (2016).

[249] J. P. Moening and D. G. Georgiev, Formation of conical silicon tips with nanoscale sharpness by localized laser irradiation, *J. Appl. Phys.* **107**, 014307 (2010).

[250] D. Kawamura, A. Takita, Y. Hayasaki, and N. Nishida, Bump formation on a glass surface with a transparent coating using femtosecond laser processing, *Appl. Phys. A* **85**, 39-43 (2006).

[251] Y. Hayasaki and D. Kawamura, High-density bump formation on a glass surface using femtosecond laser processing in water, *Appl. Phys. A* **87**, 691-695 (2007).

[252] L. T. Cangueiro, A. J. Cavaleiro, J. Morgiel, and R. Vilar, Mechanisms of the formation of low spatial frequency LIPSS on Ni/Ti reactive multilayers, *J. Phys. D* **49**, 365103 (2016).

[253] Y. Kohmura, V. Zhakhovsky, D. Takei, Y. Suzuki, A. Takeuchi, I. Inoue, Y. Inubushi, N. Inogamov, T. Ishikawa, and M. Yabashi, Nano-structuring of multi-layer material by single x-ray vortex pulse with femtosecond duration, *Appl. Phys. Lett.* **112**, 123103 (2018).

[254] A. F. Voter and S. P. Chen, Accurate interatomic potentials for Ni, Al and Ni3Al, *Mater. Res. Soc. Symp. Proc.* **82**, 175-180 (1986).

[255] R. C. Weast (ed.), *Handbook of Chemistry and Physics*, 64 ed., (CRC Press, Boca Raton, 1983).

[256] G. J. Gloor, G. Jackson, F. J. Blas, and E. de Miguel, Test-area simulation method for the direct determination of the interfacial tension of systems with continuous or discontinuous potentials, *J. Chem. Phys.* **123**, 134703 (2005).

[257] N. W. Ashcroft and N. D. Mermin, *Solid State Physics* (Holt, Rinehart and Winston, New York, 1976).

[258] E. T. Karim, M. Shugaev, C. Wu, Z. Lin, R. F. Hainsey, and L. V. Zhigilei, Atomistic simulation study of short pulse laser interactions with a metal target under conditions of spatial confinement by a transparent overlayer, *J. Appl. Phys.* **115**, 183501 (2014).

[259] S. G. Kaustubh and T. L. Alford, Contact angle measurements for adhesion energy evaluation of silver and copper films on parylene-n and SiO_2 substrates, *J. Appl. Phys.* **93**, 919-923 (2002).

[260] J. Byskov-Nielsen, J. -M. Savolainen, M. S. Christensen, and P. Balling, Ultra-short pulse laser ablation of copper, silver and tungsten: experimental data and two-temperature model simulations, *Appl. Phys. A* **103**, 447-453 (2011).

[261] B. C. Gundrum, D. G. Cahill, and R. S. Averback, Thermal conductance of metal-metal interfaces, *Phys. Rev. B* **72**, 245426 (2005).

[262] R. B. Wilson and D. G. Cahill, Experimental validation of the interfacial form of the Wiedemann-Franz law, *Phys. Rev. Lett.* **108**, 255901 (2012).

[263] R. Cheaito, K. Hattar, J. T. Gaskins, A. K. Yadav, J. C. Duda, T. E. Beechem, J. F. Ihlefeld, E. S. Piekos, J. K. Baldwin, A. Misra, and P. E. Hopkins, Thermal flux limited electron Kapitza conductance in copper-niobium multilayers, *Appl. Phys. Lett.* **106**, 093114 (2015).

[264] J. Pudell, A. A. Maznev, M. Herzog, M. Kronseder, C. H. Back, G. Malinowski, A. von Reppert, and M. Bargheer, Layer specific observation of slow thermal equilibration in ultrathin metallic nanostructures by femtosecond X-ray diffraction, *Nat. Commun.* **9**, 3335 (2018).

[265] A. D. Rakić, A. B. Djurišić, J. M. Elazar, and M. L. Majewski, Optical properties of metallic films for vertical-cavity optoelectronic devices, *Appl. Opt.* **37**, 5271-5283 (1998).

[266] E. L. Gurevich, Y. Levy, S. V. Gurevich, and N. M. Bulgakova, Role of the temperature dynamics in formation of nanopatterns upon single femtosecond laser pulses on gold, *Phys. Rev. B* **95**, 054305 (2017).

[267] T. Q. Qiu and C. L. Tien, Femtosecond laser heating of multi-layer metals—I. Analysis, *Int. J. Heat Mass Transf.* **37**, 2789-2797 (1994).

[268] T. Q. Qiu, T. Juhasz, C. Suarez, W. E. Bron, and C. L. Tien, Femtosecond laser heating of multi-layer metals—II. Experiments, *Int. J. Heat Mass Transf.* **37**, 2799-2808 (1994).

[269] G. -M. Choi, R. B. Wilson, and D. G. Cahill, Indirect heating of Pt by short-pulse laser irradiation of Au in a nanoscale Pt/Au bilayer, *Phys. Rev. B* **89**, 064307 (2014).

[270] A. Vrij, Possible mechanism for the spontaneous rupture of thin, free liquid films, *Discuss. Faraday Soc.* **42**, 23-33 (1966).

[271] B. N. Chichkov, C. Momma, S. Nolte, F. von Alvensleben, and A. Tünnermann, Femtosecond, picosecond and nanosecond laser ablation of solids, *Appl. Phys. A* **63**, 109-115 (1996).

[272] R. L. Harzic, N. Huot, E. Audouard, C. Jonin, P. Laporte, S. Valette, A. Fraczkiewicz, and R. Fortunier, Comparison of heat-affected zones due to nanosecond and femtosecond laser pulses using transmission electronic microscopy, *Appl. Phys. Lett.* **80**, 3886-3888 (2002).

[273] B. R. Tull, J. E. Carey, E. Mazur, J. P. McDonald, and S. M. Yalisove, Silicon surface morphologies after femtosecond laser irradiation, *MRS Bull.* **31**, 626-633 (2006).

[274] A. Y. Vorobyev and C. Guo, Effects of nanostructure-covered femtosecond laser-induced periodic surface structures on optical absorptance of metals, *Appl. Phys. A* **86**, 321-324 (2007).

[275] Q. -Z. Zhao, S. Malzer, L. -J. Wang, Self-organized tungsten nanospikes grown on subwavelength ripples induced by femtosecond laser pulses, *Opt. Express* **15**, 15741-15746 (2007).

[276] Y. Dai, M. He, H. Bian, B. Lu, X. Yan, and G. Ma, Femtosecond laser nanostructuring of silve film, *Appl. Phys. A* **106**, 567-574 (2012).

[277] E. Borsella, S. Botti, R. Giorgi, S. Martelli, S. Turtù, and G. Zappa, Laser-driven synthesis of nanocrystalline alumina powders from gas-phase precursors, *Appl. Phys. Lett.* **63**, 1345-1347 (1993).

[278] J. Heitz and J. T. Dickinson, Characterization of particulates accompanying laser ablation of pressed polytetrafluorethylene (PTFE) targets, *Appl. Phys. A* **68**, 515-523 (1999).

[279] P. Ayyub, R. Chandra, P. Taneja, A. K. Sharma, and R. Pinto, Synthesis of nanocrystalline material by sputtering and laser ablation at low temperatures, *Appl. Phys. A* **73**, 67-73 (2001).

[280] S. Barcikowski, A. Hahn, A. V. Kabashin, and B. N. Chichkov, Properties of nanoparticles generated during femtosecond laser machining in air and water, *Appl. Phys. A* **87**, 47-55 (2007).

[281] J. Perrière, C. Boulmer-Leborgne, R. Benzerga, and S. Tricot, Nanoparticle formation by femtosecond laser ablation, *J. Phys. D: Appl. Phys.* **40**, 7069-7076 (2007).

[282] N. Haustrup and G. M. O’Connor, Impact of wavelength dependent thermoelastic laser ablation mechanism on the generation of nanoparticles from thin gold films, *Appl. Phys. Lett.* **101**, 263107 (2012).

[283] A. Miotello and N. Patel, Pulsed laser deposition of cluster-assembled films for catalysis and the photocatalysis relevant to energy and the environment, *Appl. Surf. Sci.* **278**, 19-25 (2013).

[284] A. Okano and K. Takayanagi, Neutral silicon clusters produced by laser ablation in vacuum, *Appl. Surf. Sci.* **127-129**, 362-367 (1998).

[285] D. E. Hare, J. Franken, and D. D. Dlott, Coherent Raman measurements of polymer thin-film pressure and temperature during picosecond laser ablation, *J. Appl. Phys.* **77**, 5950-5960 (1995).

[286] M. Handschuh, S. Nettesheim, and R. Zenobi, Laser-induced molecular desorption and particle ejection from organic films, *Appl. Surf. Sci.* **137**, 125-135 (1999).

[287] G. Paltauf and H. Schmidt-Kloiber, Microcavity dynamics during laser-induced spallation of liquids and gels, *Appl. Phys. A* **62**, 303-311 (1996).

[288] L. V. Zhigilei, D. S. Ivanov, E. Leveugle, B. Sadigh, and E. M. Bringa, Computer modeling of laser melting and spallation of metal targets, *Proc. SPIE* **5448**, 505-519 (2004).

[289] C. Schäfer and H. M. Urbassek, Metal ablation by picosecond laser pulses: a hybrid simulation, *Phys. Rev. B* **66**, 115404 (2002).

[290] L. V. Zhigilei and B. J. Garrison, Molecular dynamics simulation study of the fluence dependence of particle yield and plume composition in laser desorption and ablation of organic solids, *Appl. Phys. Lett* **74**, 1341-1343 (1999).

[291] L. V. Zhigilei, Computational model for multiscale simulation of laser ablation, *Mater. Res. Soc. Symp. Proc.* **677**, AA2.1.1-AA2.1.11 (2001).

[292] X. Wang and X. Xu, Molecular dynamics simulation of heat transfer and phase change during laser material interaction, *J. Heat Transfer* **124**, 265-274 (2002).

[293] L. V. Zhigilei, P. B. S. Kodali, and B. J. Garrison, Molecular dynamics model for laser ablation and desorption of organic solids, *J. Phys. Chem. B* **101**, 2028-2037 (1997).

[294] R. F. W. Herrmann, J. Gerlach, and E. E. B. Campbell, Ultrashort pulse laser ablation of silicon: an MD simulation study, *Appl. Phys. A* **66**, 35-42 (1998).

[295] P. Lorazo, L. J. Lewis, and M. Meunier, Short-pulse laser ablation of solids: from phase explosion to fragmentation, *Phys. Rev. Lett.* **91**, 225502 (2003).

[296] P. Lorazo, L. J. Lewis, and M. Meunier, Thermodynamic pathways to melting, ablation, and solidification in absorbing solids under pulsed laser irradiation, *Phys. Rev. B* **73**, 134108 (2006).

[297] L. V. Zhigilei and E. Leveugle, Computer simulations of laser ablation of molecular substrates, *Chem. Rev.* **103**, 321-347 (2003).

[298] N. N. Nedialkov, P. A. Atanasov, S. E. Imamova, A. Ruf, P. Berger, and F. Dausinger, Dynamics of the ejected material in ultra-short laser ablation of metals, *Appl. Phys. A* **79**, 1121-1125 (2004).

[299] C. Cheng and X. Xu, Mechanisms of decomposition of metal during femtosecond laser ablation, *Phys. Rev. B* **72**, 165415 (2005).

[300] S. Amoruso, R. Bruzzese, X. Wang, N. N. Nedialkov, and P. A. Atanasov, Femtosecond laser ablation of nickel in vacuum, *J. Phys. D: Appl. Phys.* **40**, 331-340 (2007).

[301] E. Leveugle and L. V. Zhigilei, Molecular dynamics simulation study of the ejection and transport of polymer molecules in matrix-assisted pulsed laser evaporation, *J. Appl. Phys.* **102**, 074914 (2007).

[302] L. Zhang and X. Wang, Hybrid atomistic-macroscale modeling of long-time phase change in nanosecond laser-material interaction, *Appl. Surf. Sci.* **255**, 3097-3103 (2008).

[303] L. V. Zhigilei, A. N. Volkov, E. Leveugle, and M. Tabetah, The effect of the target structure and composition on the ejection and transport of polymer molecules and carbon nanotubes in matrix-assisted pulsed laser evaporation, *Appl. Phys. A* **105**, 529-546 (2011).

[304] S. Sonntag, C. Trichet Paredes, J. Roth, and H. -R. Trebin, Molecular dynamics simulations of cluster distribution from femtosecond laser ablation in aluminum, *Appl. Phys. A* **104**, 559-565 (2011).

[305] G. J. Ackland and A. P. Jones, Applications of local crystal structure measures in experiment and simulation, *Phys. Rev. B* **73**, 054104 (2006).

[306] C. Deng and F. Sansoz, Fundamental differences in the plasticity of periodically twinned nanowires in Au, Ag, Al, Cu, Pb, and Ni, *Acta Mater.* **57**, 6090-6101 (2009).

[307] J. C. E, L. Wang, Y. Cai, H. A. Wu, and S. N. Luo, Crystallization in supercooled liquid Cu: homogeneous nucleation and growth, *J. Chem. Phys.* **142**, 064704 (2015).

[308] C. Desgranges and J. Delhommelle, Molecular mechanism for the cross-nucleation between polymorphs, *J. Am. Chem. Soc.* **128**, 10368-10369 (2006).

[309] H. -J. Zhang, S. -M. Peng, X. -S. Zhou, and X. Ju, Polymorphic crystals selected in the nucleation state, *Europhys. Lett.* **107**, 46002 (2014).

[310] T. E. Itina, K. Gouriet, L. V. Zhigilei, S. Noël, J. Hermann, and M. Sentis, Mechanisms of small clusters production by short and ultra-short laser ablation, *Appl. Surf. Sci.* **253**, 7656-7661 (2007).

[311] T. E. Itina and L. V. Zhigilei, Generation of nanoparticles by laser ablation: combined MD-DSMC computational study, *J. Phsy.: Conf. Ser.* **59**, 44-49 (2007).

[312] M. I. Zeifman, B. J. Garrison, and L. V. Zhigilei, Multiscale simulation of laser ablation of organic solids, evolution of the plume, *Appl. Surf. Sci.* **197-198** 27-34 (2002).

[313] M. I. Zeifman, B. J. Garrison, and L. V. Zhigilei, Combined molecular dynamics-direct simulation Monte Carlo computational study of laser ablation plume evolution, *J. Appl. Phys.* **92**, 2181-2193 (2002).

[314] S. Noël, J. Hermann, and T. Itina, Investigation of nanoparticle generation during femtosecond laser ablation of metals, *Appl. Surf. Sci.* **253**, 6310-6315 (2007).

[315] S. Amoruso, R. Bruzzese, C. Pagano, and X. Wang, Features of plasma plume evolution and material removal efficiency during femtosecond laser ablation of nickel in high vacuum, *Appl. Phys. A* **89**, 1017-1024 (2007).

[316] S. Amoruso, R. Bruzzese, X. Wang, and J. Xia, Propagation of a femtosecond pulsed laser plume into a background atmosphere, *Appl. Phys. Lett.* **92**, 041503 (2008).

[317] O. Albert, S. Roger, Y. Glinec, J. C. Loulergue, J. Etchepare, C. Boulmer-Leborgne, J. Perrière, and E. Millon, Time-resolved spectroscopy measurements of a titanium plasma induced by nanosecond and femtosecond lasers, *Appl. Phys. A* **76**, 319-323 (2003).

[318] N. Jegenyes, J. Etchepare, B. Reynier, D. Scuderi, A. Dos-Santos, and Z. Tóth, Time-resolved dynamics analysis of nanoparticles applying dual femtosecond laser pulses, *Appl. Phys. A* **91**, 385-392 (2008).

[319] Y. Okano, K. Oguri, T. Nishikawa, and H. Nakano, Observation of femtosecond-laser-induced ablation plumes of aluminum using space- and time-resolved soft X-ray absorption spectroscopy, *Appl. Phys. Lett.* **89**, 221502 (2006).

[320] H. Nakano, K. Oguri, Y. Okano, and T. Nishikawa, Dynamics of femtosecond-laser-ablated liquid-aluminum nanoparticles probed by means of spatiotemporally resolved X-ray absorption spectroscopy, *Appl. Phys. A* **101**, 523-531 (2010).

[321] H. M. Urbassek, Sputtered cluster mass distributions, thermodynamic equilibrium and critical phenomena, *Nucl. Instrum. Methods Phys. Res. B* **31**, 541-550 (1988)

[322] A. Bershadskii, Multiscaling and localized instabilities in fracture, fragmentation, and growth processes, *Eur. Phys. J. B* **14**, 323-327 (2000).

[323] J. A. Aström, R. P. Linna, J. Timonen, P. F. Möller, and L. Oddershede, Exponential and power-law mass distributions in brittle fragmentation, *Phys. Rev. E* **70**, 026104 (2004).

[324] G. Timár, J. Blömer, F. Kun, and H. J. Herrmann, New universality class for the fragmentation of plastic materials, *Phys. Rev. Lett.* **104**, 095502 (2010).

[325] E. Leveugle, L. V. Zhigilei, A. Sellinger, and J. M. Fitz-Gerald, Computational and experimental study of the cluster size distribution in MAPLE, *Appl. Surf. Sci.* **253**, 6456-6460 (2007).

[326] A. Wucher and B. J. Garrison, Cluster formation in sputtering: a molecular dynamics study using the MD/MC-corrected effective medium potential, *J. Chem. Phys.* **105**, 5999-6007 (1996).

[327] Th. J. Colla, H. M. Urbassek, A. Wucher, C. Staudt, R. Heinrich, B. J. Garrison, C. Dandachi, G. Betz, Experiment and simulation of cluster emission from 5 keV Ar → Cu, *Nucl. Instrum. Methods, Phys. Res. B* **143**, 284-297 (1998).

[328] T. Muramoto, M. Okai, Y. Yamashita, K. Yorizane, and Y. Yamanura, MD simulation of cluster formation during sputtering, *Nucl. Instrum. Methods, Phys. Res. B* **180**, 222-229 (2001).

[329] K. B. Shepard, C. B. Arnold, and R. D. Priestley, Origins of nanostructure in amorphous polymer coatings via matrix assisted pulsed laser evaporation, *Appl. Phys. Lett.* **103**, 123105 (2013).

[330] S. -H. Lai, K. -H. Chang, J. -L. Lin, C. -L. Wu, and C. -H. Chen, Sinapinic acid clusters distribution from monomer to mega Dalton's region in MALDI process, *Chem. Phys. Lett.* **561-562**, 142-146 (2013).